Dissertation

submitted to the
Combined Faculties for the Natural Sciences and for Mathematics
of the Ruperto-Carola University of Heidelberg, Germany
for the degree of
Doctor of Natural Sciences

Presented by
Siva Rama Krishnan, M. Sc.
Born in Chennai, India

Oral examination: 09.12.2011

Doped Helium Nanodroplets in Intense Few-Cycle Infrared Pulses

Referees: **Prof. Dr. Joachim Ullrich**
Prof. Dr. Ulf Saalmann

Zusammenfassung

Die vorliegende Arbeit beschreibt experimentelle Untersuchungen zur Wechselwirkung ultrakurzer (10 fs, 800 nm) Laserpulse mit Helium-Nanotröpchen. In Einpulsmessungen konnte bei Spitzenintensitäten im Bereich von 10^{14} bis $10^{15}\,\mathrm{W/cm^2}$ gezeigt werden, dass weniger als 10 Dotierungsatome in einem aus 10^4 Heliumatomen bestehenden Tröpchen um eine vollständige Ionisierung zu "zünden" ausreichen. Diese experimentellen Beobachtungen, die durch theoretische Modellrechnungen gestützt werden, zeigen erstmalig die sehr effiziente Absorption und resonante Kopplung intensiver Laserfelder im nahen Infraroten an Cluster-Nanoplasmen auf einer Zeitskala von 10 fs. Anhand von Pump-Probe Messungen, die mit zwei zeitlich verzögerten Laserpulsen durchgeführt wurden, konnte die Auswirkung der Dotierung auf die bei der Ausdehnung des teilweise ionisierten Clusters auftretende Nanoplasma-Resonanz untersucht werden. Die Rolle der sich im Zentrum des Clusters befindlichen hochgeladenen Dotierungsatome (typischerweise Xenon) und der sie umgebenden Schale aus Helium-Ionen auf die auf (Sub-) Pikosekunden-Zeitskalen stattfindende Clusterexpansion wurde untersucht. Hierbei wurde erstmalig die Wichtigkeit der sich schnell ausdehnenden Helium-Schalen experimentell erkannt, wodurch die vorliegende Arbeit den Anstoß zu einer neuen Betrachtungsweise der expansionsinduzierten Resonanz in dotierten Nanotröpchen liefert.

Summary

In this dissertation, experimental studies on the interaction of intense few-cycle pulses with doped helium nanodroplets are reported. In single-pulse measurements, the dopant induced ignition of He nanodroplets by 10 fs near-infrared (NIR) pulses of peak intensities in the range of $10^{14} - 10^{15}\,\mathrm{W \cdot cm^{-2}}$ is demonstrated. This results in the complete ionization of all the 10^4 He atoms in the droplet triggered by less than 10 dopant atoms residing at the center. These experimental observations aided by a theoretical model demonstrate for the first time, a very efficient absorption and resonant coupling of intense NIR laser fields to cluster nanoplasmas on a 10 fs timescale. In pump-probe studies performed with two 10 fs pulses, the effects of doping these large He nanodroplets with few atoms (1... 50) on the previously known nanoplasma resonance due to ionic expansion are investigated. The crucial roles played by the highly-charged dopant ions at the center and the surrounding by helium ions on this expansion occurring on sub- or few-picosecond timescales are studied. This highlights the prominent dynamical role of the fast expanding shells of He ions, which was not apparent from previous experiments. Hence, the pump-probe studies reported in this work call for a revised view of the expansion-induced resonance in such composite nanoplasmas.

List of publications

The following articles resulting from the work presented in this dissertation were accepted/published in peer-reviewed journals:

- *Dopant-induced ignition of He nanodroplets in intense few-cycle laser pulses,* **S. R. Krishnan**, L. Fechner, M. Kremer, V. Sharma, B. Fischer, N. Camus, J. Jha, M. Krishnamurthy, T. Pfeifer, R. Moshammer, J. Ullrich, F. Stienkemeier, M. Mudrich, A. Mikaberidze, U. Saalmann and J. -M. Rost, *Physical Review Letters (accepted)*, 2011. (http://arxiv.org/abs/1107.4482v1).

Articles in preparation:

- *Time-resolved intense field ionization dynamics of doped He nanodroplets in the ionic expansion regime,* **S. R. Krishnan**, L. Fechner, M. Kremer, V. Sharma, B. Fischer, N. Camus, J. Jha, M. Krishnamurthy, T. Pfeifer, R. Moshammer, J. Ullrich, F. Stienkemeier, M. Mudrich.

Contents

Chapter 1

Introduction

The emergence of femtosecond dynamics is often marked on the time-line by the Nobel prize in chemistry awarded to Ahmed H. Zewail in 1999 [Gre03, Zew02]. In the epilogue of his Nobel lecture, Zewail remarks:

> "As the ability to explore shorter and shorter timescales has progressed from the millisecond to the present stage of widely exploited femtosecond capabilities, each step along the way has provided surprising discoveries, new understanding and new mysteries. Developments will continue and new directions, of research will be pursued. Surely, studies...will remain active for exploration in new directions, from simple systems to complex enzymes and proteins, and from probing to controlling matter."

True to this expectation, active research in femtosecond dynamics is undergoing an explosive growth during the current times. Few- and many-particle atomic systems are being studied with increasingly shorter probes facilitated by several key developments in the technology of photon, electron and ion sources. In particular, laser sources in near-infrared (NIR), visible and shorter wavelengths offer excellent resolution and control in both the time and the frequency domain, which have improved continuously over the years [Hec10, HKP10]. While the invention of the laser itself was revolutionary [Tow02], a major breakthrough in pulsed laser technology employing solid-state gain media, most notably Ti:Sapphire, enabled access to sufficiently intense coherent light pulses on the femtosecond timescale [SM85, SKS91]. Ultrafast science is also moving rapidly from the femtosecond to the attosecond domain [CK07]. Opportunities to probe atomic systems on increasingly shorter timescales are becoming routinely available in laboratories around the world.

A natural outcome of femtosecond laser science is the availability of intense laser pulses in the ultra-violet (UV), visible (VIS) and near-infrared (NIR) domains. In this range of frequencies, table-top laser systems can deliver intense femtosecond pulses. We may qualify the adjective "intense" better by comparing the laser electric field to that experienced by the bound electron in the 1s level of the hydrogen atom. This corresponds to an intensity of $\approx 3.5 \times 10^{16}\,\mathrm{W{\cdot}cm^{-2}}$ [PKK97]. For a typical NIR laser pulse with a central wavelength of $\approx 800\,\mathrm{nm}$ and intensities of the order of $10^{14}\,\mathrm{W{\cdot}cm^{-2}}$, the electric field of the laser can deform the atomic Coulomb barrier sufficiently so that bound electrons in the outer shell of the atom

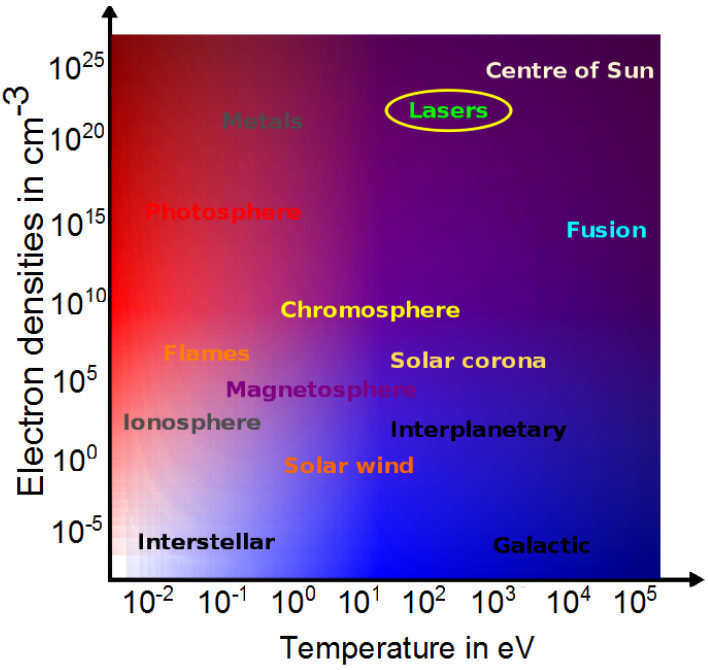

Figure 1.1: Ranges of plasmas: A wide variety of natural and man-made plasmas are represented in this temperature-density diagram. Laser-plasmas can have high densities and temperatures simultaneously. Adapted from [Per96].

may escape by tunneling. The oscillating electric field can also drive the wavepacket of the released electron back to its parent ion. This leads to very interesting complex quantum dynamics in the process of ionization by such intense laser fields [WSKD96, MUF+03, RdJE+07]. The quantum dynamics of isolated atoms and molecules is sufficiently complex to evoke continuing interest and curiosity [GSM+09, KFF+09, FKP+10].

A natural step forward in intense field science is the study of increasingly complex atomic and molecular systems. Ionization of atomic aggregates or bulk matter leads to the formation of a plasma. Plasmas constitute 99% of (non-dark) matter in the universe and are interesting for a variety of reasons. The temperature-density plot of naturally occurring and man-made plasmas is shown in figure 1.1. This summarizes the scope of the rich variety of phenomenology occurring in this state of matter. In terms of complexity, the most interesting plasmas are those occurring at high densities and high temperatures. Particles constituting such systems interact repeatedly with each other. When both the number of interactions and the interaction energy are sufficiently large, *collective* behavior emerges. A measure of the collective nature of interactions is provided by the ratio of the potential energy and thermal energy of interacting particles in the plasma in the form of the dimensionless Coulomb coupling parameter defined by [CL84], $\Gamma = e^2/ak_BT$ where e is the electron charge, a the inter-particle spacing, T the electron temperature and k_B the Boltzmann constant. For $\Gamma \ll 1$ the behavior is similar to that of an ideal gas. On the other hand, in the strong coupling regime characterized by $\Gamma \gg 1$ interaction between particles is a dominant factor in plasma behavior. This is realized, for example, in ultracold plasmas which are becoming possible to create in laboratories [KKB+99]. Many interesting properties of ultracold gaseous plasmas such as

self-organization and crystallization for $\Gamma > 174$ have been predicted [PPR04]. The intermediate regime of $\Gamma \approx 1$ where collective electronic behavior begins to gain importance, indeed presents a curious and interesting scenario [BHB10]. Plasmas in solid or liquid matter formed by the ionization with intense laser pulses fall into this category. Thus, we may expect emergent collective phenomena in these plasmas.

We may go a step further and consider plasmas in ionized atomic aggregates with near-solid density whose size is comparable to the inter-particle separation. In such mesoscopic plasmas, in addition to electron density and temperature, the plasma boundary plays an important role. Plasma morphology is crucial in determining the properties and behavior of these systems. Van der Waals bound atomic clusters ($1-100\,\mathrm{nm}$ in diameter) [HO72, Hab94] are easy targets for intense field-ionization and the creation of mesoscopic nanoplasmas. The type of dynamics that ensues upon intense field-ionization of clusters depends on the photon energy. A very wide range of intense coherent photon sources are currently being used to investigate the ionization of atomic clusters. These range from table-top systems to unique free-electron lasers (FELs) which are international facilities [SSR06, FMBT$^+$10, TGB11]. This also ensures that these intense photon sources cover the entire spectrum from the infrared frequencies to hard X-rays. The type of collective behavior in these nanoplasmas is determined largely by the relation of the frequency of the driving laser field to the eigenfrequency Ω of the fundamental mode of charge oscillations given by [Ros09], $\Omega = \sqrt{4\pi e^2 Z^2 \varrho/m}$, where ϱ is the density of particles with a charge of eZ and mass m. When the photon frequency remains far away from this eigenfrequency during ionization, the dynamics is characterized by a multiphoton picture [HWY02]. However, if the frequency of the driving field approaches Ω during the dynamics, collective behavior emerges almost independent of the specific nature of plasma constituents. Plasmas resulting from the intense field-ionization of atomic clusters by NIR laser pulses fall in this category [SSR06, FMBT$^+$10]. Not only do these systems provide ample scope for studying complex phenomena specific to individual systems, but they also provide opportunities to learn about several generic aspects of intense NIR laser-matter interactions. This is also very true for the studies being presented in this dissertation, as will become clear in the detailed description of our work. Pristine or homonuclear clusters have been investigated extensively in intense NIR laser fields [KSS07, SSR06, FMBT$^+$10]. Some recent experimental [JK08b, HBT$^+$08, DDP$^+$07] and theoretical [MSR09] investigations have drawn attention to composite two-component clusters. We study the ionization dynamics of composite clusters in the form of doped He nanodroplets [TV04, SL06] in intense few-cycle ($\sim 10\,\mathrm{fs}$) NIR pulses. Ionization of doped He nanodroplets by such laser pulses has not been investigated before.

The organization of this dissertation is as follows. The two forthcoming chapters (2 and 3) prepare the ground work for the results presented in chapters 4 and 5. In chapter 2, we survey the important aspects of the ionization dynamics of atomic cluster systems in intense NIR laser pulses with durations ranging from ~ 25 to several hundred femtoseconds. To begin with, we introduce the concepts of intense field-ionization of isolated atoms. Then we present the salient features of cluster ionization in such laser fields. The central feature of this discussion is the nanoplasma resonance arising out of collective driven electron oscillations. Although this resonance relates to the coupling of the laser electric field to nanoplasma electrons,

it is achieved only when the cluster expands due to ionic motion which occurs on sub- or few-picosecond timescales. The consequences of this resonant interaction on the local electric field within the cluster and the enormous gain in electron kinetic energy due to multiple rescattering in the cluster potential are presented. General aspects of ion, electron and characteristic X-ray emission are also discussed in sufficient detail.

Chapter 3 presents the methodology employed to perform experiments on the intense NIR laser ionization of doped He nanodroplets. We describe the details of He nanodroplet generation. The characteristics of these nanodroplets and general aspects of rare-gas cluster beams produced by supersonic expansion are discussed. The process of controlled doping of He nanodroplets with foreign rare-gas atoms and the careful procedure for estimating doping levels are elucidated. Then we present the details of the femtosecond laser system used in these experiments and the time-of-flight spectrometer employed for the measurement of ion yields and kinetic energies resulting from the ionization of the doped nanodroplets.

The results of these experiments are presented in chapters 4 and 5. Under single-pulse excitation (chapter 4), we find that less than few dopant atoms dramatically alter the ionization dynamics of a large droplet containing 10^4 He atoms. This surprising effect which we call dopant induced ignition (DII) is studied in detail. The combined effort of experiment and theory reported here confirms that DII is due to the formation of a cigar-shaped nanoplasma around the dopant ions which reside at the center of the droplet. A clear distinction between the ionizing effect of the static field of dopant ions on the surrounding He atoms and the resonant DII effect is made. This establishes the unique role played by the ignition mechanism. DII completely ionizes all He atoms in nanodroplets independent of their size, triggered by dopant atoms of different species. The most important consequence of DII is that the well-known slow cluster expansion [Saa06] occurring on ps timescales is no longer a necessity for very efficient energy absorption by cluster nanoplasmas. Thus, DII provides a route to ultrafast resonant energy transfer on a $\sim 10\,\mathrm{fs}$ timescale. This resonant interaction is not restricted to doped clusters alone and it can be extended to other forms of matter where ionic expansion may not be possible.

The doping dependent dynamics of He nanodropets occurring on timescales of cluster expansion, i.e. ionic motion, are examined in chapter 5. In the dual-pulse excitation studies performed with a pump-probe set up, we find that the few dopant atoms in the large nanodroplet cause significant differences also to the expansion-induced dynamics. The consequences of DII occurring during the interaction with the pump remain important in determining the large scale dynamics occurring at long pump-probe delays. We examine the effect of laser intensities, droplet sizes and dopant species in this context. Finally, we observe that He ions resulting from these interactions are emitted preferentially along the laser polarization direction after cluster disintegration. This dissertation ends with a brief summary and outlook.

This thesis describes the experiments performed in the Experimental Quantum Dynamics division, Max Planck Institut für Kernphysik (MPIK), Heidelberg, Germany, in collaboration with the Molecular and Nanophysics division, Physikalisches Institut, University of Freiburg, Germany. The theoretical work and numerical simulations on DII which go hand in hand with the experiment are a result of the efforts

of colleagues at the Max Planck Institut für Physik Komplexer Systeme (MPIPKS), Dresden, Germany. Since the work being presented here is the result of a collaboration involving three research groups, the contributions of the author may be stated clearly. The author of this dissertation was responsible for the reconstruction and maintenance of the He nanodroplet source during the experimental campaign, the design of the complete ultra-high vacuum system, the design and execution of the time-of-flight mass spectrometer, the performance and running of the experiment itself (including the maintenance of a working laser system), the complete analysis of the experimental data and the conceptual understanding of the physics resulting therefrom. Extensive assistance was received from colleagues at MPIK in setting up the operation and troubleshooting of the laser system, when necessary.

Chapter 2

Intense IR laser ionization of rare-gas clusters

The study of intense laser ionization in near-infrared (NIR) fields has largely been a consequence of breakthroughs and developments in femtosecond laser technology. The invention of Kerr lens mode-locking [SKS91] and chirped pulse amplification [SM85] made intense ultrashort pulses at NIR, visible and ultraviolet frequencies available. This ushered in an era of novel experiments in which atoms, molecules, clusters and condensed media have been subject to scrutiny in intense femtosecond laser fields generated using table-top laser systems. The electric fields in such pulses become comparable to the Coulomb field binding the electron in the hydrogen atom. Pulses with intensities in the range of $10^{16} - 10^{18}\,\mathrm{W{\cdot}cm^{-2}}$ are routinely generated in laboratories. The perturbative approach for dealing with low-order nonlinear photoionization processes based on multiple photons interacting with individual electrons in atoms is replaced by one where the oscillating electric field enables electrons to tunnel out of their parent atoms or ions on a timescale of the order of one optical cycle or less. Electron wavepackets that escape the binding Coulomb potential into the continuum are strongly driven and accelerated by the laser field. When the laser field reverses its direction this electron is driven back to the parent ion causing a "recollision" during their "quiver" motion [PKK97].

In this chapter we begin with a discussion on the ionization of isolated rare-gas atoms in intense NIR fs pulses with peak intensities in the range of $10^{14-17}\,\mathrm{W{\cdot}cm^{-2}}$. Then we present a brief mathematical description of these pulses. The main discourse of this chapter is on the interaction of these intense fs pulses with rare-gas clusters. Within this, we use the harmonic oscillator description of cluster nanoplasmas to visualize the dynamics of quasi-free electrons. In the process, we highlight the importance of expansion-induced Mie resonance in the cluster. The implications of this resonant interaction on optical absorption and the emission of highly-charged ions, energetic electrons and characteristic X-rays by the cluster nanoplasma are discussed in detail. We present the dynamics of quasi-free electrons within the cluster from the perspective of multiple rescattering in the cluster potential. Thus, we build an intuitive picture of electron dynamics similar that observed in atoms. We close the chapter with a brief preview of the two most widely used *ab initio* computational methodologies that have helped in gaining insights into the nanoplasma dynamics observed in experiments.

2.1 Single atoms in intense IR laser fields

The study of linear and nonlinear photo-ionization processes is intimately related to the *annus mirabilis* in physics - 1905 - when Einstein enunciated the theory which successfully explained the escape of bound electrons from a metal surface [Ein05]. This occurs when a quantum of light [Pla01], the photon, with energy greater than the binding energy of a bound electron is absorbed by the atom. This theory of the photoelectric effect or photo-effect puts forward an elegant explanation for single photon ionization. Subsequently, theoretical investigations by Goppert-Mayer [GM31] revealed that two-photon transitions and consequently multi-photon ionization (MPI) in atoms and molecules are possible. MPI yields itself to a description in terms of the lowest-order perturbation theory [FFC82, PFA$^+$84, Lam76]. The rate of MPI involving n-photons is given by

$$\Gamma_n = \sigma_n (I/\hbar\omega)^n \tag{2.1}$$

where σ_n is the generalized cross section of the n-photon MPI process, I is the intensity and ω the frequency of the incident electromagnetic (EM) field. This n-photon ionization process occurs by a set of successive transitions via virtual states inter-spaced by the photon energy $\hbar\omega$ starting from the initial to the final state as shown in figure 2.1 (a) [Boy08]. Consequently, the rate of MPI is enhanced if any of the intermediate states turns out to be an eigenstate of the unperturbed system (e.g., a low-lying Rydberg state) leading to resonance enhanced multiphoton ionization (REMPI) [BZW$^+$94]. This result of perturbation theory breaks down when the electric field of the incident laser pulse becomes comparable to the electric field seen by the electron in the unperturbed atom. The intensity corresponding to the electric field experienced by the 1s electron in the hydrogen atom (5.1422×10^9 V/cm) is 3.51×10^{16} W/cm^2, which is one atomic unit of intensity. First signs of the insufficiency of the perturbative approach were observed in an experiment where a six-photon free-free transition was observed by Agostini et al. [AFM$^+$79]. For an ionization potential Φ_{IP} and laser frequency ω, if n is the smallest integer such that $^{n\hbar\omega}/_{\Phi_{IP}} > 1$, it was observed that an atom can absorb more than n photons resulting in above threshold ionization (ATI). The electrons released in this process had a kinetic energy spectrum with peaks at

$$K = (n+s)\hbar\omega - \Phi_{IP} - U_P; \qquad s \geqslant 1, \tag{2.2}$$

where U_P is the ponderomotive energy acquired by the electron in the laser field which will be explained in section 2.1.2. Underlying the origin of ATI is the distortion of the potential of the unperturbed atom by the laser field. This leads us to the discussion of atoms in electric fields and Keldysh theory.

2.1.1 Keldysh theory and ADK rates

When an electric field of magnitude E polarized along the r coordinate is incident on an atom, in addition to the Coulomb potential V_{Coul} the electron experiences the external potential $V_{\text{Ext}} = E \cdot r$ as shown in figure 2.1 (b). Here, we adopt a one-dimensional treatment of the problem to highlight its salient features. Thus,

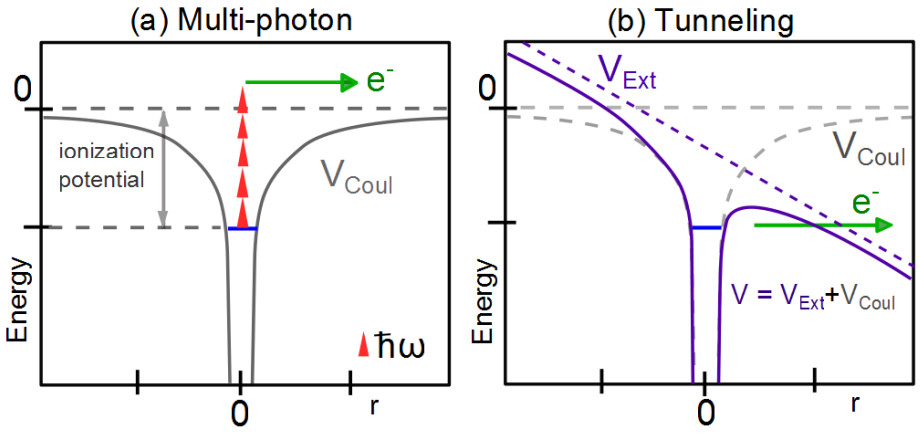

Figure 2.1: Schematic depicting (a) multi-photon ionization (MPI). Within the perturbative limit more than one photon of energy $\hbar\omega$ are simultaneously absorbed to release the electron in a bound state of the Coulomb potential V_{Coul} into the continuum. (b) Tunnel ionization: the external field (V_{Ext}) deforms the Coulomb potential (V_{Coul}) and the electron tunnels out of the deformed potential $V = V_{\text{Coul}} + V_{\text{Ext}}$.

the total potential is $V(r) = V_{\text{Coul}} + V_{\text{Ext}}$, which in the case of hydrogen-like ion with charge Z (in atomic units) reads:

$$V(r) = -\frac{Z}{r} + E \cdot r \tag{2.3}$$

Clearly the addition of a substantially large electric field leads to the deformation of the native Coulomb potential seen by the electron as in figure 2.1 (b). A classical analysis of this deformed potential reveals an alternative route for electrons to escape the binding potential. For negative values of r the electron remains bound. We can now find r_{barr} such that $^{\partial V}/_{\partial r} = 0$ for $r = r_{\text{barr}}$. From equation 2.3, $r_{\text{barr}} = \sqrt{Z/E}$. For $r > r_{\text{barr}}$ electrons in the states above the barrier at r_{barr} can escape to the right. Appropriately, this mechanism is called *over-the-barrier-ionization* (OBI) or *barrier-suppression ionization* (BSI). The field required for barrier-suppression as a function of the initial ion charge-state Z and its ionization potential Φ_{IP} is

$$E_{BSI} = \frac{(\Phi_{IP})^2}{4Z} \qquad \text{in atomic units.} \tag{2.4}$$

This expression is sometimes called the Bethe rule referring to the work in ref. [BS57]. If the EM field is a laser pulse, then it is useful to write down the corresponding barrier suppression intensity as

$$I_{BSI} = \frac{c}{128\pi}\frac{(\Phi_{IP})^4}{Z^2} \qquad \text{in atomic units,} \tag{2.5}$$

where c is the speed of light in atomic units. In arriving at this classical expression for I_{BSI} we have not considered the Stark-shift of the initial state due to the external field. These details are considered in ref. [SPDC90]. This intensity corresponds to the "appearance" or "threshold" intensity often mentioned in literature [AMSC91].

This instructive classical analysis clearly ignores quantum effects. A complete barrier suppression is not necessary for the electron to escape the bounding potential. Electrons can tunnel out of this barrier, to the right in figure 2.1 (b), as one may expect. Also, thus far we have implicitly considered the deformation of the atomic Coulomb field by a static field. But in the laboratory, this intense electric field is applied in the form of a laser pulse. Hence, the analysis presented above is valid when the time-dependent field deforming the native Coulomb potential is adiabatic. Thus, the introduction of an adiabaticity parameter that defines this adiabatic limit is pertinent and was first done by Keldysh [Kel64]. For an oscillating electric field with amplitude E, the Keldysh parameter γ is the ratio of the frequency of the laser field ω_0 and the tunneling rate or frequency ω_t:

$$\gamma = \frac{\omega_0}{\omega_t} = \sqrt{\frac{\Phi_{IP}}{2 \cdot (E^2/4\omega_0^2)}}. \tag{2.6}$$

It is clear from equation 2.6 that at high intensities when $\gamma \ll 1$ the laser frequency is smaller than the rate of tunneling of electrons. Thus, *tunneling ionization* occurs for $\gamma \ll 1$. At small intensities $\gamma \gg 1$, the change of the electric field is not adiabatic any more[1]. Hence, in this limit, ionization is more appropriately described in the photon picture by the absorption of n photons, which is the case of multiphoton ionization.

Perelemov, Popov and Terent'ev derived an expression for the rate of tunneling ionization in hydrogen-like ions [PPT66]. The ionization rate for complex atoms calculated by Ammosov, Delone and Krainov is popularly referred to as the ADK rate [ADK86] which is given by (in atomic units)

$$w_{ADK} = C_{n^*}^2 f(l,m) \frac{Z^2}{2(n^*)^2} \sqrt{\frac{3En^{*3}}{\pi Z^3}} \left(\frac{2Z^3}{En^{*3}}\right)^{2n^*-|m|-1} \exp\left(-\frac{2Z^3}{3n^{*3}E}\right), \tag{2.7}$$

with

$$C_{n^*} = \left(\frac{2\mathrm{e}}{n^*}\right)^{n^*} (2\pi n^*)^{1/2}, \; f(l,m) = \frac{(2l+1)(l+|m|)!}{2^{|m|}\,|m|!\,(l-|m|)!},$$

where $\mathrm{e} = 2.71\overline{828}$, $n^* = {}^{Z}/_{\sqrt{\Phi_{IP}}}$ is the effective quantum number, l and m are the (effective) angular quantum numbers of the initial state with ionization potential Φ_{IP}. This expression is valid in the tunneling regime $\gamma \ll 1$. A modification of the ADK rate for the non-adiabatic regime where $\gamma \approx 1$ has been derived by Yudin and Ivanov [YI01] and is qualitatively similar.

2.1.2 Ponderomotive energy and Quiver motion

The electron (wavepacket) released from the atomic bound state due to ionization by the laser field is still under the influence of the oscillating field. A classical analysis can reveal many important aspects of this phenomenon. In this analysis

[1]Strictly speaking, tunneling time in Keldysh theory is necessarily an imaginary parameter. But, it serves the purpose of developing an intuitive picture.

we follow refs. [PKK97, Gop09] and use atomic units. Let us consider the linearly polarized laser electric field

$$\overrightarrow{E} = \hat{z} E_0 \sin(\omega_0 t), \tag{2.8}$$

where E_0 is the electric field amplitude and ω_0 is the laser frequency. Considering only the $\hat{z}$-component so that we can drop the vector signs, the instantaneous momentum of the electron $p(t)$ can be derived from Newton's second law (in atomic units)

$$\dot{p}(t) = -E(t). \tag{2.9}$$

For an electron released at a time t_0 into the continuum, the momentum acquired due to driving by the laser field (or quiver motion) is

$$p(t) = -\int_{t_0}^{t} E(t')\, dt'. \tag{2.10}$$

The integration yields

$$p(t) = \frac{E_0}{\omega} (\cos\omega_0 t - \cos\omega_0 t_0). \tag{2.11}$$

The first in this equation is the time varying quiver term and the second refers to the drift motion. We can examine the above equation for the case of a laser pulse of a finite time duration so that $E(t \to \infty) = 0$. Hence the momentum acquired at the end of the pulse is

$$p = p(\infty) = -\frac{E_0}{\omega_0} \cos(\omega_0 t_0). \tag{2.12}$$

We may write $E(t)$ in terms of its vector potential $A(t)$ so that

$$E(t) = -\frac{\partial A(t)}{\partial t} \text{ and} \tag{2.13}$$

$$A(t_0) = A_0 \cos\omega_0 t_0 = -\int_{-\infty}^{t_0} E(t') dt' = \frac{E_0}{\omega} \cos\omega_0 t_0. \tag{2.14}$$

So, in view of equation 2.12 we may write

$$p + A(t_0) = 0. \tag{2.15}$$

Clearly, the momentum acquired is dependent on the phase $\phi_0 = \omega_0 t_0$ at which the released electron is "born" during the laser pulse. Since the electron can be born with any phase during the pulse, the cycle-averaged kinetic energy acquired by the electron is given by (in atomic units)

$$U_p = \frac{1}{2\pi} \int_0^{2\pi} \left(-\frac{E_0}{\omega_0} \cos\phi_0 \right)^2 d\phi_0. \tag{2.16}$$

This yields

$$U_p = \frac{E_0^2}{4\omega_0^2}. \tag{2.17}$$

U_p is called the *ponderomotive energy* which the electron gains from the driving laser field. U_p can be written in terms of laser intensity I and wavelength λ in convenient units as

$$U_p = 9.33 \times 10^{-14} I \left(\mathrm{W{\cdot}cm^{-2}}\right) \lambda^2 \left(\mu\mathrm{m}\right). \tag{2.18}$$

Thus, $U_p \propto I\,\lambda^2$ also provides a scale for electron kinetic energies involved in the quiver motion. Now we can write the maximum momentum gained by the electron using equations 2.12 and 2.17 as

$$p_{\max} = \frac{E_0}{\omega_0} = A_0 = 2\sqrt{U_p}. \tag{2.19}$$

Thus, maximum momentum is gained by electrons that are born when $\omega_0 t_0 = n\pi$, $n = 0, 1, 2, 3, ...$ Clearly, these are the times when the electric field is zero but correspond to maxima in the vector potential. Electrons released at different times can have trajectories such that they return to the parent atom or ion ($z = 0$). This is shown in figure 2.2 and the process is termed recollision. In terms of U_p the drift energy gained by an electron born at a phase $\phi_0 = \omega_0 t_0$ is given by $K_{\mathrm{drift}}(t_0) = 2U_p \sin^2(\omega_0 t_0)$. One can immediately see that the recolliding electron can cause a subsequent ionization releasing another bound electron in an (e,2e)-like process if the recollision kinetic energy is sufficiently large as has indeed been observed e.g. by Rudenko et al. [RdJE+07]. This also brings to attention the need to look beyond the single active electron approach implicit in what has been discussed here. It opens up the exciting possibility of studying correlated emission of electrons and signatures of so-called non-sequential processes [WSD+94, MFS+00, MFCLU+02].

Further, this classical analysis reveals that the maximum kinetic energy that can be acquired by an electron in one recollision is $3.17 \cdot U_p$ [Cor94] which corresponds to a phase of $\phi_0 = 17°$ or $197°$ at the birth of the electron. This recollision picture, popularly referred to as the *three-step model,* has been successfully applied to understand several features of the high-harmonic generation process and most impressively, the cut-off of harmonics at $3.17 \cdot U_p$ [Cor94, BK00]. In combination with the expression in equation 2.18, it can be easily seen that harmonics in the photon energy range $1 - 100\,\mathrm{eV}$ can be generated with laser pulses with intensities of the order of $\sim 10^{14}\,\mathrm{W{\cdot}cm^{-2}}$.

We can also integrate equation 2.11 once more to obtain the excursion of the electron from the nucleus of the parent atom as a function of time. The maximum excursion from the nucleus - the quiver amplitude - is given by

$$a_{\mathrm{quiv}} = \frac{E_0}{\omega_0^2} \quad \text{(in a.u.)}, \tag{2.20}$$

For fields of strength $\sim 10^{15}\,\mathrm{W{\cdot}cm^{-2}}$ the quiver amplitude is $\sim 1\,\mathrm{nm}$ which is several times the Bohr radius ($0.0529\,\mathrm{nm}$).

2.1.3 Brief preview of femtosecond IR pulses

Apart from offering better time resolution to study ionization processes, the need for femtosecond laser pulses is imperative in the study of photoionization by high-order nonlinear processes like tunneling. In long pulses ($\sim 50\,\mathrm{ps}$), saturation of

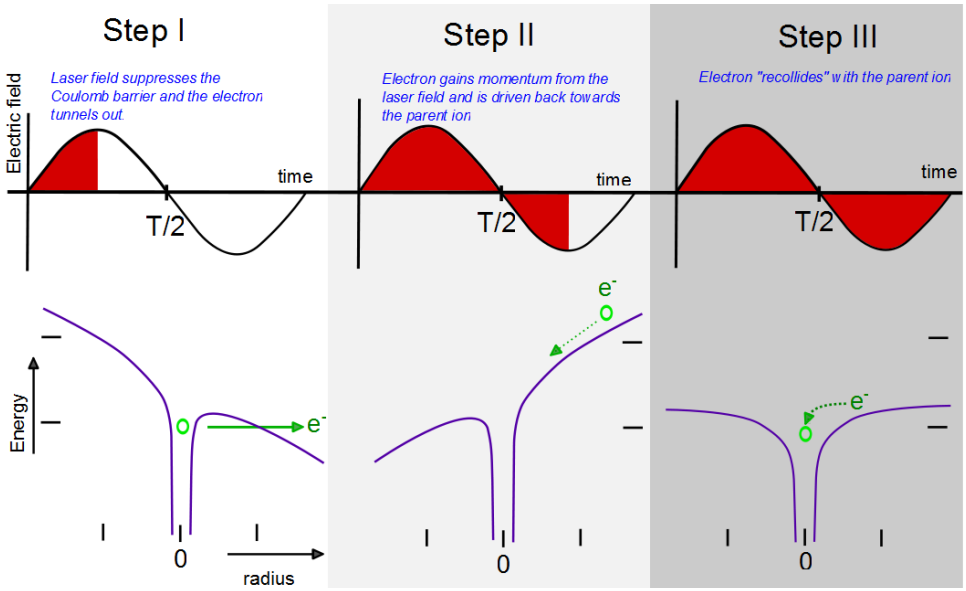

Figure 2.2: Recollision process and the three step model. Step I: The laser electric field suppresses the Coulomb barrier leading to tunneling ionization. Step II: The electron in the continuum gains energy from the laser field while it is driven back towards the parent ion as the field reverses direction with respect to step I. Step III: The electron "recollides" with parent ion.

ionization by lower order nonlinear processes occurring before the peak intensity can prove to be undesirable. For instance, L'Huillier et al. measured, for a target of xenon atoms driven by a 36 ps pulse, the yield of Xe^+ ions saturates at an intensity $I_{sat} = 2.5 \times 10^{13} W \cdot cm^{-2}$ while the intensity necessary for BSI is $\approx 8 \times 10^{13} W \cdot cm^{-2}$, using equation 2.5. This occurs because an experimental target containing a finite number of atoms is depleted by lower order processes (here, MPI) taking place in the leading edge of the pulse. In an experiment designed to study a process like BSI or even tunneling ionization of the type $Xe \rightarrow Xe^{1+} + e^-$, the use of long pulse lengths turns out to be parasitic as neutral atoms never "see" the peak of the laser pulse in such a case. The need to preempt saturation is wittingly spelled out as the "Lambropoulos curse" after the work in [Lam85]. Although a pulse of several 1−100 fs in duration is still too long compared to one atomic unit of time ($\tau_{at} = 2.4188 \times 10^{-17}$s), saturation makes femtosecond pulses necessary in the study of atomic systems in intense NIR and optical fields apart from the fact that they are a natural choice to attain high peak intensities owing to their short duration.

At a fixed point in space the time-varying component of the electric field of a linearly polarized laser pulse $\vec{E}(\vec{r}, t) = E(t)$ is given by

$$E(t) = \frac{1}{2} E_0(t) e^{i\omega_0 t} + \text{c.c.} = \frac{1}{2} |E_0(t)| e^{i\varphi(t)} e^{i\omega_0 t} + \text{c.c.}, \tag{2.21}$$

where c.c. stands for complex conjugate, $E_0(t)$ is the pulse envelope, $\varphi(t)$ is the time-dependent phase and ω_0 is the mean frequency around which the spectral amplitude of the pulse has appreciable values in an interval $\Delta\omega$. While the validity of this definition is obvious for the case $\frac{\Delta\omega}{\omega_0} \ll 1$ which is true for slowly-varying

envelopes viz. $\mid \frac{\partial E_0}{\partial t} \mid \ll \omega_0 \mid E_0(t) \mid$, the relevance of the same in the case of few-cycle pulses and those approaching the single-cycle limit, where this condition is not strictly true, has been examined in [BK97]. For propagating fs pulses produced in mode-locked lasers by the coherent superposition of the longitudinal modes of a resonator we can Fourier decompose $E_0(t)$ along the propagation direction $\hat{z}$ as

$$E_0(z,t) = \int \tilde{S}(z,\omega) e^{i\omega t} d\omega = \int S(0,\omega) e^{i\omega t} e^{i\mathcal{F}(0,\omega)} d\omega, \tag{2.22}$$

where $\tilde{S}(z,\omega)$ is the complex spectral amplitude and $\mathcal{F}(z,\omega)$ the spectral phase after propagation by a distance z. In a linear loss-less medium, which holds good for propagation from the exit of a laser to the interaction volume in the experiment, the spectral amplitude remains unchanged while the spectral phase is affected [JCD06]. We can Taylor expand $\mathcal{F}(z,\omega)$ as

$$\begin{aligned} \mathcal{F}(z,\omega) &= \mathcal{F}(\omega_0) + \frac{\partial \mathcal{F}}{\partial \omega}\bigg|_{\omega_0} (\omega - \omega_0) + \tfrac{1}{2} \frac{\partial^2 \mathcal{F}}{\partial \omega^2}\bigg|_{\omega_0} (\omega - \omega_0)^2 + ... \\ &= \varphi(\omega_0) + \mathrm{GD}|_{\omega_0}(\omega - \omega_0) + \tfrac{1}{2}\mathrm{GDD}|_{\omega_0}(\omega - \omega_0)^2 + ... \\ &= \varphi_0 + \omega_0 z\, n(\omega_0)/c + k_1|_{\omega_0} z\, (\omega - \omega_0) + \tfrac{1}{2} k_2|_{\omega_0} z\, (\omega - \omega_0)^2 ... \end{aligned} \tag{2.23}$$

The coefficients k_i characterize the dispersive medium. The coefficient k_1 is related to the the group delay ($\mathrm{GD} = k_1 z = \frac{z}{v_g}$) which results in a difference between the velocity of the carrier wave, phase velocity v_{ph}, in the pulse and the velocity of the pulse envelope - the group velocity (v_g). The resultant phase slip leads to a change in the shape of the electric field within the pulse quantified by the relative phase difference between the maximum of the envelope and the carrier of the pulse [UHH02, BK97]. While the group delay has no effect on the shape of the envelope, it affects the shape of the electric field. However, the group delay dispersion ($\mathrm{GDD} = k_2 z$) changes the temporal profile of the envelope. If k_2 is non-zero, the different frequency components constituting the pulse propagate with different phase velocities resulting in a "chirp" of the pulse [JCD06] leading to relative shifts between them in time. Consequently, the pulse is broadened with the carrier frequency changing within the pulse. Higher order terms lead to significant distortion, splitting, and the formation of satellite pulses. Obviously, for a given bandwidth ($\Delta\omega$) of the pulse spectrum, the shortest pulses in time are those that are not chirped. This is expressed by the following inequality relating the pulse width in time defined by the full-width at half-maximum (τ_0) to the bandwidth $\Delta\omega$ by [DR06]

$$\Delta\omega\tau_0 \leq \vartheta \tag{2.24}$$

where ϑ is a constant depending on the shape of the envelope ($\vartheta = 0.441$ for a Gaussian envelope in time).

Self-phase modulation and self-steepening

In a laser system generating few-cycle pulses like the one used in the current work, propagation of a pulse in a nonlinear medium (Kerr effect [Boy08]) is exploited to

broaden the frequency spectrum of 25 fs laser pulses so that the pulse can be compressed to < 10 fs. The idea here is to make use of self-phase modulation (SPM). At sufficiently high intensities, the refractive index of a medium (n) becomes dependent on the pulse intensity (I) [Boy08] so that

$$n = n_0(\omega) + n_2 I(t), \tag{2.25}$$

where n_2 is the nonlinear refractive index. This results in the time-dependent phase after propagation through the nonlinear medium by a distance z to become

$$\varphi(z,t) = \frac{\omega_0}{c} n_2 I(t) z, \tag{2.26}$$

whereby an intensity dependent frequency within the pulse is introduced. The amount of spectral broadening due to SPM is

$$\Delta\omega_{\mathrm{SPM}} = \frac{d\varphi}{dt} \propto \frac{\omega_0}{c} n_2 \frac{I_0}{\tau_0} z. \tag{2.27}$$

Further, the dispersion in $n_2(\omega) = n_2(\omega_0) + \frac{dn_2}{d\omega}\,|_{\omega_0}$ is unavoidable in the case of few-cycle pulses. This modifies the spectral broadening due to SPM and is referred to as self-steepening [Boy08, JCD06]. These processes are at play in the generation of few-cycle pulses as will be described in section 3.5.

2.2 Clusters in intense IR laser pulses

Clusters are an intermediate state of matter between isolated atoms and molecules on one hand, and solids on the other [Hab94]. These are aggregates of atoms or molecules which are held together either by Van der Waals forces due to induced or pre-existing permanent dipole moments or in other cases by metallic or even ionic bonds. The important feature that distinguishes clusters from single atoms and solids is the scaling of physical properties with cluster size - either number of atoms/molecules per cluster or the cluster radius. Many interesting properties are a consequence of a very favorable ratio of surface atoms to those in the interior volume. Properties such as the melting point and optical absorption depend on size and morphology of the cluster [Hab94, VK95].

In this work, we will be interested mainly in rare-gas clusters. Barring the case of He, all other rare-gas clusters are formed in the solid phase, i.e., it is meaningful to ascribe a lattice to their structure which can be determined from electron or X-ray diffraction patterns [FDFRT81]. Helium clusters, which we will also encounter in this work, exist uniquely in a superfluid phase [TV04]. We will discuss the formation of rare-gas clusters and some of their characteristics in Chapter 3.

2.2.1 Inner- and outer-ionization

Rare-gas clusters considered in this work contain $\sim 10^2 - 10^6$ atoms per cluster and have diameters in the range $1 - 50$ nm. These sizes are much smaller than the NIR laser wavelengths ($\sim 1\,\mu$m) which are of interest to us. Since atoms in

rare-gas clusters are bound by weak Van der Waals forces [Hab94], it makes sense to address individual atoms within the cluster although they are now in a more complex environment. Thus, we can carry forward many of the concepts addressed in the ionization of isolated rare-gas atoms in intense IR fields naturally into the domain of clusters while keeping in mind that collective effects play an important role in the latter. We will restrict our attention to the interaction of clusters with intense NIR laser pulses at a central wavelength of $\sim$ 800 nm with intensities in the range of $10^{14-17}\,\mathrm{W/cm^2}$ and pulse durations of the order of $\sim 1-100$ fs. Single-component atomic clusters containing rare-gas or metal atoms are also referred to as "homonuclear" or "pristine" clusters.

Harmonic cluster potential

First, let us ignore collective electron dynamics and resonant interaction so that we extend the approach used for isolated rare-gas atoms to understand the intense field-ionization process in clusters. In the high intensity range, ionization proceeds mainly by the tunneling and over-the-barrier routes since the Keldysh parameter $\gamma \lessapprox 1$. In the case of an intense NIR pulse, all the atoms in the cluster see the same laser electric field since the cluster size $1-50$ nm is much smaller than the laser wavelength. For the same reason, the cluster can be considered to have a spherical geometry. In the leading edge of the pulse, a significant fraction of atoms in the cluster are singly ionized by tunnel ionization. Since some of the electrons released from their parent atoms can leave the cluster boundary and never return to the cluster, it acquires a net positive charge Q. The electric potential of such a cluster U is given by [KSS07, Saa06]:

$$U(r) = \begin{cases} -\frac{Q}{2R}\left(3 - \frac{r^2}{R^2}\right), & r \leqslant R, \\ -\frac{Q}{r}, & r \geqslant R, \end{cases} \tag{2.28}$$

where R is the cluster radius and r is the distance from the cluster center. The quantities U, Q and R in equation 2.28 are weakly time-dependent, and vary adiabatically. Electrons born by subsequent laser ionization in the cluster "see" this potential due to the ions which we will refer to as the *background* potential. Implicit to equation 2.28 is the approximation that the cluster is a uniformly charged sphere of ions which carry an average of Z. If the number density of ions is n_i, the charge density is $\varrho_i = n_i \cdot Z$. It is clear from equation 2.28 that $U(r \leqslant R) \propto r^2$, thus the electrons within the cluster experience a harmonic potential due to the ionic background within the cluster boundary. The potential becomes anharmonic for $r \geqslant R$ as shown in figure 2.3. This potential traps electrons released from the parent ions resulting in the formation of a plasma which is a few nanometers in size. We will refer to this as the *nanoplasma.*

We can qualify the above-mentioned adiabaticity better. We recall that for a plasma of electron density n_e and temperature T_e the Debye length λ_D is given by (in SI units)

$$\lambda_D = \left(\frac{\epsilon_0 k_B T_e}{n_e e^2}\right)^{1/2} = 7430 \cdot \left(\frac{k_B T_e}{n_e}\right)^{1/2}, \tag{2.29}$$

where k_B is the Boltzmann constant. In this equation, when $k_B T_e$ is expressed in eV with the given prefactor, λ_D is in meters. Spatial electric field fluctuations on

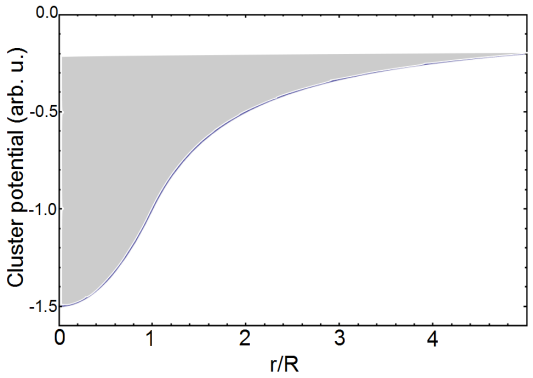

Figure 2.3: Cluster potential. Plot of equation 2.28 in units of $\frac{r}{R}$for the representative case of $Q = 1$. The potential is harmonic for $\frac{r}{R} \leqslant 1$ and anharmonic for $\frac{r}{R} > 1$.

length scales smaller than λ_D are shielded by a "quick" rearrangement of electrons and hence can be ignored. Field variations on length scales much larger than λ_D are adiabatic in space. From equation 2.29, for typical cluster plasmas ($\sim 5\,\mathrm{nm}$) which have electron temperatures of $k_B\,T_e \gtrsim 100\,\mathrm{eV}$ and solid-like electron densities ($\sim 10^{22}\,\mathrm{cm}^{-3}$) this condition is valid. Similarly, variations in time much slower than the plasma frequency (in SI units)

$$\omega_p = \sqrt{\frac{n_e e^2}{\epsilon_0 m_e}} \quad [\mathrm{rad/s}] \tag{2.30}$$

are adiabatic and provide sufficient time for the electrons to establish a dynamic equilibrium. At solid densities ($\sim 10^{22}\,\mathrm{cm}^{-3}$) this of the order $\sim 10^{17}\,\mathrm{Hz}$. Since rare-gas clusters are formed at solid densities (or liquid in the case of He), in our studies, the plasma frequency starts off being much higher than the laser frequency at 800 nm. This is subsequently lowered as the plasma becomes dilute due to ionic motion, i.e. cluster expansion, so that the plasma frequency is lowered to values similar to the laser frequency. Thus, the timescale of laser oscillation also serves to define the temporal adiabaticity. Quantities which vary much slower in time than the laser period, like the pulse envelope, are adiabatic both from the point of view of the electric field oscillations and plasma equilibration. It is in this sense that it is meaningful to talk of electron temperatures or other thermodynamic quantities in these transient cluster nanoplasmas.

Electrons released from the parent atoms are trapped within the cluster unless they have sufficient kinetic energy to escape the trapping potential U. Such electrons that remain quasi-free within the cluster boundary are said to be *inner-ionized*. Thus, the photoionization process is "frustrated" by this potential. However, some of the inner-ionized electrons can acquire sufficient kinetic energy from the laser field of the order of the ponderomotive energy or more, and leave the cluster boundary becoming truly free. These are said to be *outer-ionized*. Last and Jortner [LJ99] introduced this classification of electrons as inner- and outer-ionized which is very useful conceptually. It should be mentioned that the time evolution of U depends on the ratio of inner-ionized electrons that are trapped within the cluster and the outer ionized electrons that leave the cluster potential during and after the laser

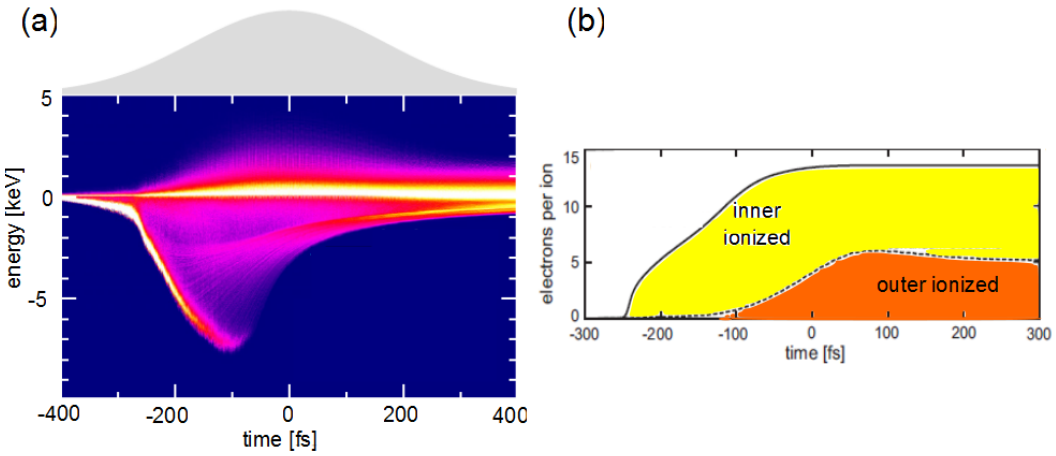

Figure 2.4: Inner- and outer-ionized electrons (a) and (b) are results of microscopic molecular dynamics simulations by Saalmann et al. [Saa06] and Fennel et al. [FMBT+10] respectively, depicting inner- and outer-ionized electrons during the laser pulse. Panel (a) shows the electron kinetic energy distributions (bright color → large number of electrons) in a Xe cluster of 9093 atoms for a pulse of duration 400 fs (full-width-half-maximum) and peak intensity of $\sim 10^{15}\,\mathrm{W{\cdot}cm^{-2}}$. The corresponding pulse intensity profile is shown on top in grey shading. Negative energies correspond to inner-ionized electrons while positive energies imply outer-ionized electrons. (b) Distributions of the number of inner- and outer-ionized electrons per ion in a Xe_{5053} cluster for a 250 fs pulse, again with a peak intensity of $\sim 10^{15}\,\mathrm{W{\cdot}cm^{-2}}$. Both results use laser pulses with a central wavelength of 800 nm.

pulse. The assumption of a uniform radial ionic charge distribution is not entirely true even for pristine clusters [JGZB04] although it is a very good approximation. We will see implications of this in ion kinetic energy spectra.

The state of inner- and outer-ionization during the laser pulse are shown in figure 2.4: Panel (a) shows the result of an atomic scale calculation by Saalmann et al. [Saa06], where the electron kinetic energy distribution is plotted as a function of time within the laser pulse. Negative energies correspond to inner-ionized electrons and positive energies imply that these electrons have been outer-ionized. The result of a simulation by Fennel et al. [FMBT+10] presented in panel (b) shows the increase in the number of inner- and outer-ionization during a 250 fs laser pulse.

2.2.2 Nanoplasma resonance

It is clear from figure 2.4 (a) that the distribution of electron kinetic energies varies with time during the pulse. The increase in the abundance of electrons at higher energies as the pulse ramps up to its peak gives a measure of the depth of the cluster potential U as a function of time within the pulse. Also an increasing fraction of electrons acquire sufficient kinetic energy to leave the cluster potential as is clear from both panels (a) and (b) in figure 2.4. These motivate the need for a model to understand the electron dynamics during the laser pulse. Ditmire et al. [DDR+96] introduced a simplified picture of the collective motion of the electrons against the background of ions where the two are treated as uniformly charged spheres.

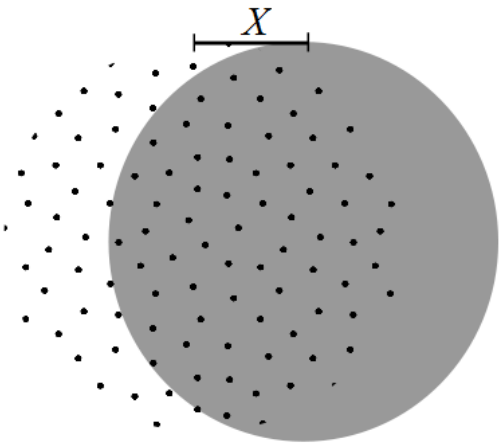

Figure 2.5: Cluster nanoplasma: showing the electron cloud (black dots) being displaced against the sphere of background ions (grey).

This was later validated by *ab initio* atomic scale computations by Saalmann et al. [SR03] leading to a harmonic oscillator model for the collective dynamics. Along this approach, we can set up a driven harmonic oscillator system in view of equation 2.28 for the displacement X of the center of mass of the electron sphere from that of the stationary ion sphere so that

$$\ddot{X}(t) + 2\Gamma\dot{X}(t) + \Omega^2 X(t) = -E_0 \cos(\omega_0 t), \tag{2.31}$$

where Γ is the damping coefficient for the oscillator and Ω is the eigenfrequency, both of which vary slowly in time compared to the driving laser frequency ω_0. E_0 is the amplitude of the driving field, which can be replaced with the pulse envelope in the calculation. The damping coefficient Γ incorporates absorption of the energy from the pulse and inelastic collisional processes [SSR06]. From the form of the potential (equation 2.28), we can write the eigenfrequency in terms of the adiabatically varying ionic charge in the cluster and its radius as

$$\Omega = \sqrt{\frac{Q}{R^3}} = \sqrt{\frac{4\pi\varrho_i}{3}} \tag{2.32}$$

for small displacements, where ϱ_i is the ionic charge density. We need Γ and Ω to solve equation 2.31. However, an accurate analytic description of cluster nanoplasmas involving all atomic scale processes is not available. Hence, this equation is useful to build a phenomenological description and to interpret results of large-scale *ab initio* simulations.

The "nanoplasma model" initiated by Ditmire et al. [DDR$^+$96] has so-far been the most successful phenomenological description. This model employs the result of Mie scattering theory [VdH81] and the Drude model [AM76] to build a framework for understanding the properties of the electron-ion system. To this end, we introduce the dielectric function $\epsilon(\omega)$ and ϱ_e the electron density. The local field E_{loc} within the nanoplasma can be determined by using the dielectric function $\epsilon(\omega)$ and solving Maxwell's equations with appropriate boundary conditions in the presence of an external electric field, which is the laser. The solution for the dipole field within the cluster can be written as

$$E_{\text{loc}} = \frac{3}{\mid 2 + \epsilon(\omega_0) \mid} E_0 \quad \text{(in a.u.)}, \tag{2.33}$$

where E_0 is the vacuum electric field with a frequency ω_0 [Jac62]. The dielectric function for the plasma according to Drude theory [DDR$^+$96] is given by

$$\epsilon\left(\omega_0\right) = 1 - \frac{\omega_p^2}{\omega_0\left(\omega_0 + i\nu\right)}, \tag{2.34}$$

where $\omega_p = \sqrt{4\pi\varrho_e}$ is the plasma frequency expressed in atomic units and ν the electron-ion collision frequency. For a laser field of frequency ω_0, the critical electron density is defined by $\varrho_{\text{crit}} \triangleq {}^{\omega_0^2}/_{4\pi}$ so that $\omega_p(\varrho_{\text{crit}}) = \omega_0$. From equation 2.33, the local field E_{loc} is maximized when $\epsilon\left(\omega_0\right) = -2$, which occurs when

$$\omega_p = \sqrt{3}\,\omega_0, \text{ or } \varrho_e = 3\varrho_{\text{crit}}. \tag{2.35}$$

This is the familiar *Mie resonance* condition [VK95] which was first presented by Gustav Mie in the context of light scattering and absorption by a spherical particle [Mie08, VdH81]. Thus, within purview of the nanoplasma model, we have arrived at the condition for $\Omega = \omega_0$ in terms of plasma properties, namely the plasma electron density. This is the highlight of the nanoplasma model and the reason why it is very useful despite its obvious macroscopic approach. Now, using Poynting's theorem, the cycle-averaged rate of energy deposited per unit volume within this formalism can be written as [DDR$^+$96, SSR06] (in atomic units)

$$\frac{dU}{dt} = \frac{\omega_0}{8\pi} Im\left(\epsilon\right)\left|E_0\right|^2 = \frac{9}{8\pi}\frac{\nu\left(4\pi\varrho_e/\left\{\omega_0^2 + \nu^2\right\}\right)}{\left|3 - \left(4\pi\varrho_e/\omega_0\left\{\omega_0 + i\nu\right\}\right)\right|}\left|E_0\right|^2. \tag{2.36}$$

When the Mie resonance condition is met, the energy absorption by the cluster nanoplasma is also maximized as a consequence of equation 2.36. Integrating this equation over the temporal profile of the pulse also gives a experimental observable, namely the total absorption of the pulse.

Since atoms in a rare-gas cluster are at solid density, considering a minimal average charge per atom in a cluster of 1+ due to intense laser field-ionization, a quick estimate reveals that the wavelength corresponding to the resonance frequency is $\lambda_{\text{crit}} \approx 350\,\text{nm}$ which is significantly smaller than the central wavelength of 800 nm. As the average ionic charge in the cluster grows, λ_{crit} becomes smaller. Thus, rare-gas clusters *must* expand so that the electron density is sufficiently diluted and the condition $\varrho_e = 3\varrho_{\text{crit}}$ is achieved for incident NIR frequencies. A similar resonance condition ($\varrho_e = \varrho_{\text{crit}}$) was also found when a cluster plasma with non-uniform radial electron density was considered [MMP01] instead of the homogenous plasma assumed hitherto following ref. [DDR$^+$96].

Now, we note that two mechanisms can operate in a cluster nanoplasma which lead to the expansion of the cluster on sub-picosecond timescales. Due to the net positive ionic charge in the cluster as a result of outer-ionization, an outward *Coulomb* pressure P_C operates to increase the cluster radius

$$P_C = \frac{3Q^2}{8\pi R^4} \quad \text{(in a.u.)}, \tag{2.37}$$

which is derived by treating the cluster as a spherical capacitor of radius R containing a net charge Q [Jac62]. The potential energy stored in such a capacitor is $\frac{Q^2}{2R}$. A second mechanism operates to dilute the nanoplasma. The hot electron gas

in the cluster also expands at its "speed of sound", much like a gas-filled balloon in a vacuum chamber. Conservation of energy of the expanding fluid (plasma) with a uniform density, decreasing in time, sets up the equation for the *hydrodynamic* pressure P_H as

$$P_H = n_e k_B T_e, \tag{2.38}$$

where k_B is the Boltzmann constant and T_e is the electron temperature [DDR$^+$96]. The scaling $P_H \propto r^{-3}$ and $P_C \propto r^{-4}$ holds for steady-state from equations 2.37 and 2.38. Thus, the Coulomb pressure P_C is expected to be dominant for small clusters with a large degree of outer-ionization, while P_H should be important for large quasi-neutral clusters which have a deep trapping potential. In reality, Q and T_e are not static during the laser pulse. Hence, a clear identification of the dominant mechanism on the basis of the initial conditions of cluster size and laser intensity is not possible. The total pressure of expansion is $P_{\text{exp}} = P_C + P_H$ with both mechanisms operating simultaneously. We will use these mechanisms for a qualitative description.

The results of an atomic scale molecular dynamics (MD) simulation by Saalmann et al. [SR03, Saa06] performed on a Xe_{923} cluster interacting with a laser pulse is presented in figure 2.6. The intensity profile of the pulse is depicted by the grey-shading in panel (a). Panel (b) shows that the radius of the cluster - the inner- and outermost shells - increases with time and, as a consequence density drops. These MD calculations were *ab initio* in that they did not assume rigid, uniformly charged spheres or a Drude function for the dielectric constant. Hence, the calculation is more fundamental in approach than the conventional nanoplasma model. Thus, they stand to validate the important features of the nanoplasma model due to Ditmire et al. [DDR$^+$96].

We can now go back to the harmonic oscillator equation 2.31 and consider a sinusoidal solution of the form

$$X(t) = X_0 \cos\left(\omega_0 t - \varphi\right). \tag{2.39}$$

We can solve for X_0 and φ as

$$X_0 = \frac{E_0}{\sqrt{\left(\Omega^2 - \omega_0^2\right)^2 + \left(2\Gamma\omega_0^2\right)}} \text{ and } \varphi_t = \arctan\left(\frac{2\Gamma\omega_0}{\Omega^2 - \omega_0^2}\right) \tag{2.40}$$

and conversely for Ω and Γ as

$$\Omega = \omega_0^2 + \frac{E_0}{2X_0\omega_0 \cos\varphi} \text{ and } \Gamma = \frac{E_0}{2X_0 \sin\varphi}. \tag{2.41}$$

The average charge in the cluster and electron center of mass velocity (v_{CM}) are plotted as a function of time within the pulse in panels (a) and (c) of figure 2.6. It is not surprising now that both average charge and v_{CM} show a sharp rise when $\varphi = \pi/2$ which is a signature of resonance [LL09] . Figure 2.7 emphasizes the fact that the eigenfrequency (blue circles and solid line) of the oscillator meets the laser frequency at 780 nm (dash-dotted line) at $t \approx 20$ fs. The outer radius of the cluster is almost doubled with respect to the original cluster radius. Damping (red diamonds) is maximum at this point in time. Hence, optical absorption should maximize as well when the resonance condition is met.

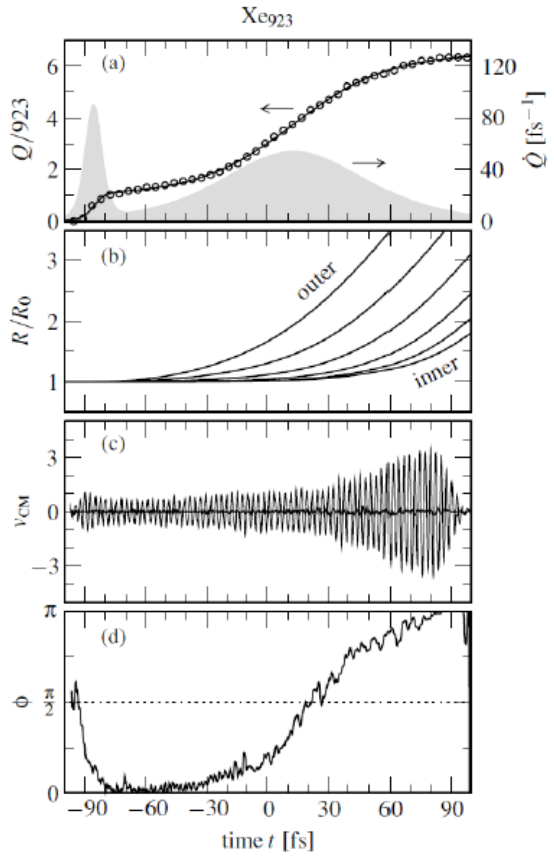

Figure 2.6: Molecular dynamics simulation results reported by Saalmann et al. [SSR06]. The following parameters are shown as a function of time during the laser pulse. (a) average charge per atom in the Xe_{923} cluster, the grey-shading shows the pulse profile used in the calculations, (b) instantaneous radii (R) of different shells in the cluster in units of the initial cluster radius R_0, (c) v_{CM} the center of mass velocity of quasi-free electrons within the cluster and (d) the phase shift φ between electron motion and the driving laser electric field, see equation 2.40. The peak intensity of the pulse between $t = -80 \cdots + 80$ fs is $9{\times}10^{14}$ W·cm^{-2}.

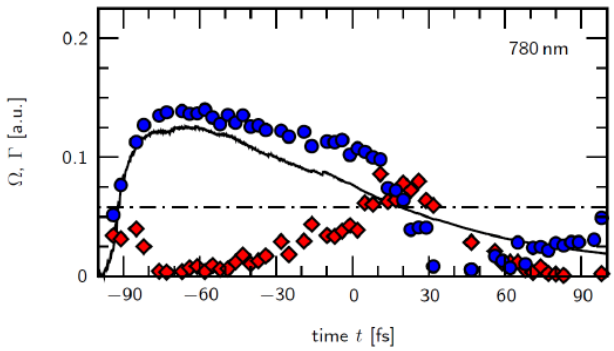

Figure 2.7: Eigenfrequency Ω (blue circles) and damping coefficient Γ (red diamonds) of the cluster nanoplasma obtained from equation 2.31 using the dynamical variables X_0 and φ of the MD simulation and laser electric field amplitude E_0, for the same case as in figure 2.6. These correspond to the driven and damped harmonic oscillator (adapted from [SR03]). Solid line: Eigenfrequency $\Omega = \sqrt{Q/R^3}$ as a function of time from the instantaneous net cluster charge Q and cluster radius R during in the MD simulation. Dash-dot line: Laser frequency ω_0 at 780 nm.

This has indeed been the case in experiments where absorption was measured as a function of pulse width or delay between pulses in two-pulse experiments. Absorption (figure 2.8 (a)) as a function of delay observed by Zweibeck et al. [ZDP99], maximum charge-state produced as a function pulse widths (figure 2.8 (c)) observed by Köller et al. [KSK$^+$99] and ion yield (He^{2+}) as a function of two-pulse delay in our studies (figure 2.8 (d)) are all maximized as a consequence of optimal time durations in experiments performed at similar peak intensities ($\sim 10^{15}$ W·cm^{-2}). These studies and several others, including those on metal clusters [DFD$^+$05, DFR$^+$06], establish the picture of resonant interaction which occurs as a consequence of appropriate nanoplasma densities being attained due to cluster expansion. In fact, even optimal control experiments which use evolutionary (or genetic) algorithms to shape the amplitude and phase of the incident laser pulse seeking to enhance preselected ionic charge-states turned out to be nothing more than complicated ways to find the same resonance condition being discussed here [ZMN$^+$04, THG$^+$10]. A highlight of the resonant interaction is the very efficient absorption of the laser pulse by the electron-ion system (as high as 90%), as has been observed in the case of D_2 clusters which lead to d-d nuclear fusion during cluster explosion [DZY$^+$99]. This is a unique feature when compared to the interaction of individual molecules or solid targets with intense IR laser pulses [Dit97] making the expansion-induced resonance a truly mesoscopic phenomenon.

We should note that the original nanoplasma model due to Ditmire et al. [DDR$^+$96] uses the Drude dielectric function (equation 2.34) assuming a uniform charge density within the cluster and adiabatic changes of system parameters, particularly in electron density. These assumptions are not strictly true although the model provides a framework for good qualitative understanding of the underlying processes. Milchberg et al. [MMP01], observed in their 1-D hydrodynamic simulations that a non-uniform plasma density within the cluster leads to the existence of a "critical density layer", as occurring in laser-plasmas at the surfaces of bulk solids [Kru03], where the resonance condition is met for prolonged times. In full 3D-simulations,

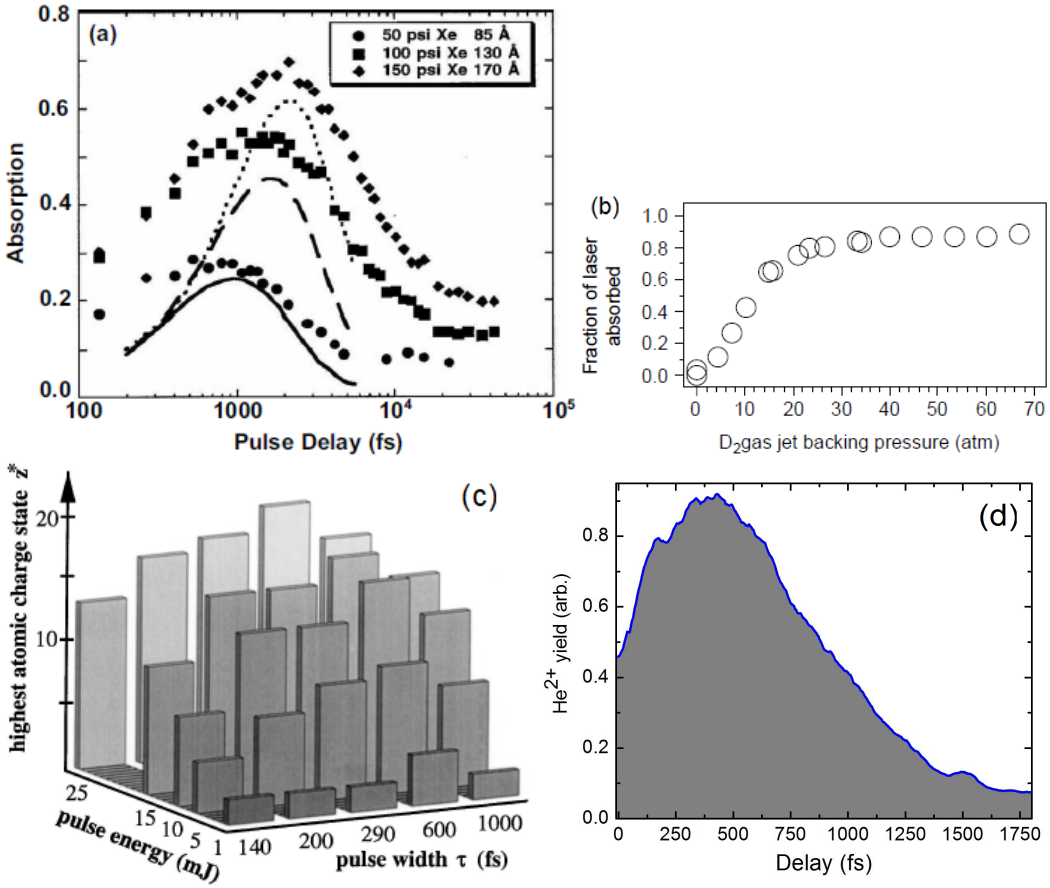

Figure 2.8: Resonance absorption and charging observed in experiments: (a) probe absorption as a function of delay between two pulses as reported in ref. [ZDP99], (b) fraction of laser pulse absorbed by D_2 clusters as a function of backing pressure (equivalently cluster size) demonstrating $\approx 90\,\%$ absorption for large clusters by Ditmire et al. [DZY$^+$99], (c) dependence of the highest observed charge of Ag ions on pulse width and energy in the studies reported in ref. [KSK$^+$99] and (d) dependence of He^{2+} ion yield as a function of pump-probe delay in a two-component $Xe_{11}@He_{15000}$ cluster obtained in our experiments. All the measurements were done at similar peak intensities $\sim 10^{15}\,\mathrm{W{\cdot}cm^{-2}}$.

an equivalent interpretation of the "critical density layer" is replaced by differing velocities of expansion of the outermost and innermost shells because of different net ionic charge densities in these two regions [FMBT$^+$10, IB00]. We may observe from panel (d) in figure 2.6 that in the rising edge of the pulse ($t \approx 85\,\mathrm{fs}$) the phase $\varphi = \pi/2$, this is due to a brief meeting of the resonance condition in the leading edge of the pulse in the early stages of intense field-ionization[2]. This resonance condition is quickly lost because of the exponential rise in ionization rates with electric field as the ADK rate (equation 2.7) suggests. A strong case for nonlinear resonance has been made in several studies [KB06, PZB08, FZBB05] on similar timescales. Here, a strong driving of the electron cloud to anharmonic regions of the cluster potential (cf. equation 2.28) leads to the resonance condition being met at a multiple of the laser frequency. Explicit verification of nonlinear resonance can be done best by employing very short pulses, $\lesssim 5\,\mathrm{fs}$ so that processes occurring at longer pulse durations ($\gtrsim 15\,\mathrm{fs}$) are suppressed. A predicted consequence of this mechanism is optical emission resulting from nonlinear resonance. These have not yet been observed in the laboratory. We also should mention that for small clusters (~ 15 atoms) an enhanced ionization (ENIO) rate due to optimal inter-ionic spacing resulting from cluster expansion was proposed by Siedschlag and Rost [SR02] to explain the wavelength independence of optimal pulse-widths or delays for the occurrence of Mie resonance observed in experiments. This is based on charge resonance enhanced ionization (CREI) in molecules where a similar effect occurs [ZB95]. However, explicit signatures of this have not yet been seen in experiments.

Finally, we may point out that, in general, electronic (plasmon) processes are very fast and have dephasing times of $\sim 10\,\mathrm{fs}$ in metallic nanoparticles with sizes similar to the nanoplasmas considered here [KPG$^+$98]. However, in the case of intense NIR laser ionization, the resonances are rather slow in both rise and decay. This is because they rely on ionic motion which occurs on sub- or few-picosecond timescales. We will show later that this caveat in the case of intense field nanoplasmas can be overcome by suitable cluster design. Now, we proceed to discuss the mechanisms behind the high charge-states of ionic fragment (figure 2.8(c)) and other energetic phenomena observed in experiments.

2.2.3 Local fields in the nanoplasma

The simple nanoplasma model predicts (equation 2.33) an enhancement of local electric field within the cluster over the laser field in vacuum. From the scenario in section 2.2.2 and figure 2.5, we can estimate the local field following Krainov et al. [KS02]. The relative displacement of the electron and ion centers of charge results in a dipolar field within the cluster which exhibits a maximum at the cluster surface due to the uncompensated charge. A snap-shot of this situation is shown in figure 2.9 (a). The local field in the "pole" regions which are left unshielded due to relative displacement between electron and ion spheres is obtained as a function of the angle ξ and the net charge per atom in the cluster Z as

$$E_{pole} = \frac{ZN}{4R^2}(2 - 3\cos\xi + \cos^3\xi)\left(3 - 2\sin\frac{\xi}{2}\right)\sin^2\frac{\xi}{2}. \tag{2.42}$$

[2]This is avoided in metal clusters because of conduction band electrons whose density is already overcritical at NIR wavelengths even before the incidence of the laser pulse.

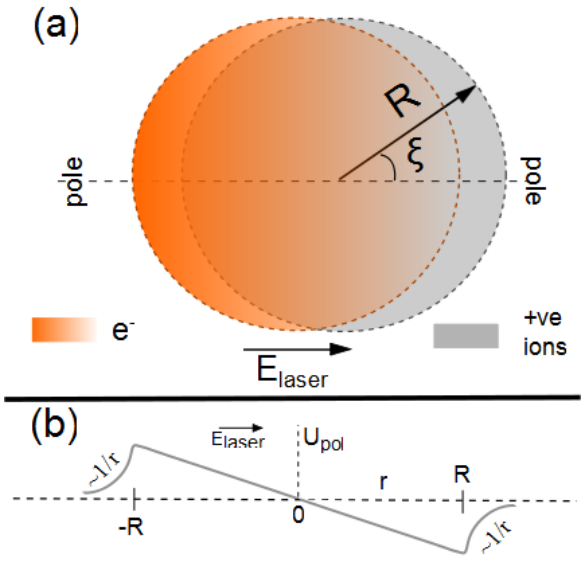

Figure 2.9: (a) Charge separation leading to a strong local field at the poles (r is the radial coordinate and ξ the azimuthal angle) which is enhanced compared to the electric field of the laser in vacuum. (b) The potential (U_{pol}) induced by the relative displacement of the electron cloud from the center of the ion sphere.

Using the enhanced electric field E_{pole} as the barrier-suppression field in equation 2.4, the resulting ionic charge $Z_{pole}(\xi)$ as a function of ξ can be obtained as [KS02]

$$\frac{1}{N}\left(\frac{\Phi_{IP}R^2}{Z_{pole}(\xi)}\right)^2 = \left(2-3\cos\xi+\cos^3\xi\right)\left(3-2\sin\frac{\xi}{2}\right)\sin^2\frac{\xi}{2}, \qquad (2.43)$$

where N is the number of atoms in the cluster and Φ_{IP} the ionization potential of the ion with charge-state Z_{pole}. The charge at poles due to barrier-suppression grows linearly with cluster size N but depends on the level of outer-ionization which leads to a net charge of Z per atom in the cluster.

2.2.4 Ion emission

Several experiments over a wide range of intensities and laser wavelengths have observed the emission of highly-charged ions. In early studies, Snyder et al. [SBC96] observed a maximum charge-state of 20+ for Xe ions resulting from the the irradiation of Xe clusters with 350 fs pulses with peak intensities of 10^{15} W·cm^{-2}. For the case of isolated Xe atoms Palaniyappan et al. [PDG$^+$06] observed a maximum charge-state of Xe^{12+} at intensities $\sim 10^{18}$ W·cm^{-2} where nonsequential processes are important. In the case of metal clusters (Pb, Ag, Pt, Au) experiments performed with pulses from Ti:Sapphire laser systems at peak intensities of $\sim 10^{16}$ W·cm^{-2} charge-states as high as 30+ have been observed consistently [LVC$^+$02, STK$^+$99]. Similar ion emission from molecular clusters has also been seen in $(CH_3I)_N$ and H_2O-clusters [FZPCJ99, KKM03b]. An enhancement in the maximum charge-state as a result of doping clusters with foreign atoms or molecules with lower ionization potential than the host matrix was observed by Purnell et al. [PSW$^+$94]. They found Ar ions up to a charge-state of 8+ in two-component $Ar_N(HI)_M$ clusters

while such high charge-states were not found in pristine Ar_N clusters when both cluster systems were irradiated under identical conditions - 350 fs pulses with a peak intensity of $1 \times 10^{15}\,\mathrm{W{\cdot}cm^{-2}}$. Since the first ionization potential of atomic Ar is higher than that of HI, the latter acts as a chromophore which releases electrons that can impact ionize Ar atoms in the matrix.

The local potential seen by the inner-ionized electrons due to the separation of the two charged spheres U_{pol} is depicted in 2.9 (b). The corresponding electric field has been referred to as the *polarization* field or the *ignition* field because it aids ionization by lowering the tunneling barrier [FMBT$^+$10]. Alternatively, this can be viewed as a lowering of the effective ionization potential or the continuum into which a bound electron can escape. Figure 2.9 (b) is a schematic representation of the polarization field assuming rigid electron and ion spheres. This field is stronger along the laser polarization than in the direction perpendicular to it.

At this point, we note that the nanoplasma model using the Drude dielectric function does not predict this anisotropy. The anisotropic ion emission, first seen by Kumarappan et al. [KKM01], demonstrates the action of the polarization field. Kinetic energy spectra of ions (without charge-state resolution) measured by them from Ar_{40000} clusters are shown in figure 2.10 (a). Faster ions are emitted along the laser polarization direction as compared to the direction perpendicular to it. Microscopic *ab initio* particle-in-cell (PIC) simulations have reproduced this behavior (panel (b) in figure 2.10) [JGZB04]. In spite of the good qualitative agreement, quantitative agreement between experiment and theory is often not possible due to the averaging over the cluster size distribution and laser intensities in the focal volume always present in laboratory measurements. The heavy numerical burden involved in atomic scale calculations forbids the possibility of performing simulations which can take these averaging effects into account.

Ions emanate from the cluster following a Coulomb explosion after the laser pulse is gone. The anisotropy arises from the fact that the charge-state of ions at poles ($\xi \sim 0$), which can be quantified by the maximum ionic charge-state q^{max} , is greater than in the equatorial region ($\xi \sim \pi/2$) which is clear referring to equation 2.42. In fact, once in every half-cycle ions at the poles face a greater barrier suppression field than those at the equator. When the laser pulse leaves the cluster q^{max} is higher at the poles than the equator. In a Coulomb explosion the energy carried by an ion of charge q_i is proportional to q_i^2. Ions emitted along $\xi \sim 0$ are faster than those emitted along $\xi \sim \pi/2$. This effect has been referred to as "charge-flipping" acceleration [KKM01] following the work in ref. [IB00].

The original idea of charge-flipping acceleration as stated by Ishikawa et al. [IB00], following their classical molecular dynamics simulations, is a dynamic acceleration of ions at the poles by the laser field. Ions within the cluster experience the Lorentz force due to the laser field. Since the laser field reverses direction every half-cycle of the laser period, the net force on an ion of constant charge-state would be zero. But in the ionized cluster, the relative displacement of the center of mass of the electron sphere with respect to that of the ion sphere leaves one of the poles unshielded every half-cycle as shown in figure 2.9 (a). This scenario flips every half-cycle. Ishikawa et al. [IB00] observed that ions in the unshielded pole either retain their charge-state or get ionized further by tunneling. Conversely, electrons recombine at the shielded pole during this half-cycle so that the ion charge-state at this pole decreases (see

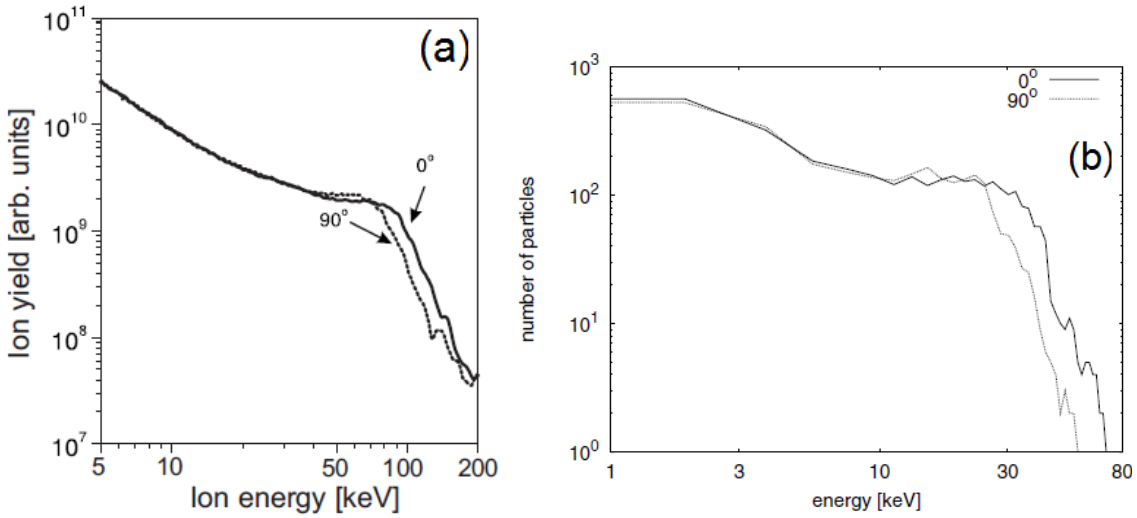

Figure 2.10: Asymmetric ion emission: (a) experimentally measure ion kinetic energy spectra for Ar_{40000} clusters exposed to 150 fs pulses of a peak intensity $8 \times 10^{15}\,\mathrm{W{\cdot}cm^{-2}}$ in ref. [KKM01] and (b) result of a microscopic PIC by Jungreuthmayer et al. as reported in ref. [JGZB04] performed for single clusters using with similar parameters as in (a).

figure 12 in ref. [IB00]). Thus, acceleration due to the laser field experienced by the ion when it is unshielded is greater than the deceleration suffered in the next half-cycle when it is shielded. This results in a net force along the laser polarization. In the equatorial region the electron cloud always shields the ions. In this simulation as the authors state [IB00], the consideration of recombination is classical and no quantum mechanical or empirical rates are used. It is possible that the rate of recombination may be over-estimated by the classical procedure[3]. In this context this classical recombination may be seen as a measure of screening of the ions by the electron cloud. Subsequent full-scale microscopic simulations have reproduced the anisotropy qualitatively and have interpreted it as a consequence of the polarization force [JGZB04, FMBT$^+$10]. The presence of ions of higher charge-state at the poles than at the equator leads to higher ion kinetic energies along the laser polarization than perpendicular to it as a result of Coulomb explosion[4]. This is qualitatively different from the dynamic acceleration mechanism proposed by Ishikawa et al. [IB00]. This further highlights the dominant role played by the polarization field.

Thus far, we have not considered collisional phenomena and electron emission observed in the interaction of rare-gas and metal clusters in intense laser fields. We discuss these in the following section.

[3]For electron temperatures of 1−1000 eV radiative and dielectronic recombination rates are of the order of $10^{-10}\,\mathrm{cm^3{\cdot}s^{-1}}$ (or $10^{-5}\,\mathrm{nm^3{\cdot}fs^{-1}}$) [SKK$^+$08]. Hence, these are not fast enough and three-body recombination is important in such considerations [PF10].

[4]The same also holds for the case of hydrodynamic expansion where the kinetic energy carried away by the ion is proportional to its charge (cf. equation 2.51).

2.2.5 Electrons: Collisions and emission

Collisions

In equation 2.31, the factor Γ was used to account for processes damping the oscillations of the electron cloud. In the Drude model absorption depends on $\mathrm{Im}\,(\epsilon)$ which in turn is related to the electron-ion collision frequency ν_{ei} . These motivate a detailed consideration of collisional processes in the cluster nanoplasma. inner-ionized electrons are continuously driven by the laser field. The kinetic energy gained by these electrons from the laser field in each half-cycle can be of the order of the ponderomotive energy U_p, which was defined in equation 2.17. For a laser pulse with a peak intensity of $10^{15}\,\mathrm{W{\cdot}cm^{-2}}$ the ponderomotive energy is of the order of 100 eV while the quiver amplitude is about 1 nm. Thus, energetic electrons can traverse the cluster and en route collide with ions which they can further ionize, leading to electron impact ionization (EII) [KS02]. In addition to ionization by barrier-suppression resulting from the local field, EII operates to create highly-charged ions within the cluster. These inelastic collisions transfer energy from the laser field to the electron-ion system of the nanoplasma. The total cross section for collisional ionization is given by the semi-empirical Lotz formula [Lot68]

$$\sigma_c = a_i\, f_i \frac{\ln\left(\frac{K_e}{\Phi_{IP}}\right)}{K_e \cdot \Phi_{IP}}, \tag{2.44}$$

where K_e is the electron kinetic energy and Φ_{IP} the ionization potential of the ion. The number of electrons in the valence shell of this ion is f_i. a_i is a constant which depends on the atomic species under consideration which has the value $4.5 \times 10^{-14}\,\mathrm{cm^2(eV)^2}$ for elements from H to Cs. With a consistent choice of units for a_i, K_e and Φ_{IP}, equation 2.44 can be adopted to both SI and atomic units. The Lotz cross section is valid when $K_e > \Phi_{IP}$. Lotz cross sections are widely used in atomic scale simulations of laser-cluster interactions [IB00, SSR06, FMBT$^+$10]. Using equation 2.44, the cycle-averaged electron impact ionization rate can be written (in SI units) as [DDR$^+$96]

$$W_{EII} = \frac{f_i}{2\pi m_e^{1/2} \Phi_{IP} U_p^{1/2}} n_e \times \cdots$$

$$\times \left\{ \left[3 + \frac{E_Z}{U_p} + \frac{3}{32}\left(\frac{\Phi_{IP}}{U_p}\right)^2 \right] \times ln\left(\frac{1+\sqrt{1-\Phi_{IP}/2U_p}}{1-\sqrt{1-\Phi_{IP}/2U_p}} \right) - \sqrt{1-2\Phi_{IP}} \times \left(\frac{7}{2} + \frac{3\Phi_{IP}^Z}{8U_p} \right) \right\}, \tag{2.45}$$

where n_e is the electron number density, m_e the electron mass and Φ_{IP} and U_p are expressed in eV. U_p is the ponderomotive energy defined by equation 2.17. This rate was used in conjunction with the nanoplasma model to explain the dependence of X-ray emission from laser cluster interactions on pulse durations and cluster size [MJP08]. Such models provide alternatives to large scale atomistic calculations like MD or PIC simulations, although their applicability is limited due to issues discussed in the context of the nanoplasma model. EII operates irrespective of whether or not the Mie resonance condition is satisfied. But, when the Mie resonance occurs, electrons are more strongly driven by the laser field than otherwise.

This leads to higher electron kinetic energies which produces higher charge-states of ions within the cluster by EII. Thus, these energetic collisions result in a heating of the cluster nanoplasma both on and off resonance.

Another important collisional mechanism resulting in the heating of the nanoplasma is the absorption of a photon from the laser field during the scattering of electrons in the Coulomb field of the ions. This process is referred to as *inverse Bremsstrahlung scattering* (IBS). The IBS heating rate per electron written in terms of the ponderomotive energy is given by [Kra00]

$$\left\langle \frac{dU_{IBS}}{dt} \right\rangle = 2U_p \frac{\nu_{ei}\omega_{las}^2}{\omega_{las}^2 + \nu_{ei}^2}, \tag{2.46}$$

where ν_{ei} is the electron-ion collision frequency and ω_{las} the laser frequency. The IBS heating process is a volumetric and not a collective effect like Mie resonance. But the number of fast electrons is maximized when the resonance condition is met. Thus, IBS heating is enhanced by Mie resonance. In general, both EII and IBS are most effective when expansion-induced resonance occurs. As a result, these mechanisms transfer energy from the EM field to the electron-ion system leading to a strong heating of the nanoplasma at resonance.

Emission

From the experimental point of view, these processes lead to the emission of energetic electrons which can be measured in the laboratory. inner-ionized electrons which can gain energy from these cluster heating mechanisms escape the cluster potential during and after the laser pulse. In both rare-gas [KKM03a, SAZV03] and metal cluster systems [FDP$^+$07], electrons with much greater kinetic energy than what is expected for isolated atoms [PBNW94] have been observed in experiment [DDR$^+$96, SSR06, FMBT$^+$10]. From cluster systems high-energy tails of the electron distribution extend to more than $50\,U_p$ [FDP$^+$07, FMBT$^+$10] while for isolated atoms the cut-off is around $10\,U_p$ (which is a classical limit) [PBNW94]. This was first observed by Shao et al. [SDT$^+$96]. In this work a bimodal distribution of electrons was found. The lower energy peak at about 1 keV was termed as "warm", while "hot" electrons formed the peak at higher kinetic energies ($2-3$ keV). However, it turned out that the "hot" electron peak resulted from a misinterpretation of the time-of-flight signals due to high energy (EUV or XUV) photons. No discriminating fields were applied in the experiment to differentiate very fast electrons from photons. This was revealed later in studies that followed [KKM03a, SAZV03]. So, the warm component is true and electrons with energies of nearly 1 keV for peak laser intensities of $\sim 10^{16}\,\mathrm{W{\cdot}cm^{-2}}$ have been observed unambiguously. Although, electron kinetic energy distributions with two temperatures has been observed [KKM03a], a bimodal distribution has not been found yet.

Kumarappan et al. [KKM03a] measured anisotropic electron emission in Xe clusters as a function of delay between two identical 100 fs pulses of peak intensity $8 \times 10^{15}\,\mathrm{W{\cdot}cm^{-2}}$. The anisotropy is quantified by the ratio of electron yield in the direction parallel to the laser polarization ($Y_{||}$) to that in the direction perpendicular to it ($Y_\perp$). In this case, a maximum anisotropy $\frac{Y_{||}}{Y_\perp} \approx 3$ was observed when the

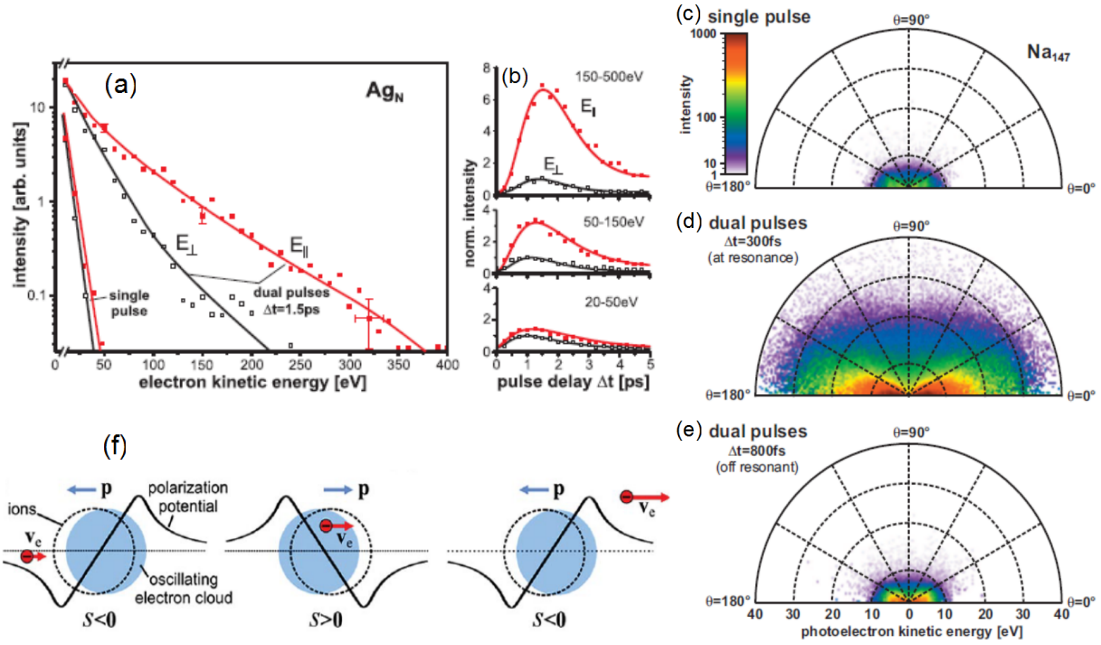

Figure 2.11: Anisotropic electron emission. Panels (a) and (b): Experimentally observed electron emission from Ag_N clusters irradiated by 100 fs pulses with a peak intensity of 8×10^{13} W·cm^{-2} (800nm) for the single-pulse and dual-pulse cases. Emission along the laser polarization direction (red) and along the direction perpendicular (black) to it as presented in ref. [FDP$^+$07]. Panels (c)-(e): Angular distribution of electron emission as seen in MD simulations by Fennel et al. [FMBT$^+$10] for Na_{147} clusters for the cases of single-pulse, dual-pulse on- and off-resonance illumination, respectively. Panel (f) is a schematic of the polarization potential and laser driven oscillations of the electron cloud (blue) (cf. discussion in text).

Mie resonance condition was met. In a more recent study by Fennel et al. on Ag_N clusters [FDP$^+$07], a maximum anisotropy ratio of 6.5 at Mie resonance was observed using twin pulses of 100 fs duration and peak intensity of 8×10^{13} W·cm^{-2} at a central wavelength of 800 nm. The results are shown in figure 2.11. In panel (a) electron kinetic energy spectra of electrons emitted parallel (red) and perpendicular (black) to the laser polarization direction are compared for single-pulse excitation and when two identical pulses are optimally delayed by 1.5 ps. The asymmetric emission is greater for higher energies (150 − 500 eV) than the lower energies as panel (b) shows.

Once again, *ab initio* calculations by Fennel et al. [FDP$^+$07] on Na_{147} clusters reproduce these findings qualitatively and reveal the mechanism in action. Panels (c), (d) and (e) show the single-pulse, on-resonance and off-resonance cases, respectively. The anisotropy is evidently much larger at optimal delay (300 fs in this case). The choice of Na atoms for simulations is to keep numerical burden under control since Na has 11 electrons ([Ne] $1s^1$) whereas Ag has 47 ([Kr] $4d^{10}$ $5s^1$). In order to explain the anisotropic electron emission, Fennel et al. [FDP$^+$07] analyzed the trajectories of the electrons in the Na-cluster. The objective of the analysis is to explain the mechanism behind the acceleration of the electrons during the laser pulse and it is not restricted to metal clusters alone. As the nanoplasma evolves and reaches the

resonance condition, a strong polarization field enhanced by Mie resonance acts on the electrons. The displacement of positive and negative charge centers results in an induced polarization as shown in figure 2.11 (f). This is similar to the induced polarization of any dielectric medium under the influence of an external electric field [Jac62]. In the case of clusters, the collectively driven electron cloud is referred to as a *plasmon*. Individual electrons enter, traverse or exit the cluster boundary at any given time depending on the phase of their motion with respect to the driving laser field. Those with the right phase can take advantage of the plasmon induced polarization field within the cluster. To visualize this, we can introduce a projection parameter s for each electron trajectory using the plasmon induced polarization $\boldsymbol{p}$ and the electron velocity $\boldsymbol{v_e}$ as, $s = \boldsymbol{p} \cdot \boldsymbol{v_e}$. Electrons with favorable s parameters are accelerated by the polarization field. These are, electrons which enter or leave the cluster such that $s < 0$, and electrons which traverse the interior of the cluster with $s > 0$. In both the favorable cases, electrons gain energy from the laser field. We may note here that the quiver amplitude (cf. equation 2.20) is of the order of the cluster size for laser intensities considered here. Thus, electrons can be driven well-outside the cluster boundary and back to the interior by the laser field. This reminds us of the recollision processes in isolated atoms (cf. section 2.2). Multiple recollisions and back-scattering of electrons with the appropriate phase can result in a continuous gain of energy since the plasmon polarization oscillates at the laser period. The optimal case is that of electrons entering or leaving the cluster field when the plasmon excursion is zero, i.e., when the charge centers of the electron cloud and the ionic sphere coincide. This phenomenon has been referred to as *s*urface *p*lasmon *a*ssisted *r*e*c*ollision (SPARC).

An elegant generalization of rescattering to clusters and extended atomic systems has been put forward by Saalmann and Rost [SR08]. Considering the rescattering of an electron from an attractive square-well potential of length L and depth V, they have shown that the maximum gain in kinetic energy of the electron ΔK_e on account of rescattering from such a potential is

$$\Delta K_e = 4\sqrt{U_p}\sqrt{V}, \tag{2.47}$$

where U_p again is the ponderomotive energy defined in equation 2.17. This equation is derived by optimizing the length of the potential well such that the momentum imparted to the electron in a single rescattering is a maximum: $p_{max} = 2\sqrt{A_0 \cdot 2V^{1/2}}$ where A_0 is the maximum amplitude of the vector potential of the laser field [SR08]. We may note from the analysis in section 2.1.2 that under the equivalent condition for isolated atoms, the maximum momentum of the rescattered electron is $p_{max} \propto A_0$ (cf. equation 2.19). For electrons resulting from rescattering effects in above threshold ionization of isolated atoms, a similar classical trajectory analysis yields maximum kinetic energies of $\approx 10\,U_p$ which corresponds to a p_{max} of $\sqrt{5}\,A_0$ [PBNW94]. Thus, for isolated atoms, in this classical picture, the maximum momentum imparted to the electron is not dependent on the scattering potential. But, for an extended atomic system, it is. The physical meaning and consequences of optimizing the potential width are as follows and we discuss this briefly without mathematical details [SR08]: Obtaining equation 2.47 involves maximizing the final electron momentum p_f at the end of rescattering to the above-mentioned value of p_{max}, which is a result of optimizing the width L of the potential well to L_{opt}. This optimal value is related to the laser frequency and potential depth as $L_{opt} = \frac{\pi}{\omega_0}\sqrt{2V}$.

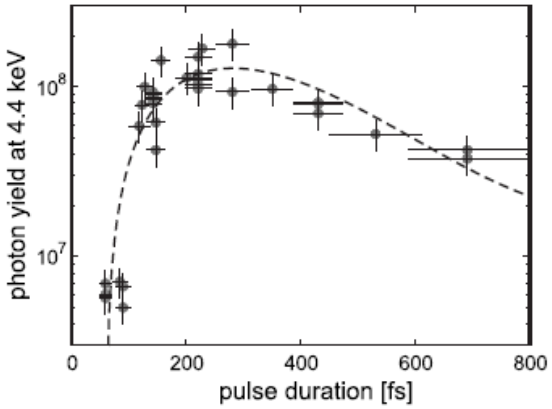

Figure 2.12: Pulse width dependence of 4.4 keV X-ray yield from Xe_{40000} clusters irradiated by 50 fs, 800 nm pulses with a peak intensity of 3×10^{16} W·cm^{-2} adapted from ref. [LPRV05a].

If an electron enters the cluster potential at the beginning of a half-cycle, it traverses the potential from end to end in one half-cycle if the width of the well is L_{opt}, the optimal value. In a wider potential the electron starts losing the energy it gained when the field reverses direction. In fact, in a full cycle the electron would lose as much energy as it gained since it is quasi-free. In a shorter potential, clearly, the electron does not utilize the driving field to the maximum extent to gain momentum. In a potential of optimal width, the electron can gain in kinetic energy from the oscillating field by multiple recollisions which act like sling shots within each half-cycle[5]. In analogy with a simple pendulum, the optimal condition is equivalent to giving the pendulum a "kick" when it passes the point of minimum potential energy, where the kick is most effective. The electron temperatures estimated from the rescattering approach agree well with those experimentally measured and those resulting from *ab initio* calculations [SR08].

2.2.6 X-ray emission

McPherson et al. [MTB$^+$94] reported X-ray emission in the intense laser ionization of Xe clusters due to radiative transitions of weakly bound electrons to core levels. This is not surprising considering the production of highly-charged ions in cluster nanoplasmas discussed earlier. MD simulations [Saa06] reveal that more than 50 keV per atom is transferred from the laser field to the nanoplasma due to the expansion-induced Mie resonance. X-rays emitted from clusters play the role of an *in situ* thermometer as they provide an estimate of the nanoplasma temperature and extent of heating by the intense laser pulse. The energetic $K_{\alpha,\beta}$ radiation from Ar, Kr and Xe clusters has been observed in experiment [IVE$^+$04, KKMT01, MTB$^+$94]. The timescale of emission has been measured using a streak camera and by other methods [DDFP95, KMS02]. The ns duration shows that X-ray emission is indeed related to radiative recombination which takes place on similar timescales. This X-ray emission disappeared when weak non-ionizing pre-pulses were used to dis-

[5]It should be noted that the ballistic transport implicit in this picture is true for fast electrons whose mean free path is larger than the cluster size.

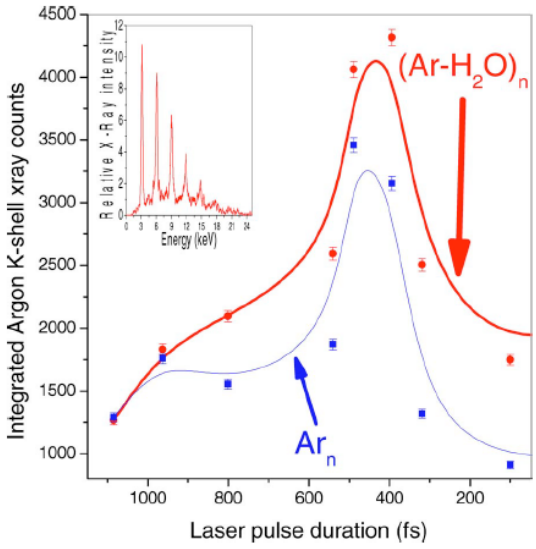

Figure 2.13: Comparison of X-ray yields from pure Ar and Ar-H_2O clusters of similar sizes as a function of pulse duration while keeping the peak intensity $\sim 10^{15}\,\mathrm{W{\cdot}cm^{-2}}$ as measured by Jha et al. [JK08b]. The inset shows the measured X-ray spectrum due to K_α emission ($\approx 3\,\mathrm{keV}$) from Ar. The multiple peaks are due to detector pile-up [Leo94].

integrate clusters well-before the arrival of the main pulse [SFM+02, WBK+01]. This emphasizes the need for collective excitation of atoms in the cluster. X-ray emission studies have been performed using laser pulses with peak intensities in the range of $10^{16-19}\,\mathrm{W{\cdot}cm^{-2}}$. Amplified spontaneous emission (ASE) from such laser systems frequently leads to long pedestals which can play the role of pre-pulses to disintegrate the cluster and prevent X-ray emission.

Early single-pulse experiments used pulses of 100 fs or longer [MTB+94, KKMT01]. Such pulses are already in the regime where significant absorption takes place due to the broad expansion-induced Mie resonance. The dominant role of resonance absorption due to cluster expansion is also seen in X-ray emission. This was highlighted by the work in refs. [LPRV05b, PDL+08]. The representative result in figure 2.12 shows the dependence of 4.4 keV X-rays from Xe clusters on laser pulse width as a result of 3d $\rightarrow$ 2p transitions in Xe^{24+} ions or those with higher charge-states. This dependence clearly points to the role of the nanoplasma resonance as one may expect. Parra et al. [PAF+00] observed a similar pulse width dependence in the yield of X-rays and EUV radiation from clusters as well as large $\sim 1\mu$m droplets.

While the generation of X-rays in long pulses is explained by resonant cluster heating, Lamour et al. [LPRV05a] found a comparatively low intensity threshold ($2.2 \times 10^{15}\,\mathrm{W{\cdot}cm^{-2}}$) for X-ray generation for relatively short pulse durations $\approx 50\,\mathrm{fs}$ in Ar_N clusters. Since this timescale is too short for (Mie) resonant heating to kick-in [Saa06, FMBT+10], an alternative mechanism for the transfer of 4.4 keV of energy to individual atoms in the Ar-cluster is required, which was proposed by Deiss et al. [DRB+06]: The multiple scattering of inner-ionized electrons at large backward angles $\gtrsim 90°$ which has large cross sections for non-Coulombic short-range potentials for ionic cores derived from the Hartree-Fock theory[6] (see e.g. chapter 8

[6]The authors state that conventionally used soft-core ion potentials under estimate the cross

in [BJ03]). The tenfold increase of X-ray emission which this mechanism estimates successfully explains the observations of [LPRV05a].

Jha et al. [JK08b], compared X-ray yields of mixed or doped clusters (Ar-H_2O, 2-8% doping) and pure Ar-clusters as a function of pulse width. This is shown in figure 2.13. The inset shows the measured K_α X-ray spectrum and multiple peaks in the spectrum are due to pile-up in the detector [Leo94]. The role of nanoplasma resonance is evident from the optimal pulse width $\sim 500\,\mathrm{fs}$ at which the yields are maximized in both pure and doped clusters. The authors attributed this to the enhancement of ionization rates in the mixture when compared to pure Ar. In the context of the current discussion, this reinforces the role of the expansion-induced resonance in X-ray generation while emphasizing the effect of cluster composition on nanoplasma heating.

2.2.7 Cluster disintegration

Having discussed the general features of the rich dynamics in rare-gas clusters during the laser pulse, we focus now on eventual cluster disintegration. The importance of the disintegration process may be highlighted by mentioning that the fusion reaction observed in D_2-clusters [DZY+99] is a consequence of fast ions resulting from cluster explosion.

For a cluster containing only bare ions so that all electrons are completely outer-ionized, it is clear that the system will Coulomb explode. The hallmark of Coulomb explosion is that an ion with a charge Z carries away a kinetic energy proportional to Z^2 in the explosion process. The Coulomb potential of bare ions is given by [LSJ+97]

$$U_{Coul} = 144 \sum_i \sum_{j>i} \frac{Z_i Z_j}{r_{ij}}, \tag{2.48}$$

where Z_i is the ion charge-state and r_{ij} the inter-ionic distance in nm which with the prefactor results in U_{Coul} being expressed as above in eV. Using this equation, the final kinetic energy of the ion with charge Z depends on its initial position r [nm] within the cluster [FMBT+10]

$$K_{Coul}(r) = \frac{4\pi}{3} n_I r^2 Z^2 \times 144 \ \ [\mathrm{eV{\cdot}nm}], \tag{2.49}$$

where n_I is the ion density in the cluster. Hence, ions at the surface gain the most energy from the Coulomb potential. This has been demonstrated by measuring ion kinetic energy spectra as a function of cluster size [KMK04, TDF+01]. Coulomb explosion is expected to be the dominant mechanism of disintegration in small clusters. Here, the ionic potential can be more easily overcome by laser driven inner-ionized electrons resulting in a high degree of outer-ionization and large net positive charge in the cluster [SSR06, FMBT+10].

On the other hand, if the cluster nanoplasma is quasi-neutral at all times, the Coulomb energy is small. In this case the cluster disintegrates by *quasi-neutral*

section for such large angle back-scattering. This explains why other theoretical investigations did not find such an effect.

expansion as against Coulomb explosion. This has also been called the regime of "hydrodynamic" expansion [DDR+96]. The gas of quasi-free electrons in the nanoplasma expands pulling the ions along. The velocity of this ion acoustic wave or the the plasma sound speed is [Kru03]

$$c_s = \sqrt{\frac{k_B}{m_i}\left(ZT_e + 3T_i\right)} \approx \sqrt{\frac{k_B}{m_i} ZT_e}, \tag{2.50}$$

where m_i is the ion mass and T_i the ion temperature. If the plasma is quasi-neutral, $ZT_e \gg 3T_i$, so that the ion temperature can be neglected as above. The kinetic energy transferred to the ion as a result of the hydrodynamic expansion is [KKM03a]

$$K_H = Zk_BT_e. \tag{2.51}$$

The important difference between the Coulomb and hydrodynamic regimes is the dependence of the kinetic energy on ion charge: $K_{Coul} \propto Z^2$ and $K_H \propto Z$. This proportionality applies to the *mean* kinetic energy of ions. The maximum energy of an ion with charge Z_i in the Coulomb case is $K_{Coul}^{max} \propto {}^{Z_iQ}/_R$ where R is the cluster radius and Q the cluster charge. Thus, $K_{Coul}^{max} \propto Z_i$ in the case of Coulomb expansion as it is for the hydrodynamic case. Thus, the dependence of mean kinetic energy on ion charge, which can be measured in an experiment, provides a method to determine the expansion regime.

Early reports on large clusters ($\gtrsim$ 10 nm, Ar_N) reported hydrodynamic expansion as the mechanism that imparts high kinetic energy to ions [DDR+96] when the peak laser intensity was $\sim 10^{16}\,\mathrm{W{\cdot}cm^{-2}}$. Kumarappan et al. saw that large Xe_{150000} clusters explode hydrodynamically while smaller Ar_{40000} clusters exposed to $\sim 10^{16}\,\mathrm{W{\cdot}cm^{-2}}$ pulses followed Coulomb explosion [KKM03b]. But their experiment revealed that the kinetic energy of O^{Z+} ions from small ($N \sim 60$) H_2O clusters depends linearly on Z. These experiments had limited charge-state resolution because of high ion kinetic energies ($10 - 1000$ keV). Lezius et al. studied the expansion of rare-gas clusters [LDNS98] using a magnetic field assisted time-of-flight spectrometer to resolve charge-states unambiguously even at high ion kinetic energies. Large ($N \approx 2.0 \times 10^6$ atoms) Xe clusters exposed to pulses with a peak intensity of $\sim 10^{17}\,\mathrm{W{\cdot}cm^{-2}}$ exploded in mixture of the Coulombic and hydrodynamic mechanisms. This is shown in figure 2.14. Ions with charge-states $Z > 12$ follow the hydrodynamic expansion regime while for the lower charge-states the distribution is closer to the Coulombic regime. We may point out that averaging effects in experiments are mostly inevitable[7], both over the broad distribution of cluster sizes (cf. equation 3.5) and the distribution of intensities in the focal volume. These mask many features of single-cluster features in ion spectra making it difficult to compare experiment with microscopic simulations which are used to calculate kinetic energy spectra of ions and electrons from single clusters [ISR06].

In the case of clusters made of light elements, in particular hydrogen or helium, it is possible to achieve a very high degree of outer-ionization using super-high intensity

[7]Effects of averaging over cluster sizes and laser intensities may be overcome in experiments with X-ray FELs employing imaging detectors [TGB11]. Overcoming effects of averaging over size distributions could be with mass selected clusters in storage rings as also using chemically synthesized nanoparticle introduced into vacuum environments with aerodynamic lens systems [WM06].

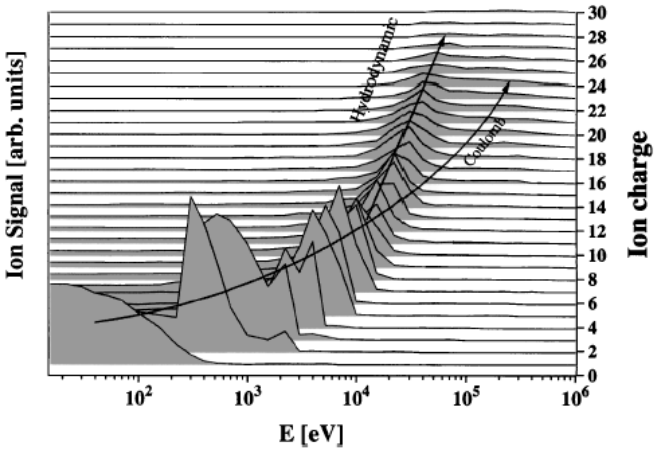

Figure 2.14: Kinetic energy distributions of Xe^{Z+} ions as observed by Lezius et al.[LDNS98]: The arrows indicate the hydrodynamic and Coulombic regimes, respectively. While the higher ($Z > 12$) charge-states essentially follow hydrodynamic expansion, lower charge-states show mixed features.

pulses. In such a scenario, Last et al. [LSJ+97] have proposed "cluster vertical ionization" (CVI). In this case, the cluster is ionized by a super-high intensity ($10^{17-19}\,\mathrm{W{\cdot}cm^{-2}}$) short pulse whose duration is much less than the cluster expansion times. The laser pulse has sufficient intensity to cause complete inner- and outer-ionization leaving bare ions to Coulomb explode. In a CVI scenario, nanoplasma dynamics does not have a major role. Obviously, ion kinetic energies in CVI are much higher than those in the nanoplasma scenario [LJ06]. This may provide routes to realizing complex nucleo-synthesis [HJL06, LJ01b].

In mixed clusters containing a combination of elements with low and high atomic numbers, the lighter ions are accelerated to velocities that are greater than what is expected from a purely Coulombic process. This acceleration leads to kinetic energy distributions which are significantly different from those of homonuclear clusters where equation 2.49 is obeyed [LJ01a, JL05]. In the mixed cluster case, the highly-charged heavy-element ions create a strongly repelling background for the light ions. This results in a dynamic acceleration effect because, during the explosion lighter ions *overtake* the heavier ones so that the potential energy of the light ion continuously changes (increases) during the explosion and equation 2.49 does not hold. Hohenberger et al. [HSM+05] demonstrated the effect of ion overtaking explicitly by comparing the explosion of CH_4- with that of CD_4-clusters. The advantage of heteronuclear environments in producing faster ions was demonstrated in a study comparing deuterium to deuterated methane clusters [MPP+04]. Jha et al. [JMK06], generated heteronuclear clusters by the supersonic expansion of a gas mixture - Ar with $\sim 2-6\%$ of H_2O. They found that the high kinetic energy component ($\sim 100\,\mathrm{keV}$) of ions is enhanced because of the doping which they attributed to more efficient cluster heating due to quasi-free electrons being released earlier during the pulse in the mixed cluster than in its un-doped or pure counterpart. It may be noted that in this experiment the location of the dopant H_2O within the Ar cluster was not known.

2.3 Theoretical and computational approaches

In this section we will present a brief preview of a few theoretical methods employed in performing *ab initio* calculations on rare-gas and metal cluster systems interacting with an IR laser pulse with non-relativisitic peak intensities ($< 10^{18}\,\mathrm{W{\cdot}cm^{-2}}$ at 800 nm). The Hamiltonian for the interaction of an N particle system with an electromagnetic field $\boldsymbol{E}(t)$ is

$$\mathcal{H} = \sum_{1\leq i\leq N} \frac{\mathbf{p}_i^2}{2m_i} + \sum_{1\leq i<j\leq N} \frac{q_i q_j}{|\mathbf{r}_i - \mathbf{r}_j|} + \sum_{1\leq i\leq N} q_i \left(\mathbf{r}_i \cdot \boldsymbol{E}(t)\right), \tag{2.52}$$

where $\mathbf{r}_i$, $\mathbf{p}_i$ and q_i are the positions, momenta and charge of the particles. The second term is due to the Coulomb interaction between particles and the third term is the interaction of the time-dependent laser electric field under the dipole approximation. For rare-gas and metal clusters with less than 10^7 atoms per cluster the radius $R \ll \lambda$, the laser wavelength for NIR pulses. The interaction with the magnetic field of the wave is ignored since only non-relativistic intensities are considered. For a linearly polarized pulse with its electric field along the z-direction having an envelope $E_0(t)$ and central frequency ω_0 $\boldsymbol{E}(t) = \hat{\boldsymbol{z}} E_0(t)\, cos(\omega_0 t + \varphi)$, where φ is a constant phase.

The problem is essentially one of solving the time-dependent Schrödinger equation using this Hamiltonian (equation 2.52). In the case of intense field-ionization, for the $N = 1$ case, i.e. a single atom with a single active electron, an analytical solution is possible [Fed97]. Complete numerical solutions are also feasible, but only for very simple systems with one or two electrons. Hence, approximations are required. It is instructive to consider the de Broglie wavelength of electrons with a temperature T_e: $\lambda_{dB} = \hbar/\sqrt{2\pi m_e k_B T_e}$ as in ref. [Mik11]. In the case of quasi-free or inner-ionized electrons in the cluster, quantum effects may be neglected if they are hot and dilute enough so that their λ_{dB} is smaller than the average distance between them. This leads to the condition

$$\lambda_{dB} n_e^{1/3} \lesssim 1, \tag{2.53}$$

where n_e is the number density of electrons. At solid-like densities ($\sim 10^{22}\,\mathrm{cm^{-3}}$) which prevail in (unexpanded) clusters, for an electron temperature of 50 eV and an average ion charge of 3+ in the cluster, the product $\lambda_{dB} n_e^{1/3} \approx 0.01$. This represents typical electron temperatures and densities in rare-gas and metal clusters in intense IR pulses [Saa06]. Thus, a *classical* treatment of electron-ion and electron-electron interactions of inner-ionized electrons and ions in the cluster nanoplasma is valid for the case of intense IR pulse excitation. In this context, two major approaches to *ab initio* classical simulation methodologies are popular. These are:

- Molecular dynamics (MD) methods and
- Particle-in-cell (PIC) methods.

Even these classical treatments are not easy because the Coulomb interaction is long range and cannot be terminated. In essence, every particle interacts with every other particle in the system.

MD methods are essentially particle-particle methods. In a system of N charged particles, each particle interacts with the remaining $(N-1)$. Considering all the N particles, the number of interactions to be handled by MD codes is $N\,(N-1) \simeq N^2$. Clusters with $N > 10^2$ would be intractable by regular MD methods [Saa06]. Several groups have performed MD calculations to address different aspects of intense laser-cluster interactions [RPSWB97, IB00, Saa06, FMBT$^+$10]. In typical MD simulations, the initial configuration is determined by optimizing the interatomic distance r to the lowest energy configuration in a Lennard-Jones potential $U_{LJ}\,(r) = 4\epsilon\left[(\sigma/r)^{12} - (\sigma/r)^{6}\right]$ where, ϵ is the depth of the potential well and σ the characteristic length [Mik11]. Thereafter, MD codes solve Newton's equations of motion for the particles. Although classical, this is a true atomic scale simulation. The singularity in Coulomb potentials between two charges separated by r_{ij} is avoided by using a smoothening parameter a [JES88]:

$$U_{soft} = \frac{q_i q_j}{\sqrt{r_{ij}^2 + a^2}}. \tag{2.54}$$

Iner-ionized electrons scatter off this potential. However, the ansatz of Deiss et al. [DRB$^+$06] which was successful in explaining the low thresholds for X-ray generation in rare-gas clusters (cf. section 2.2.6) involves the backscattering of quasi-free electrons from non-Coulombic short-range potentials of ionic cores. Such details are usually not accounted for in MD simulations which focus on modelling collective behavior [Saa06, SSR06]. A major step forward in tackling large clusters with $N \gtrsim 10^3$ atoms was made by Saalmann et al. [Saa06] to reduce the scaling of the problem from N^2 to $N \log(N)$ by using hierarchical tree-codes. This allowed them to treat clusters with $N \approx 10^4$ atoms for hundreds of fs in time where collective effects manifest. For more details about the method, refer to [Mik11, Saa06, IB00, SSR06, FMBT$^+$10, AT93].

PIC methods on the other hand are well-suited for *ab initio* large scale simulations [Kun, LB70, VLG95, BL] as the problem of simulating an N-particle system scales with size as $\sim N \log(N)$. Rare-gas and metal clusters have sizes ($< 50\,\mathrm{nm}$) much smaller than the laser wavelength ($\sim 700 - 1000\,\mathrm{nm}$) and the skin depth[8] $\delta \sim c/\omega_p$ (ω_p is the plasma frequency, cf. section 2.2.2). A complete PIC code can be applied in general to all kinds of plasmas including the relativistic laser-plasmas created by pulses with intensities $> 10^{18}\,\mathrm{W{\cdot}cm^{-2}}$. This involves solving all of Maxwell's equations in the PIC code. However, in our current discussion we have considered the interaction of clusters with laser pulses of intensities $\lesssim 10^{17}\,\mathrm{W{\cdot}cm^{-2}}$. Thus, PIC simulations in this intensity regime do not need to consider the magnetic field explicitly. A PIC code typically involves the following sequence of actions which are performed at each time step over the entire simulation volume: First, charge densities are calculated from particle positions. Then the Poisson equation is solved for this configuration to obtain the self-consistent electric field in the entire volume. With a combination of the self-consistent field and the laser field, the equations of motion of the particles are solved to compute the new positions and velocities.

The key aspect of PIC simulations is that the simulation volume is discretized into cells containing more than one particle. In their study on rare-gas clusters

[8] Skin depth is the depth to which electromagnetic radiation can penetrate the plasma.

($N \sim 10^3$), Kundu et al. [Kun, KB06] considered a minimum of about 10 particles per cell to reduce noise and instabilities. The reduction in numerical burden as compared to MD methods is due to this treatment. But clearly PIC is not well-suited to consider interactions between individual particles (collisional phenomena) explicitly. Recently, Jungreuthmayer et al. [JGZB04] were successful in developing a hybrid microscopic PIC code where atomistic simulations could be performed on a very large cluster systems like Xe_{25000} and Ar_{10000} where each cell contains only one particle. This simulation used 16 SUN UltraSparc III processors and took 23 days for the calculation on a single Ar_{10000} cluster.

Finally, it should be mentioned that methods based on density functional theory have also been applied to study the behavior of small clusters especially in the short wavelength (VUV) domain [SSR06, FMBT$^+$10]. But, MD and PIC remain the most popular choices for large cluster systems in intense IR fields which are central to our interest in this work.

Summary

In this chapter we have surveyed the main ideas emerging from investigations hitherto on the interaction of intense NIR laser pulses with rare-gas clusters. This provides a good idea of the major outcomes in benchmark experiments in the last two decades. In summary, it is apt to look at the dynamics of rare-gas and metal cluster systems in intense laser fields in terms of the following *three* stage picture [SSR06]:

- In the first stage, ionization of individual atoms in the cluster by the intense field occurs oblivious of the cluster environment, as though they were isolated. Typically, this occurs in the leading edge of the pulse in durations of ~ 10 fs. The electrons released by parent atoms are trapped by the space charge within the cluster resulting in a frustration of the photoionization process and leading to inner-ionization. This marks the birth of the nanoplasma.

- The second stage is determined by nanoplasma dynamics. The quasi-free inner-ionized electrons leave the cluster boundary on account of laser driving. A harmonic oscillator picture of the quasi-free inner-ionized electrons in the nanoplasma driven by the laser field serves to explain the process. The resulting cluster expansion lowers the eigenfrequency of the nanoplasma so that it interacts resonantly with the laser. This explains features like the near-complete absorption of the laser pulse energy and maxima in ion and electron emission at optimal pulse lengths or delays. The local polarization field within the cluster results in an anisotropy in the charging of the cluster and this manifests in anisotropic ion and electron emission spectra. Very energetic electrons in the nanoplasma are a result of multiple rescattering in the cluster potential. These could also arise from scattering at non-Coulombic ion core potentials which was qualitatively explains the low thresholds of characteristic X-ray emission observed. Both barrier suppression due to the local polarization field and impact ionization by fast electrons lead to the formation of highly-charged ions within the cluster nanoplasma.

- In the third and final stage, the cluster disintegrates after its interaction with the laser pulse. The dynamics in the previous stages leave imprints in the final kinetic energy spectra of ions. Two mechanisms of explosion - Coulombic and hydrodynamic - are at play in this phase of the dynamics. The high ion kinetic energies can result in extremely energetic phenomena like fusion reactions. In molecular clusters, explosion can result in dynamic acceleration effects due to ion overtake which results in non-Coulombic profiles in ion kinetic energy spectra.

This sets the stage for a discussion on the experimental methods employed to realize this rich and complex dynamics in the laboratory and to possibly uncover new phenomena. These are presented in the next chapter.

Chapter 3

Experimental methodology

This chapter describes the details of the experimental methodology used in the present studies on intense IR laser ionization of doped He nanodroplets. The general idea in designing an experiment to study the ionization dynamics of gas phase clusters consisting of rare-gas or metal atoms, or molecules, in intense near-infrared (NIR), vacuum-ultra violet (VUV), soft X-ray or even X-ray pulses is as follows [SDT98, DFD$^+$05, TBH$^+$09]. The photon beam is crossed with a jet of clusters which is either pulsed or continuous. The interaction volume, where the laser beam is focused to a very small spot, is at the center of the spectrometer that collects the fragments from the interaction. These are ions, electrons and/or photons. The type of spectrometer could be a simple time-of-flight mass spectrometer or a comprehensive state-of-the-art instrument like the CAMP-ASG system [Sc10]. Photon sources used in intense-field-ionization studies cover a wide range of wavelengths, pulse lengths and intensities. Table-top Ti:Sapphire based femtosecond laser systems that primarily generate intense NIR pulses ($\sim 800\,\mathrm{nm}$, $10^{14-16}\,\mathrm{W{\cdot}cm^{-2}}$) of durations in the range ($5-100\,\mathrm{fs}$) have been used to study laser-cluster interactions. These sources can also be applied to produce VUV and soft X-ray pulses by high-harmonic generation. A different class of laser systems producing super-high intensities are also available in many laboratories. These range from table-top systems capable of producing peak intensities in the range $10^{16} - 10^{18}\,\mathrm{W{\cdot}cm^{-2}}$ [BDD$^+$04] to petawatt class laser facilities [PM94] capable of producing peak intensities $> 10^{20}\,\mathrm{W{\cdot}cm^{-2}}$, at NIR wavelengths. Large state-of-the-art free-electron laser facilities like FLASH in Hamburg, Germany and LCLS, Stanford, USA, are used to explore linear and nonlinear photoionization processes at photon energies from the VUV to the hard X-ray range. These are now being widely used to study clusters. Considering all these sources together, rare-gas and metal cluster systems have been studied over a wide range of wavelengths - from $1\,\mu\mathrm{m}$ to less than $1\,\mathrm{nm}$. The portable experimental set-up described in this chapter is generic and can be used with almost all of these photon sources with very little or no modification.

In this chapter, we first discuss the details of rare-gas cluster generation. Then we present the details of helium nanodroplet generation - the source, its design and its characteristics. Thereafter, the doping process, the accompanying statistics and the formulation used for the estimation of the doping levels are elucidated. After presenting the details of the time-of-flight (TOF) mass spectrometer employed to detect ions, a brief description of the laser system producing intense few-cycle

pulses is given. Finally, these components are put together in the description of the complete experimental arrangement. The experimental studies were carried out at the Max Planck Institut für Kernphysik, Heidelberg, Germany, using the He nanodroplet source from the Molecular and Nanophysics Group, University of Freiburg, Germany.

3.1 Rare-gas cluster generation

3.1.1 Supersonic expansion and jets

The most common method used for the generation of large rare-gas clusters is based on the supersonic expansion of the desired gas into a vacuum chamber [HO72]. The gas is held at a sufficiently high-pressure and expanded into a vacuum chamber through a nozzle with a diameter in the range of 1-100 μm. If the source holds gas at pressure P_0 (the stagnation pressure) and temperature T_0 before expansion while the other side of the nozzle is maintained at P_b, the condition for supersonic expansion of gas through the nozzle is [SBBL88]

$$\frac{P_0}{P_b} > 2.1. \tag{3.1}$$

The characteristic of supersonic expansion is that the ratio of the mean velocity v of the atoms in the beam to the natural speed of sound in the medium[1] c_s, is greater than unity. This ratio $M = v/c_s$ is also known as the Mach number. This process is essentially non-adiabatic. The consequent cooling of the atoms in the beam thus produced is due to the fact that the random 3D distribution of velocities (internal thermal energy) is converted to a beam with a supersonic velocity in a preferred direction and a near-zero velocity spread. The interaction of this expanding beam with the low-pressure ambient gas in the expansion chamber creates a well-defined free-jet shock-wave system [SBBL88], which is cold (5 mK) and well-separated from the warm background gas at room temperature. Supersonic expansion occurs within the "zone of silence" shown in figure 3.1 (a). Outside this zone, there is a shock wave at the interface between the jet and the background gas. To extract the delicate supersonic part, a skimmer is placed inside this zone of silence. This limits the transverse jet size and the temperature distribution, thereby preventing the supersonic beam from collapsing [Cam84]. The quality of a supersonic jet is quantified by the ratio of the mean velocity of the atoms v to the velocity spread Δv which is called the "speed-ratio" [SBBL88, Mil88]:

$$S = \frac{v}{\triangle v} = \frac{v}{\sqrt{2kTm^{-1}}}, \tag{3.2}$$

where T is the local translational temperature and m the mass of the expanding atoms or molecules. This technology has been a key component in momentum spectroscopy providing the "cold target", for example, in a cold target recoil ion

[1] $c_s = \sqrt{\frac{\gamma kT}{m}}$ where γ is the ratio of specific heat constant pressure and specific heat at constant volume, and the other symbols are as explained in the text (cf. equation 3.2).

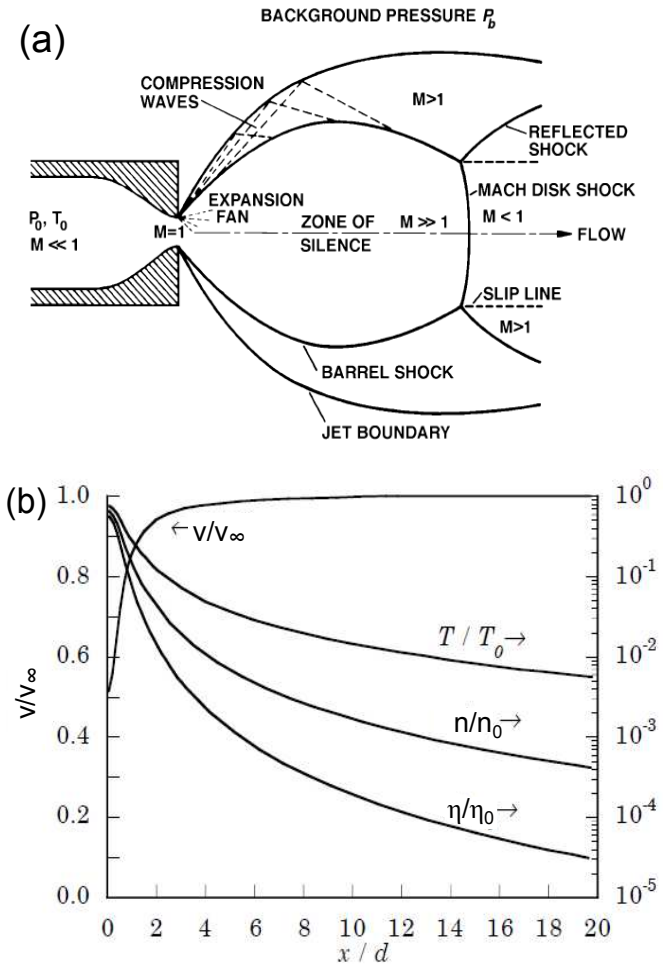

Figure 3.1: Supersonic expansion: The different zones of expansion at the exit of the nozzle are shown in (a). The normalized flow parameters velocity ($^{v}/_{v_\infty}$), temperature ($^{T}/_{T_0}$), density ($\frac{n}{n_0}$) and collision frequency ($^{\eta}/_{\eta_0}$) are shown in (b) as a function of the normalized distance x/d with d the nozzle diameter. The relevance of these parameters to cluster formation is discussed in the text (cf. section 3.1.2). (Adapted from [SBBL88]).

momentum spectrometer - COLTRIMS [MFK02]. The supersonic jet target is replaced with a magneto-optically cooled atomic target [SZS+11] within a momentum spectrometer, which although technically more challenging to realize, can deliver atoms in a trap with temperatures in the μK range.

Due to cold internal temperatures, the atoms or molecules in the jet can form aggregates which are bound by the Van der Waals force with small binding energies of a few meV. Thus, the basis for the formation of these aggregates, or clusters, in the gas-phase is the supersonic expansion process. We describe the formation process and the characteristics of clusters thus produced in the following section.

3.1.2 Formation of rare-gas clusters

For a nozzle of diameter d, the normalized flow parameters - velocity (v/v_∞), temperature (T/T_0), density (n/n_0) and collision frequency (η/η_0) - are plotted figure

3.1 (b) as a function the ratio x/d, where x denotes the distance from the nozzle. The denominators are limiting values of the parameters when $(x/d) \to 0$ or $(x/d) \to \infty$, as indicated. v_∞ is the terminal velocity of the beam, T_0 the backing temperature, n_0 the gas density and η_0 the collision frequency before expansion. The local temperature of the expanding atoms can be lower than the condensation point. Thus, if a sufficiently large number of collisions take place in the flow, the gas condenses into clusters. The size of these clusters depends on the duration over which the collisions takes place. It should be mentioned that figure 3.1 (b) presents a numerical solution of the flow equations ignoring clustering and thus serves only illustrative purposes here. Hagena and co-workers extensively studied the clustering process for rare-gas clusters and evolved a semi-empirical formalism in terms of the Hagena parameter [HO72, WVGM01, SDT98]

$$\Gamma = kP_0 \left(\frac{d}{\tan\alpha_{1/2}} \right)^{0.85} T_0^{-2.29}, \tag{3.3}$$

where k is a species dependent parameter (e.g., 1700 for Ar and 5500 for Xe), $\alpha_{1/2}$ is the half-angle of the nozzle opening, d is expressed in μm, P_0 and T_0 are expressed in mbar and K respectively. The backing parameters are also referred to as "stagnation" parameters. Clustering begins for $\Gamma > 300$ [SDT98]. The Hagena parameter also provides an estimate for the number of atoms per cluster [SDT98]

$$n = 33 \times \left(\frac{\Gamma}{1000} \right)^q, \tag{3.4}$$

where q $\approx 2 - 2.5$, so that $n \sim P_0^{2-2.5}$. For $\Gamma \leq 10^4$, the average number of atoms per cluster is given by setting $q = 2.35$. For $\Gamma \gg 10^4$, which corresponds to the case of high-backing pressures, Dorchies et al. [DFBG03] have reported a weaker dependence in the scaling of n when compared to equation 3.4 so that the modification $n = 100 \times \left(\frac{\Gamma}{1000} \right)^{1.8}$ was found to be necessary in the parameter space of their experiments. A more recent and detailed study [CKAK10] of the scaling law for n with nozzle half-opening angle $\alpha_{1/2}$ also found a weaker scaling with the backing pressure than what the Hagena formulation (equation 3.4) puts forth.

Clusters thus produced have a log-normal size distribution given by:

$$f(N) = \frac{1}{N} \frac{1}{\sqrt{2\pi\sigma}} \exp\left[-\frac{\ln^2 \left({}^{N}/_{N_0} \right)}{2\sigma^2} \right], \tag{3.5}$$

where N_0 is the most probable cluster size and σ is related to the full-width at half-maximum (FWHM) of the distribution. The mean or average cluster size $\overline{N}$ is related to N_0 and σ by the relation $\overline{N} = N_0 \cdot \exp\left({}^{\sigma^2}/_{2}\right)$. The FWHM of the distribution ΔN is given by $\Delta N = \sqrt{N_0^2 \cdot \exp\left({}^{\sigma^2}/_{2}\right) \cdot \left(\exp\left({}^{\sigma^2}/_{2}\right) - 1\right)}$. Its characteristics for different values of $\overline{N} = 2000 \cdots 6000$ for $\sigma = 0.46$ are shown in figure 3.2. This broad distribution of cluster sizes in a beam produced by supersonic expansion often enforces interpretation of experimental results in terms of the scaling of experimental parameters with $\overline{N}$, or equivalently with P_0 or T_0, instead of individual cluster sizes.

From the point of view of experimental design, it is important to note that in order to achieve cluster sizes in the range of $10^2 - 10^6$ atoms per cluster, large stagnation

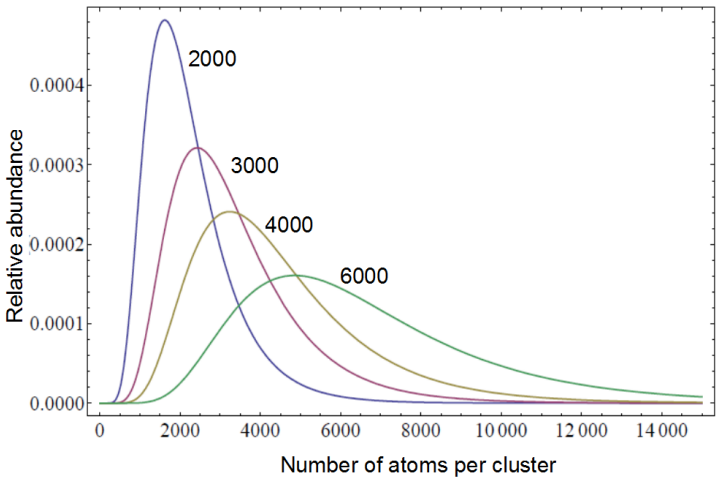

Figure 3.2: Log-normal distribution of sizes: The horizontal axis shows the number of atoms per cluster and the vertical axis is the relative abundance. The curves are labeled with the values of $\overline{N}$ used, with $\sigma = 0.46$ (cf. equation 3.5). The area under the curve is normalized to 1.

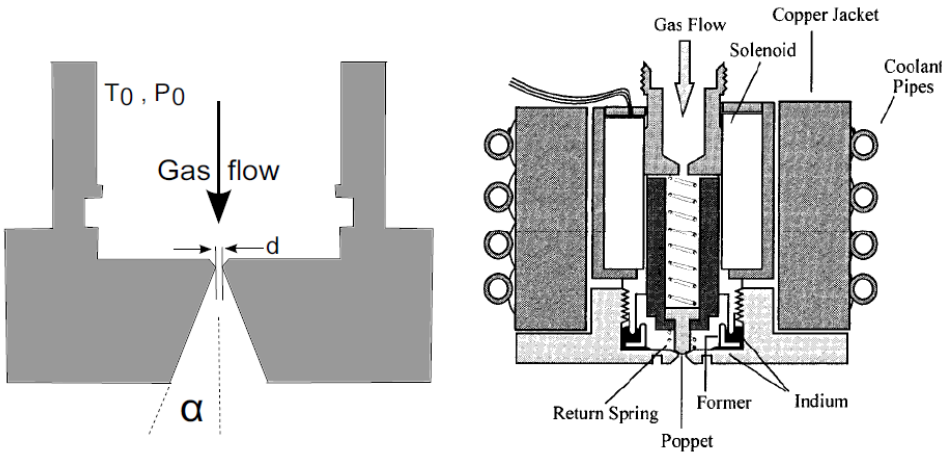

Figure 3.3: (left) Schematic of a conical nozzle. (right) An implementation of a solenoid driven pulse valve by Smith et al. [SDT98] (details explained text, cf. section 3.1.2).

pressures $\sim 1-100$ bar with nozzles of diameter $\sim 5-100\,\mu$m are required. Indeed, this leads to enormous gas throughputs into the vacuum chamber where the cluster source is housed. For the successful propagation of the cluster beam, a background pressure of 10^{-3} mbar should be maintained in the chamber. This also facilitates the operation of an ultrahigh vacuum pump (turbo-molecular or oil diffusion). If operated in a continuous beam mode, sizable throughputs >10 mbar$\cdot$L$\cdot$s^{-1} reaching even up to 10^3 mbar$\cdot$L$\cdot$s^{-1} may have to be managed. Hence, large pumping speeds typically of the order of 1000 L/s or more are required if a background vacuum better than 10^{-3} mbar is to be maintained. In order to manage the gas load, often it is necessary to employ a pulsing mechanism. A popular scheme using a spring-loaded poppet or stopper which is actuated by a solenoid is shown in the right panel of figure 3.1. This design by Smith et al. [SDT98] also shows a copper jacket and coolant pipes for carrying a suitable fluid (often liquid nitrogen) to cool the nozzle and the gas flowing through it. Commercial solenoid driven nozzles available from Parker (*Parker Hannifin Corp.*) - e.g., general purpose solenoid valve *IOTA ONE* - are a popular choice for low-repetition rate operation (up to 100 Hz) at room temperature or higher. During the initial stages of work being reported in this thesis, one such valve was used. It is important to note that leak rates better than 10^{-6} cm^3/s per bar of backing pressure are necessary when the poppet is closed. For operation at higher repetition rates (~ 1 kHz), piezo-electrically driven systems are necessary and have also been demonstrated in the context of cold supersonic jet beams (see e.g. ref. [IKJ09]).

The work presented in this thesis concerns the production of helium clusters. In the Hagena formalism (equation 3.3), the constant k has the smallest value for He, $k_{\mathrm{He}} = 3.85$. This is much smaller compared to the other rare-gases $k_{\mathrm{Ne}} = 185$, $k_{\mathrm{Ar}} = 1650$, $k_{\mathrm{Kr}} = 2890$ and $k_{\mathrm{Xe}} = 5500$. Hence, in addition to very low stagnation temperatures, the demand on backing pressures is also higher for the production of He clusters with $10^2 - 10^5$ atoms per cluster. Thus, cooling the nozzle to low temperatures ($\sim 15-30$K) along with maintaining high stagnation pressures $20-100$ bar is necessary. Under these extreme conditions of temperature and pressure, it is simpler to employ a continuous beam source with a large pump as opposed to pulsed operation. The following section describes the He cluster source employed in this work. Recently, pulsed sources of He clusters operating at temperatures as low as 6K have been demonstrated [PRRL09], although the effect of pulsing on cluster sizes and size distributions is not yet completely understood.

3.2 Helium nanodroplet source

Helium was first liquified by Kammerlingh Onnes [Onn09]. From the phase diagram of bulk ^{4}He presented in the figure 3.4, it is clear that a phase transition to the liquid occurs at temperatures of a few kelvin.

As mentioned before, supersonic beams have internal temperatures of a few hundred mK. The helium clusters formed in these beams are in a naturally superfluid state as expected from the phase diagram in figure 3.4 [TV04, TV98, SL06]. Hence, we will refer to helium clusters as "droplets" or "nanodroplets". While early work used larger nozzle diameters ($\sim 100\,\mu$m) (e.g. ref. [Gsp81]), currently most workers use

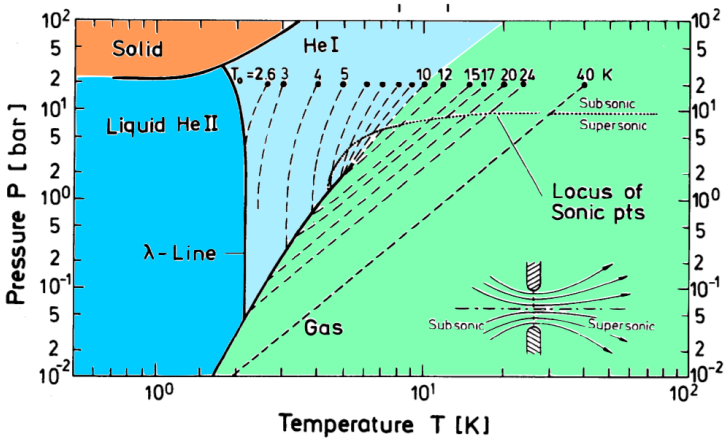

Figure 3.4: ^{4}He phase diagram: The phase diagram shows the gas(green), normal liquid phase (He-I, in light blue), the superfluid phase (He-II, in blue) and the solid phase(orange). The dashed lines are isentropes at different temperatures which label them. The thick black line between the gas and liquid phases marks the transition from subsonic to supersonic regimes in fluid flow. This phase diagram has been adapted from Buchenau et al. [BKN$^+$90]

nozzles 5-10 μm in diameter with high backing pressures $P_0 \approx 5 - 200$ bar and low backing temperatures $T_0 \approx 3 - 300$ K for droplet generation. A careful setting of the backing conditions (P_0, T_0) permits control over the mean droplet size $\overline{N}$ and longitudinal beam velocity v_D. These source conditions (P_0, T_0) broadly cover two expansion regimes of nanodroplet formation which are qualitatively different. Figure 3.5 presents the expansion regimes in the (P_0, T_0) parameter space. Panel (b) of figure 3.5 highlights the separation into the two regimes - the *subcritical* regime with $\overline{N}$ up to 10^5 and the *supercritical* regime $\overline{N} > 10^5$.

The *supercritical* regime is characterized by large droplets of size $\overline{N} > 10^5$ formed by the dispersion or break-up of liquid as shown in figure 3.5a. In this case the (P_0, T_0) parameters are in a regime where the critical point is reached from the low-temperature side. The speed distributions and size distributions have been found to be bimodal by Buchenau et al. [BKN$^+$90]. The major fraction of droplets is formed by the fragmentation of liquid He and contain more than 10^6 atoms [SL06, TV04] with an exponential distribution of sizes [KH99]. In the same beam, smaller clusters are formed due to the following reason: He atoms evaporating from the large droplets formed, seed the expanding monoatomic gas which can lead to clustering by recondensation [BKN$^+$90]. Buchenau et al. [BKN$^+$90], measured the speeds and speed ratios of both types of clusters formed in supercritical expansions by measuring the droplet time-of-flight. Typically speed ratios $S \geq 40$ were found for clusters formed in this regime. It is interesting to note that He clusters with 10^{10} atoms, with velocity as low as 15 m s^{-1} and a divergence of just ≈ 1 mrad have been demonstrated [GT03]. These very large clusters within the supercritical regime are formed by Rayleigh break-up of the liquid jet as shown in figure 3.5 (a). Here, the liquid jet ejected from the nozzle breaks up into huge droplets whose diameter is comparable to the width of the exiting jet due to Rayleigh instability [Ray78] pro-

ducing a very collimated and directional beam. This property of Rayleigh break-up is exploited in ink-jet printing technology [Wij10]. In the course of our experiments, we also generated droplets in the supercritical regime ($\sim 10^{6-7}$atoms per droplet) by lowering the nozzle temperature.

In the *subcritical* regime, droplets are formed by the aggregation of atoms as described in section 3.1.2. This is the most common mode of operation for helium droplet machines especially in spectroscopic studies [SL06]. In this regime the expanding helium behaves approximately like an ideal gas. The size of droplets can be adjusted by changing the nozzle temperature or the backing pressure of the gas. Benchmark experiments reported by Toennies and co-workers [TV04] are commonly used to calibrate droplet sizes. The droplet size distribution was determined experimentally by the deflection of atomic beams from droplets in scattering experiments [HTK96, HJPTP01]. These have been collated and presented in ref. [SL06] for the case of a $5\,\mu m$ nozzle for different stagnation pressures. In our studies, the same were used for droplet size calibration. However, care should be taken in comparing the experimental conditions to these calibration curves. Measurement of absolute nozzle temperatures could have systematic errors. To overcome this issue, a signal proportional the droplet flux measured as a function of nozzle temperature can be employed [SOBP04] to determine the critical point where the transition from the subcritical to the supercritical regime occurs. Stienkemeier et al. [SL06] used the strength of the signal from laser induced fluorescence for this purpose as shown in figure 3.6. The maximum in the signal at $\approx 15\,\mathrm{K}$ marks the critical point. Thereafter, the transition temperatures can be compared with those in the calibration curves to get an estimate of the mean of the log-normal distribution equation 3.5 of droplet sizes (cf. section 3.1.2). We measured the changes in pressure in a carefully designed beam dump which was used like a Pitot tube[2] [SSM10] as will be explained in section 3.6. A similar transition in the pressure of the beam dump also gives a measure of the critical point. In this regime, speed-ratios $S \gtrapprox 100$ have been measured by Buchenau et al. [BKN$^+$90]. Lewerenz et al. reported $S = 100$ for $P_0 = 80\,\mathrm{bar}$ and $T_0 = 24\,\mathrm{K}$ which are similar to the conditions in our experiments [LST93]. Typical axial speeds of these beams in this expansion regime are in the range of 250–450 m/s depending on backing pressure and temperature. These speed ratios are important for spectroscopic measurements and for the preparation of a cold target. A high quality beam with a large S number usually ensures sufficiently high droplet densities for photoionization experiments owing to low beam divergence.

3.2.1 Source details

The He nanodroplet source used in the experiments being described in this dissertation was designed and constructed at the University of Freiburg in the Molecular and Nanophysics group [3]. This delicate source was transported by road (ca. 200km) to Max Planck Institut für Kernphysik, Heidelberg during the course of the work

[2]Strictly speaking, Pitot tubes are used for the measurement of jet velocities. We use it only to obtain relative estimates of gas flow into the beam dump as a function of nozzle temperature. The design idea is borrowed from conventional Pitot tubes.

[3]Group of Prof. F. Stienkemeier: http://www.nanophysik.uni-freiburg.de/

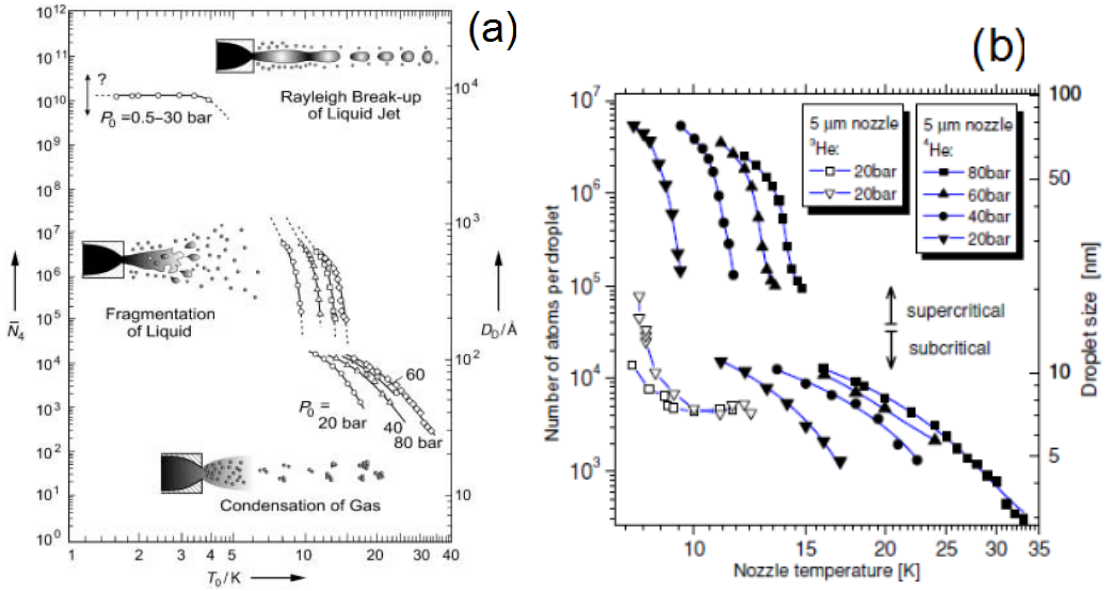

Figure 3.5: (a) Mean number of ^{4}He atoms per droplet ($\overline{N}_4$) as function of nozzle temperature in different expansion regimes. Subcritical regime where droplets are formed by the condensation of gas upon supersonic expansion, and the supercritical regime where large droplets are formed by the fragmentation of liquid He formed before the exit of the nozzle are shown. At temperatures $< 4\,\mathrm{K}$, jet break-up due to Rayleigh instability occurs. This compilation from the work done in the group of J. P. Toennies [TV04] is often used as the standard for calibration of droplet sizes. The vertical axis on the right shows droplet diameters in angströms. (Note: The subscript in $\overline{N}_4$ stands for the isotope mass in atomic units as used in the original source of this plot.) (b) Mean droplet sizes as a function of temperature for different backing pressures for a $5\,\mu$m nozzle at parameters relevant to our work as compiled by Stienkemeier et al. [SL06]. The data for ^{4}He droplets from panel (a) are included in panel (b).

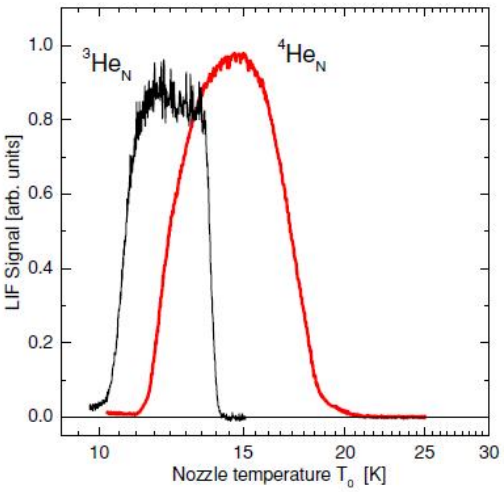

Figure 3.6: Laser induced fluourescence (LIF) signal during the cooling down of the nozzle is plotted as a function of nozzle temperature for ^3He_N (black) and ^4He_N (red) droplets doped with Na as reported by F. Stienkemeier et al. [SL06]. The LIF signal gives a measure of the droplet flux. The maximum in the flux of ^4He_N droplets at $\approx 15\,K$ is due to a transition from the subcritical to the supercritical regime, and similarly for ^3He_N droplets. At temperatures below this transition value, the number of atoms per droplet increases but the number density of the doped droplets decreases, which leads to a decrease in the LIF signal.

to carry out experiments. It may be mentioned that this essentially meant a dismantling and complete reconstruction of the source [4]. A detailed view of the source is presented in figure 3.7. The basic principle of the design is the same as that of a generic supersonic jet source. However, the need to maintain the nozzle at temperatures $< 10\,K$ requires a very careful design and choice of materials. We will describe the source in the direction of gas flow.

Pressurized He gas is delivered into the gas inlet from a gas bottle ($\sim 200\,bar$, initially) by a system of valves. The purity of gas used is crucial to successful operation of the source without clogging the nozzle. ^4He gas of grade He 6.0 which has a purity of 99.99999% (total impurities $< 1\,ppm$) should be used when the nozzle is cooled down. Since He 6.0 is relatively expensive, He 4.0 (99.99%, impurity $<$ 0.01%) gas can be used for maintenance purposes when the system is at room temperature to keep gas flowing through the nozzle to avoid clogging. A system of high-pressure valves (*SS-0RM2-S2-A, Swagelok*) is used to exchange the gases. In this process, the gas line is pumped out with a rotary pump after shutting off the flow of He 4.0 and before the introduction of He 6.0. The pressure in the gas line is monitored by a thermocouple gauge. The pressure of the inlet gas was measured using a gauge (*PGI-63B-BG100-LAOX, Swagelok*) for pressures in the $1-100\,bar$ range. A high-pressure release valve (*SS-4R3A5, Swagelok*) was integrated in to this inlet system to prevent accidental build-up of over-pressure.

The next stage of operation is the cooling process. The most common procedure used to achieve cooling up to $4\,K$ is to employ a two-stage cold head. Several groups operating He nanodroplet sources have favored cold-heads manufactured by Sum-

[4]reconstruction time ≈40 man-hours

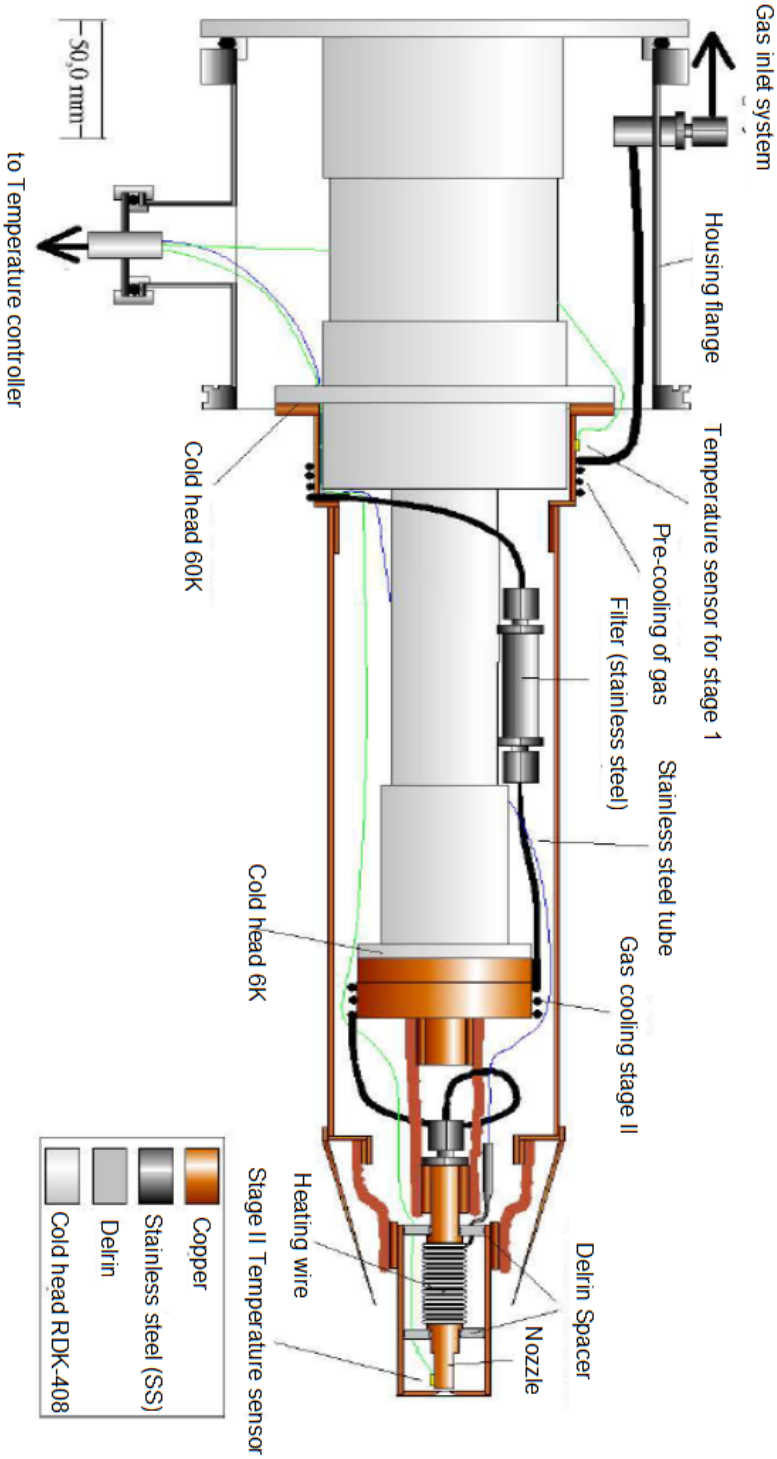

Figure 3.7: Detailed schematic of the He nanodroplet source. (courtesy: M. Mudrich)

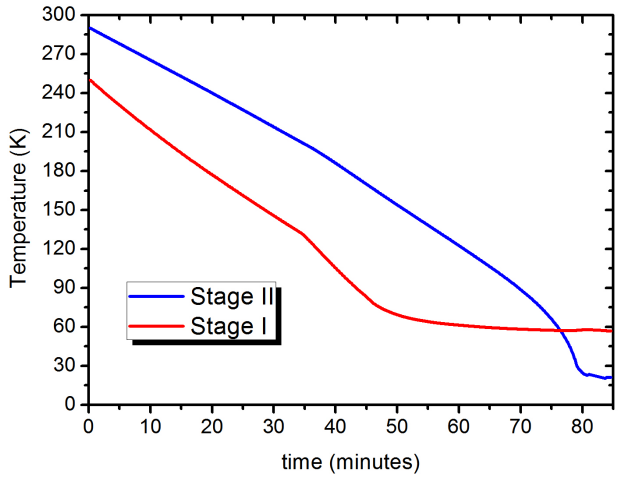

Figure 3.8: Cooling curve for stage I (pre-cooling) and stage II (nozzle) as a function of time. The backing pressure in this case was 90bar and the nozzle diameter was 5μm.

itomo Heavy Industries[5]. We used the *RDK-408* cold-head with the appropriate compressor system (*CSW-71D*) provided by the same manufacturer. It should be mentioned that the compressor also uses the expansion of high-purity helium in a closed-cycle to achieve cooling by the Gifford-McMahon process [Jou08]. In the first stage (stage I), the gas is cooled from room temperature to 60 K. Helium gas is contained during the cooling process in a 1/8 inch stainless steel tubing. This is wound (10 rounds) around stage I of the cold head made of copper in a bobbin-like manner and bound to it using a high thermal conductivity silver alloy. Cooling down this steel tube results in lowering the temperature of the ^{4}He gas. At this cooling stage, the heat load in reducing the temperature from 295 K to 60 K is $\approx$ 810 mW, as estimated using a temperature independent specific heat of C_p= 20.8 J·K^{-1}·mol^{-1}. The temperature at this stage is measured by a sensor (TS1) which is a silicon diode (*DT-670C-SD*). The leads of this sensor are connected by high-purity copper wires via feedthroughs to the temperature controller. Thereafter, the gas is passed through a sinter filter with a pore size of 0.5 μm in a stainless steel housing (*SS-3F-MM-2, Swagelok*). At the end of this cooling stage, the gas at 60 K carried in the steel tube is let into a nozzle holder made of high purity copper.

The second and final cooling stage (stage II) of the cold head is connected (soldered) to the nozzle holder which is fabricated using high purity copper instead of the usual ETP copper. This connector is a set of 3 braided cables made of fine copper strands. This offers flexibility to the nozzle holder thus allowing the nozzle to be manipulated in the transverse direction for alignment purposes. This stage of cooling takes the gas from 60K to the desired final temperature in the range of 15$-$25 K in our case. The heat load handled by the cooling system in this case is $\approx$220 mW. Another diode-based temperature sensor (TS2) of the aforementioned type is connected to the nozzle holder using an appropriate cryogenic adhesive (obtained from *Cryophysics GmbH*). High-purity copper wires (99.9999%) are used to

[5]http://www.shi.co.jp/english and http://www.shi.co.jp/english/products/precision/cryogenic.htm

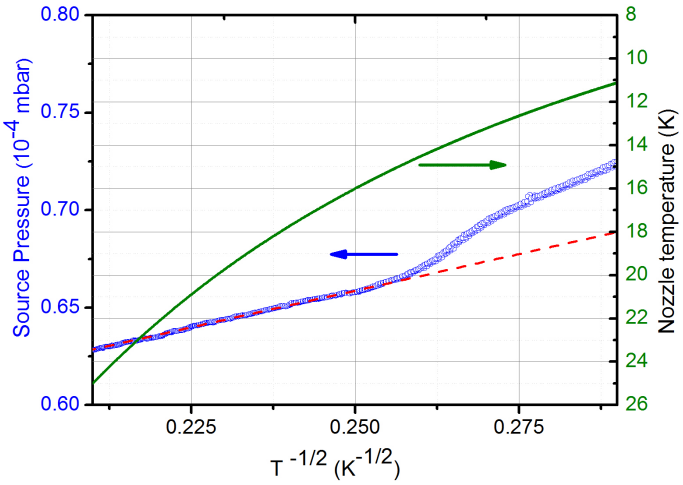

Figure 3.9: (left axis) Source chamber pressure in arbitrary units (blue) as function of $T^{-\frac{1}{2}}$ showing the deviation of gas flow from ideal gas behavior (red) according to equation 3.6. (right axis) The nozzle temperatures corresponding to different values of $T^{-\frac{1}{2}}$ shown in green.

make connections to the sensors. Signals from TS1 and TS2 are transmitted using appropriate feedthroughs to a PID-controller (proportional-integral-derivative) *LakeShore333* (Lakeshore Cryotronics Inc.[6]). This controller does not manipulate the two stage cooling process or the compressor which works at full power at all times. Instead, in order to maintain the desired temperature, the PID-controller controls the current flowing through the resistive heating coil wound around the nozzle holder (as shown in figure 3.7) with inputs of temperature reading from TS1 and TS2 which are part of the feedback loop. The heating coil is made of a wire of resistance $\approx 32\,\Omega$.

The gas thus cooled to a desired temperature in the range of $15 - 25\,\mathrm{K}$ flows out through a $5\,(\pm 1)\,\mu$m nozzle orifice in platinum foil of 100μm thickness (from Plano GmbH [7]). The platinum foil with the nozzle orifice is a commercial electron microscope aperture which is widely used. As mentioned before, this tiny orifice required careful attention to prevent clogging. After using He 6.0 to produce droplets, whenever the system is restored to room temperature, He 4.0 gas is kept flowing through the nozzle to ensure that it does not get clogged. In spite of this, nozzle clogging over a period of time cannot be completely avoided and the platinum foil with the orifice had to be replaced, although infrequently (once in a few weeks of operation). Fixing the platinum foil to the copper housing was done by deforming the tip of this housing by applying pressure using a simple custom-built tool which could be attached to a standard drill machine or a lathe. Very slow rotation of the tool during the application of the deforming force is advisable. Thus, a leak free operation without the use of any adhesives even with backing pressures of up to 100 bar was achieved. In practice, this source can be operated at temperatures as low as 6 K. The entire source is housed in a cylindrical copper shield (not shown in figure 3.7)

[6]http://www.lakeshore.com/
[7]http://www.plano-em.de/

which is water-cooled. This is required due to the substantial heating of the parts contained within the shield by black-body radiation. This is estimated to be ~ 1W.

In figure 3.8, the cooling curve of the He nanodroplet source is presented when stage I is cooled to 57 K and stage II is cooled to 21 K from room temperature (295 K). The desired temperatures are reached from room temperature after about 80 min of operation, which is typical. The flow of an ideal gas F depends on the backing pressure P_0, nozzle diameter d and nozzle temperature T as [POW, And02]

$$F \propto P_0\, d^2\, T^{-\frac{1}{2}}. \tag{3.6}$$

A measurement of the source chamber pressure as a function of the nozzle temperature (figure 3.9) reveals that the flow deviates from what is expected of an ideal gas. This deviation occurs in the region where the gas to liquid phase transition occurs. It is important to note this fact because a substantial amount of He gas is input into the vacuum chamber housing the nanodroplet source during operation. Since the scaling of pressure in this vacuum chamber is underestimated by the approximation of a ideal gas flowing through the nozzle, we must take notice of this while lowering the nozzle temperature. The enormous gas load in this chamber necessitates a vacuum pump of a speed $\sim 8000\,\mathrm{L{\cdot}s^{-1}}$. In our case, this was an oil diffusion pump with a two stage backing, the details of which are presented in a subsequent section.

3.2.2 Size characteristics of He droplets

The He nanodroplets produced by supersonic expansion have size characteristics similar to other rare-gas clusters. Lewerenz et al. [LST93] determined the size distribution by the deflection of an atomic beam from nanodroplets at experimental parameters which are nearly identical to those used in our experiment - nozzle diameter of 5μm and a backing pressure of 80 bar in the temperature range $14-25$K. This is shown in figure 3.10. Evidently, the mean droplet size is higher for lower nozzle temperatures as expected from the Hagena scaling (equation 3.3) and distribution of droplet sizes is log-normal (equation 3.5). Indeed, these experimental values in [LST93] form a part of the calibration curves widely used and were presented in figure 3.5. The radius of an individual ^{4}He droplet containing N atoms is [TV04]

$$R_{^4He} = 0.222 N^{\frac{1}{3}}[\mathrm{nm}]. \tag{3.7}$$

3.3 Doping nanodroplets with foreign atoms

He nanodroplets offer an excellent host medium for designing two- or even multi-component clusters since they readily capture foreign atoms or molecules - which we call *dopants* - from the gas phase by inelastic collisions. In comparison to liquids at room temperature, immersing foreign species into He nanodroplets at mK temperatures readily provides a system to study quantum dynamical and statistical phenomena [SL06]. Since these nanodroplets constitute a finite system, they make it possible to study various phenomena of interest as a function of cluster size and

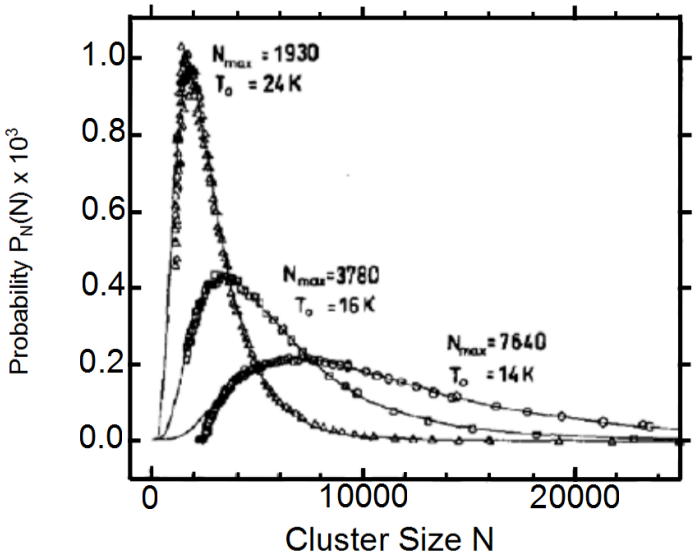

Figure 3.10: Size distribution of He nanodroplets (nozzle diameter: 5μm, backing pressure: 80bar) for various nozzle temperatures as measured by Lewerenxe et al. [LST93].

surface area. These are of fundamental interest since they act as ideal quantum-classical hybrid systems for experimental investigation. The dopant can be virtually any atomic species which is either immersed inside the droplet or is held on the droplet surface. This makes He nanodroplets a versatile target for experiments where one can assemble and stabilize a large combination of dopants to perform high-resolution spectroscopy in cold environments [SL06]. Two popular methods of doping a nanodroplet beam are widely used:

1. Pick-up from a gas phase target -

   (a) Pick-up from a gas cell: Atoms are picked up by the droplet beam which passes through a differentially pumped gas cell which contains the desired dopant in the gas phase;

   (b) Crossed beam: The desired dopant is rendered into a supersonic beam which can be crossed with the droplet beam to enable pick-up.

2. Pick-up from a laser ablation of a solid target - a solid target is ablated by a pulsed laser and the ablated atoms/ions are captured by droplets in a beam passing close to the point of ablation.

Each of these techniques offers exclusive advantages. Pick-up from gas phase is simple and can be used for both atoms or molecules already in the gas phase at room temperature or for those which can be easily vaporized. Cross sections for pick-up are determined to be about 50–90% of the total integral geometrical cross section of the droplets [LST95]. Doping of metals requires vaporization at temperatures exceeding 1500 K and has been successfully carried out [RUMS00]. Pyrolysis has been employed to introduce radicals into He droplets [KMM02]. In these cases

the high temperature thermal radiation in the doping region does not affect the droplet since dipole transitions in He require at least 20 eV. The crossed-beam doping technique offers the following advantage: The dopant atoms in the beam have well-directed velocity vectors as against the effusive case where the velocities are in random directions. Therefore, the dopant beam can be directed on to a pump so that the residual dopant atoms remaining in the beam after its interaction with the droplets are quickly removed from the system. Thus, one can ensure that residual dopant atoms do not enter the reaction chamber where the beam of doped droplets is studied. This ensures high signal-to-noise ratios.

Doping of droplets by laser ablation is a relatively new technique and was introduced by the group of Frank Stienkemeier [CMS03, SL06]. This offers unique advantages especially in doping with metal atoms/ions. In many cases (e.g. Vanadium) it is non-trivial to obtain a sufficiently dense vapor of the desired metal atoms or ions by electrical heating which can be used for doping droplet beams. Laser ablation offers a remarkable solution to this situation. The material to be ablated is usually held in the form of a rod. The rod is simultaneously rotated and translated as laser pulses (few ns in duration with energy of $\sim 100\,\mathrm{mJ}$) from a frequency doubled Nd:YAG or excimer system are focused on it to cause ablation. The ablation plume produced at the surface of the rod is kept a few millimeters away from the He droplet beam to achieve doping. Even metals like vanadium which require very high temperatures for vaporization ($\sim 1800\mathrm{K}$) could be loaded into droplets successfully by this method [SL06]. In this work, we are interested mainly in rare-gas dopants which we load into droplets by passing the beam through a pick-up cell containing the desired dopant gas whose partial pressure is carefully regulated [SL06]. We present this in detailed below.

3.3.1 Pick-up statistics

Several studies have demonstrated that the statistics of pick-up of foreign atoms by He nanodroplets is a Poisson distribution for doping with rare-gases and molecules [LST95, NM00, KGS$^+$07, TS07]. Hence, the probability to pick-up k dopants follows the distribution function:

$$p(k) = \frac{K^k}{k!}\mathrm{e}^{-K}, \tag{3.8}$$

where K is the mean of the Poisson distribution which is proportional to the pressure of the dopant gas in the doping cell. An example of the Poisson distribution is shown in panel (a) of figure 3.11. Underlying the Poisson distribution is the assumption that we can neglect the change in the capture cross section of the droplet during the doping process, that is, it does not change with the number of atoms or molecules previously trapped in the nanodroplet. In addition to this approximation if we neglect the (relative) velocity of the dopant atoms, the mean of the Poisson distribution K is related to ρ the number density of the dopants in the pick-up cell, L the cell length and σ the capture cross section as [LST95, NM00, KHGM07, TS07]:

$$K = \sigma\rho L. \tag{3.9}$$

The capture cross section due to the geometric size of the nanodroplet (equation

3.7) with N atoms of He within can be approximated by

$$\sigma_{geo} \approx 0.15 \times N^{\frac{2}{3}} [\mathrm{nm}^2]. \tag{3.10}$$

It should also be noted that the nanodroplets have a log-normal size distribution and in view of equation 3.10, K will be affected by the nanodroplets size distribution. A representative case of a model calculation for the case of Na doping ($K = 3$) for mean nanodroplet size of 5000 He atoms per droplet is presented in panel (b) of figure 3.11. We will always refer to the mean value of the doping distribution while stating the number of dopants or doping number in the context of experiments.

The doping distribution deviates from Poisson statistics for large doping numbers. The assumption of a constant pick-up cross section σ, which underlies equation 3.9, is strictly true only for sufficiently low densities of dopant atoms in the doping cell. The change of the pick-up cross section occurs due to the release of the binding energy due to collisional, internal and complexation mechanisms during the doping process. This leads to the evaporation of helium atoms from the nanodroplets and consequently to an overall shrinkage of the droplet. It should be mentioned that the doping distribution deviates strongly from the current description for dopants like Rb which are weakly bound to the droplets and reside in surface dimples. In such a case, desorption of dopants from the droplet leads to a change of the distribution from the expected Poisson statistics [VK03]. Further, due to the superfluidity of the droplets, the trapped dopants aggregate to form complexes. Rare-gas atoms reside at the center, while alkali atoms are on the surface and alkaline-earth atoms are in between [ALC95, TV04, SL06]. The location of the dopant is governed by the binding energy of the dopant-He interaction.

3.3.2 Evaporation of He atoms during the doping process

It is appropriate to examine the doping process in greater detail now. The He nanodroplet beam travels at a velocity of ≈ 350 m/s. Following a sticking collision between the nanodroplets in the beam and the dopant atoms/molecules, energy involved in the binding process is released. This energy consists of - the collisional kinetic energy E_{coll}, the internal energy of molecules E_{int}, the binding energy of the dopant to the He atoms E_{HeX}, and the binding energy E_{XX} of adding successive dopant atoms to those already within the droplet. Here X represents the dopant atom or molecule. Thus, the total budget of energy released in the pick-up process is

$$E_{pickup} = E_{coll} + E_{int} + E_{HeX} + E_{XX}. \tag{3.11}$$

We will discuss the estimation of E_{pickup} for the case of rare-gas doping with Xe, Kr and Ar, which is relevant to this work. E_{int}, the internal energy of the dopant is the vibrational (~ 1000 cm^{-1}) and the rotational energy ($\sim 1 - 10\,\mathrm{cm}^{-1}$) of the dopant molecules. For rare-gas doping this term can be dropped from equation 3.11. We can estimate the other contributions. The collisional kinetic energy is estimated after Lewerenz et al. [LST95] as:

$$E_{coll} = \frac{3}{2} k_B T + \frac{1}{2} m_X v_{He}^2 \tag{3.12}$$

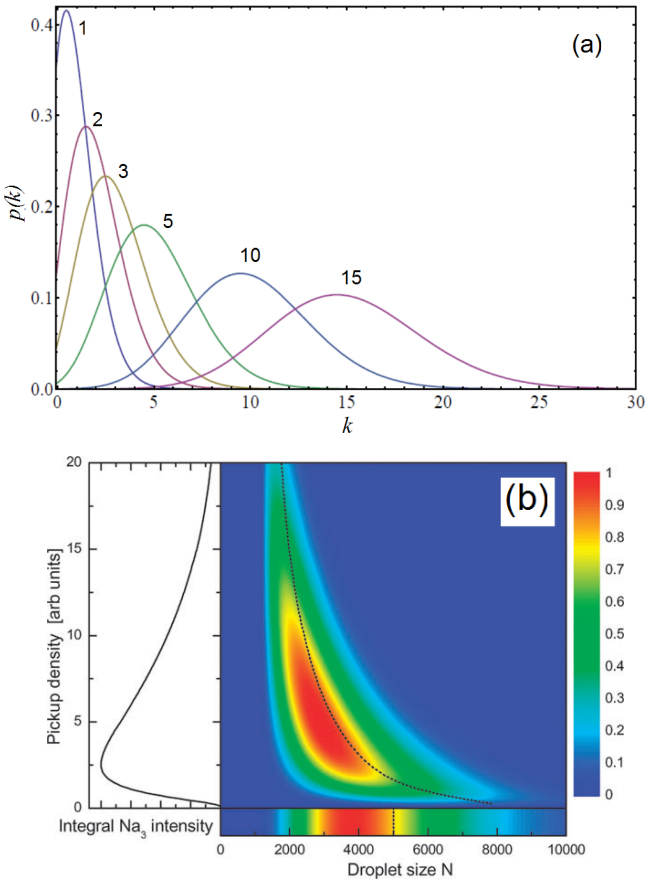

Figure 3.11: (a) Poisson distribution: the number of dopants k, the probability $p(k)$ and the mean of the distribution K (shown in curve labels) are shown. (b) Probability of finding a Na-trimer in an individual droplet of size N dependent as a function of the (relative) density of atoms in the pick-up cell (in arbitrary units). Droplets were assumed to have a log-normal size distribution with a mean size of 5000 He atoms/droplet before entering the pick-up cell, which is represented in the bar at the bottom. The dotted line in the 2D-plot indicates the mean droplet size. To the left in this panel, the Na_3 intensity integrated over all droplet sizes is plotted as a function of density of atoms in the pickup cell. This panel is adapted from ref. [TS07].

where k_B is the Boltzmann constant, T the temperature of the gas of dopant atoms, m_X the mass of the dopant atom and v_{He} the average velocity of the He nanodroplet beam. The binding energies for the cases of the 3 rare-gas dopants Xe, Kr and Ar are as follows. The binding energy of one dopant atom to others already immersed in the droplet is approximated by the "cohesive energy" of the bulk as, $E_{ArAr} = 645.5$ cm^{-1}, $E_{KrKr} = 931.9$ cm^{-1} and $E_{XeXe} = 1319$ cm^{-1} [HS09]. The binding energies to He are, $E_{ArHe} = 27$ meV, $E_{KrHe} = 27$ meV and $E_{XeHe} = 26$ meV [LST95]. These contributions to E_{pickup} are sufficient to model the shrinkage process [LST95, KGS$^+$07, MMNSV07]. One He atom is evaporated for every 5 cm^{-1} binding energy released. So that the number of evaporated He atoms N_{evap} per dopant atom picked up is given by:

$$N_{evap} = \frac{E_{coll} + E_{XX} + E_{HeX}}{5\,\mathrm{cm}^{-1}}. \tag{3.13}$$

In this work, we will be mainly concerned with doping He nanodroplets with the above-mentioned rare-gases atoms. And we will not limit the doping levels only to very small numbers. Doping in the range of $K \gtrapprox 15$ requires that one takes droplet shrinkage due to evaporation during the doping process into account [KHGM07, MMNSV07]. The formalism used for the same is detailed in the following section.

3.3.3 Estimation of number of dopants (considering evaporation)

Before we estimate the mean number of dopants, we will present the details of the experimental arrangement used for the doping process. Figure 3.12 presents the arrangement of the doping cell which is 30 mm long and has two collinear orifices (diameter = 3 mm) through which the He nanodroplet beam passes. Importantly, the doping cell is connected directly to a long range cold cathode gauge ($10^{-3} \cdots 10^{-6}$ mbar). The gauge measures the pressure of the dopant gas introduced into the cell through a dosing valve with a leak rate $< 10^{-10}$ mbar. The cell is mounted on a CF 150 flange as shown.

The simplicity of this doping methodology both in terms of design and execution make this a popular choice in implementing one or more cells in a series when multiple dopant species are required to be loaded to form complexes in the nanodroplet [KGS$^+$07]. We used the formulation of Kuma et al. [KGS$^+$07], to estimate the average number of dopants in the nanodroplet beam. As pointed out earlier, the dopant distribution is Poissonian and the mean of the distribution K is dependent on the partial pressure of the dopant gas P_X in the cell so that

$$K = \chi P_X, \tag{3.14}$$

where χ is a constant of proportionality. Earlier, it was stated that the mean of the doping distribution $K = \sigma_{geo}\rho L$ (cf. equation 3.9) with the underlying assumption that the probability of picking up a dopant atom remains constant through the doping process. However, from section 3.3.2 it is clear that the nanodroplet shrinks due to evaporation and the pick-up cross section changes during the sequential doping process. Further, using the geometric cross section σ_{geo} as it is for estimating

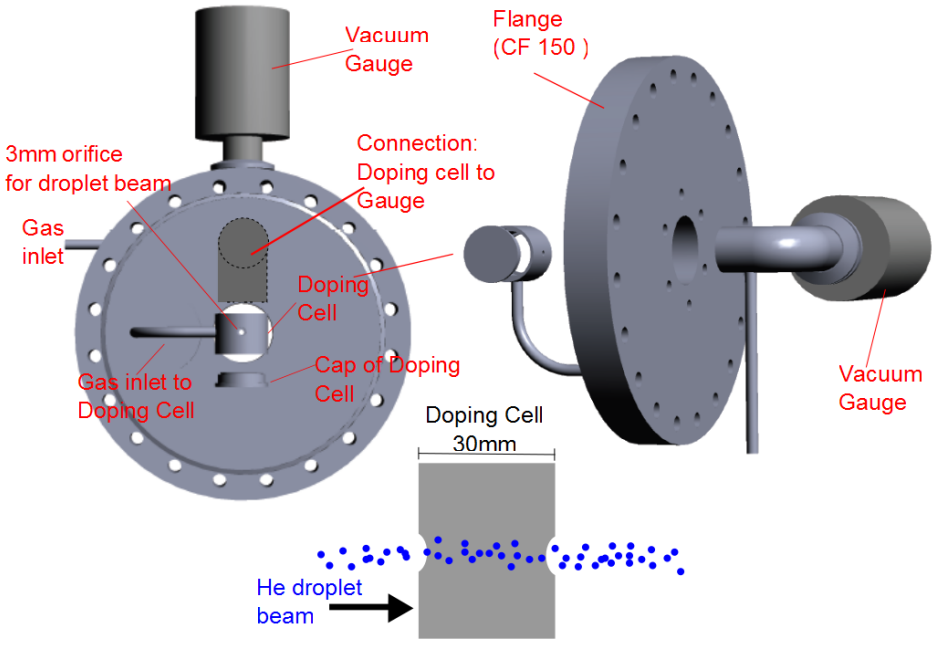

Figure 3.12: Doping cell with vacuum gauge attached: Two views of this arrangement are shown.

the doping level is too simplistic. Therefore, we will outline a better method for estimating the capture cross section σ_{cap} which is related to the σ_{geo}. The changes to the probability of pick-up during the doping process can be incorporated via the parameter χ following the seminal work of Lewerenz et al. [LST95] as

$$\chi = \frac{\sigma_{cap} L}{k_B T} \sqrt{\frac{\langle v_{He}^2 \rangle + \langle v_X^2 \rangle}{\langle v_{He}^2 \rangle}}, \tag{3.15}$$

where σ_{cap} is the capture cross section of the nanodroplet at the start of the doping process, L is the length of the doping cell and T its temperature. The velocities of He atoms in the beam and the dopant atoms in the cell are $v_{He}$and v_X, respectively. Then, the formulation of Kuma et al. [KGS+07] postulates the following semi-empirical equation for the average number of dopants K picked up by the He droplet:

$$dK = \left(1 - \frac{N_{evap}}{N_0} K\right)^{2/3} \chi \, dP, \tag{3.16}$$

where P is the pressure in the doping cell, N_0 is the number of He atoms in the droplet before doping and N_{evap} is the number of He atoms evaporated due to the capture of Kdopant atoms. Integrating equation 3.16, we get

$$K = \frac{N_0}{N_{evap}} \left[1 - \left(1 - \frac{N_{evap} \chi}{3 N_0} P\right)^3\right]. \tag{3.17}$$

The studies reported in ref. [MMNSV07] validate equation 3.17 for doping with propyne molecules. Kuma et al. [KHGM07], estimate the error involved in using this formulation to be $\pm 20\%$ for the case of Ar and H_2 doping.

Now, in order to apply this formulation, we need a reliable way to estimate the capture cross section σ_{cap}. This is related to the geometric cross section of the nanodroplet σ_{geo} through a sticking coefficient ζ:

$$\sigma_{cap} = \zeta \cdot \sigma_{geo}. \tag{3.18}$$

As noted by Lewerenz et al., ζ can take values in the range of $0.5-0.9$ [LST95]. In our case, we used an *ab initio* approach using Monte-Carlo simulations to estimate the capture cross section[8]. This is detailed in the next section.

3.3.4 Monte-Carlo calculation and capture cross section

Recently, Bünermann et al. developed a successful Monte-Carlo (MC) approach to simulate the doping process of high-spin alkali clusters in He nanodroplets [BS11]. This program was adapted for the case of rare-gas doping. Thus, one could validate the formulation of Kuma et al. [KGS+07] with an *ab initio* approach. In short, this MC program starts with a 4-dimensional ($N \times M \times k \times s$)-grid, where N represents the droplet size, M the number of collisions of the droplet, k the number of dopant atoms, and s the spin state of the doped cluster. Starting with a log-normal size distribution of droplets, the droplets are propagated over a doping cell of length l in steps of dl. The size of the steps is chosen so that it is consistent with Poisson statistics so that within one step the probability to collect two particles is much smaller than only collecting one. For more details of the approach, see [BS11]. At the end of the propagation, one can determine the distribution of doping levels for a given pressure (or equivalently the density) of the dopant gas in the doping cell. This is done over the desired range of pressures.

A typical result of the MC calculation for Xe doping is shown in figure 3.13 where the relative doping efficiency, which is proportional to the probability of finding a dopant cluster of a given size ($0 \cdots 100$) is plotted as a function of doping cell pressure (cell length = 30mm). The calculation was performed for a nanodroplet sample with a log-normal distribution of sizes which had a mean value of 1.5×10^4 He atoms/droplet. Clearly, (top panel of figure 3.13) the probability of finding a dopant cluster of a given size follows a Poisson distribution as expected for the doping statistics. The bottom panel in figure 3.13 shows the same dependence on a logarithmic scale to emphasize the robustness of the this calculation also for large dopant cluster sizes which is very important in our study. From these MC calculations we were able to obtain a simple estimate for σ_{cap} by comparing the MC calculation to Kuma's semi-empirical formulation (section 3.3.3). Figure 3.14 presents the case where the mean number of dopants is plotted as a function of doping cell pressure comparing the result of the *ab initio* MC calculations (red) to the semi-empirical formulation (blue) using a capture cross section $\sigma_{cap} = (0.5) \times \sigma_{geo}$ or $\zeta = 0.5$. The comparison is excellent considering the error involved ($\pm 20\%$) in the analytical formulation. This was found to be the case for all three dopants Xe, Kr and Ar of interest to the present study. Using this capture cross section, the mean number of dopants (Xe, Kr and Ar) as a function of doping cell pressure is

[8]The program code was available due to the collaboration in this work with Dr. M. Mudrich and Prof. F. Stienkemeier.

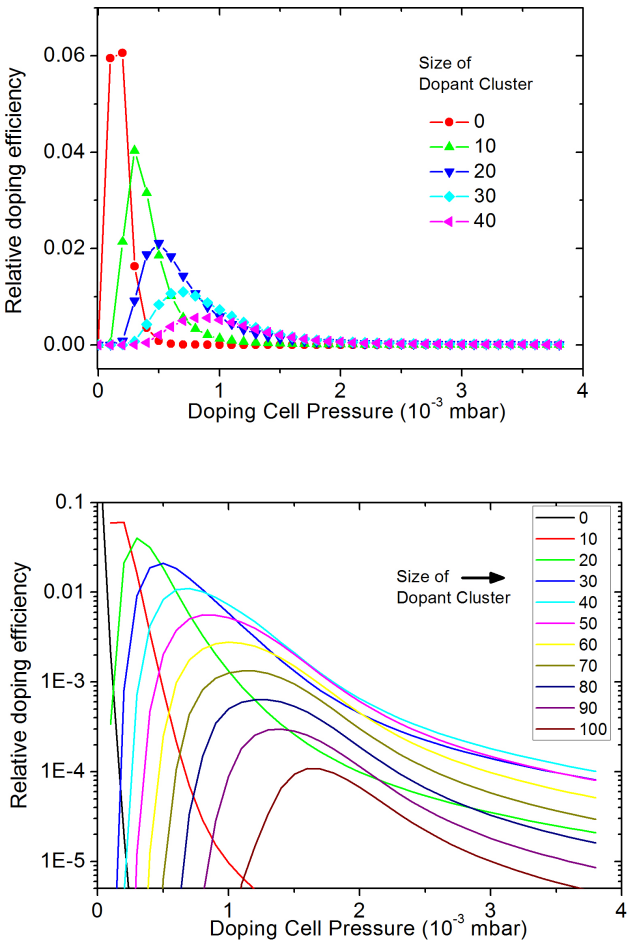

Figure 3.13: Results of the Monte-Carlo calculation for the case of Xe doping: Relative doping efficiency for various sizes of dopant cluster as a function of the doping cell pressure (in mbar) in linear scale (top) which shows the Poisson distribution and in $\log_{10}$ scale (bottom).

calculated using the semi-empirical formulation and is plotted in figure 3.15. The deviation of the semi-empirical formula from the MC result for large cell pressures $\lessapprox 3 \times 10^{-3}$ mbar is due to the fact that the semi-empirical description does not take into account the fact that droplets are lost due to heavy doping. It is easy to take care of this condition in the MC calculation. The Monte-Carlo calculation also provides an estimate of the loss of nanodroplet from the beam due to the evaporation of He atoms from droplets. Consequences of this inevitable process will be presented later in the context of experimental results.

3.4 Time-of-flight spectrometer

In this section we will briefly discuss the time-of-flight (TOF) mass spectrometer used in this work. The geometry of a simple TOF spectrometer is shown in figure 3.16 (a). The working principle of the spectrometer, as the name suggests, is to make measurements by determining the flight times of the ions which are created at the source point S. These reach the detector passing through different regions with suitably designed electric field. The geometry here is based on the Wiley-McLaren configuration [WM55]. It consists of an acceleration region and a drift region. Referring to figure 3.16 (a), it consists of - region I containing the source point S, where the ions are accelerated or "pushed" towards the detector and region II the drift region which is usually field-free.

Ions produced by a reaction (in our case ionization by an intense laser field) are located at S in the spectrometer. Let us consider ions having a mass M and charge q located at S. If the initial kinetic energy of the ions is negligible compared to qU which is the energy acquired by the ion in region I, then the arrival time (in ns) of the ion at the detector is [WM55, MFK02]:

$$t_0 = f\sqrt{\frac{M}{qU}}\,(2a + d)\,, \tag{3.19}$$

where a and d are travel lengths (in cm) in different regions of the spectrometer as defined in figure 3.16 (a) and $f = 719.7\,\sqrt{\mathrm{eV}\cdot\mathrm{amu}^{-1}}\cdot\mathrm{ns}\cdot\mathrm{cm}^{-1}$ when M and q are specified in atomic units, and U in volts. The simple dependence $t_0 \propto \sqrt{Mq^{-1}}$ implies well-separated peaks in a TOF spectrum corresponding to different values of the mass to charge ratio. Equation 3.19 also assumes that the spatial extent of the ion cloud at S is negligible. If this were not the case, additional conditions on the geometry and potentials applied are required for so-called space or position focusing (cf. refs. [WM55, MFK02]). In our case, the source of ions is the focus of laser beam which causes the ionization of a neutral atomic target. The diameter of the focal spot has an extent of $\sim 20\,\mu$m which is negligible compared to the travel length for ions in the spectrometer. Therefore, the corresponding error in the time-of-flight calculated using equation 3.19 due to the finite extent of the interaction volume is also negligible. Hence, in our case S can be treated as a point-like source and an unambiguous resolution of ions becomes possible.

If we consider ions having an initial kinetic energy $E_{||}$ along the spectrometer axis

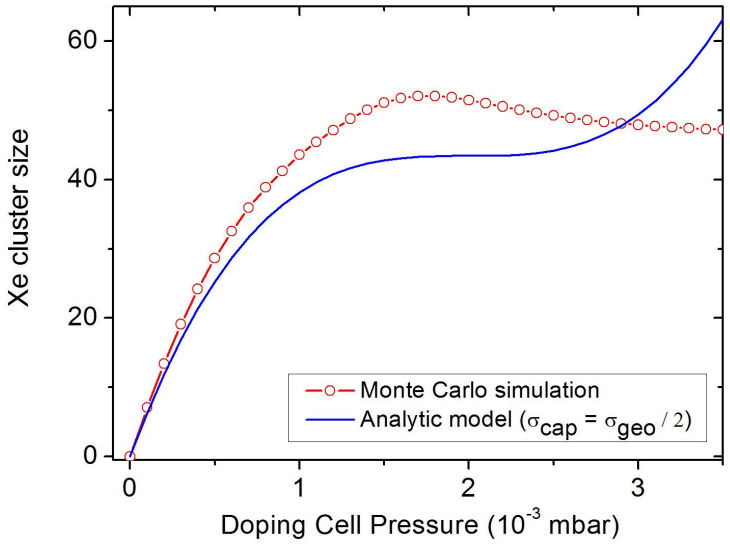

Figure 3.14: Comparison of the MC calculation with the semi-empirical formulation.

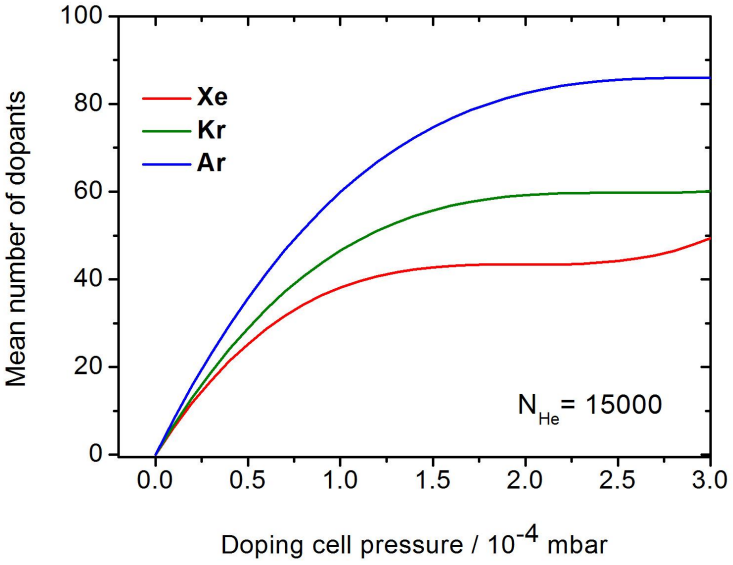

Figure 3.15: Number of dopants in the embedded cluster as a function of pressure estimated using equation 3.17.

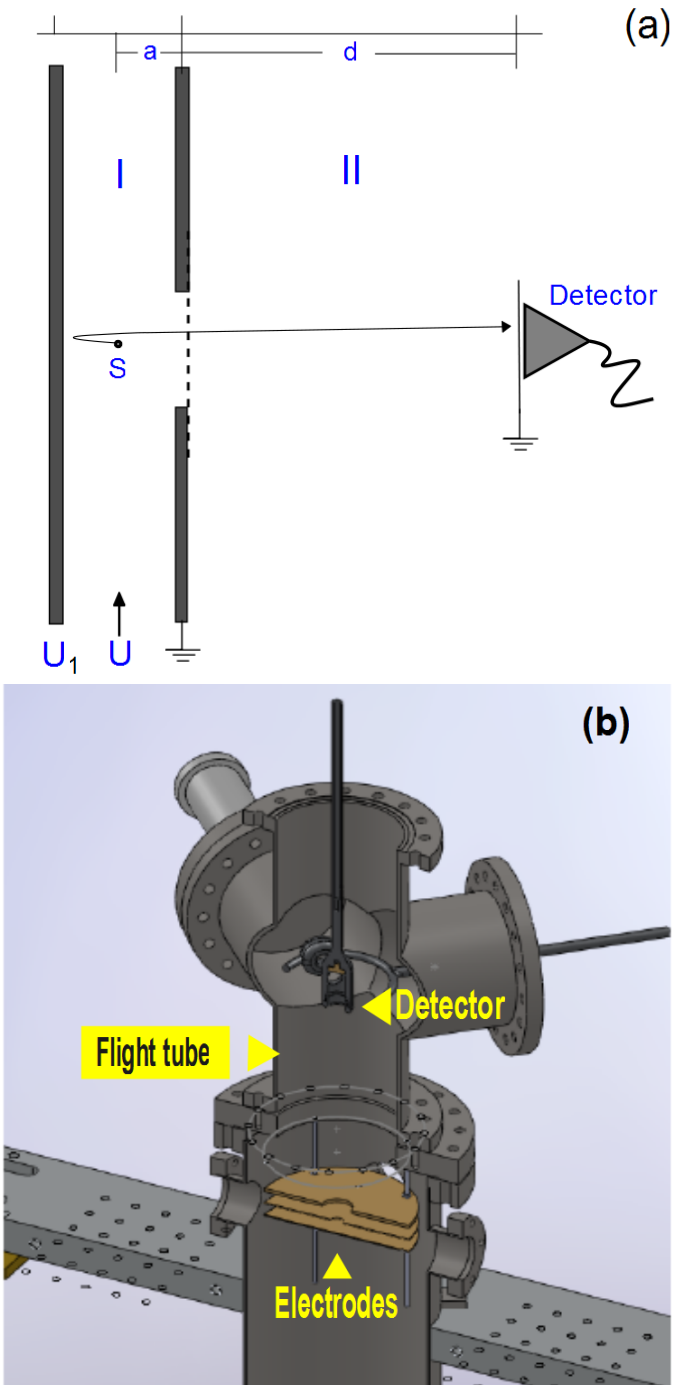

Figure 3.16: Time-of-flight spectrometer (a) schematic used for discussion in the text. (b) Laboratory realization of a Wiley-McLaren design.

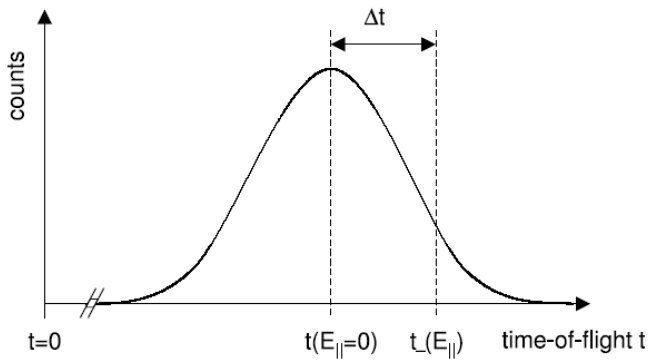

Figure 3.17: Schematic of time-of-flight distribution and the time-of-flight peak. This illustrates equation 3.21 (after Moshammer et al. [MFK02]).

which cannot be neglected in comparison to qU, then the time-of-flight becomes:

$$t_{+/-}(E_{||}) = f\sqrt{M}\left[\frac{2a}{\sqrt{E_{||}+qU}\pm\sqrt{E_{||}}}+\frac{d}{\sqrt{E_{||}+qU}}\right], \tag{3.20}$$

where $+$ corresponds to ions with initial momenta towards the detector and $-$ to those that have momenta away from the detector, which is the case depicted in figure 3.16 (a). Thus, measuring the TOF spectrum gives information about $E_{||}$ the kinetic energy release (KER) in the reaction occurring at S. From equation 3.20 it is clear that $t_0 = t(E_{||} = 0)$. We can expand $t_{+/-}$ about $E_{||} = 0$. For the case $qU \gg E_{||}$ the time difference $\Delta t = t_0 - t(E_{||})$ is related to $E_{||}$ as:

$$E_{||} = \frac{1}{4M}\cdot\left(\frac{U\cdot\Delta t}{a\cdot f}\right). \tag{3.21}$$

This is illustrated in figure 3.17. It may be mentioned that the ion momentum component along the spectrometer axis $P_{||}$ can be determined similarly since $E_{||} = P_{||}^2/2M$.

The analysis above breaks down if the condition $qU \gg E_{||}$ is not satisfied. In such cases, resolving M/q by time-of-flight is not possible. This is not uncommon in the context of intense field-ionization of rare-gas clusters using laser intensities of the order of $10^{15}\,\mathrm{W\cdot cm^{-2}}$ [DDR+96]. However, in the experiments with He nanodroplets being presented in this thesis, the condition $E_{||} \ll qU$ is satisfied. The design of the TOF spectrometer used in our studies is shown in figure 3.16 (b). In our spectrometer an additional electrode is introduced before the drift region following Wiley and McLaren [WM55], which offers additional operational flexibility. Using the geometry and distances between electrodes as shown in figure 3.16, we performed a simulation with an ion optics workbench (SIMION^{TM} [Dah00]) to determine the optimal combination of voltages for the so-called pusher and puller electrodes (see ref. [WM55] for details) which were found to be 3000 V and 2000 V, respectively. A TOF mass spectrum from our arrangement is presented in figure 3.18. From a knowledge of the target being ionized, the different mass/charge values have been assigned to the products of intense laser ionization. These are He^{2+}, He^+, the singly charged oligomer ions (He_2^+ and He_3^+) and H_2O^+ due to water vapor present in the reaction chamber. The broadening of the He^+ peak allows the determination of

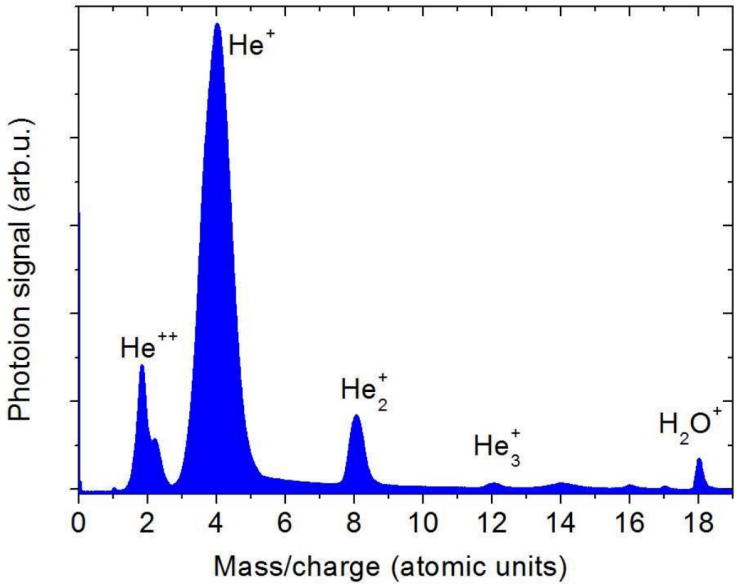

Figure 3.18: TOF mass spectrum obtained in our study where different ions in the spectrum have been identified from their mass by charge ratios.

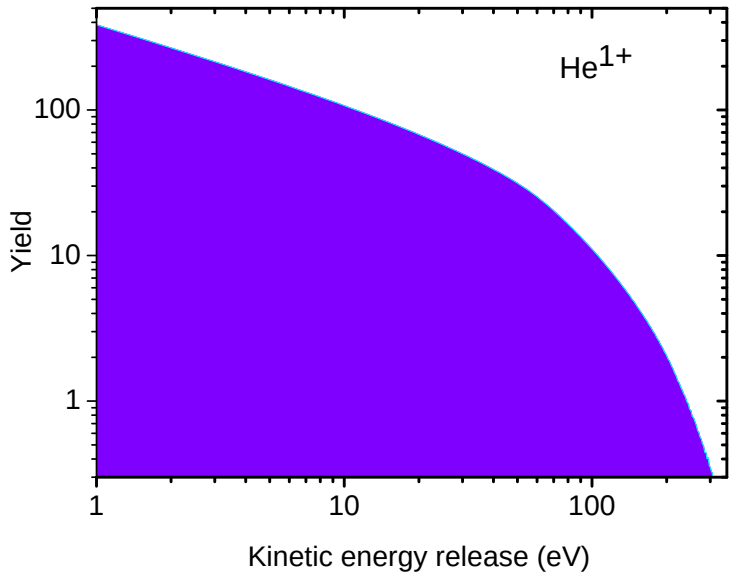

Figure 3.19: KER distribution deduced from the He^{1+}peak in the TOF mass spectrum using equation 3.21.

the KER distribution of this ion (using equation 3.21) resulting from the reaction and is presented in figure 3.19. The maximum KER of He^+ ions is observed to be $\approx 300\,eV$. This is much lower than the energy of 2500 eV gained by these ions from the electrode potentials. This plays a crucial role in understanding the ionization dynamics as we will see later. The unusual shape of the He^{2+} peak due to large KER resulting from the Coulomb explosion of nanodroplets in the reaction will be a matter of further study in later sections.

3.4.1 Daly detector

Our time-of-flight spectrometer employed a Daly detector (also called the "doorknob" detector) to detect charged particles . Most often, TOF spectrometers employ microchannel plates (MCPs) [Wiz79, MFK02] with a suitable anode to collect the amplified charge. However, the detection efficiency of MCPs decreases with increasing atomic mass of the fragments to be detected [Fra02]. Hence, MCPs are not the best choice for detecting very large masses ($\gtrapprox 1000$ amu[9]). In our studies we used large mass He nanodroplets ($\approx 2-5 \times 10^4$ amu). To detect possible large mass ionic fragments following intense laser ionization of these clusters, we employed the Daly detector [Dal60].

The schematic of the Daly detector is presented in figure 3.20 (a). The ions entering the detector impinge on the the cup of the detector (also referred to as the "doorknob" [Dal60]) and release secondary electrons as in a Faraday cup [BT56]. A high voltage, $-34\,kV$ in our case, is applied on the cup. As shown in figure 3.20 (b), which is the experimental realization, electrons are directed towards a "ring" maintained at ground. The ring houses a "scintillator" where the accelerated electrons produce a light pulse which is detected using a photomultiplier tube (PMT) behind the scintillator (shown in figure 3.20 (a)). Maintaining potential differences of order of 30kV requires that apart from the regular requirements imposed on ultra-high vacuum components, the surfaces of the electrodes be polished to avoid sparking. In our case these components were electroplated to a "mirror-like" finish. The key to the high efficiency of this detector is that it allows for a high acceleration after the field-free region of the flight tube of the TOF spectrometer. This improves the sensitivity for large-mass fragments impinging on the detector. Single particle hits produced pulses less than 10ns in width which enabled high-resolution mass spectrometry.

3.5 Laser system

For the intense field-ionization studies being presented here, femtosecond pulses ($\sim 10\,fs$) from a Ti:Sapphire (Ti:Sa) laser system lasting only a few optical cycles were employed. The system in our laboratory is capable of generating sub-10 fs at a central wavelength of 800 nm. In this section we will outline the working principles of this laser system. First, laser pulses are generated using a commercial

[9] amu = atomic mass unit $\frac{1}{12}C^6_{12}$

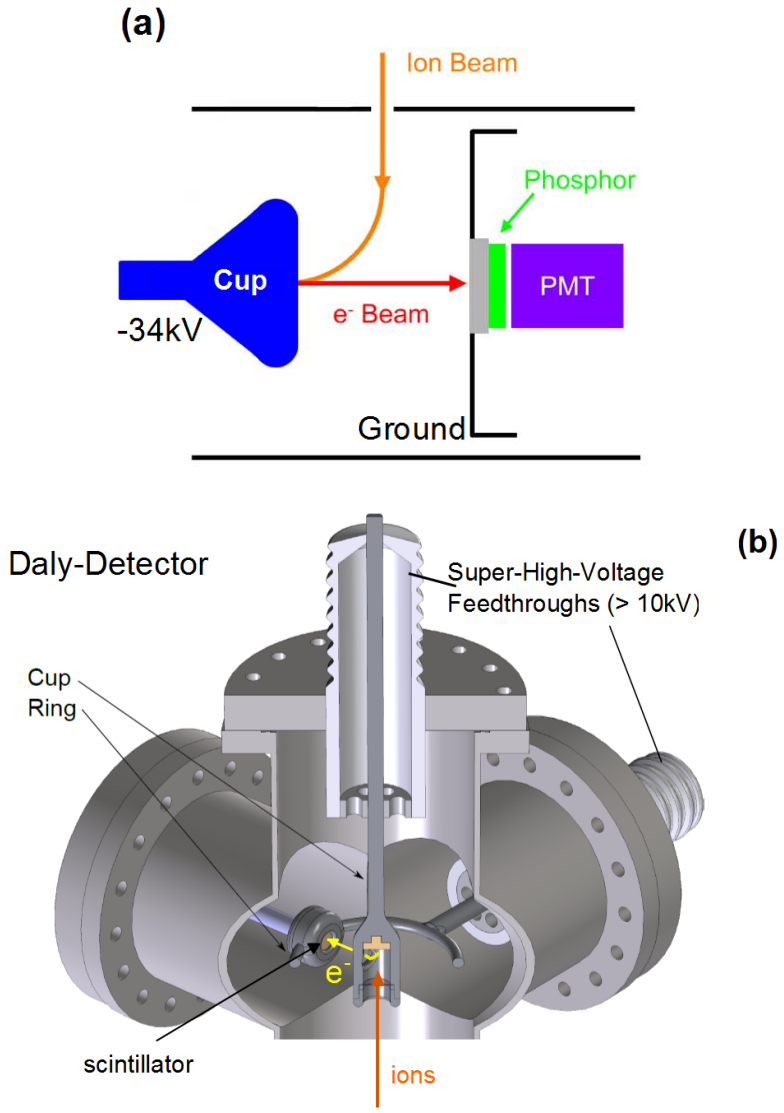

Figure 3.20: Daly detector (a) schematic (adapted from [Dal60]) and (b) experimental realization.

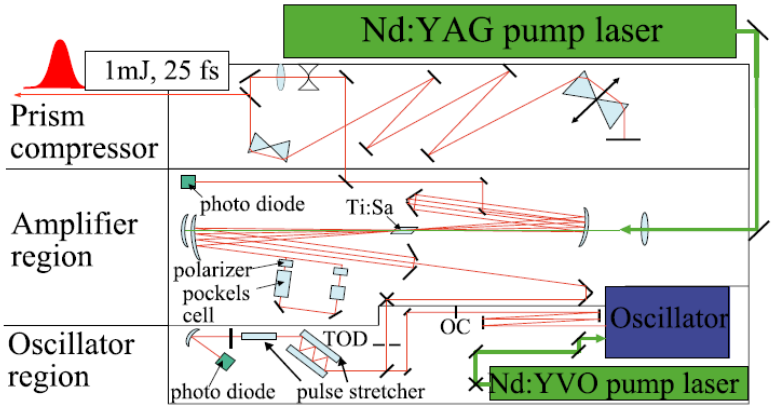

Figure 3.21: Laser system: The schematic shows the *oscillator region* where $\sim$ 6 fs pulses are created with a pulse energy $\sim$ nJ, then the *amplifier region* where the multiple passes amplify the pulse by chirped pulse amplification to $\sim$ 1 mJ after being stretched and the *prism compressor* where the chirp of the pulses is compensated to obtain $\sim$ 25 fs, 1 mJ, pulses.

laser system[10] which is depicted schematically in figure 3.21. This generates 25 fs pulses with an energy of about 1 mJ. Subsequently, these 25 fs pulses are further compressed to 10 fs by a fiber compressor which employs self-phase modulation (cf. section 2.1.3). These 10 fs pulses are then split by a Mach-Zehnder interferometer to produce two identical pulses for pump-probe studies as well as for autocorrelation measurements.

3.5.1 Oscillator

The oscillator of this laser system containing a Ti:Sapphire (Ti:Sa) crystal pumped by a Nd:YVO laser (pump power $\approx$ 3 W) as an active medium uses dispersion compensated mirrors within the cavity (prisms would be the other option). Pulses are created by locking the modes in the oscillator cavity by the well-known Kerr-lens-mode-locking (KLM) mechanism [SKS91, BSCK92]. Pulse formation starts in the form of a spike (an intensity fluctuation) in the continuous wave (CW) mode of the oscillator. Spikes are a result of spontaneous emission. Although, there are many spikes in the noise, the most intense spike gets selected at the expense of the weaker ones. It is then amplified into a well-defined laser pulse by passive mode-locking. The mode-locking process relies on the intensity dependent refractive index due to Kerr effect in the Ti:Sa gain medium. The intensity dependent refractive index $n(I)$ can be expressed as [DR06]

$$n(I) = n_0 + n_2 \cdot I(\mathbf{r}, t), \tag{3.22}$$

[10] *Femtopower Compact Pro* : FEMTOLASERS Produktions GmbH, Fernkorngasse 10, 1100 Vienna, Austria

where n_0 is the linear refractive index and n_2 the Kerr coefficient. If one considers the transverse Gaussian profile of the laser beam, then the so-called self-focusing is obvious from equation 3.22. This also leads to an intensity-dependent focusing of the beam, whereby pulses of higher intensities are more tightly focussed than weaker ones in the Kerr medium. In addition, the pump beam from the Nd:YVO laser is focused in the Ti:Sa crystal in such a way that its transverse profile in the gain medium matches that of the strongly self-focused high-intensity pulses better than the profile of the weaker pulses or the CW mode traversing the the resonator cavity. In effect, mode selection happens due to the introduction of this "soft-aperture" [SCFR94]. In the time domain this also means that the wings or the edges of the pulse see a smaller gain in the amplifying medium than the center once in every round trip, consequently shortening the pulse. Thus, the amplifying medium acts as a saturable absorber. Further, in terms of the eigenfrequencies of the cavity, this periodic modulation results in the "locking" of the relative phases of the different frequency components periodically in time. Thus, mode-locking occurs. Positive dispersion due to optical components and air in the cavity accumulates due to the many round trips the pulse makes in the oscillator cavity. This is compensated by special multi-layered dielectric mirrors, called chirped mirrors, which add appropriate negative dispersion to the traveling pulse [SCFR94, SLS$^+$95, ST99]. The result of this dispersion management are pulses with a duration of approximately 6 fs at a central wavelength of 800 nm with a pulse energy of about 2.5 nJ at a repetition rate of 80 MHz.

3.5.2 Multi-pass amplifier and prism compressor

Since the oscillator pulses have a pulse energy of only a few nJ, they need to be amplified to perform intense field-ionization experiments. To attain pulse energies of about 1 mJ which are desirable, an amplification by a factor of $\sim 10^6$ is required. Chirped pulse amplification provides a solution to this issue [SM85]. This scheme has been applied to several high-power femtosecond laser systems over a wide range of intensities. The CPA scheme is shown in figure 3.22. In this scheme, pulses from the oscillator are stretched in time. In our case, this is done using a thick glass block and chirped mirrors resulting in pulses which have a length of a few picoseconds when they enter the amplifier. The need for pulse stretching arises from the fact that for unstretched pulses high peak intensities resulting from the amplification process would exceed the damage threshold of the amplifier optics. The amplifier has a multi-pass configuration where the stretched pulses pass the gain medium nine times in a bow-tie like geometry(see figure 3.21). As in the oscillator, the gain medium is a Ti:Sa crystal now pumped by a pulsed Nd:YAG laser (pulse duration $\approx$ 120 ns, pulse energy $\approx$ 10 mJ) at a repetition of 3 kHz. However, the train of pulses from the oscillator has a repetition rate of 80 MHz. Consequently, only oscillator pulses that meet the pump pulse synchronously in time are amplified. In order to reject the unamplified pulses, one oscillator pulse per pump pulse is picked out by a Pockels cell after the fourth pass in the amplifier. After completing all the nine passes in the amplifier, pulses with an energy of $\approx$ 1 mJ/pulse at a repetition rate of 3 kHz exit the amplifier. These pulses have a ps width in time, after the amplification process. However, they are sufficiently broad in bandwidth for compression to 25 fs since the gain-bandwidth of Ti:Sa spans $\approx$ 100 nm about

a center of 800 nm. The chirp in the amplified pulses is compensated by a prism compressor [FMG84].

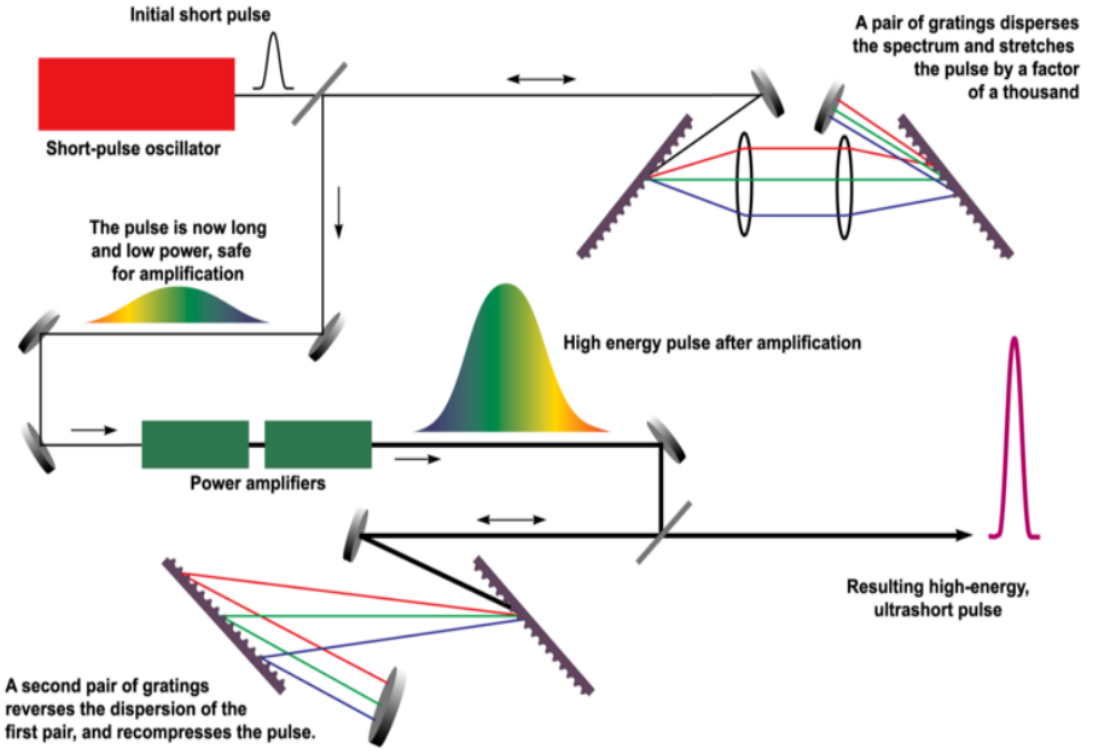

Figure 3.22: The CPA scheme: A weak femtosecond pulse (nJ) is stretched by a pair of gratings to produce a *chirped pulse* that enters one or more *amplification* stages which increase the pulse energy ($\sim$ mJ). Then, another pair of gratings compress the stretched pulse back to a fs duration which is determined by the pulse bandwidth. (Illustration: M. D. Perry in [Per95].)

3.5.3 Fiber compressor

To further compress the 25 fs pulses is not possible since they are already close to their transform limit [11] and do not possess sufficient bandwidth for compression to pulse durations of 10 fs or less. Their bandwidth can be enhanced by the nonlinear effects of self-phase modulation and self-steepening which were detailed in section 2.1.3. For these broadening effects in the frequency domain, the prerequisite is the interaction of a high intensity pulse with a nonlinear medium over a sufficiently long length. This is made possible by launching the pulses into a hollow fiber filled with a noble gas [NDSS96], where the noble gas acts as a nonlinear medium. The design of this system is shown in figure 3.23. The hollow fiber employed in our system has an inner diameter of 250 μm and a length of 90 cm length. The fiber is held in a chamber where Ne gas is maintained at a pressure in the range of 2.0$-$2.5 bar. A lens of 1.5 m focal length is used to couple the laser beam into the fiber so it

[11] Pulses which satisfy the condition $\Delta\nu \cdot \Delta t = 1$, where $\Delta\nu$ is the frequency bandwidth of the pulse and Δt is the full-width half maximum in time, are said to be transform limited.

propagates in the fundamental Gaussian mode. The confinement of the laser beam in the fiber of such a small diameter leads to high intensity in the Ne filled volume.

As a result of the nonlinear interaction inside the hollow fiber the pulse spectrum is broadened - a comparison of spectra before and after the fiber is presented in figure 3.24 [Fis10]. The Fourier transform limit of this spectrum is about 5 fs. The asymmetry in the spectrum about central frequency is a result of self-steepening [Boy08]. The pulses at the exit of the fiber suffer a considerable amount of third-order dispersion (or quadratic chirp). Chirped mirrors can compensate this dispersion [Kär04]. A set of six chirped mirrors compensate the third-order dispersion and compress the pulses subsequent to the spectral broadening. Further, the pulses are pre-compensated for the positive dispersion of the air and the glass window on the experimental chamber so that they are delivered at the shortest possible length inside the reaction chamber. Pulses shorter than 10 fs are achieved routinely in our laboratory.

3.5.4 Mach-Zehnder interferometer

Twin pulses necessary for pump-probe experiments and also for auto-correlation measurements must be created out of the same wavefront of the laser pulse so that their time structure and mutual coherence are maintained after the splitting process. This is achieved using a Mach-Zehnder (MZ) interferometer as shown in figure 3.25 [Erg06]. The beam is first split by a 50:50 beam splitter (BS1). One of the equal parts of the beam is directed into one of the arms of the MZ interferometer and the other into the second arm. Both the arms contain delay stages which can be moved back and forth by electronic control. One of these stages is driven by a piezoelectric transducer[12] (PZT), which is controlled by a PID controller to achieve reproducible delays as small as 0.5 fs per step. The beams are recombined at a second beam splitter (BS2). The two identical beam splitters (coating: 500 μm, six Si_2/TiO_2 layers) can withstand high intensities (10 GW/cm^2) and support a broad spectral range (520−1150 nm) while introducing a very small amount of dispersion. The long-term stability and repeatability of two-pulse scans with short delay steps and over large ranges (about 1.8 ps) has been demonstrated in refs. [Erg06, Fis10] and this work.

3.6 Experimental arrangement

Having described the details of the He nanodroplet source and the doping methodology, in this section we will present the complete experimental arrangement used in our studies. In figure 3.26 a schematic diagram of the source chamber, the reaction chamber and the beam dump are shown. The source chamber houses the He nanodroplet source detailed in section 3.2. As mentioned in section 3.2, this continuous beam source imposes considerable pumping requirements. We used a 8000 L/s oil diffusion pump (*Leybold, DIP 8000*), for this purpose [Ley]. This was backed by a

[12]Physik Instrumente (PI) GmbH & Co.KG, Auf der Römerstr. 1, D-76228 Karlsruhe (http://www.pi.ws/)

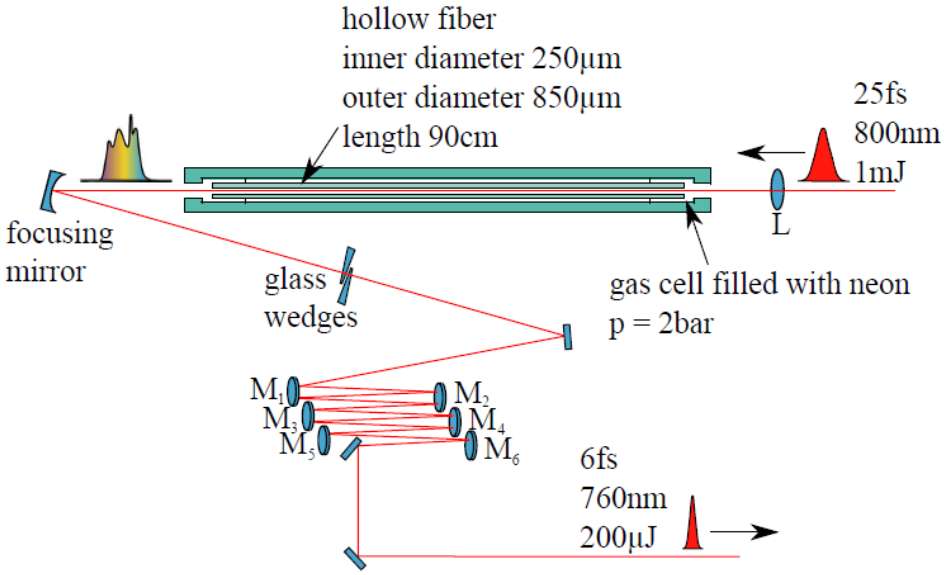

Figure 3.23: Fiber compressor: Pulses with a width of 25 fs, at 800 nm and pulse energy of 1 mJ are focussed in a neon filled hollow fiber in which self-phase modulation broadens the spectrum of the pulse. Thereafter, a set of 6 chirped mirrors compensate the third-order dispersion induced by propagation in the hollow fiber.

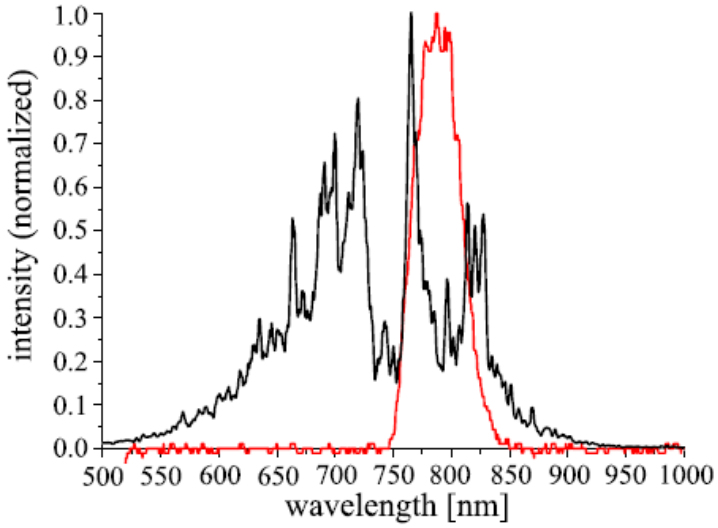

Figure 3.24: Pulse spectrum before (red) and after (black) propagation through the Ne filled hollow fiber.

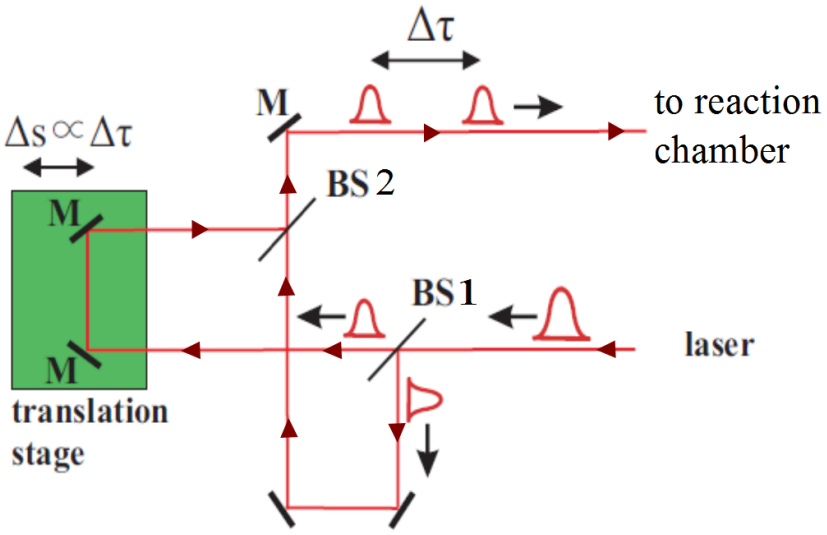

Figure 3.25: Schematic of the Mach Zehnder interferometer (M: mirror, BS: beam splitter). A delay $\Delta\tau$ between the pulses is introduced by a displacement Δs of the translation stage, as shown.

Roots pump (*RUVAC WA501, Leybold*) with a pumping speed of 500 m^3/h which was connected to a 65 m^3/h rotary vane roughing pump (*TRIVAC D65B, Leybold*). The use of these pumps is necessary due to the high gas throughputs which increase with decreasing nozzle temperature (cf. section 3.2.1). The background pressure in the source chamber is $\approx 5\times10^{-7}$ mbar (foreline pressure $\approx 3\times10^{-3}$ mbar) which rises to $\approx 1\times10^{-4}$ mbar (foreline pressure $\approx 3\times10^{-2}$ mbar) with ^{4}He gas at 90 bar behind the nozzle. Downstream from the nozzle, at a distance of $\approx$40mm, a skimmer with a 400 μm orifice (*Model 2, Beam Dynamics*[13]) is placed. The skimmer also forms a removable vacuum-tight seal between the source and the reaction chambers. Thus, a pressure difference across the skimmer can be maintained. Since the nozzle could be manipulated using two rotary vacuum feedthroughs along the two orthogonal degrees of freedom transverse to the He droplet beam, the jet could be aligned to pass through the orifice of the skimmer during the experiment. It was found necessary to do this just once after each start up of the source. The pointing of the droplet beam remained stable throughout the experimental runs. We chose this orifice diameter for the skimmer to make sure that only manageable gas loads are inlet into the reaction chamber. The reaction chamber is pumped by a turbo-molecular pump with a speed of 1500 L/s (*TPU 1500 Balzer, Pfeiffer*) which is backed by a rotary pump (*TRIVAC D40B, Leybold*). The background pressure in this chamber was 6×10^{-8} mbar without the jet and 1×10^{-7} mbar with the He droplet jet.

About 100 mm downstream from the skimmer, the doping cell (discussed in section 3.3.3) was placed in the reaction chamber with the apertures of the cell (cf. figure 3.12) aligned to the skimmer orifice (by visual inspection). The desired dopant gas - Xe, Kr or Ar - was leaked into this cell using a dosing valve with a leak rate $< 10^{-10}$ mbar·L·s^{-1}. A cold cathode gauge connected to the cell as shown in figure

[13] http://www.beamdynamicsinc.com/skimmer_specs.htm

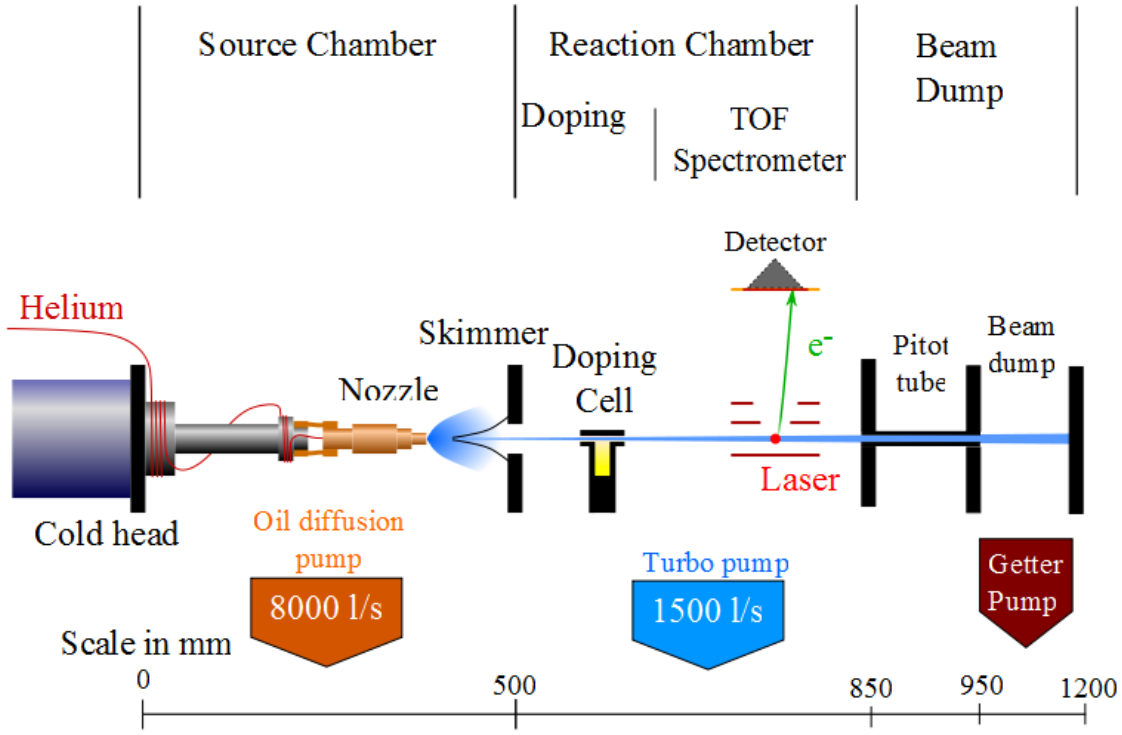

Figure 3.26: Experimental arrangement: Schematic of the assembly consisting of the He nanodroplet source, the doping chamber, the TOF spectrometer and the beam dump.

3.12 was used to read out the pressure directly. The doping level inside the droplet could be calculated from this according to the formulation in section 3.3.3.

Following the doping process in the cell, the beam of droplets loaded with dopants encounters the 10 fs pulses from the laser system (section 3.5) focused using a spherical mirror (focal length = 100 mm). The focal spot had a diameter of about 20μm with a Rayleigh range of about 1.5 mm. The position of the laser focus could be adjusted in 3 mutually perpendicular directions using a XYZ-stage on which the mirror was mounted. The laser was initially focused roughly to the geometric focus of the reaction chamber in air by observing the light emission from the breakdown of air with naked eye (protected by appropriate laser safety eye-wear). A good initial alignment in air usually helps in finding the jet whose width was estimated to be 3−4 mm.

The fragments from the photoionization of the doped nanodroplets following their interaction with the intense laser pulses at the focus are collected by the TOF spectrometer, the details of which were presented in figure 3.4. Thereafter, the droplet beam reaches the beam dump via the Pitot tube as shown in figure 3.26. The beam dump is pumped by an ion getter pump (*VacIon Plus 75, Varian*) which has pumping speed of 75 m^3/h. Using the getter pump has the another advantage apart from the very efficient pumping out of the droplet beam itself. Measuring the current of the getter pump gives a reliable measure of chamber pressure at the beam dump. Since the response of the current drawn by the getter pump to changes in chamber pressure is fast, it can be used to align the nozzle through the skimmer and the apertures of the doping cell. When the droplet beam was on, the nozzle

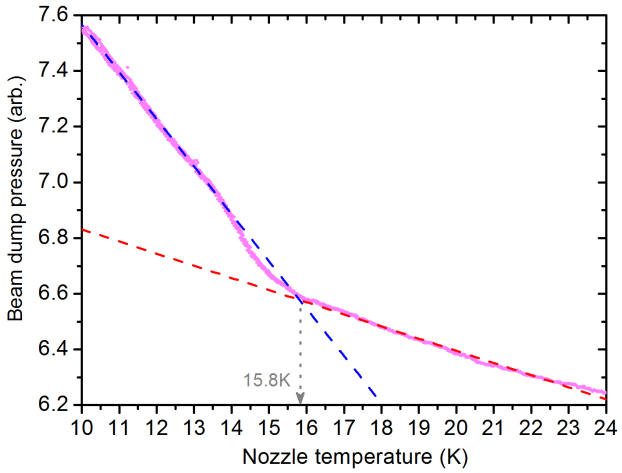

Figure 3.27: Pressure in the beam dump as a function of nozzle temperature. From the two-line fit (red and blue dashes) to the data (pink) the transition temperature is estimated to be 15.8 ($\pm$ 0.05) K.

alignment was manipulated in situ to maximize the pressure in the beam dump by reading the current of the getter pump.

Following the alignment of the nozzle, the change of pressure in the beam dump gives an estimate of the flux of ^{4}He gas in the jet. Our design for the beam dump comes close to conventional Pitot tubes which are used to measure particle velocities in jets [SSM10]. We measured the pressure in the dump by measuring the current drawn by the getter pump as a function of the nozzle temperature as shown in figure 3.27. The plot clearly shows two linear regions corresponding to the subcritical and supercritical regimes. A marked transition to the supercritical regime occurs at 15.8 K which is determined by a two-line fit. We use this transition temperature to calibrate the droplet size using figure 3.5b. We employ the differences in nozzle temperatures from the transition point instead of absolute readings.

Summary

In this chapter we presented the details of the experimental methodology employed to generate doped He nanodroplets and study the intense field-ionization of such droplets by few-cycle NIR laser pulses. Having surveyed the basic ideas in the intense field-ionization of rare-gas clusters in chapter 1, we are now ready to go into the details of the experiments performed on doped He nanodroplets. This will be the subject of discussion in the two forthcoming chapters (4 and 5) where the results of single-pulse and pump-probe studies are described.

Chapter 4

Doped helium nanodroplets in intense few-cycle laser pulses: single-pulse excitation

In the previous chapters we motivated the need to study the dynamics of rare-gas and metal cluster systems in intense IR pulses and the methodology which can be used to perform experiments on such systems. The growing interest in these mesoscopic nanoplasmas in recent years has been surveyed in refs. [SSR06, FMBT$^+$10]. As we saw in sections 2.2.4 and 2.2.5 doped or two-component clusters have shown remarkably different behavior when compared to pristine homonuclear clusters demonstrating phenomena such as enhancements of characterisitc X-ray yields and electron temperatures, when ionized by intense NIR laser pulses [JK08a]. In this chapter we will focus on the effects of local fields in well-characterized and well-designed two-component clusters. It was observed in the VUV domain that field-ionization in clusters with an Xe_M core and Ar_N shell leads to the Ar atoms playing the role of a sacrificial layer or a tamper [HBT$^+$08]: In the core-shell system the maximum observed Xe charge-state was 1+, while under identical conditions Xe ions with charge-states up to 19+ were detected from pristine Xe clusters of a similar size.

Our focus remains in the NIR regime. We recall that the most interesting properties of rare-gas and metal clusters in the NIR domain result from resonant coupling of laser light to the nanoplasma (cf section 2.2.2). The underlying mechanism is the resonance absorption by the electronic nanoplasma [DDR$^+$96, SR03, Saa06]. The resonance occurs when the background ions of total charge Q occupy a sufficiently large sphere of radius R such that the nanoplasma eigenfrequency $\Omega = \sqrt{Q/R^3}$ matches the frequency ω_0 of the laser light [SSR06]. The resonance condition $\Omega = \omega_0$ is achieved on the time scale of atomic or ionic motion (sub- or few-picoseconds) since the cluster, i.e. the ions, must *expand* in order for the ions to become sufficiently dilute. These features have been verified in several experiments [ZDP99, DFD$^+$05] as well as in calculations [Saa06]. The fact that this resonance absorption at NIR frequencies relies predominantly on atomic expansion has two consequences: Firstly, it requires timescales of ionic motion in spite of its electronic nature. Secondly, it does not occur in isolated atoms or those inside the bulk in condensed matter. This resonance resulting from an expanding ionic core can be

switched off if the duration of the laser pulses employed is well-below the timescales of ionic motion so that the cluster is "frozen". One may ask if there is another possibility for this resonant coupling of energy from the light pulse to the electrons which is not only extremely efficient but also fast, bypassing atomic expansion. Indeed this can be achieved as theoretically proposed and demonstrated [MSR09], if one uses a two-component system with a few seed atoms with ionization potentials lower than the majority of atoms which belong to the other component. If the spherical symmetry of the system is suitably broken (e.g. Xe atoms in the center of a He droplet irradiated by linearly polarized light) a "cigar-shaped" nanoplasma is formed. It has two eigenfrequencies which bracket the eigenfrequency of a spherical plasma. The lower one (along the linear laser polarization) is resonant with 790 nm laser light right away at typical atomic cluster densities leading to almost immediate resonance absorption without the need for atomic expansion. This allows not only to realize the efficient energy transfer very quickly, now limited essentially by the rise time of the laser pulse, but also opens the resonant light absorption to other forms of matter which do not (Coulomb) explode.

In this chapter, we report on experiments which demonstrate for the first time this purely electronic resonance absorption with rare-gas doped helium droplets illuminated by a few-cycle pulse of a duration as short as 10 fs at 790 nm. This rules out the influence of any kind of atomic motion. Reducing the pulse length even further must eventually prevent even this electronic resonance absorption. Indeed, this is predicted in molecular dynamics calculations [KFK$^+$11]. There is a clear transition from dopant induced resonance absorption to a regime dominated by static field-ionization [GSR09] if the pulse length falls below a critical value which depends of course on the intensity of the laser pulse.

4.1 Dopant induced ignition of He nanodroplets

4.1.1 Ion yields

As detailed in section 3.3 He nanodroplets can be doped with a well-controlled number of rare-gas atoms. These aggregate at the center of the droplet [TV04, SL06]. Doped nanodroplets are exceptionally suitable to demonstrate the role of seed atoms in resonance absorption, since the laser intensity can be chosen such that the light couples almost exclusively to the dopants whereas the pristine He droplet is transparent. Interestingly this applies to NIR [MSR08, MSR09] as well as to X-ray [GSR09] frequencies. Despite its transparency, the droplet becomes highly active once the core of seed atoms is ionized.

In the experiment a beam of He nanodroplets is produced by expanding pressurized ^{4}He gas (70-90 bar) through a nozzle (5 μm in diameter) maintained at a temperature of 15-25 K. By varying the nozzle temperature in this range the mean number of He atoms per droplet is adjusted in the range 10^3-10^5. The droplet sizes were calculated by the methodology detailed earlier (section 3.2). Owing to their low internal temperature $\sim$ 370 mK, these droplets are in a superfluid state [TV04, SL06]. As shown in figure 3.26 these droplets are doped by passing the skimmed beam of

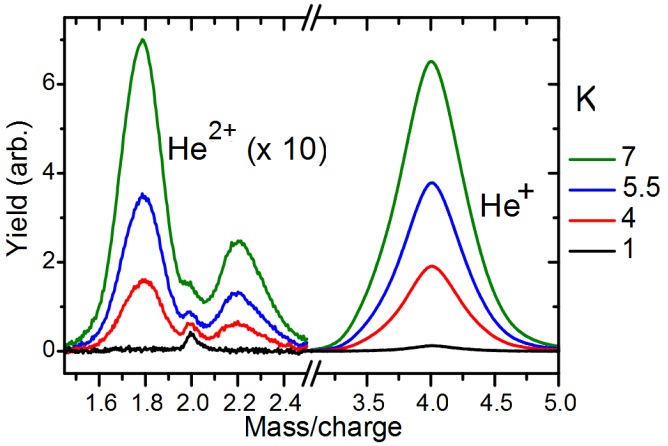

Figure 4.1: Time-of-flight mass spectra of He^{2+} and He^{+} ions. The splitting of the He^{2+} peak results from the finite angular acceptance of the spectrometer due to ions with high momentum components in the forward and backward directions with respect to the detector. The legend shows the mean number of doped Xe atoms (K) in the nanodroplet.

pure droplets through a cylindrical doping cell that is 3 cm long with collinear apertures ($\varnothing$ = 3 mm). The mean number of dopants K per nanodroplet is regulated through controlled leaking of the desired rare-gas into this cell using a dosing valve (leak rate $< 10^{-10}$ mbar·l/s). The pressure in the doping cell is monitored by a directly attached vacuum gauge (cf. section 3.12). We described the use of Kuma's semi-empirical formulation [KGS+07] for determining the mean number of doped atoms in the nanodroplets in section 3.3. We also used the Monte-Carlo model [BS11] mentioned therein, adapted to rare-gas dopants, to validate the estimate of doping levels and to estimate the loss of He due to evaporation caused by the doping process. Thus, the number of dopant atoms K is ascertained from the cell pressure and the droplet size according to the modified Poissonian pick-up statistics [SL06] using the semi-empirical formula of Kuma et al. [KGS+07] which takes evaporation of He atoms into account. Henceforth, we will refer to mean value of this Poisson distribution as when we mention the number of doped atoms or doping number in the context of experimental data. Intense few-cycle laser pulses ($\sim$ 10 fs) at a central wavelength of 790 nm with peak intensities in the range 10^{14}–10^{15} W/cm^2 are generated from the Ti-Sapphire based mode-locked laser system described in section 3.5. Photoions are detected by a time-of-flight (TOF) spectrometer in the Wiley-McLaren geometry (cf. section 3.4).

TOF mass spectra of He^{2+} and He^{+} ions for different doping numbers of Xe (K) in a droplet containing 1.5×10^4 He atoms are shown in figure 4.1 when the doped nanodroplets were exposed to 10 fs pulses with a peak intensity of 7×10^{14} W/cm^2. The He^{2+} peak, which is characteristic for the ionization of doped He droplets, is essentially absent in mass spectra of atomic He gas[1]. It is split as a result of the finite angular acceptance of the spectrometer into two components due to ions with high momenta directed towards and away from the detector, respectively. The yield

[1]The appearance of He^{2+} depends on the laser intensity. The barrier suppresion intensity for He^{2+} is $\approx 7 \times 10^{15}$ W/cm^2.

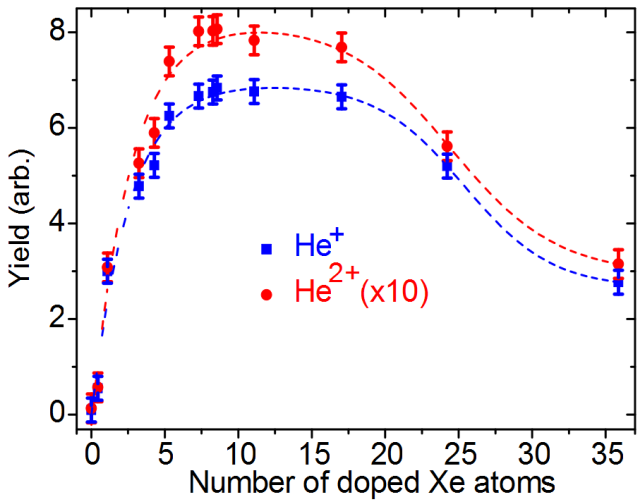

Figure 4.2: Yields of He^{2+} and He^{+} ions as a function of the mean number of Xe dopants in a nanodroplet containing $1.5{\times}10^4$ He atoms at a peak laser intensity of $7 \times 10^{14}\,\mathrm{W/cm^2}$. The ion yields were determined by integrating the TOF mass peaks of the ions which were presented in figure 4.1 (lines to guide the eye).

of He^{2+} and He^{+} ions is extracted from the TOF mass spectra by integrating over the respective mass peaks. Figure 4.2 presents the doping dependence of the yields of He^{2+} and He^{+} at a peak laser intensity of $7 \times 10^{14}\,\mathrm{W/cm^2}$. A gradual increase of doping number $K = 1$ up to 10 leads to a dramatic step-like increase in the yields of He^{+} and He^{2+} ions. We refer to this as dopant-induced ignition (DII). Note that the He droplet is completely transparent, i.e. no ions are detected at all for undoped species. The decrease in ion yields for doping numbers $K > 20$ is due to droplet evaporation and is discussed in what follows. The saturation of ion yields, and equivalently the build-up of charge in the nanoplasma, occurs for a critical doping number K_{cr} of just $\sim 7(\pm 1.4)$. The ionization of the He droplet is not enhanced any further by adding more dopants beyond K_{cr}, which also defines this quantity. This saturation of ion yields points to a saturation in the charging process. A major fraction of atoms in the nanodroplet, if not all, are ionized to 1+ or 2+ He ions. Thus, an energy transfer from the laser field into the droplet nanoplasma of at least 24.4 eV per He atom should occur on a timescale of 10 fs. This suggests that the mechanism underlying DII is a resonant mechanism. We will show later that this indeed is the case.

Next, we consider the question of how droplet sizes and droplet evaporation affect He^{2+} ion yields when DII is operative. The critical doping number is remarkably independent of the mean droplet size having the same value for mean droplet sizes of 4500 and 15000 atoms at a peak laser intensity of $1.5 \times 10^{14}\,\mathrm{W/cm^2}$, as shown in Fig. 4.3. This points to the fact that the underlying mechanism is a collective effect in which all the atoms in the nanodroplet participate irrespective of their location in the matrix. The error in estimating the number of dopants using Kuma's approach [KGS+07] is also shown. The decrease in the yield of He ions for increasing K in figures 4.2−4.4 is related to the doping process: When dopant atoms are picked up sequentially and aggregate inside the droplet, collisional as well as binding energy are released. This leads to an increasing fraction of He atoms that evaporate from

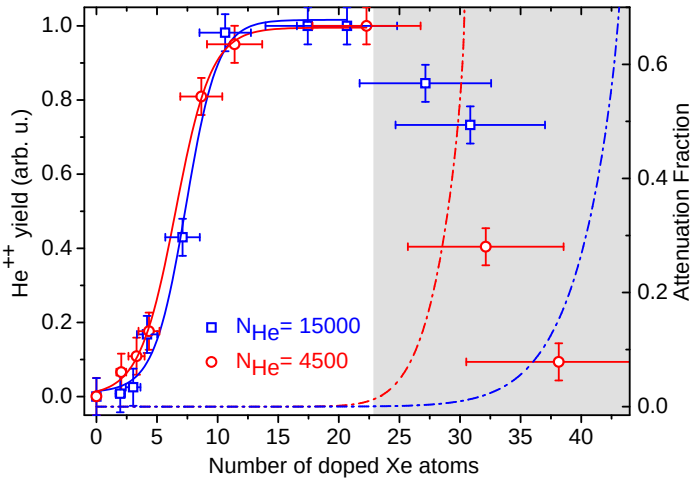

Figure 4.3: Xe doping dependence of He^{2+} yields at a peak laser intensity of $1.5 \times 10^{14}\,W/cm^2$ for droplets with a mean number of He atoms per droplet N_{He}=4500(red) and N_{He}=15000(blue) (lines to guide the eye). Horizontal bars present the error in estimating the number of doped Xe atoms using Kuma's approach [KGS+07]. The dash-dot curves present the fraction of droplets lost due to complete evaporation, which is significant only for number of Xe dopant atoms $K \gtrapprox 20$ (grey shading).

droplets at high doping pressure. As mentioned in section 3.3, we used the Monte-Carlo model of Bünermann et al. [BS11] to estimate the loss of droplets from the beam due to the evaporation of He atoms during the doping process. The results of this calculation performed for the case of Xe doping are shown in figure 4.3 as dashed lines. Clearly, the onset of significant nanodroplet destruction in this case of Xe doping occurs well beyond the K_{cr} (~ 10) observed in the experiment. The range of doping numbers affected by droplet evaporation is shown by the grey-shading. Thus, the process of dopant-induced ignition is not influenced by evaporation effects.

Next, we investigated the dependence of DII on laser intensity and the dopant species. These are shown in figure 4.4. In the plot of yield vs. number of doped Xe atoms, panel (a), we clearly see that the critical doping number increases with decreasing intensity. Likewise, the critical doping number is the smallest for the case of Xe ($\Phi_{IP} = 12.1\,eV$) increases for Kr ($\Phi_{IP} = 13.9\,eV$) and Ar ($\Phi_{IP} = 15.8\,eV$), in that order. Both these observations show that the extent of ionization of the embedded dopant cluster is crucial to DII. Thus, the role of dopants in *seeding* the ionization of the surrounding He atoms is emphasized. The electrons released from the dopants seed the avalanche-like ionization of He atoms. At a lower pulse intensity or higher dopant ionization potential, a smaller number of seed electrons per dopant atom is available for the ionization of helium. Consequently, a larger number of dopants per droplet is required to trigger DII and for the saturation of ion yields.

The He^{2+} ion yield as a function of the number of dopants suggests a step-like charging behavior of individual doped nanodroplets. However, in the experiment, the signal collected by the detector is an average over the modified Poisson distribution for the number of doped atoms. We can examine the effect of the Poisson

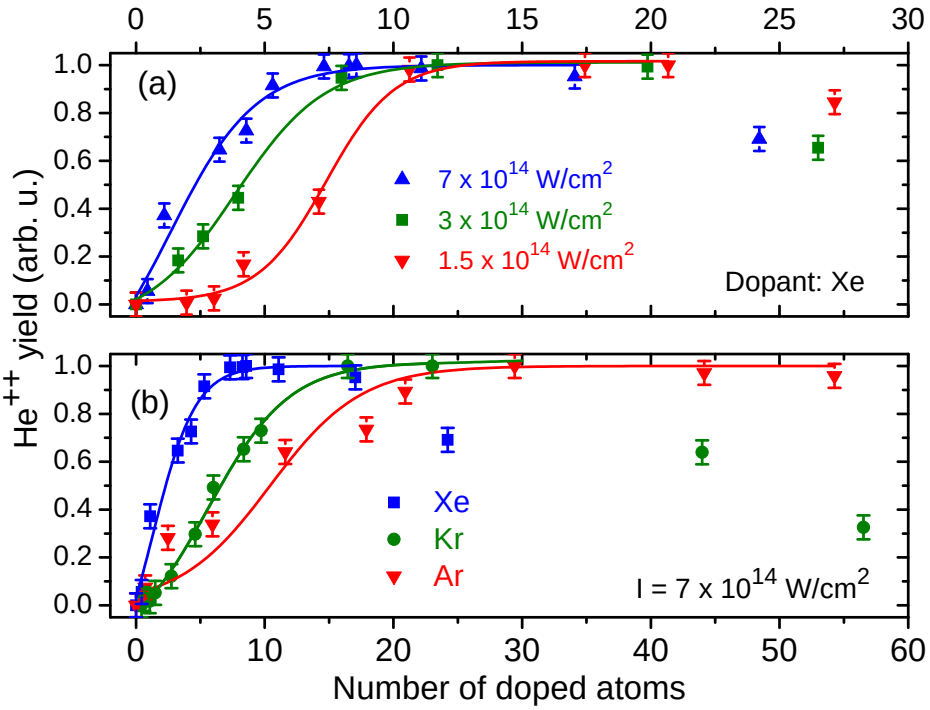

Figure 4.4: The He^{2+} yields for a droplet containing 15000 He atoms as function of the number of Xe dopant atoms (a) for different laser intensities I and (b) for different dopant species at $I = 7 \times 10^{14}\,\mathrm{W/cm^2}$ (all lines to guide the eye).

distribution on the DII curves (figures 4.2−4.4). If $y(k)$ is the dependence of He^{2+} yield from a single droplet containing exactly k dopant atoms and $P\,(k, K)$ is the Poisson distribution function in k with mean K. Then, the observed ion yield is given by:

$$Y_{fold}(K) = \int_0^{k_{max}} P(k, K) \cdot y(k) dk. \tag{4.1}$$

From this equation it is clear that the function $y(k)$ must reflect the step-like behavior of the observed ion yields (figures 4.2−4.4). Some aspects of the charging in individual doped nanodroplets can be discerned by deconvoluting the Poisson distribution from the experimental curves in figure 4.4 (b). To this end, we replace $y\,(k)$ with the step function Θ:

$$y\,(k) = \Theta(k - K_{sat}), \tag{4.2}$$

where K_{sat} determines the location of the step. An exhaustive analysis should include the effects of intensity averaging at the laser focus which requires a knowledge of the intensity dependence of $y(k)$. However, this is beyond the scope of the current discussion. Now, we fit the experimental data in figure 4.4 (b), to the function $Y_{fold}(K)$ by optimizing the parameter K_{sat}. The role of K_{sat} is obvious. It is the number of dopants required to saturate ionization in the droplet. The results of this fitting are shown in figure 4.5. The values of K_{sat} emerging from this analysis are 2.5, 7 and 13 for Xe, Kr and Ar doping, respectively. The reasonable agreement of this model with experimental data, especially in the case of Xe doping, reinforces the fact that there is a sharp rise in the charging of individual droplets. The underlying charging mechanism is not seriously affected by averaging involved

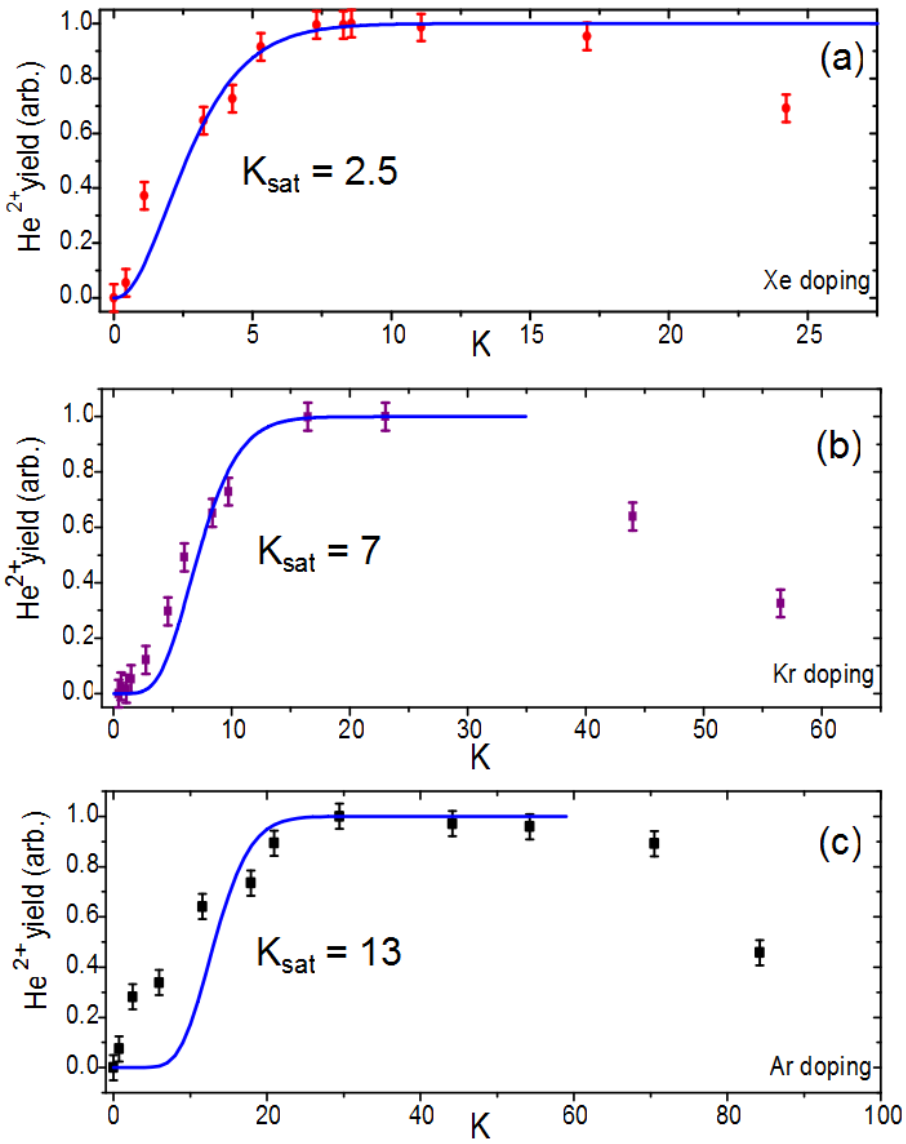

Figure 4.5: Fitting $Y_{fold}(K)$ in equation 4.1 (blue lines) to the experimental data (symbols) in figure 4.4 (b) by optimizing K_{sat}. Panels (a), (b) and (c) present the cases of Xe, Kr and Ar doping respectively. The fitted curves in (a)-(c) have K_{sat} values of 2.5, 7 and 13 in that order.

in the experiment. The discrepancy between fit curves and the data in the case of Kr and Ar at low doping numbers are due to the limitations of this model. The assumption of the step function is too simplistic as revealed by MD simulations presented in the next section. The gradual increase in ion yields in this case is not completely explained by the averaging over the doping distribution. This indicates that single droplet charging is more gradual. Thus, a more exact treatment through atomic scale simulations is required and was performed by Mikaberidze et al. [MSR09, Mik11].

4.2 Comparison with MD simulations [2]

Mikaberidze et al. [MSR09, KFK$^+$11] used *ab initio* classical molecular dynamics simulations [SR03, Saa06] tailored to the present problem of Xe doped He droplets containing 4000 He atoms each (for details of the approach see [Mik11, MSR09, MSR08]). The result from these calculations depicted in the bottom panel of figure 4.6 clearly shows the characteristic of DII. The simulations are performed over a single nanodroplet and the plot illustrates the charge per He atom as a function of the number of doped Xe atoms. The top panel presents the experimentally measured He^{2+} ion yield as a function of the number of doped Xe atoms. It is evident that theory and experiment show qualitatively the same behavior. A direct comparison of the charge per He atom to ion yields is difficult since the experiment is an average over the droplet size and doping distributions as well as over intensities in the focal volume. Moreover, in the theoretical result electron recombination is not taken into account. Yet, the curves agree well qualitatively and even quantitatively regarding the critical dopant number at which the saturation of charging occurs. This agreement points to a robust underlying mechanism - DII - which is not overshadowed by averaging effects. This was also demonstrated in the preceding section where the effect of the Poissonian doping distribution on the step-like growth of yields was examined.

4.2.1 DII and "cigar-shaped" nanoplasma

We showed in figure 4.6 that the consequences of DII are also observed in *ab initio* numerical investigations. These simulations enable access to information about the microscopic dynamics within the nanodroplet. In section 2.2.2, we discussed the possibility of resonant interaction of the nanoplasma with the driving laser field when the eigenfrequency of the former meets the laser frequency. We also noted that this requires an expansion of the cluster by atomic motion which occurs on ps timescales. MD simulations which uncover the dynamical mechanism underlying DII reveal that ignition results from a resonant interaction of the nanoplasma with the laser field.

It is observed in these MD simulations that the resonant interaction results from the non-spherical evolution of the nanoplasma in the doped as depicted in figure

[2] The MD calculations in this section were performed by A. Mikaberidze and not by the author of this dissertation.

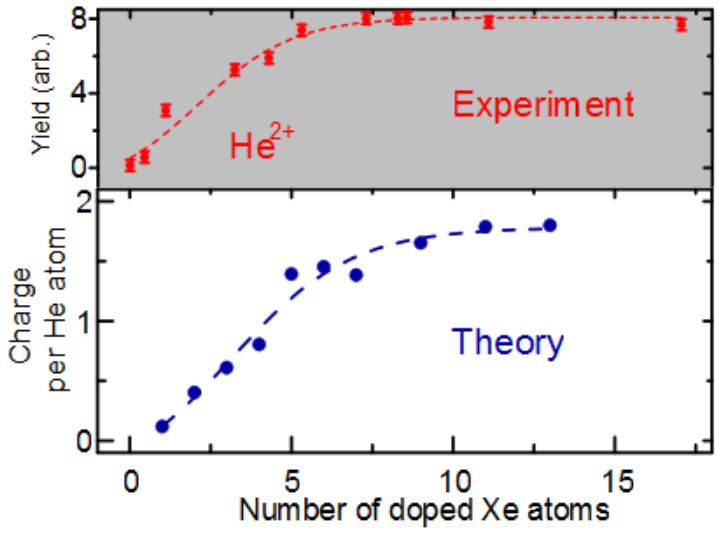

Figure 4.6: *Bottom:* Charge per He atom as a function of the number of doped Xe atoms from an MD simulation for a 10 fs pulse (7×10^{14} W·cm^{-2}) interacting with a nanodroplet containing 4000 He atoms. *Top:* Corresponding experimental result showing the yield of He^{2+} ions (from the same case as in figure 4.2). All lines to guide the eye.

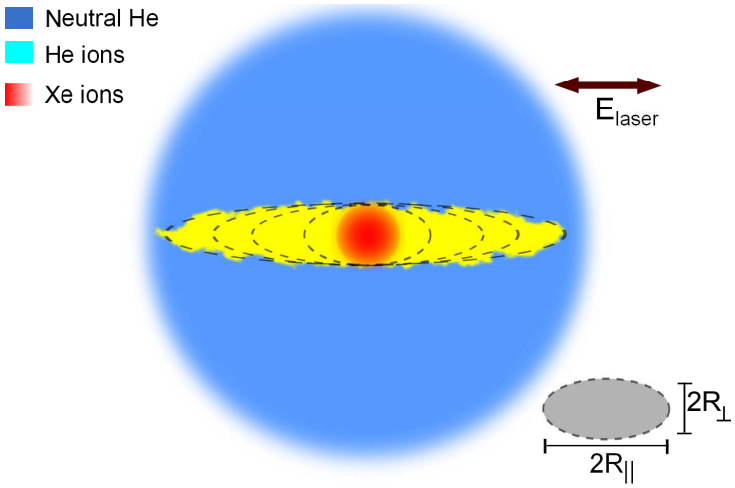

Figure 4.7: Anisotropic evolution and the formation of a "cigar-shaped" nanoplasma: This sketch qualitatively illustrates the cigar-shaped nanoplasma created due to ionization of neutral He atoms (blue) by laser driven electrons released from the ionization of embedded Xe atoms (red shading) along the laser polarization direction. As predicted by theory, the ionized region of the He droplet (yellow) grows and the anisotropy of the nanoplasma increases (dashed lines).

4.7. The formation of this ellipsoidal nanoplasma within the doped He nanodroplet is initiated by the ionization of the embedded dopant (red) cluster (~ 10 atoms) at the center of the large He sphere (blue). As mentioned in section 4.1.1, with the laser field not being strong enough, tunnel ionization of He atoms is not possible. The electrons released from the dopant atoms are driven by the laser field and this subsequently ionizes the He atoms surrounding the dopants. This occurs preferentially along the laser polarization axis as strong dipolar fields in this direction arise due to the local seperation of positive and negative charges (the ionized atoms are shown in yellow in figure 4.7). Thereby, a "cigar-shaped" nanoplasma ellipsoid is formed whose major axis is along the laser polarization direction. The aspect ratio of the ellipsoid grows as the ionization by these electrons increases. Now, we recall that the eigenfrequency of a spherical nanoplasma in terms of the ionic density ϱ_i is $\Omega = \sqrt{4\pi\varrho_i/3}$ (cf. equation 2.32) assuming the mathematical form of the cluster potential equation 2.28. Similarly, we can analyze the ellipsoidal nanoplasma whose shape is given in cylindrical coordinates (ρ, θ, z) by

$$\frac{\rho^2}{R_\perp^2} + \frac{z^2}{R_{||}^2} = 1, \tag{4.3}$$

where $R_{||}$ and $R_\perp$ are the semi-major and semi-minor axes of the ellipsoid. The major axis of the ellipsoid is along the direction of laser polarization. We will refer to this as the parallel direction and the one transverse to it as perpendicular, henceforth. In terms of the ionic charge density ϱ_i, the electric potential of the prolate ellipsoid ($R_{||} > R_\perp$) can be written in terms of its aspect ratio $\alpha = {}^{R_{||}}/_{R_\perp}$ as

$$U_{ellipsoid} = \pi\varrho_i \left[\{1 - g(\alpha)\}\rho^2 + 2g(\alpha)z^2 - h(\alpha)R^2\right], \tag{4.4}$$

where

$$h(\alpha) = \alpha^{-2/3}\left[1 + f^2(\alpha)\, g(\alpha)\right], \tag{4.5}$$

$$g(\alpha) = \left[\alpha ln\left(\alpha + f(\alpha)\right)/f(\alpha) - 1\right]/f^2(\alpha) \tag{4.6}$$

and

$$f(\alpha) = \sqrt{\alpha^2 - 1}. \tag{4.7}$$

For a cigar-shape or a prolate ellipsoid $\alpha > 1$. From equation 4.4, the eigenfrequency along the laser polarization $\Omega_{||}$ and that perpendicular to it $\Omega_\perp$ can be obtained after separating variables ρ and z. In terms of the eigenfrequency of the spherical plasma Ω $(= \sqrt{4\pi\varrho_i/3})$ these are

$$\frac{\Omega_{||}}{\Omega} = \sqrt{3g(\alpha)} \tag{4.8}$$

and

$$\frac{\Omega_\perp}{\Omega} = \sqrt{3\left[1 - g(\alpha)\right]/2}. \tag{4.9}$$

These ratios of eigenfrequencies are plotted in figure 4.8, clearly bracketing that of the sphere ($\alpha = 1$). We note that equations 4.8 and 4.9 are identically the eigenfrequencies of a spheroidal plasma in Penning traps where they can be measured directly in experiment [BPB$^+$88, BHM$^+$93].

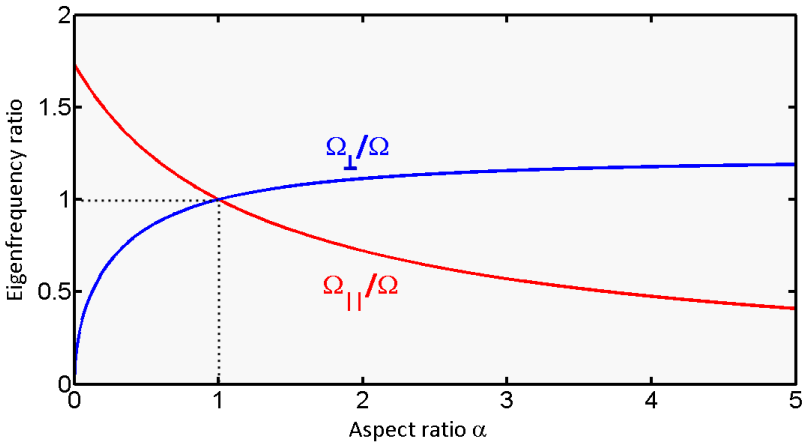

Figure 4.8: Eigenfrequencies of the cigar-shaped nanoplasma along the major ($\Omega_{||}$) and minor ($\Omega_{\perp}$) axes as a function of the ellipsoid aspect ratio α, scaled by the eigenfrequency (Ω) for a spherical plasma with identical ionic density.

In section 2.2.2, we found ionic motion or cluster expansion necessary for the lowering of the nanoplasma eigenfrequency so that it matches the laser frequency ω_0 corresponding to the laser wavelength of 800 nm. Here, we have found another mechanism which can achieve the same. As the aspect ratio α grows from 1 to 5, the ratio $\Omega_{||}/\Omega$ decreases monotonically as seen in figure 4.8. Hence, the resonance condition

$$\Omega_{||} \approx \omega_0 \tag{4.10}$$

is met even at high electron densities as the cigar-shaped nanoplasma within the droplet is elongated preferentially along the laser polarization direction. Since He atoms can have a maximum charge-state of +2, complete inner-ionization of the spherical nanodroplet without expnasion results in a maximum eigenfrequency of 0.16 a.u. The frequency corresponding to a laser wavelength of 800 nm is 0.057 a.u. The condition $\Omega_{||} = \omega_0$ is achieved when the ratio $\Omega_{||}/\Omega$ is in the range of $0.4 - 0.5$. From figure 4.8 this corresponds to a value of $\alpha \approx 3$ which can be achieved as the nanoplasma elongates driven by purely *electronic* motion. Thus, it can occur on the timescale of a few fs. This is indeed revealed by MD calculations. Figure 4.9 adapted from ref. [MSR09] shows the elongation of the nanoplasma in a 20 fs pulse. Panel (a) illustrates the extent of the nanoplasma along ($L_{||}$) and perpendicular ($L_{\perp}$) to the laser polarization direction. The aspect ratio ($L_{||}/L_{\perp}$) is shown in panel (b). It is evident that the nanoplasma attains the favorable aspect ratio $\alpha \approx 3$ in about 10 fs. This ratio is maintained for a substantial duration of the pulse. Thus, the resonance condition is achieved, very efficient coupling of the laser field to the electron-ion system happens and DII occurs.

Comparing the case of 780 nm with 200 nm illumination in the calculation reveals important aspects of DII. The laser frequency at 200 nm is 0.23 a.u. where DII never occurs. Thus, 780 nm corresponds to DII and 200 nm does not. In figure 4.10 (a), we notice that at 780 nm the rise of charging is very different from that of the 200 nm case. Moreover, in panel (b) we see that the charge per He atom decreases as the droplet size increases. For an extremely large droplet containing 10^5 He atoms, the average charge is negligible. As a detailed analysis shows, the mechanism underlying

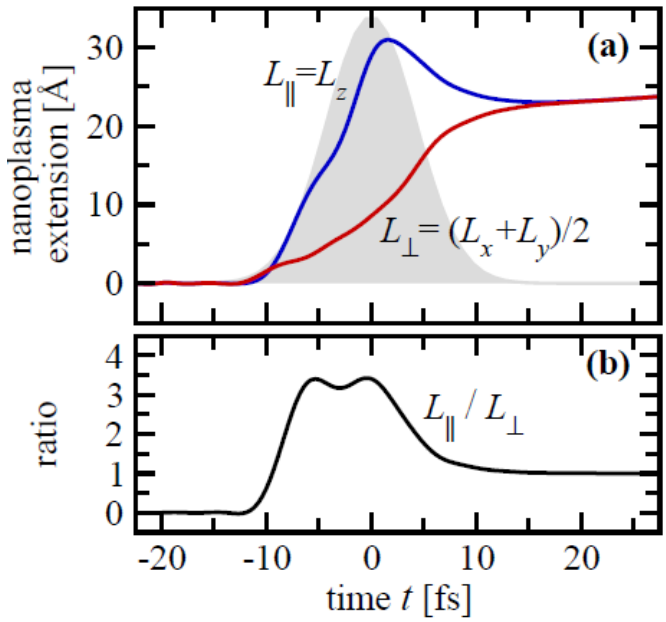

Figure 4.9: Elongation of the cigar-shaped nanoplasma in a 20 fs pulse of peak intensity 7×10^{14} W·cm^{-2}. Panel (a) shows the evolution of the dimensions of the nanoplasma along the laser polarization direction (z) and those perpendicular to it during the laser pulse. The intensity profile of the pulse is shown in grey-shading. Panel (b) presents the aspect ratio resulting from the elongation of the nanoplasma during the laser pulse. It is evident that the favorable aspect ratio $\alpha \approx 3$ is maintained for a substantial duration of the laser pulse after it is attained on a timescale of about 10 fs. Adapted from ref. [MSR09].

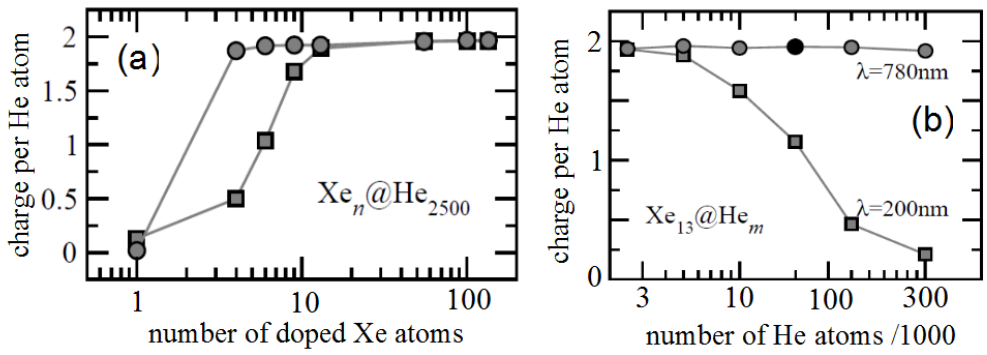

Figure 4.10: Average He charge of doped He nanodroplets in a 20 fs pulses with central wavelengths of 780 nm (circles) and 200 nm (squares) at the same peak intensity of 7×10^{14} W·cm^{-2}, (a) as a function of the number of doped Xe atoms and (b) as a function of the number of He atoms per droplet for a constant doping level, as reported in ref. [MSR09].

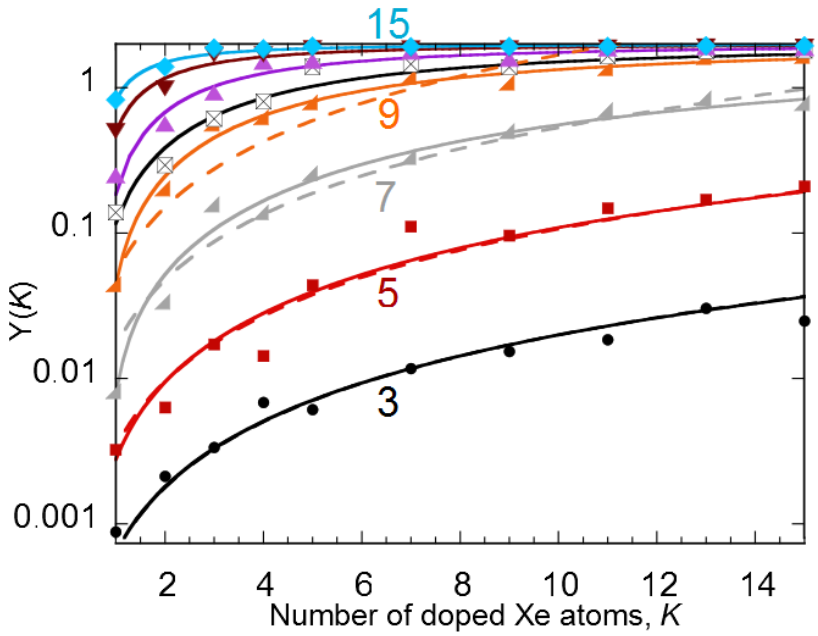

Figure 4.11: Calculated average charge per He atom $Y(K)$ as a function of the number of doped Xe atoms K for a droplet containing 4000 He atoms and intensity as in figure 4.2 from MD calculations. The different symbols and curves distinguish from bottom to top laser pulse lengths (full width half maximum) from 3 to 15 fs in steps of 2 fs, which are indicated for a few cases. Additionally, $Y(K)$ for 10 fs (crossed boxes) is shown, see also figure. 4.2. The lines are fits of the data points resulting from MD simulations according to equation 4.12 (solid) and with the power law $Y \propto K^{3/2}$ corresponding to ionization by a static field for $T \leq 9$ fs (dashed). For details, see text.

the ionization of He atoms at an excitation wavelength of 200 nm is field-ionization (FI). Here, Xe atoms are efficiently ionized by a multiphoton process. There, the local field within the cluster results in He ionization: Bound electrons escape from He atoms due to a suppression of the Coulomb barrier caused by the static field of the highly-charged Xe core, i.e. FI occurs. Consequently, the effect of FI relative to the droplet size diminishes as the droplet grows.

MD simulations [KFK+11] reveal that DII occurs only for pulses longer than a minimum pulsewidth (FWHM). The numerically determined average He charge in a droplet $Y(K)$ as a function of the number of Xe dopants K is shown in figure 4.11 at a peak intensity of 7×10^{14} W/cm^2 as a function of the pulse length. A qualitative change of the average charge per He atom $Y(K)$ occurs between 7 and 9 fs pulse length: For longer pulses DII is operative with a fast rise followed by saturation at full ionization of the He atoms ($Y = 2$). For shorter pulse lengths the average charge shows a gradual rise $Y \propto K^{3/2}$ (dashed lines) which is a characteristic of FI - the ionization of He atoms due to the static electric field of the laser ionized Xe ions in the center of the droplet. Döppner et al. [DDP+07] attributed FI as the mechanism behind the ionization of He atoms in droplets embedded with Pb_N, Cd_N and Ag_N clusters ($N \approx 10 - 100$) at peak intensities of $\leq 1.5 \times 10^{14}$ W·cm^{-2}.

To derive this dependence ($Y \propto K^{3/2}$) for the case of FI, we assume that all Xe ions constitute a point charge at the center of the droplet and that the density of He

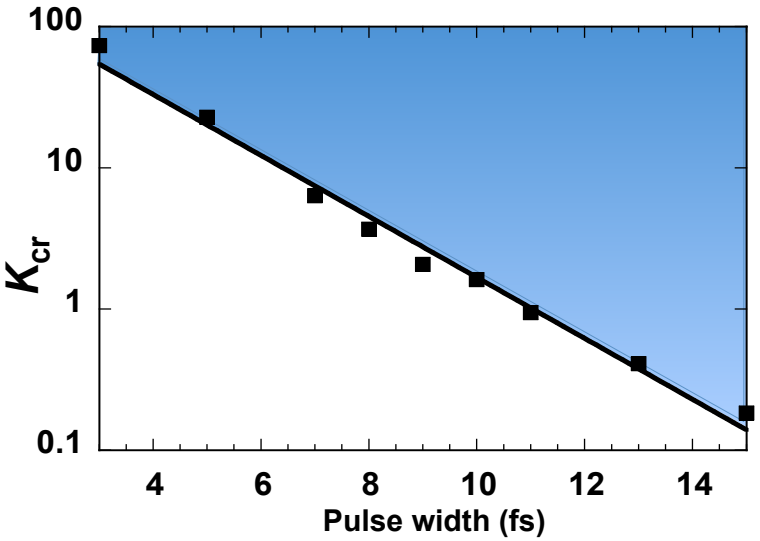

Figure 4.12: The number of dopants for which the average charge per He atom Y in Fig. 4.11 has a turning point, $Y''(K_{\mathrm{cr}}) = 0$. The shaded area distinguishes the regime of dopant induced ignition (DII) from the field-ionization regime (not shaded), at a peak intensity of $7 \times 10^{14}\,\mathrm{W/cm^2}$.

atoms is uniform within the spherical droplet. Then the problem is of purely radial nature and a sphere exists which contains only doubly ionized helium atoms. Its radius is given by $R_{++} = \sqrt{q_{\mathrm{Xe}} K / E_{\mathrm{bs2}}}$ where q_{Xe} is the average charge of each of the K dopant atoms and E_{bs2} is the electric field necessary to ionize the second electron in He through barrier suppression (Bethe rule) [BS57, GSR09]. The number of He atoms inside this sphere is given by $N_{++} = 4\pi\rho_{\mathrm{He}} R_{++}^3/3 = 4\pi\rho_{\mathrm{He}}(q_{\mathrm{Xe}} K/E_{\mathrm{bs2}})^{3/2}/3$, where ρ_{He} is the density of He in the droplet. We find the number of singly ionized helium atoms N_+ in a similar way and obtain the average ion charge per He atom using $Y = (N_+ + 2N_{++})/N_{\mathrm{He}}$, where N_{He} is the total number of He atoms in the droplet. This yields

$$Y(K) = \frac{4\pi\rho_{\mathrm{He}}}{3N_{\mathrm{He}}} \left(E_{\mathrm{bs1}}^{-3/2} + E_{\mathrm{bs2}}^{-3/2} \right) q_{\mathrm{Xe}}^{3/2} K^{3/2}, \tag{4.11}$$

where E_{bs1}, E_{bs2} are the first and the second barrier suppression fields for He. Assuming that q_{Xe} does not depend strongly on the number of Xe atoms K (this is fulfilled very well for K between 2 and 15 as seen from the MD simulations), we conclude that $Y \propto K^{3/2}$, i.e. the static field-ionization due to positively charged dopants follows a characteristic power law.

Although it is clear from figure 4.11 that for increasing pulse lengths the average charge per He atom $Y(K)$ is no longer well described by the field-ionization power law (dashed lines), a well defined transition from field-ionization to DII for increasing pulse length is difficult to extract. To determine the minimal pulse length T for which DII dominates, we parametrize the shape of $Y(K)$ with a function which can describe both limits (solid line in figure 4.11)

$$Y(K) = Y_\infty \frac{(K/\delta)^{3/2} - 1}{(K/\delta)^{3/2} + \beta}\,. \tag{4.12}$$

For $\beta \gg K/\delta$, equation 4.12 describes the field-ionization behavior, $Y(K) \propto K^{3/2}$, while for $\beta \ll K/\delta$, the typical DII shape emerges with a sharp onset followed by saturation at Y_∞. The latter is characterized by a negative second derivative $Y''(K)$ while for the field-ionization power law $Y''(K) > 0$ holds for all K. Hence, $Y''(K_{\rm cr}) = 0$ can be interpreted as the conditional equation for the critical number of dopant atoms where field-ionization dominated absorption goes over into DII dominated absorption. Using equation 4.12, we get $K_{\rm cr} = \delta(\beta/5)^{2/3}$. The parameters (δ, β) are obtained for each pulse length T by fitting equation 4.12 to the numerically generated data in figure 4.11. $K_{\rm cr}$ exhibits an exponential dependence on the pulse length T, as can be seen from figure 4.12. The shaded area indicates DII with $Y'' < 0$, while below the line of $K_{\rm cr}$ field-ionization rules. Since physically, at least one dopant atom is necessary for ionization, DII dominates for T larger than about 9 fs. This is consistent with the qualitative conclusion from figure 4.11 as well as with our experimental result which demonstrates DII for a pulse length of $\sim$ 10 fs. Additionally, the numerical simulations reveal that DII may also be suppressed by employing pulses shorter than $\sim$ 7 fs.

Thus, the experiment and numerical simulations in combination demonstrate that it is possible to transfer energy resonantly from a 790 nm intense few-cycle pulse to bound electrons without the need of atomic expansion of the target. This brings down the time scale of this extremely efficient but relatively slow process from the sub-picosecond regime down to a few femtoseconds and, at the same time, allows it to be applied to any form of matter that can be suitably doped with seed atoms. DII demonstrated here, may also explain the surprising enhancement of light absorption in water doped argon clusters [JK08a].

4.3 Kinetic energy spectra of ions

The TOF mass spectra presented in figure 4.1 can be used to determine the kinetic energy release (KER) into the He ions resulting from the disintegration of the doped nanodroplets. The details of the procedure were presented in section 3.4. Figure 4.13 shows the KER distributions for various Xe doping numbers in nanodroplets containing 15000 He atoms.

Numerical simulations presented in the preceding section reveal important details of the dynamics during the pulse. It has been observed in simulations by Fennel et al. [FMBT$^+$10] that, when the nanoplasma gets under-critical ($\Omega < \omega_{las}$) after resonant heating has occurred, the mean kinetic energy of quasi-free electrons decreases on account of the continuing expansion of the ionic background according to $\langle K_e(t) \rangle = b_1 R^{-2} t + b_0$, where R is the instantaneous cluster radius and b_0 and b_1 are expansion parameters. This is similar to the cooling of an electron gas in an expanding spherical vessel - an expanding balloon. It is assumed commonly that after such cooling, inner-ionized electrons remaining in the cluster eventually recombine after the laser pulse. Thus, only outer-ionized electrons contribute to the final charge-state of ions observed in experiment. But Fennel et al. [FRB07] showed that such inner-ionized electrons within the cluster boundary may be freed by electric fields applied in experiments. Currently, theoretical investigations do not carry us any further in our understanding of dissipative process which occur

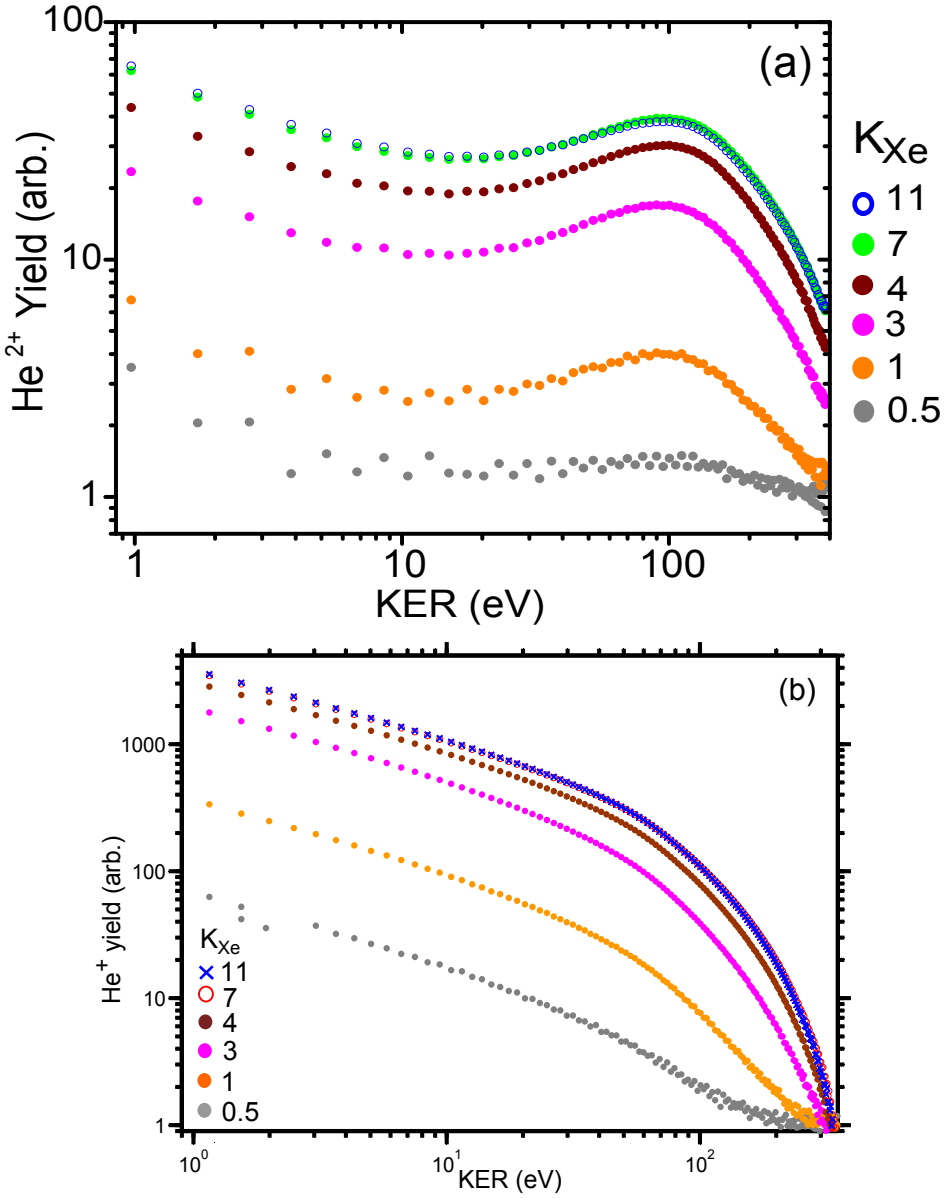

Figure 4.13: Kinetic energy release (KER) distributions of He ions resulting from the interaction of a 10 fs pulse with Xe doped He nanodroplets of a peak intensity of 7×10^{14} W·cm^{-2}. Panels (a) and (b) show the KER distributions of He^{2+} and He^{+} ions, respectively. The legend in both panels show the number of doped Xe atoms. In panel (a), the KER distributions are terminated at a value of ≈ 390 eV on the horizontal axis due to the limited range offered by the TOF spectrometer. He^{2+} ions of higher kinetic energies have flight times which overlap with that of H^{+} ions and the two cannot be distinguished unambiguously.

on sub-nanosecond timescales (e.g. duration of characteristic X-ray emission from cluster nanoplasmas [Dit97]). Thus, ion KER spectra provide us with important information about the eventual fate of the ions in the nanoplasma while naturally accounting for processes occurring on such timescales.

The mean KER of the ions derived from the distributions in figure 4.13 are presented as a function of the number of Xe dopants in figure 4.14 (a). We define the mean KER by $\langle E_{\mathrm{KER}} \rangle = \sum_i E_i \cdot Y_{\mathrm{KER}}(E_i) \,/\, \sum_i Y_{\mathrm{KER}}(E_i)$ and consider only ions with $E_i > 1\,\mathrm{eV}$. The mean KER follows the same trend as ion yields (cf. figure 4.2). We may conclude from this that the dissipative processes do not overshadow the consequences of the dynamics during the laser pulse. We noted in section 2.2.4 that the final kinetic energy of ions resulting from cluster disintegration is a combination of the Coulomb energy of the ionic background in the cluster and the hydrodynamic energy proportional to the temperature of the expanding (quasi-free) electron gas (cf. section 2.2.4). This variation of the mean KER with doping suggests that both the net ion charge after recombination and electron temperatures depend on the doping levels as dictated by DII. This conclusion enables us to provide a self-contained picture of the ionization of weakly doped nanodroplets in terms of DII.

From figure 4.14 (a), we also note that the ratio of mean KER values of He^{2+} ions to that of the He^{+} ions is ≈ 3.5. For pure Coulomb explosion this ratio should be 4 and 2 for purely hydrodynamic expansion, since the ratio of charge-states is 2. But both pure Coulomb explosion and pure hydrodynamic expansion are extreme and idealistic cases as has been pointed out by Peano et al. [PPM+06]. Hence, the ratio ≈ 3.5 is not surprising and indicates that the Coulomb energy of the electron-ion system is significantly greater than the temperature of the electron gas in the nanoplasma. This motivates an analysis of the shapes of the KER distributions on the basis of a Coulombic process using the analytical model formulated by Islam et al. [ISR06]. We outline the approach here. This simple model assumes a pure Coulomb explosion of a spherical cluster of radius R with a uniform charge q per atom. The Coulomb energy of an ion located at r within is $E_{\mathrm{Coul}}(r,\ q,\ N) = Nq^2r^2/R^3$, where N is the number of atoms in the cluster. We scale ion energies by the factor $E_R := E_{\mathrm{Coul}}(R, q, N) = Nq^2/R$. In terms of this scaling, the kinetic energy release (KER) distribution of ions resulting from Coulomb explosion is

$$\frac{dP}{d\varepsilon} = \frac{3}{2}\sqrt{\varepsilon}\ \Theta(1-\varepsilon)\,, \tag{4.13}$$

where $\varepsilon = E/E_R$ and E being the kinetic energy of an individual ion. This is shown in figure 4.15, with the label (0). We have noted earlier that the experimentally measured ion yields include averaging over the cluster size distribution and intensities at the laser focus. The effect of these is also visible in figure 4.15: To account for the cluster size distribution we must fold the result in equation 4.13 with the log-normal distribution (equation 3.5). This results in the curve (1). The effect of averaging over intensities at the laser focus is curve (2). We assume that the average charge q is linearly proportional to the amplitude of the laser electric field "seen" by the cluster by virtue of its location at the laser focus. This is true for resonant charging of the cluster in the laser field (cf. equation (6) in ref. [Saa06]). Finally, curve (3) takes both these effects into account and the fact that the charging of

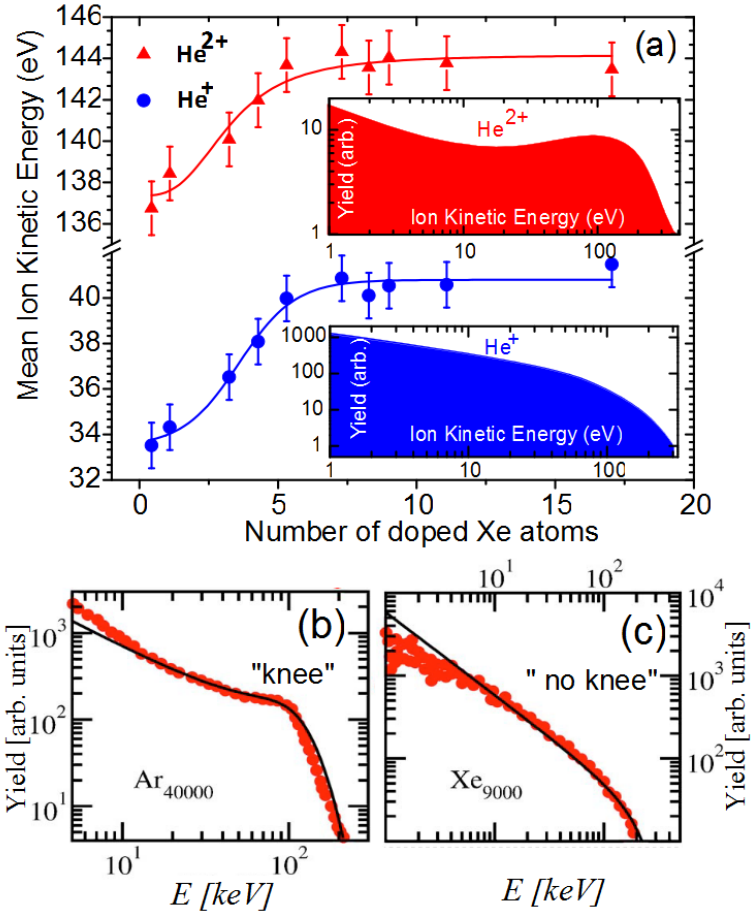

Figure 4.14: (a) Mean kinetic energies of He^{2+} (red) and He^{+} (blue) ions determined from the KER distributions in figure 4.13 (lines to guide the eye). The dependence of mean KERs strongly resembles that of ion yields in both cases (cf. figure 4.2). The insets show the KER distributions for the case of doping with 11 Xe atoms. Illustration of the "knee" feature from ref. [ISR06]: KER distributions of (b) Ar_{40000} clusters and (c) for Xe_{9000} clusters. The red dots are experimental data and the black curves are fits to the model by Islam et al. [ISR06]. The prominent "knee" in the Ar_{40000} case is a signature of saturation in charging. This feature is absent in the Xe_{9000} case.

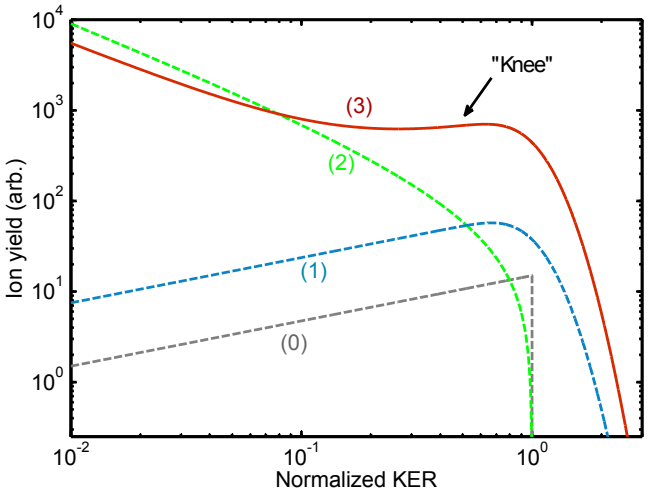

Figure 4.15: Kinetic energy release (KER) distribution of ions: (0) is the distribution of ion KER resulting from pure Coulomb explosion of a single uniformly charged cluster, (1) is the result of folding the log-normal cluster size distribution (equation 3.5) with (0), (2) is the result of folding the distribution (0) with the intensity distribution at the laser focus and (3) incorporates both the folding products in (1) and (2), and accounts for a saturation of the cluster charging process which can occur due to finite laser intensity. We note that the well-known "knee" feature pointed to here occurs on account of the saturation. The normalization or scaling of KER is explained in the text.

a cluster may undergo a *saturation* due to a finite maximum intensity available in laser focus and/or because individual atoms in the cluster have lost all their electrons (e.g. H_2-clusters). Saturation leads to a prominent "knee" in the ion KER distributions when represented on a double logarithmic scale [KMK04, KKM01]. The kinetic energy corresponding, also called the "knee" energy, is that of the ions residing on the surface of the cluster with the most probable size. The "knee" energy is often used to derive systematics from the experimentally observed KER distributions [ISR06, KMK04]. This model adequately explains the different shapes of KER distributions observed in experiment. But an unfortunate implication of this is that single cluster features are strongly masked by averaging effects. For example, the $\varepsilon^{1/2}$ scaling for the pure Coulombic case is not visible in the final profile (curve (3)). However, this model allows ion KER distributions to be interpreted in terms of experimental conditions - width of the Gaussian laser focus and the cluster size distribution.

From figure 4.13, we observe that the shapes of the KER distributions for He^{2+} and He^{+} ions are mainly due to the above-discussed experimental conditions. However, we may draw some qualitative conclusions from these distributions. The He^{2+} KER distribution has a prominent "knee" feature for all doping levels $K_{\mathrm{Xe}} \geq 1$, although it is less pronounced for $K_{\mathrm{Xe}} = 0.5$. This is evidently due to the fact that the ionization of He saturates. This points to the fact that DII indeed is extremely efficient, completely saturating the ionization of the entire droplet. Moreover, a significant fraction of He^{2+} ions are concluded to originate only from the most intense region in the focal volume - regions where there is strong charging. This is

similar to the KER distributions observed in Ar clusters (see ref. [KKM01]) and the case of N_2-clusters presented in ref. [KMK04]. Common to both these cases, there is a large gap in binding energy between the outermost shell (n=3 for Ar, n=2 for N) and the next inner shell. This leads to saturation in the charging process of Ar and N_2 clusters. In the case of He, the maximum charge per atom is two providing a natural upper limit which is obviously reached in DII. In contrast, the "knee" structure is absent in the He^+ KER distributions. We ascribe this to the fact that He^+ ions are also generated in regions of lower intensity where cluster ionization does not saturate. These are regions of weak charging. The He^+ ion signal is dominated by contributions from these regions which have large geometric volumes. Islam et al. [ISR06] arrived at a similar conclusion in analyzing the shape of ion KER distributions of Xe_{9000} clusters [SHT$^+$00] where charging never saturates. This also explains why the integral yield of He^+ ions is about 10 times the integral yield of He^{2+} ions although the angular acceptance of the TOF spectrometer is higher for the latter. In summary, the KER spectral shapes suggest that He^{2+} ions originate from clusters located at regions of the highest intensity within the laser focus while droplets at lower intensity locations mainly contribute He^+ ions. In focal scanning studies, Döppner et al. [DDP$^+$07] on Ag_N clusters found that Ag^{5+} ions originate from within the Rayleigh range whereas lower charge-states of Ag and oligomer ions are produced in the wings. This corroborates the observation in numerical studies that for resonant driving, charge per cluster atom is directly proportional to the laser field strength [Saa06]. Thus, our conclusions are in good agreement with what has been established in previous investigations. We note again that this model implicitly assumes a pure Coulomb explosion which is not strictly true as was discussed in section 2.2.4. Hence, we reiterate that the utility of this model lies in understanding the effect of intensity averaging and the effect of cluster size distributions in the observed KER distributions of ions. This enables us to distinguish the consequences of strongly saturated charging from weaker ionization which occur simultaneously in the experiment.

Summary

We may conclude that this investigation demonstrates ultrafast resonant energy absorption of rare-gas doped He nanodroplets from intense few-cycle (~ 10 fs) laser pulses. Less than 10 dopant atoms "ignite" the droplet containing over 10^4 He atoms by the formation of a non-spherical electronic nanoplasma resulting ultimately in complete ionization of all atoms, although the pristine He droplet is transparent for the applied laser intensities (for NIR wavelengths). As MD simulations further reveal, the minimal pulse length required for DII is about 9 fs. Thus, DII is the dominant ionization mechanism at these intensities and pulse widths where ionic motion does not set in.

This also motivates a re-interpretation of the role of He in the intense NIR laser ionization dynamics of rare-gas and metal clusters embedded in He nanodroplets studied in several experiments reported hitherto (e.g. [DDP$^+$07]). In these studies employing long fs pulses (typically $\gtrsim 100$ fs), helium atoms have been assigned a passive role. The ionization of He was interpreted as occurring only due to charge-transfer or field-ionization due to the presence of highly-charged metal ions at the

center of the droplet [DDP$^+$07]. While FI is definitely operative, an early ionization of He dominated by DII in the leading edge of long fs pulses needs to be taken into account. In addition, under such long-pulse illumination, effects of ionic motion also have to be considered. This leads to a complex dynamical scenario in which electronic and ionic motion play interdependent roles. We address this issue in the pump-probe studies presented in the forthcoming chapter.

Chapter 5

Dual-pulse excitation of doped He nanodroplets: Pump-probe studies

Now, we probe the ionization dynamics of doped He nanodroplets using dual 10 fs pulses in a pump-probe study. In the preceding chapter, we investigated the dopant induced ignition in He nanodroplets containing more than 10^4 atoms. Now we explore the dynamics in these doped droplets on longer timescales where ionic motion sets in. In this context, we review past studies on similar systems. Large He nanodroplets ($10^4 - 10^6$ He atoms/droplet) have been used extensively as host matrices in which metal clusters (e. g. Pb, Cd, Au, Ag) are formed by the pick-up of atoms from metal vapors [TS07]. The reason for employing the pick-up method lies in the difficulty of maintaining metal vapors at sufficiently high backing pressures to form large free metal clusters which follow Hagena scaling [HO72]. In some cases, small free (charged) metal clusters can be formed using magnetron sputtering sources [HKM91, Hab94] and arc cluster ion sources [SLF$^+$91].

Pioneering studies on intense NIR laser ionization of metal clusters embedded in He nanodroplets were performed in the group of K. -H. Meiwes Broer [FMBT$^+$10, DDP$^+$07, DFR$^+$06, FDP$^+$07, KSK$^+$99]. Most of these investigations were performed using intense but relatively long ($\sim$ 100 fs) pulses from a Ti:Sapphire based NIR laser system with aim to explore the dynamics in the embedded metal cluster so that the composite nature of the cluster was merely incidental. These studies, most notably, established the universality of the expansion-induced nanoplasma resonance which was first observed in rare-gas systems [DDR$^+$96]. The time dependence of the He ion yields was found to be very similar to that of the metal ions. This lead to the conclusion that the He ions were formed by the escape of bound electrons from He atoms enabled by the local electric field due to the presence of highly-charged metal ions at the droplet center. We have called this field-ionization (FI) in our earlier discussions. Further, the role of He in cluster expansion as revealed in some numerical investigations was to "slow down" the expansion process when compared to free metal clusters carrying a similar average charge [DDP$^+$07]. Consequently, larger delay times for the occurrence of expansion-induced resonance were predicted for the case of clusters embedded in He nanodroplets. But experiments revealed the contrary, expansion-induced resonance was found to occur earlier in nanoplasmas of metal clusters embedded in He nanodroplets than for free metal clusters of similar sizes when both systems were ionized under identical laser

pulse conditions [LVC+02]. These contradictions and the results of our single-pulse studies clearly point to the need for further work to investigate dynamics on the timescales of ionic motion.

5.1 Integral ion yields and pump-probe delay

In our pump-probe experiment, we used a Mach-Zehnder interferometer to split the beam of $\sim 10\,\mathrm{fs}$ pulses into two copies with a controlled time delay introduced between them, was adjusted by varying the length of one of the arms of the interferometer. This was achieved by moving a pair of retro-reflecting mirrors which were mounted on a piezo-driven translation stage (cf. figure 3.25). The ratio of peak intensities of the two pulses was varied by introducing a variable circular aperture to limit the beam diameter in one of the arms of the interferometer. The pulse that excites the clusters first is called the "pump" and the subsequent pulse that interacts with the same target is referred to as the "probe". The collinear pump and probe pulses were focused by a spherical mirror (focal length $f = 100\,\mathrm{mm}$) on the beam of doped He nanodroplets as described in section 3.6.

We investigate the case in which both pulses had identical peak intensities. First, we point to the similarity in the behavior of the He^+ and He^{2+} ions with respect to pump-probe delay. Figure 5.1 compares these ion yields as a function of delay time where it is evident that the cluster nanoplasma goes into resonance with the driving laser field as was detailed in section 2.2.2. The pump pulse excites the cluster first. Thereafter, the ionized cluster nanoplasma expands. As was also pointed out earlier the initial electron density of the droplet nanoplasma far exceeds the critical density for 800 nm excitation. Expansion dilutes the plasma density. Thus, at a certain delay time, the system achieves resonant conditions so that the nanoplasma eigenfrequency Ω matches the laser frequency ω_0 leading to a maximization of ion yields as also observed by Köller et al. [KSK+99]. Thus, this resonant condition is expansion-induced. Atomic or ionic motion is an essential feature of resonance absorption occurring on these timescales although it is due to the coupling between the electrons in the nanoplasma and the laser field. To quantify this resonance, we define the optimal delay (τ_{opt}) as the time delay between the pump and the probe pulses at which the He ion yields are maximized. The optimal delay for He^{2+} and He^+ ions has very similar values, $457\,(\pm 15)\,\mathrm{fs}$ and $476\,(\pm 15)\,\mathrm{fs}$ respectively. The small difference between the two values is explained using the observation of Döppner et al. [DDP+07] who measured the delay-dependent yields of the different charge-states of Ag ions from Ag_N clusters. Here, lower charge-states had significantly longer optimal delays than higher ones. They reasoned this occurs due to the fact that ions of different charge-states are produced in different regions of the laser focus. The lower charge-states come from regions of lower intensity while higher charges are created only at higher intensities. This has also been demonstrated by focal scanning experiments performed by the same group [DMP+07]. In our case, the difference between the optimal delay times for He^{2+} and He^+ ions is much smaller than the width of the expansion-induced resonance. Hence, we will discuss the systematics mainly in terms of the delay dependence of He^{2+} ion yields henceforth.

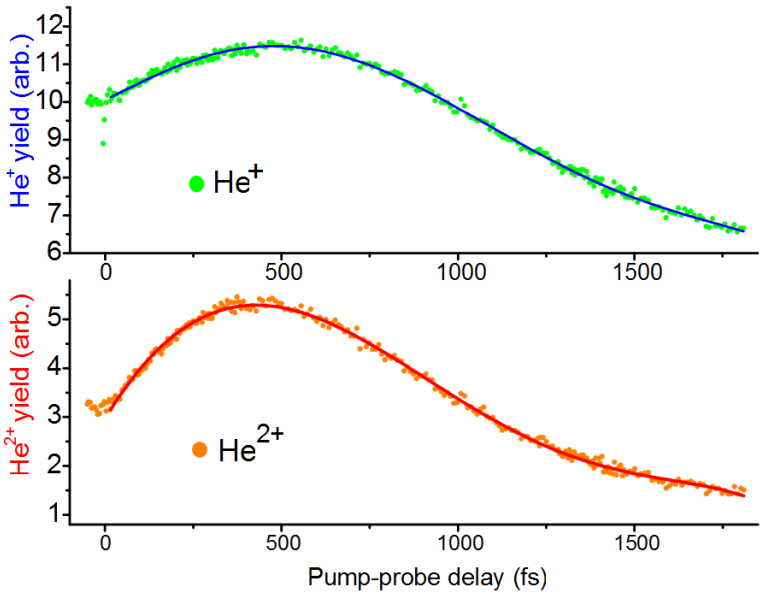

Figure 5.1: Comparison of He^+ and He^{2+} ion yields as a function of pump-probe delay when $Xe_{11}@He_{15000}$ nanodroplets are exposed to two identical pulses ($\sim 10\,fs$) of peak intensity $7 \times 10^{14}\,W{\cdot}cm^{-2}$. The He^{2+} yield is maximized at a delay time of $457\,(\pm 15)\,fs$ and the He^+ yield at $476\,(\pm 15)\,fs$. Lines to guide the eye.

In addition, we note the following about comparing our studies with previous investigations of the expansion-induced resonance. Many of these experiments have been performed by varying pulse-widths. In practice, this is achieved by manipulating the gratings in the pulse compressor of a chirped-pulse amplification system to deliberately introduce a chirp in the pulses and thereby "stretching" them. While such studies reproduce the general time-dependent features of the expansion-induced resonance, care should be taken while interpreting and comparing the various results [KKM03a, JK08a, ZDP99]. In these experiments often the pulse energy is kept constant while the pulse width is varied. Hence, the longer pulses have smaller peak intensities. Some threshold processes like ionization by barrier suppression (cf. equation 2.5) may not be triggered at smaller laser intensities. Sakabe et al. [SSH+06] have shown that cluster ion kinetic energy spectra are indeed sensitive to atomic barrier suppression thresholds. Alternatively, the pulse energy can be varied along with the pulse width to keep the peak intensity constant. However, due to the limited pulse energy available from typical laser systems, maintaining a constant high intensity during a 10- or 50-fold variation of pulse widths is often not achievable in practice. Thus, two-pulse experiments are ideally suited to study such dynamics. Further, we may point out that the duration of the pulses employed in our study, $\sim 10\,fs$ offers another significant advantage over past studies. This pulse width is much smaller than the optimal pulse delay required to achieve the expansion-induced resonance as can be seen from figure 5.1. Thus, the 10 fs pulses employed by us are truly impulse-like and the expansion of the cluster during the interaction with the laser pulse is negligible.

5.1.1 Droplet size dependence

We examine the pump-probe characteristics for different droplet sizes. Figure 5.2 presents the delay dependence of He^{2+} ion yields for the cases of Xe (panel (a)) and Kr (panel (b)) doping. The mean number of dopants per droplet (~ 15) is nearly the same in both the cases. Clearly, the optimal delay τ_{opt} increases with increasing droplet sizes in both cases. This is similar to the delay dependence measurements of optical absorption in Xe clusters of different sizes [ZDP99]. The optimal delay in this case was also found to increase with cluster size. The optimal time delay τ_{opt} required for the cluster nanoplasma to expand in order to meet the resonance condition (equation 2.35) can be written as [ZDP99]

$$\tau_{opt} = \frac{R_0}{v_{exp}} \left\{ \left(\frac{n_0}{3n_{crit}} \right)^{1/3} - 1 \right\}, \tag{5.1}$$

where R_0 is the initial radius of the cluster and v_{exp} is the expansion velocity of the cluster. For our case, n_0 is the electron density of the cluster after the interaction with the pump pulse and n_{crit} is the critical density at which the eigenfrequency of the cluster nanoplasma meets the laser frequency. This equation assumes that during the expansion process the cluster has a uniform electron density and expansion velocity. These assumptions are reasonable for the free expansion occuring between the interaction with the pump and probe pulses, as in our case. Then, from the condition for expansion-induced resonance in equation 2.35, the conservation of electron number can be written as: $n_0 \cdot \frac{4\pi}{3} R_0^3 = 3n_{crit} \cdot \left\{ \frac{4\pi}{3} \left(R_0 + v_{exp} \cdot \tau_{opt} \right)^3 \right\}$, which leads to equation 5.1. The loss of electrons from the cluster due to outer-ionization is implicitly neglected in this relation. This is reasonable for the free expansion of relatively large clusters ($\sim 10^4$ atoms/cluster) and moderately intense laser pulses as those considered here (for a simple estimate we refer to [KSS07]).

Figure 5.3 (a) shows that $\tau_{opt} \propto N_{He}$ the number of He atoms per droplet. In view of DII discussed earlier (cf. section 4.2.1) the doping levels considered here (~ 15 dopants per droplet) drive the charging of the droplet into saturation after the interaction with the pump pulse independent of the droplet size (see figure 4.3). Hence, it is reasonable to assume that the uniform electron density of the nanoplasma after the interaction with the pump pulse is independent of droplet size. From equation 5.1, $\tau_{opt} \propto R_0$ the initial cluster radius and we may note in addition that $R_0 \propto N_{He}^{1/3}$. We have observed that $\tau_{opt} \propto N_{He}$ from our experiment (cf. figure 5.3 (a)). Thus, on the basis of equation 5.1, we may conclude that the expansion velocity depends on the number of He atoms per droplet as $v_{exp} \propto N_{He}^{-2/3}$, so that the expansion of larger droplets is slower.

To obtain the values of optimal delay in each case, we fit the (broad) peak regions in figure 5.2 with a fifth-order polynomial. To obtain a goodness of fit[1] better than 98 % consistently, it was necessary to avoid the two extreme regions on the delay axis. Firstly, we avoid points close to zero delay where a temporal overlap of the pump and probe pulses occurs. Next, we also uniformly avoid the tails at long

[1]The "goodness of fit" used here is defined in terms of a least-squares fit via the R^2 parameter: If y_i are the experimental data with a mean value $\overline{y}$ and f_i are the fit values or predicted values, then $R^2 = 1 - \frac{\sum_i (y_i - f_i)^2}{\sum_i (y_i - \overline{y})^2}$. The "goodness of fit" expressed in percentage is simply, $100 \cdot R^2$.

delay to maximize the goodness of fit. This ensures that the peak region, where our interest lies, is weighted suitably over the others. The optimal delay values are obtained by differentiating the fit curves numerically and determining the point at which the derivative changes sign. This ensures that we obtain accurate values for optimal delay which are central to our discussion on the expansion-induced resonance. There are no analytic or semi-analytic models available currently that explain the shape of the pump-probe curves. Doeppner et al. [DFR$^+$05] have used a different fit-function which was found to be suitable for their pump-probe curves, although it was not based on any physical model.

In figure 5.3 (a), we also present the dependence of τ_{opt} for the case of Ar doping along with Xe and Kr. There is hardly any difference between Xe and Kr doping, indicating that the mass of the dopant cluster does not play a significant role in the expansion of the ionic core. At least for smaller droplets, the values of τ_{opt} are larger for the case of Ar doping. From figure 4.4, we note that the As doping level of 20 ± 4 ionization does not completely saturate during the interaction with the pump pulse. The lower electron density in the droplet could be the reason for slower expansion and larger optimal delays. Two recent theoretical investigations on the expansion-induced resonance dynamics of large (~ 100) Xe clusters in He nanodroplets have been reported [PF10, MSR08]. Both the studies report the occurrence of a double-resonance during the expansion of the composite system: The first resonance in time occurs due to the fast expansion of He ions in the droplet and the subsequent one is due to the slow expansion of the embedded core. This double resonance was visible in the bimodal absorption [MSR08] and electron kinetic energy spectra [PF10] computed in MD simulations. However, Peltz et al. [PF10] have pointed out that integrated ion yield spectra do not show distinct features corresponding to the double-resonance although the mechanism is under operation. On the basis of the double-resonance, it may be argued that the expansion of the dopant cluster is slower when it is made up of heavier atoms (Xe or Kr) than when the dopant atoms are lighter (Ar). But, we find the contrary here. This leads us to the conclusion that expansion of the dopant cluster is strongly dependent on the ionization level of the dopant atoms, electron temperature and local electron densities, and not just the atomic mass of the dopant.

In particle-in-cell (PIC) simulations on pristine cluster nanoplasmas, Peano et al. [PPM$^+$06] have shown that the expansion kinetics depend on the ratio of the Coulomb energy of the ionic assembly and the electron temperature. Further, Mikaberidze has shown that a Xe_{100} cluster embedded in a He droplet expands slower if it carries a larger net charge (see e.g., figure 5.10 in ref. [Mik11]) while the contrary is true for free Xe clusters. This slow down of expansion occurs in a He surrounding because the embedded cluster with a greater charge attracts a larger number of low-energy electrons towards the center of the droplet. Thus, a stable and relatively cold quasi-neutral plasma is formed at the core of the droplet. We have already noted that such plasmas have an expansion velocity which is inversely proportional to the electron temperature. Hence, the expansion is slowed down (cf. section 2.2.4). Similar damping effects also occur in two-component cluster systems under intense X-ray pulse excitation as shown by Gnodtke et al. [GSR09]. In the VUV domain, in Xe clusters with an Ar shell, the ionized Xe core trapped most of the quasi-free electrons which eventually recombined there leaving Ar ions

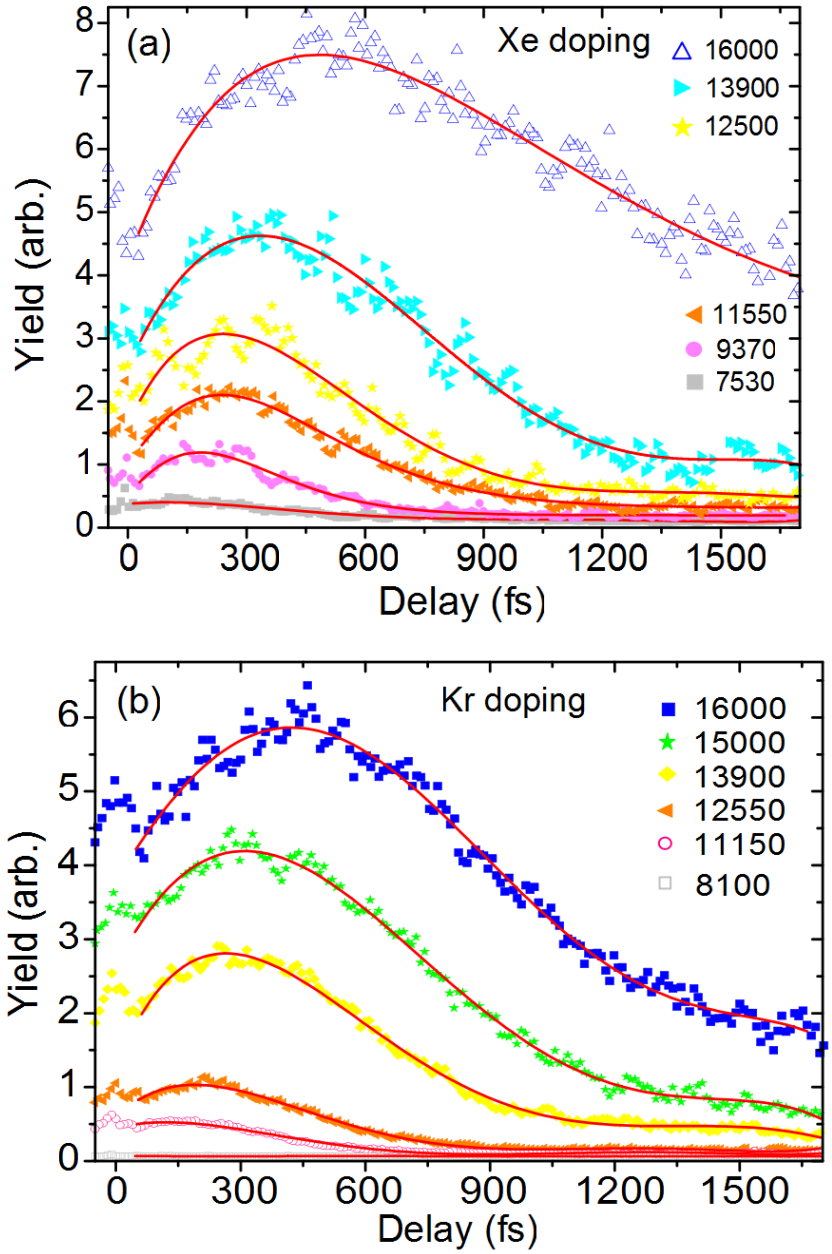

Figure 5.2: Delay dependence of He^{2+} ion yields for various droplet sizes (mean number of He atoms per droplet is indicated in the legend) for the case of Xe (a) and Kr (b) doping. Intensities of the pump and probe pulses was $7 \times 10^{14}\,\mathrm{W{\cdot}cm^{-2}}$. The mean number of doped atoms in the droplets is 15 ± 3 in the case of Xe and 14 ± 2.8 in the case of Kr. The data points are fitted with a fifth-order polynomial from which the optimal delay values (τ_{opt}) are extracted.

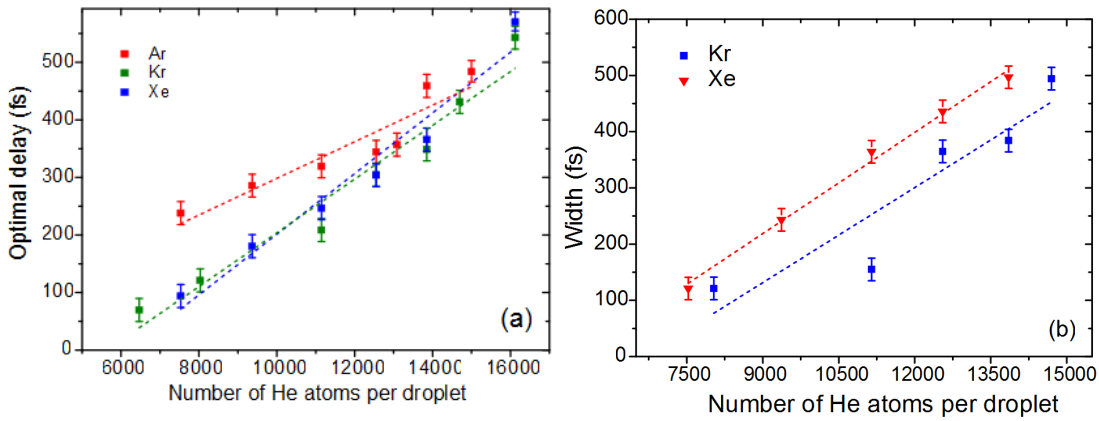

Figure 5.3: (a) Optimal delay times for Xe, Kr and Ar doped He nanodroplets of various sizes. The Xe and Kr cases are the same as shown in figure 5.2. The corresponding variation of the widths (full-width-half-maximum) of ion yield curves is shown in panel (b). The mean number of doped Xe, Kr and Ar atoms is 15 ± 3, 14 ± 2.8 and 20 ± 4 respectively. Intensities of the pump and probe pulses was $7 \times 10^{14}\,\mathrm{W{\cdot}cm^{-2}}$.

in the shell to play a sacrificial role in the dynamics [HBT+08]. Unfortunately in our studies, dopant ion signals originating exclusively from the doped nanodroplets were masked by the ionization of the residual dopant gas leaking from the doping cell which was housed in the reaction chamber (cf. figure 3.26)[2]. We also did not measure electron kinetic energies during this experimental campaign due to other constraints.

A comparison of the full-width-half-maximum of the delay-dependent ion yields presented in figure 5.2 (b) shows that larger droplets sustain near-resonant conditions for longer durations. We may explain this on the basis of the hydrodynamic simulations of Milchberg et al. [MMP01]. They observe that the electron density during the cluster expansion is not radially uniform. The density of electrons close to the cluster surface meets the resonance condition first (see equation 2.35). Thereafter, the layer of resonant electron density moves inwards until it reaches the center of the cluster. Thus, the resonance is sustained for long durations. In view of this model, bigger clusters offer a larger volume of electrons which sustains near-resonant or resonant conditions for longer periods of time.

5.1.2 Intensity dependence

Next, we investigate the delay dependence of He^{2+} yields as a function of peak intensities of the incident pulses. First, we examine this for the case when the pump and probe pulses have identical intensities and the He nanodroplets are doped with 16 ($\pm$3.2) Xe atoms. This is shown in figure 5.4 (a). The optimal delay τ_{opt}

[2]This design was adopted to ensure that a sufficiently high density of droplets remained available at the reaction zone after propagation from the source. We estimated a droplet number density of 10^8 per cm^3 for our experimental geometry. This drawback can be overcome in future studies by a more compact design which allows for similar droplet densities along with differentially doping cell.

increases with increasing laser intensity, as do the widths of these curves,which can be understood in terms of equation 5.1. The electron density n_0 due to ionization by the pump pulse depends on its peak intensity. In view of the single-pulse results presented in figures 4.2 and 4.4, it is important to note that the doping level $K = 16$ and intensities $\geq 1 \times 10^{14}\,\mathrm{W{\cdot}cm^{-2}}$, DII drives the droplet to a state of complete inner-ionization of He atoms after the interaction with the pump pulse. Thus, the optimal delays are also very similar for intensities greater than this value. For much lower intensities, inner-ionization of He atoms is partial leading to lower plasma electron densities. Consequently, in view of equation 5.1, the optimal delay is smaller. To the best of our knowledge, a study of expansion-induced resonance with a controlled doping of a few atoms in large clusters has neither been reported in experiments nor in theory, hitherto.

The alternative regime of very strong doping ($\sim$ 80 Ag atoms per droplet) has been studied by Döppner et al. [DDP$^+$07]. They observe an opposite trend in the dependence of optimal delays on pump pulse intensities, compared to the weak doping case presented here. Within the limits of our experiment, we could also consider a case of much stronger Xe doping, $K = 29 \pm 6$. In this case, the droplets in the beam had a mean size of 15000 He atoms per droplet before being introduced into the doping cell. As can be see from figure 5.5, the optimal delay decreases with the simultaneous increase in the intensity of both pump and probe pulses. This is in agreement with Döppner et al. [DDP$^+$07] who observed a decrease in the optimal delay values for increased pump intensities. They interpret this as a consequence of an increase in dopant cluster charging caused by the pump pulses of increasing peak intensities. This was corroborated in their case by the observation of dopant ions of higher charge-states at higher pulse intensities. In our case, we again view this in the light of the single-pulse doping dependence of He^{2+} yields presented in figure 4.4. Although He ionization is saturated due to DII at this doping level for intensities $\gtrsim 1 \times 10^{14}\,\mathrm{W{\cdot}cm^{-2}}$, the charging of embedded Xe atoms increases as the peak laser intensity is increased. In our case, there is also substantial droplet evaporation and shrinkage at such high doping levels ($K \approx 30$) as was shown in figure 4.3. Thus, the role of He is diminished as compared to the previous case of $K = 16$.

The roles of the pump and probe pulses are made explicit in figures 5.6 and 5.7. In figure 5.6, we present the scenario where the probe pulse intensity is kept constant at $7 \times 10^{14}\,\mathrm{W{\cdot}cm^{-2}}$ while the intensity of the pump pulse is varied between $0.1 - 7 \times 10^{14}\,\mathrm{W{\cdot}cm^{-2}}$. Panel (a) presents the dependence of He^{2+} ion yields on the pump-probe delay while (b) is a plot of optimal delays versus pump intensity. Figure 5.7 presents the complimentary situation when the pump intensity is held constant whereas the probe intensity is varied in a similar range as in figure 5.6. At first glance, panel (b) in figures 5.6 and 5.7 seem to contradict each other as they display opposite trends in the intensity dependence of optimal delays. We will resolve this in what follows by establishing that the roles of the pump and the probe in the dynamics are quite different.

Expansion-induced dynamics is an interplay between inner-ionization and recombination. As emphasized in earlier discussions, the role of the pump pulse is related to inner-ionization of the nanoplasma. At higher pump intensities, the inner-ionization of both He atoms on account of DII and the dopant atoms themselves is greater.

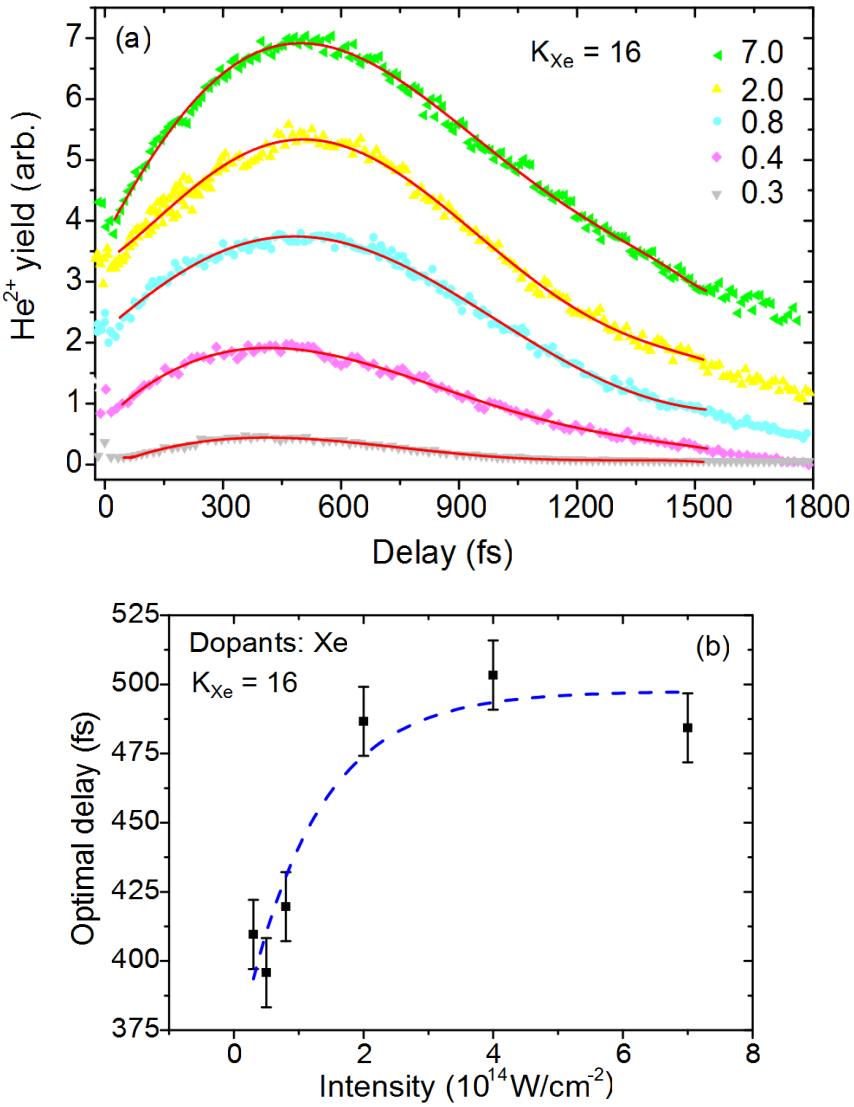

Figure 5.4: (a) Pump-probe delay dependence of He^{2+} ion yields for different peak intensities. Both pulses have identical peak intensities which are indicated in the legend in units of $10^{14}\,\mathrm{W{\cdot}cm^{-2}}$. He nanodroplets containing 1.5×10^4 He atoms are doped with 16($\pm$3.2) Xe atoms. The lines are fifth-order polynomial fits to the data points in the peak region which were used to determine the optimal delay. (b) Optimal pulse delays at which the ion yields are maximized. The statistical error in determining the optimal delay is also shown by the vertical bars (cf. figure 3.25). Line to guide the eye.

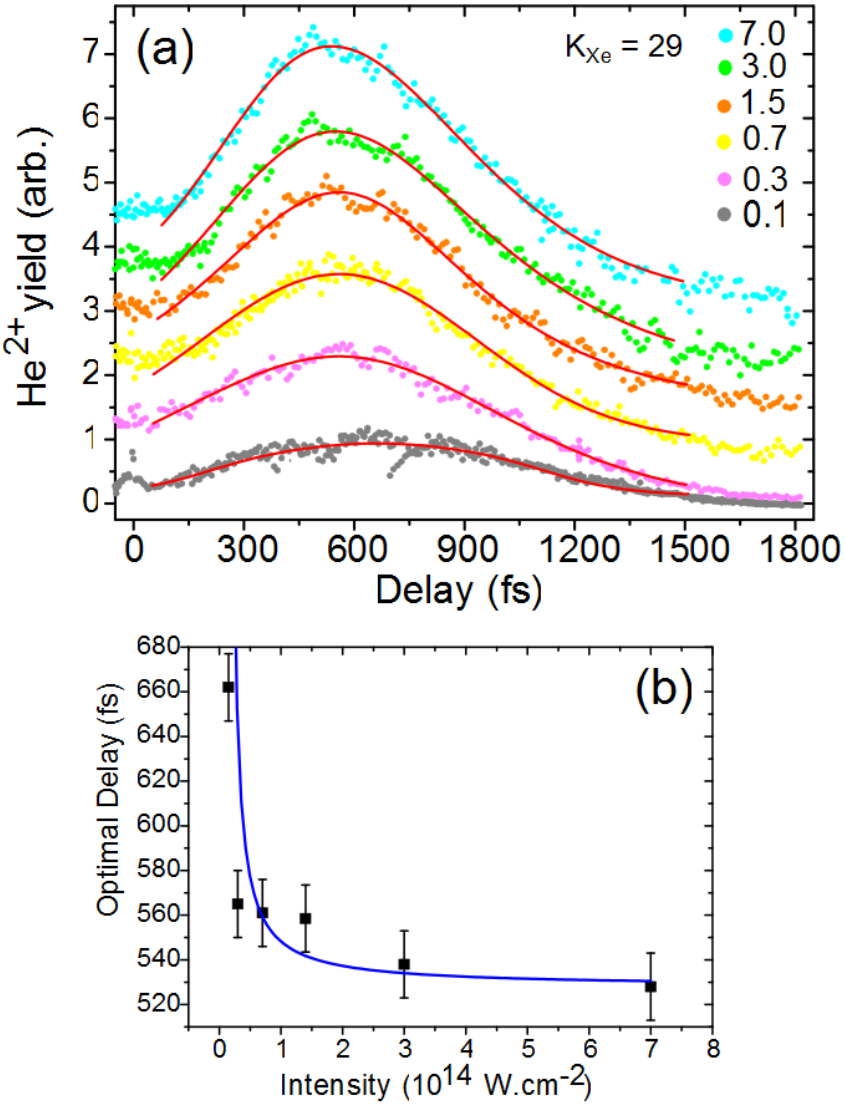

Figure 5.5: For a doped He nanodroplet with 29 (±6) Xe atoms in droplets with initially containing 15000 He atoms, panel (a) shows the delay dependence of He^{2+} ion yields for identical increase of pump and probe intensities. The legend indicates the peak intensity of the pulses in units of 10^{14} W·cm^{-2}. The lines are fifth-order polynomial fits. (b) Optimal pulse delays at which the ion yields are maximized (line to guide the eye). We contrast this to figure 5.4 (b).

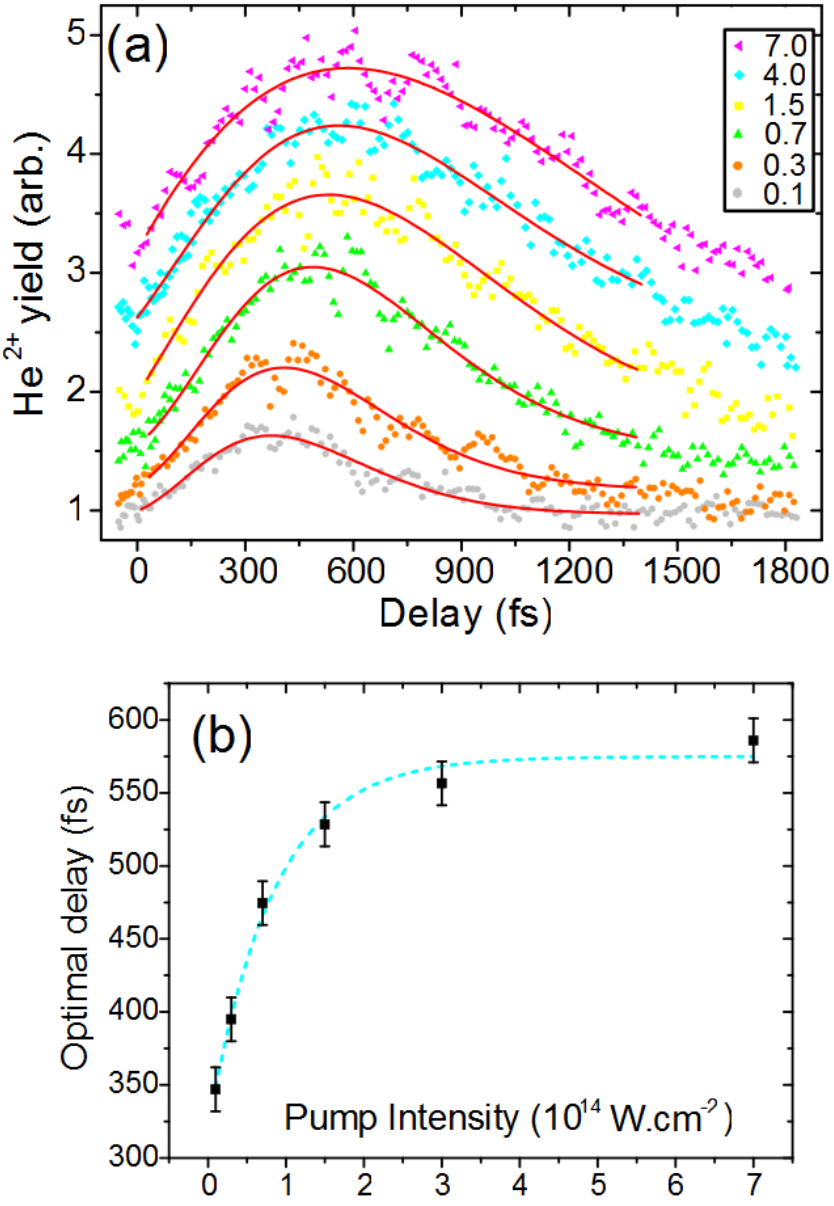

Figure 5.6: For Xe doping of 15 (±3) in nanodroplets containing 15000 He atoms, panel (a) presents the He^{2+} ion yields as a function of pump-probe delay for different pump pulse intensities in the range of $0.1 - 7 \times 10^{14}\,\mathrm{W{\cdot}cm^{-2}}$ as indicated in the legend. The probe intensity is held constant at $7 \times 10^{14}\,\mathrm{W{\cdot}cm^{-2}}$. The red lines are fifth-order polynomial fits. Panel (b) shows the dependence of optimal delays on the pump intensity (line to guide the eye).

Consequently, electron densities are greater after the interaction with stronger pump pulses. This causes the optimal delay to increase monotonically from ≈ 300 to 600 fs as the intensity of the pump pulse is increased with the probe intensity remaining constant, as long as the pump does not saturate the ionization of the composite cluster.

Recent calculations by Peltz and Fennel [PF10] reveal that the role of the probe pulse is largely related to increasing the population of ions by counteracting recombination in the nanoplasma and carrying out efficient outer-ionization. After the pump pulse is gone, with no external electric field, electron-ion recombination within the nanoplasma ensues. As noted earlier (cf. section 2.2.4), electron-ion recombination mainly proceeds via three-body recombination (3BR), i.e. the capture of a quasi-free electron following its collision with another electron in the vicinity of the ion ($A^+ + e^- + e^- \rightarrow A^* + e^-$). The 3BR rate ($k_{\mathcal{N}}$) for recombination into a bound level with principal quantum number $\mathcal{N}$ in a plasma with electron density n_e and temperature T is given by [Hah97b, Hah97a], $k_{\mathcal{N}} = \alpha \mathcal{N}^4 n_e^2 / T^2$, where α is a constant. Although 3BR into Rydberg levels with very high principal quantum numbers is possible, ambient electron temperatures determine an upper limit on the principal quantum numbers $\mathcal{N}_{cut}$, up to which recombination can take place [PF10, FRB07]. Peltz et al. [PF10] approximate the total rate of 3BR up to the cut-off level to be:

$$k_{3BR} = \alpha \, \mathcal{N}_{cut}^5 \, n_e^2 / 5T^2. \tag{5.2}$$

In view of this rate, 3BR is dominant under two conditions - when the plasma electron density is high and when the electron temperatures are lowered, i.e. during the cooling of the cluster. If the probe arrives at the optimal delay, the coupling of the probe to the electron-ion system is at its best due to resonant interaction. Hence, the probe is most efficient under these conditions in, (a) removing electrons that have recombined into excited states of ions due to 3BR and (b) outer-ionization of quasi-free electrons trapped in the cluster potential. Past the optimal delay, the electron density in the cluster falls to sub-critical levels so that the interaction with the probe is no more resonant. Thus, 3BR resumes domination over the action of the probe pulse for durations larger than the optimal delay till the eventual cluster disassembly. The effect of varying the probe intensity is shown in figure 5.7. Evidently, the optimal delay decreases for increasing probe intensities, it falls from ≈ 700 to ≈ 575 fs as the probe intensity is increased from 0.3× to 7×10^{14} W·cm^{-2} as is seen in figure 5.7 (b). We contrast this to the increase of optimal delays from ≈ 325 to 575 fs as the pump intensity is varied in a similar range with a constant probe at 7×10^{14} W·cm^{-2}. Thus, the apparent contradiction between figures 5.6 (b) and 5.7 (b) is now resolved. In the process, the role of the pump, namely inner-ionization, and the role of the probe pulse in the recombination dynamics and outer-ionization have been made clear.

5.2 Doping dependence and kinetic energy measurements

In the preceding section we saw that doping level plays an important role in the delay-dependent behavior. We may expect that the influence of DII observed un-

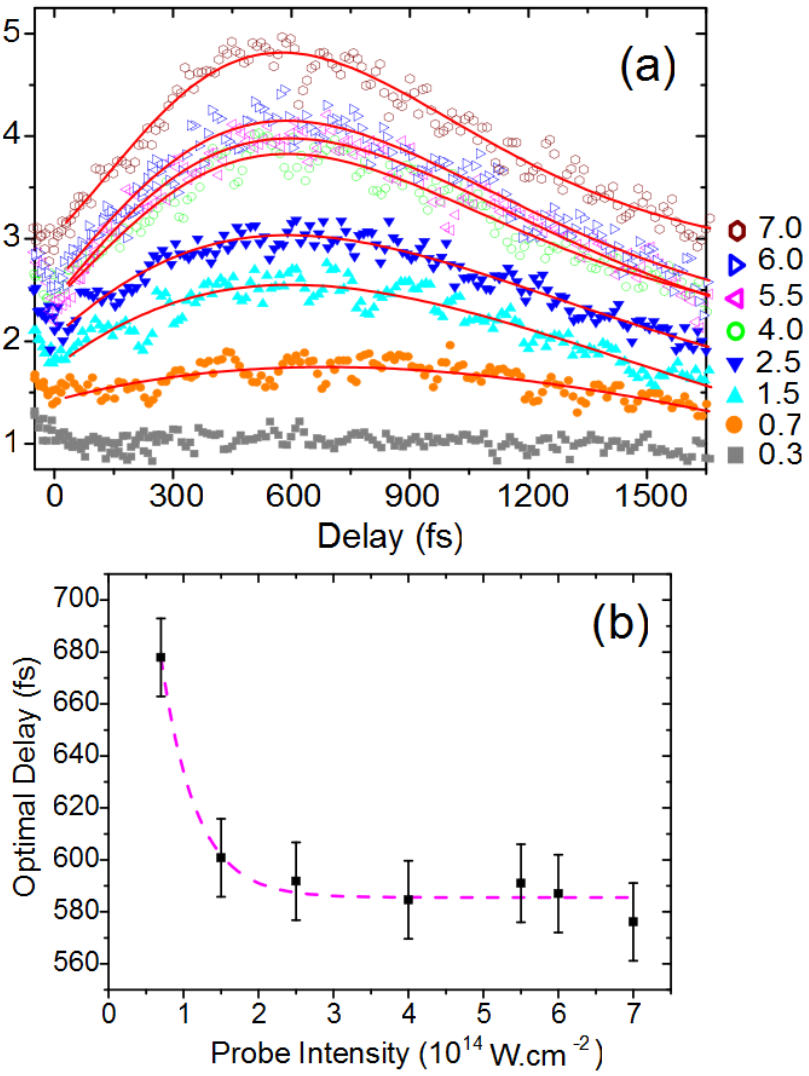

Figure 5.7: For the same doping level as in 5.6, (a) presents the He^{2+} ion yields as a function of pump-probe delay, with fifth-order polynomial fits (red lines), for different probe intensities as indicated in the legend in units of $10^{14}\,\mathrm{W{\cdot}cm^{-2}}$ for a constant peak intensity of the pump, $7\times10^{14}\,\mathrm{W{\cdot}cm^{-2}}$. Panel (b) is a plot of optimal delays vs. probe intensity (line to guide the eye).

der single-pulse illumination may also manifest in the pump-probe dynamics. We examine this closely in the current section. We will explore both, integral ion yields and kinetic energy spectra as we did in the single-pulse case (cf. section 4.3).

First, we take a look at the kinetic energy release (KER) spectra of He^{2+} ions which result from the interaction of Xe doped He nanodroplets with 15000 atoms when exposed to identical $\sim 10\,\mathrm{fs}$ pulses of peak intensity $7 \times 10^{14}\,\mathrm{W{\cdot}cm^{-2}}$. These are presented in figure 5.8. In this section we will consider the same laser pulse conditions and nanodroplet size throughout. The two-dimensional (2D) color plots, with the number of doped Xe atoms K_{Xe} indicated within, show two distinct features one at low kinetic energies $\lesssim 40\,\mathrm{eV}$ and another at high kinetic energies $\approx 100\,\mathrm{eV}$. The appearance of the two features displays itself in the shape of individual KER distributions. These contain a prominent "knee" which was described in detail in section 4.3 and a low-energy part. The 2D plots are differential KER distributions. The cumulative average ion kinetic energy for the case of 11 Xe dopant atoms within the droplet is shown in panel (e) of figure 5.8 which again has an evident "knee". In contrast, the KER distributions of He^{+} ions as a function of pump-probe delay (figure 5.9) are comparatively featureless and the absence of the "knee" in these distributions is evident in the cumulative average presented in the left panel. We will continue to focus on the He^{2+} ions in the same way as before.

Let us examine the pump-probe delay dependence of He^{2+} ion yields which are obtained by integrating over all the kinetic energies for each doping number. Figure 5.10 presents these for a few typical doping levels. Apart from the overall increase in ion yields, it is clear that the optimal delay also changes with the number of Xe dopants per nanodroplet. From 2D plots for each value of Xe doping number, we can extract KER resolved optimal delays. We obtained the optimal delay for a given KER as follows. We determined the cumulative average of ion yields as a function of pump-probe delay over a $\pm 10\%$ energy window about the desired KER value. The optimal delays were obtained from these delay-dependent yields for the 3 KER values specified in figure 5.11. These are chosen to represent the region of the "knee" ($\approx 100\,\mathrm{eV}$), the low-energy region ($\lesssim 15\,\mathrm{eV}$) and the region between the two ($\approx 40\,\mathrm{eV}$). We notice that the the optimal delay increases for doping numbers $1 \cdots 10$ and that it saturates at different values depending on the ion kinetic energy for doping number in excess of ≈ 10, which immediately reminds us of DII discussed earlier. In section 5.1 we emphasized the roles of the pump and the probe pulses in the two-pulse ionization dynamics. We associated the pump with inner-ionization and the probe with recombination and outer-ionization [PF10]. Probe absorption by the nanoplasma is delay-dependent [MSR08]. The probe couples to the nanoplasma most efficiently at the optimal delay. The value of the optimal delay is determined by the initial electron density after the interaction with the pump according to equation 5.1. The dependence of electron density on doping is implicitly determined by DII. Thus, DII indirectly controls the optimal delay as a function of doping.

In the context of the observation of DII under single-pulse illumination this observation is both crucial and redeeming. The numerical simulations that discovered the cigar-shaped nanoplasma resonance which is responsible for DII [MSR09] and those performed to go hand in hand with our experiments [KFK+11] do not take recombination into account. However, recombination does occur in the experiment.

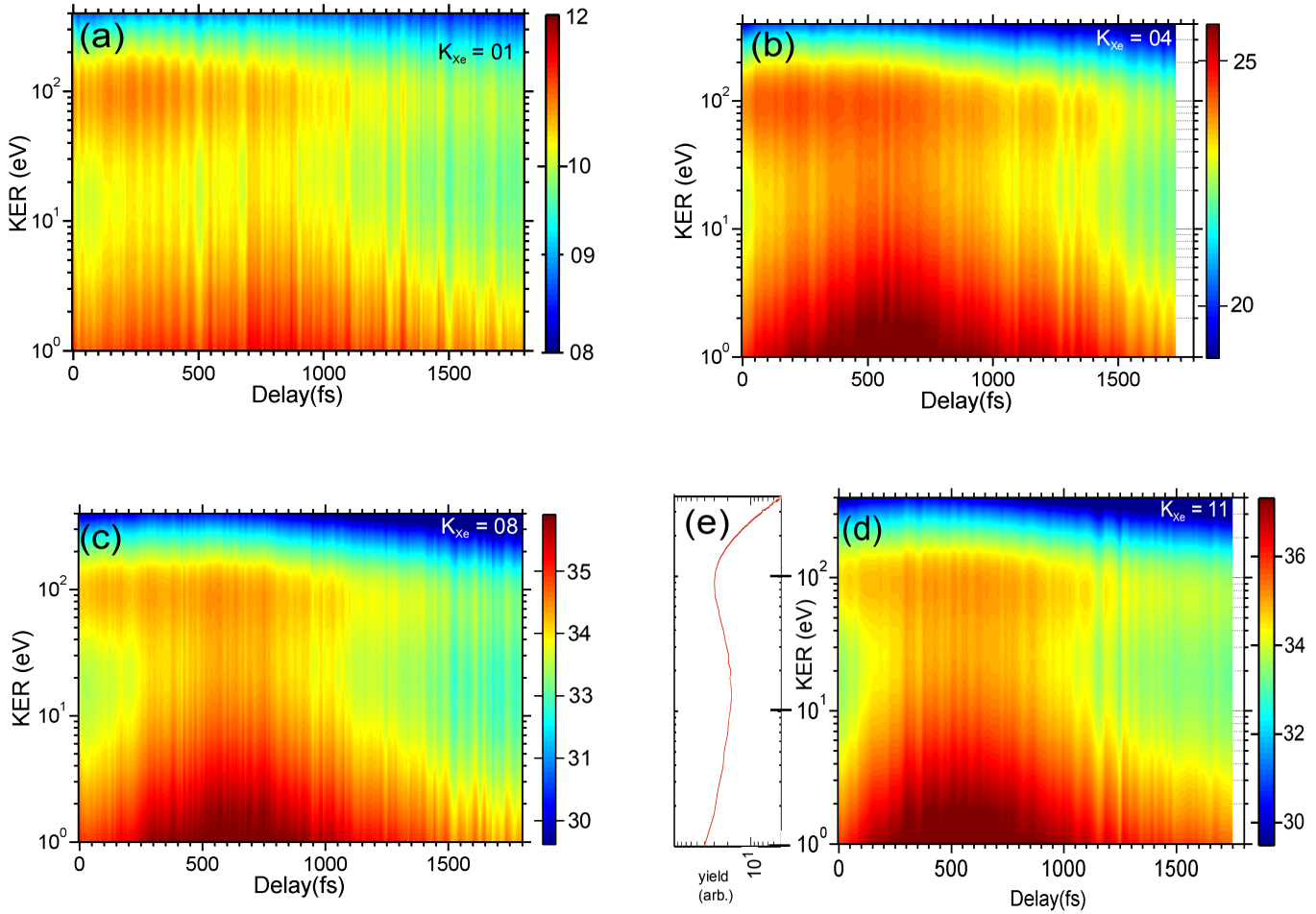

Figure 5.8: Kinetic energy release (KER) vs. pump-probe delay. Panels (a) - (d): KER spectra of He^{2+} ions for various Xe doping levels (K_{Xe}) in a He_{15000} droplet are presented as function of pump-probe delay when both the $\sim 10\,fs$ pulses have the same peak intensity ($7 \times 10^{14}\,W{\cdot}cm^{-2}$). The number of Xe dopants K_{Xe} in each case is also shown in these panels. The color scales indicate relative ion yields in arbitrary units. Panel (e): Cumulative average of ion yields as a function of KER corresponding to panel (d). We note the similarity of this KER distribution to figure 4.13.

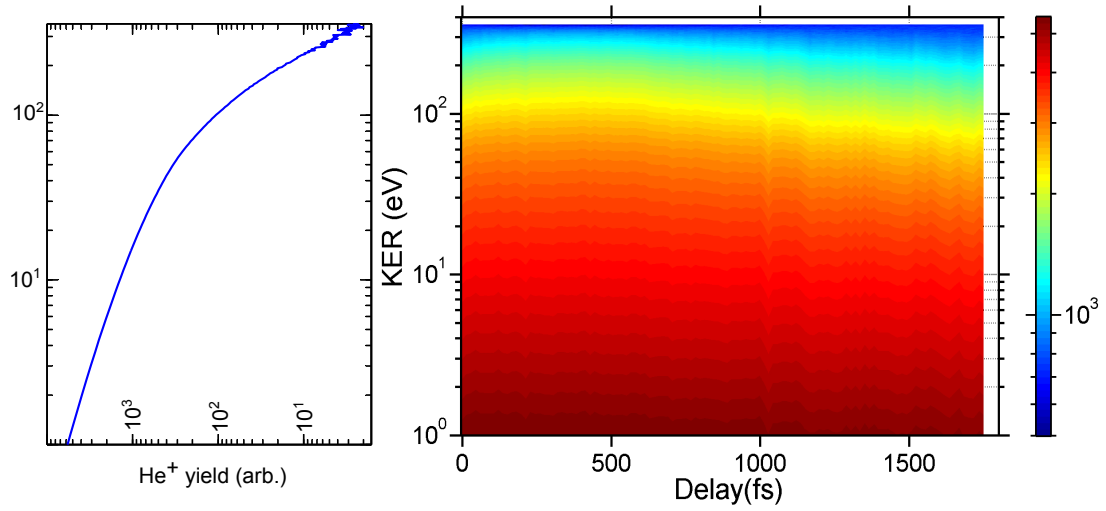

Figure 5.9: (right) KER distributions of He^+ ion as a function of pump-probe delay for doped nanodroplets (Xe_{11}@He_{15000}) under conditions identical to those in figure 5.8. (left) Cumulative average of ion yields as a function of KER obtained by averaging over all delays in the right panel. We note the similarity of this distribution with the corresponding one for the single-pulse case in figure 4.13.

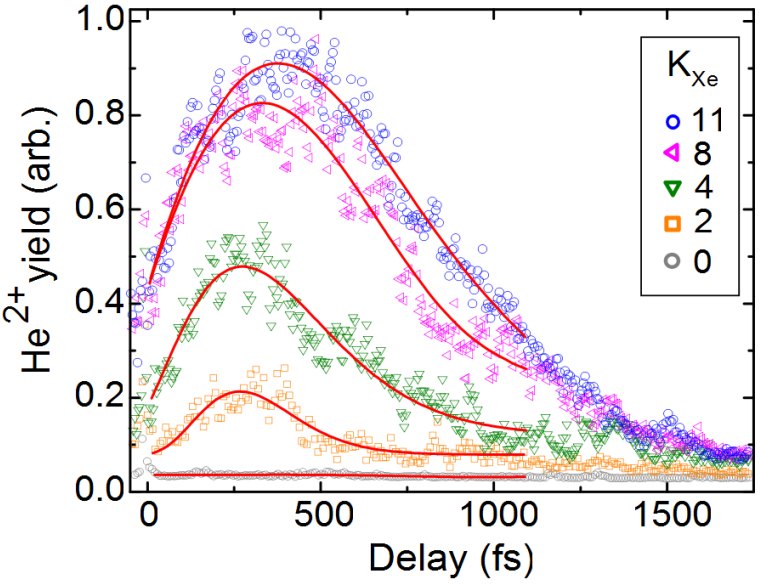

Figure 5.10: He^{2+} ion yields integrated over all kinetic energies for different Xe doping numbers (legend) as a function of pump-probe delay under conditions identical to those in figure 5.8. The lines are fifth-order polynomial fit to the peak region.

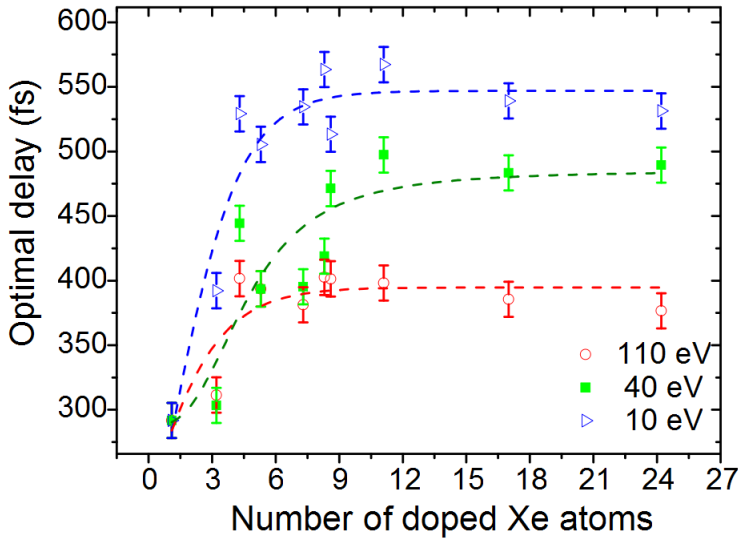

Figure 5.11: Optimal delays for He^{2+} yields from Xe_{11} doped nanodroplets under conditions identical to figure 5.8 for 3 different ion kinetic energies 10 ($\pm$1) eV, 40 ($\pm$4) eV and 110 ($\pm$11) eV. Lines to guide the eye.

Further, experimental averaging effects - over intensity, doping and size distribution - also cannot be accounted for in simulations. These observations on long timescales where recombination and other dissipative processes like cluster cooling and evaporation of electrons from the cluster potential take place, emphasize that DII is a robust phenomenon. This is also seen by comparing normalized KER distributions at selected two-pulse delays as shown in figure 5.12. The ion yield at a KER of 0.5 eV was normalized to the same value for all the curves. The black line shows the single-pulse case, while longer pulse delays are also shown. The qualitative similarity, albeit on a double logarithmic scale, reinforces the fact that dopant-induced ignition has long-lasting effects on the nanoplasma.

We may contrast the robustness of DII to the very brief resonance occurring in pristine rare-gas clusters during the build-up of the nanoplasma in the leading edge of an ionizing laser pulse as the cluster charge density grows from zero (all neutral atoms) to overcritical densities [Saa06, SR03, SSR06, FMBT$^+$10, MMP01]. This is also referred to as an "avalanche" [FMBT$^+$10] and is avoided in metal clusters. Electrons in the conduction band of metals form a plasma that is over-dense for visible and NIR frequencies. This brief resonance does not survive long enough to cause a significantly large absorption of the laser pulse as in the case of the expansion-induced resonance or DII. Hence, this brief resonance is not robust. It is important to distinguish this from DII which occurs on similar timescales.

We examine the change in optimal delay with increasing ion KER in greater detail by looking at a single value of Xe doping ($Xe_9@He_{15000}$). Figures 5.13 and 5.14 (a), show the delay dependence of KER-resolved ion yields for selected values of ion kinetic energies and the optimal delays extracted from these curves, respectively. The decrease in optimal delays with increasing KER is obvious. The optimal delay for ions with higher KER ($\geqslant$ 100 eV) is smaller than that for ions with low KER ($\leqslant$ 50 eV). In view of the discussion in section 5.1.2 (cf. figure 5.1.2 there), we

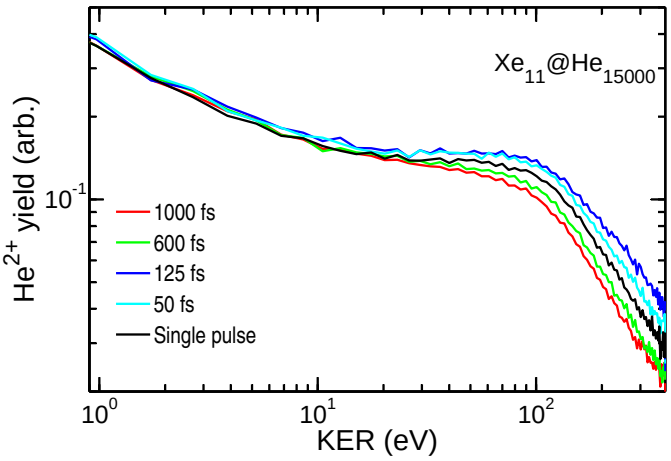

Figure 5.12: Normalized KER distributions for $Xe_{11}@He_{15000}$ droplets comparing the single-pulse case with that of various selected pump-probe delays for excitation by identical pulses with a peak intensity of $7 \times 10^{14}\,\mathrm{W{\cdot}cm^{-2}}$. The ion yield at a KER of 0.5 eV was normalized to the same value for all the curves.

may note that a simultaneous variation of pump and probe intensities resulted in a variation of optimal delays in the range of $\approx 550 - 700$ fs, whereas in KER-resolved measurements the τ_{opt} assumes values between $\approx 375 \ldots 560$ fs. Therefore, intensity averaging effects cannot account for systematics in KER-resolved measurements. Explaining this trend requires a closer look at mechanisms occurring within individual clusters.

As mentioned before, the numerical studies of Mikaberidze et al. [MSR08] and Peltz et al. [PF10], have pointed out the occurrence of a double-resonance in $Xe_K@He_N$ clusters. In such two-component clusters, two expansion-induced resonances are possible. We recall that (cf. section 2.2.2) nanoplasma resonance on sub-picosecond timescales occurs on account of the expansion of the ionic background which dilutes the electron density from over-critical to resonant densities. While in a pristine cluster this can occur only once, in composite $Xe_K@He_N$ clusters this occurs twice due to the fact that the expansion velocity of the He shells is different from that of the nanodroplet core containing the embedded Xe cluster. The He ions expand fast leading to resonant electron densities in the corresponding shells. This is followed by a slow expanding Xe cluster reaching critical densities at the inner regions of the nanodroplet. The effect of this double-resonance is seen in both the numerically determined absorption rate and the electron kinetic energy spectra presented in panels (b) and (c) of figure 5.14, respectively. These have been adapted from refs. [MSR08, PF10] for illustration.

Returning to our observations, we see that ions with kinetic energies $\gtrsim 100$ eV, the "knee" region and beyond, have similar optimal delay values ≈ 400 fs while low-energy ions have significantly higher optimal delays. This strongly suggests that ions resulting from fast Coulombic explosion of outer He shells have different velocities compared to the slower quasi-neutral inner shells. The expansion of the inner shells is governed by the ability of the dopant cluster to trap quasi-free electrons. The charge in the dopant cluster can influence the trapping of electrons well beyond its

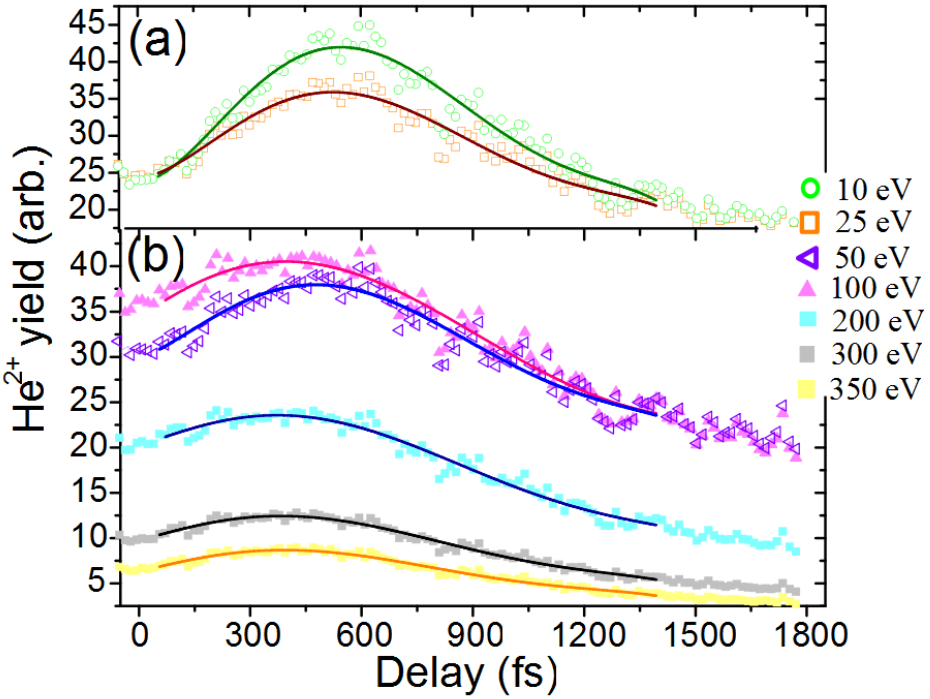

Figure 5.13: He^{2+} ion yields as a function of pump-probe delay for ions with different kinetic energies as indicated in the legend. The curves are shown in two different panels to avoid overlapping points, with fifth-order polynomial fits to the data points. Doped droplets ($Xe_9@He_{15000}$) were exposed to pump and probe pulses of the same peak intensity $7 \times 10^{14}\,\mathrm{W \cdot cm^{-2}}$.

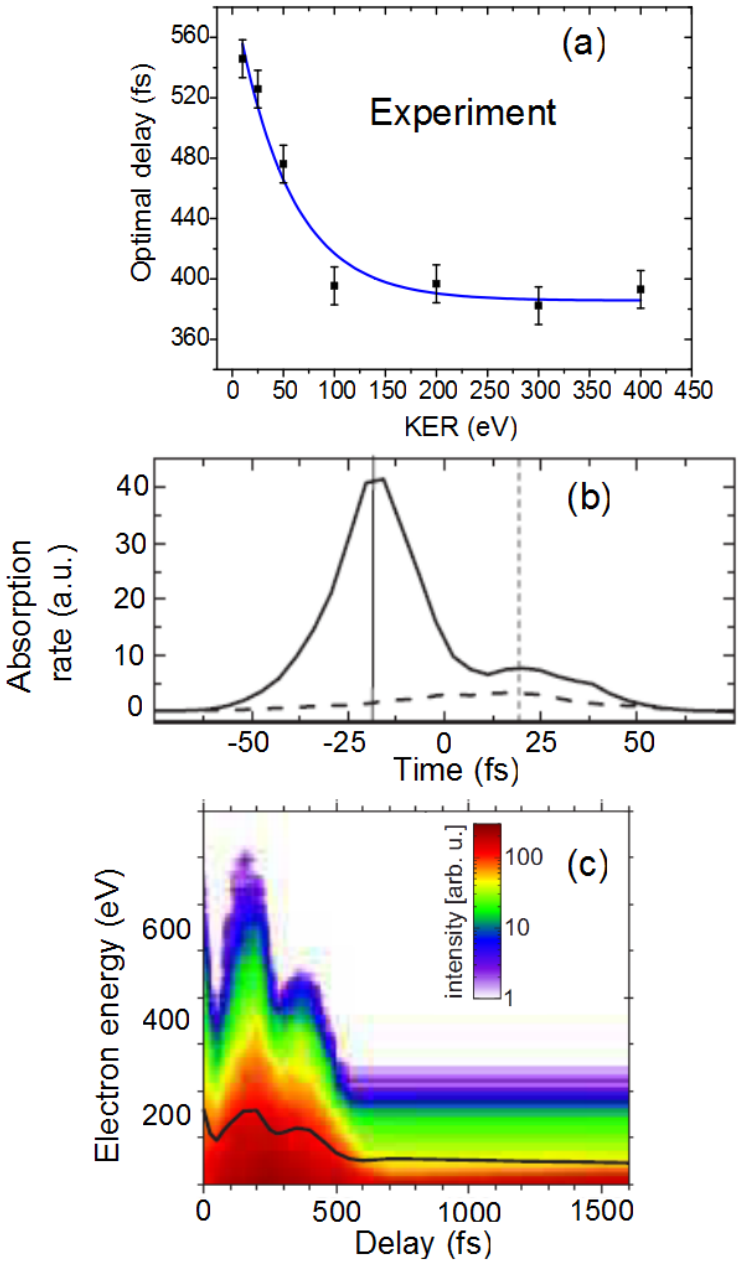

Figure 5.14: (a) KER dependence of optimal delays for $Xe_9@He_{15000}$ nanodroplets obtained from the curves in figure 5.13. Line to guide the eye. (b) Calculated energy absorption rate of $Xe_{100}@He_{1000}$ droplets for the excitation by a 200 fs pulse of peak intensity of $3.5 \times 10^{14}\,\mathrm{W{\cdot}cm^{-2}}$ (780 nm) (solid line) and free Xe_{100} clusters (dashed). Adapted from ref. [MSR08]. (c) Electron kinetic energy spectra from $Xe_{308}@He_{10000}$ clusters exposed to two 25 fs pulses of peak intensity $2.5 \times 10^{14}\,\mathrm{W{\cdot}cm^{-2}}$ as a function of delay between them. The color scale showing electron yields (arb. units) increases from blue to red and the average electron kinetic energy is the black line. Adapted from ref. [PF10].

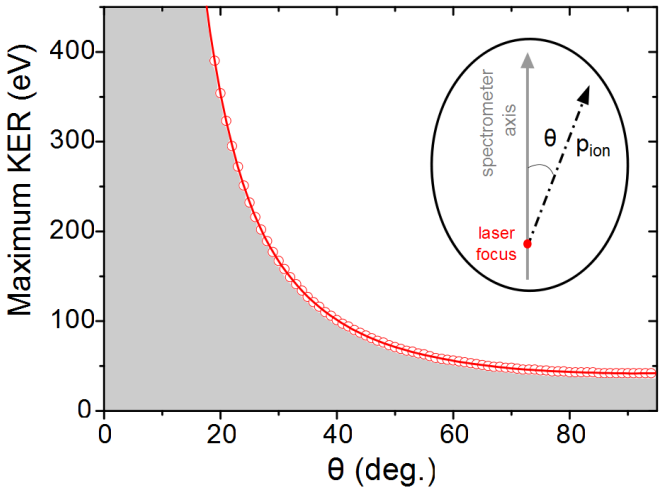

Figure 5.15: Maximum ion KER accepted by the TOF spectrometer described in section 3.4 as a function of the angle θ between the spectrometer axis and initial ion momentum $\boldsymbol{p}_{\text{ion}}$. The inset illustrates this geometry. The data points (red circles) were obtained from a SIMION simulation of the TOF spectrometer and the red line running through the points is an interpolated curve.

tiny geometric extent. We pointed this out in the discussion on field-ionization in the single-pulse case (cf. section 4.2.1). Thus, local plasma expansion at the dopant core and the He shells in its immediate surrounding is slowed down due to the high ionic charge of the dopant atoms at the center of the droplet. Thus, a double-resonance is possible. These qualitative conclusions can be better justified by more detailed studies - measurement of electron kinetic energy spectra and possible correlations between the delay-dependent behavior of the He ions and the dopant ions. It is relevant here to note that state-of-the-art X-ray free electron lasers can produce diffraction images on fs timescales with nanometer scale targets including rare-gas clusters and investigations are underway currently to study ionization dynamics combined with atomic scale imaging [TGB11, GCA+10, RPS+11]. They will provide more direct information on local electron and ion densities in the near future.

5.3 Anisotropic ion emission and cluster disintegration

We can obtain information about cluster fragmentation by comparing measured ion kinetic energies as a function of the angle between the laser polarization axis and the symmetry axis of the TOF spectrometer. We recall that ion yields and kinetic energies are measured in this study by using a TOF mass spectrometer employing the Wiley-McLaren configuration (figure 3.16) as was described in detail in section 3.4. Due to the electric fields applied in the TOF spectrometer, not only ions with momentum parallel to the spectrometer axis but also ions with a non-zero momentum orthogonal to this direction are focused onto the detector. The angular acceptance of the spectrometer is finite and depends on the initial kinetic energy release (KER) which the ion carries from cluster fragmentation. The geometry is

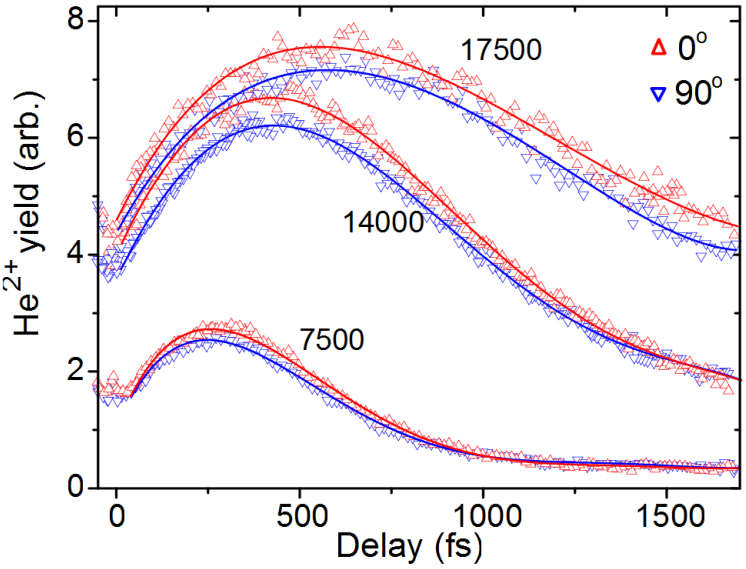

Figure 5.16: He^{2+} yields as a function of pump-probe delay in the 0°- and 90°-configurations (legend) for different droplet sizes - 7500, 14000 and 17500 He atoms per droplet as shown in the labels. In all cases the droplets were doped with 14 (±2.8) Xe atoms. Both, pump and probe pulses had the same intensity (7×10^{14} W·cm^{-2}) and direction of linear polarization. The lines are fifth-order polynomial fits with a goodness-of-fit better than 98%.

shown in the inset of figure 5.15. The angle made by the initial momentum vector $\boldsymbol{p}_{\text{ion}}$ with the spectrometer axis is θ. We simulated the particle trajectories in the spectrometer with the ion optics workbench - SIMION [Dah00]. The maximum KER of He^{2+} ions that is accepted by the spectrometer as function of θ is shown in figure 5.15. The range of acceptance is shaded in grey. In the experiment, we measure ion KER in two configurations: (i) When the laser polarization is along the spectrometer axis, the 0°-configuration, and (ii) when the laser polarization is perpendicular to the spectrometer axis, the 90°-configuration. From figure 5.15, it is clear that low-energy ions ($\lesssim$ 40 eV) will be accepted by the spectrometer for all values of θ. For $\theta = 45°$, the maximum ion KER accepted by the spectrometer is 85 eV. The TOF spectrometer measuring arrival times employed by us can only measure the longitudinal momentum component along the spectrometer axis. An ion with a total kinetic energy of 85 eV released at 45° arrives has the same time-of-flight as an ion with a kinetic energy of $\approx$ 60 eV with its total momentum vector parallel to the spectrometer axis. Hence, to obtain the He^{2+} ion yields presented in this section, we integrate all ions with kinetic energies greater than 60 eV.

In this context, we note that most previous studies on the polarization dependence of intense NIR laser ionization of rare-gas clusters employed TOF spectrometers without extraction fields (see e.g. [KKM01, HSM$^+$05]). In these experiments, huge ion KER ($\gtrsim$ 10 keV) resulting from cluster explosion, and the limits on time resolution and electrode voltages possible in practice inhibit the use of conventional TOF spectrometers employing the Wiley-McLaren design [WM55] to discriminate different ionic species. Magnetic field assisted TOF [LDNS98] or imaging spectrometers of the Thomson parabola type [RRT$^+$11] are alternatives to overcome this limitation.

We now look at the He^{2+} yields as a function of pump-probe delay in the 0°- and 90°-configurations as a function of droplet size when identical pulses with an intensity of $7 \times 10^{14}\,\mathrm{W{\cdot}cm^{-2}}$ were employed. The direction of the electric field vectors of the linearly polarized pump and probe pulses was kept parallel. Figure 5.16 shows the ion yields for both configurations for three different droplet sizes - 7500, 14000 and 17500 He atoms per droplet, doped with 14 Xe atoms in each case. As we also observed earlier in section 5.1.1 (figure 5.2), the width of the yield curves increases with droplet size. Clearly, the ion yield is greater for ions with KER $> 60\,\mathrm{eV}$ when the polarization of the pump and probe pulses is parallel to the spectrometer axis than in the orthogonal configuration. We noted earlier (cf. section 2.2.4) that the anisotropy in ion yields is a consequence of the anisotropic charging within the cluster. On account of the polarization force along the laser polarization direction, both the expansion and explosion of the cluster are anisotropic. The anisotropy in the ion yields lasts throughout the cluster expansion process. Breizman et al. [BAF05] have emphasized that for large-sized clusters and moderate laser intensities such as those considered here, electrons with low kinetic energy trapped in the cluster play an important role in the anisotropic cluster expansion. This results in the local polarization force acting within the cluster (cf. section 2.2.4). Thus, the eventual disappearance of anisotropy in the ion yields at very large delays indicates that the composite nature of the cluster is destroyed. In this sense, we may call the duration over which the anisotropy lasts as the cluster life-time. In figure 5.16, we see that for droplets with 7500 and 14000 He atoms respectively, the anisotropy disappears for delay durations greater than ≈ 3.5 times the optimal delay time τ_{opt} ($\approx 250\,\mathrm{fs}$, in this case). Thus, τ_{opt} serves as a characteristic time for the entire dynamical process. Molecular dynamics studies [Saa06, FMBT$^+$10] have revealed that on timescales larger than that of the expansion-induced resonance, electrons in the under-critical plasma undergo slow adiabatic cooling as hot electrons evaporate from the cluster potential. The decay time of $\approx 2.5 \cdot \tau_{opt}$ in nanodroplets with 7500 and 14000 He atoms is in qualitatively agreement with the expected slow cooling observed in these simulations. Identifying such a timescale could be useful for extending the results of atomic scale simulations. It may be possible to correlate numerically determined nanoplasma properties such as charge density, electron kinetic energy distributions and ion charge-state distributions at the end of the cluster life-time ($\approx 3.5 \cdot \tau_{opt}$) to initial conditions, i.e. laser pulse and cluster parameters, similar to the work Breizman et al. [BAF05] on timescales $\approx \tau_{opt}$. Generic characteristics of the nanoplasma at the cluster life-time could serve as initial conditions for a treatment of dissipative processes occuring on sub- or few-nanosecond timescales by approaches tailored to suit these durations, e.g. rate-equations.

Figure 5.17 presents the yields of He^{2+} ions for nanodroplets containing 15000 He atoms doped with 16 (± 3.2) Xe atoms when exposed to pulses of varying intensities which are shown in the curve labels in units of $10^{14}\,\mathrm{W{\cdot}cm^{-2}}$. As observed earlier, in section 5.1.2, the optimal delay at this doping level increases with increasing intensities of pump and probe. The overall anisotropy of ion yields also increases with peak intensity. Once again, this points to the role of the polarization force in the anisotropic cluster expansion.

Next, we investigate the dependence of anisotropic ion emission on doping levels in

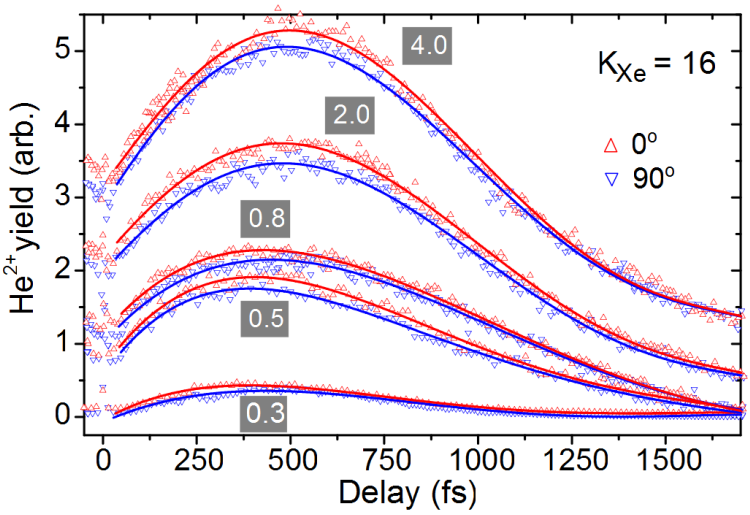

Figure 5.17: Intensity dependence of He^{2+} ion yields as a function of pump-probe delay when electric field vectors of both the linearly polarized pulses were parallel (0°) and perpendicular (90°) to the spectrometer axis, respectively. The curves are labeled by the peak pulse intensity in units of 10^{14} W·cm^{-2}, which was identical for both pump and probe. The droplets containing 15000 He atoms were doped with 16 (±3.2) Xe atoms. The lines are fifth-order polynomial fits.

the droplet. Figure 5.18 presents the He^{2+} ion yields as a function of two-pulse delay, for various values of Xe doping, K_{Xe}, in a droplet containing 15000 He atoms. In all cases, the doped droplets were exposed to identical pulses with a peak intensity of 7×10^{14} W·cm^{-2}. Panel (a) shows 3 doping levels up to 3.5 Xe atoms per droplet. In these cases, there is no conspicuous anisotropy in the ion yields. However, in the case of $K_{Xe} = 16$ (panel (b)) anisotropy is evident. The difference between the He^{2+} yield in the 0°-configuration ($Y_{0°}$) and the the 90°-configuration ($Y_{90°}$) is shown in panel (c). In addition we compare the two linearly polarized configurations to the case where the pump and the probe pulses are both circularly polarized. The conditions of laser intensity, droplet size and doping are identical in all three cases. The ion yield in the 90°-configuration is lower than for the circularly polarized case, whereas the yields in the 0°-configuration are higher at all delay times. This is also provides a cross-check for our claims thus far that the observed anisotropy is a consequence of the polarization force within the cluster. In the case of circular polarization, the action of the polarization force is symmetric in the two mutually orthogonal directions perpendicular to that of laser pulse propagation. Hence, it presents the case of isotropic emission. Recalling figure 4.2, we know that for low doping levels $K_{Xe} \leqslant 3.5$, complete ionization due to DII has not occurred after the interaction of the doped droplets with the pump pulse. Whereas, in the case of $K_{Xe} = 16$, DII ignites the entire droplet. Although for a doping level of $K_{Xe} = 3.5$ the expansion induced resonance is visible, there is no clear sign of anisotropic emission. Thus, DII is crucial to the observation of anisotropic ion emission under conditions of few-atom doping. DII changes the character of the nanoplasma drastically and this justifies using the term "ignition", as we have done throughout.

Examining the case of circular polarization also reveals the following surprise: The ion yields for circular polarization at all delay values for the $K_{Xe} = 16$ case, are

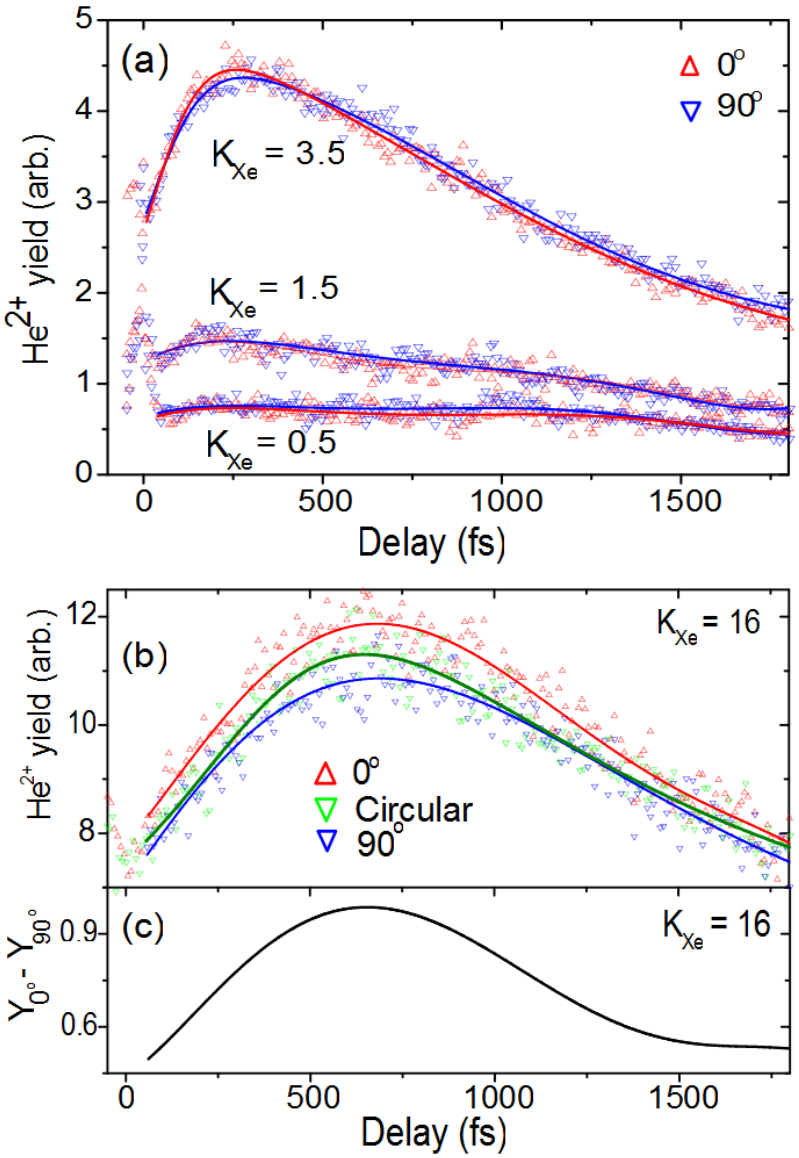

Figure 5.18: Pump-probe delay dependence of He^{2+} ion yields for increasing levels of Xe doping, K_{Xe}, within a droplet containing 15000 He atoms. Identical pulses with a peak intensity of $7 \times 10^{14}\,\mathrm{W{\cdot}cm^{-2}}$ were used in all cases. Panel (a), shows ion yields for doping levels up to 3.5 Xe atoms per droplet. (b) Anisotropy ion yield is present for the case of $K_{Xe} = 16\,(\pm 3.2)$. The green data points and fit curve shows ion yields for excitation by a circularly polarized pulse of the same intensity as before. (c) The difference in the ion yields between the 0°-configuration ($Y_{0°}$) and the 90°-configuration ($Y_{90°}$) obtained from the fitted curves in panel (b).

sandwiched between the yields for the 0^o- and 90^o-configurations. We have argued that DII is necessary for polarization dependent ion emission in the case of linearly polarized pulses. We observe that the ion yields for the circularly polarized case are correlated to the linear polarized case at each value of pump-probe delay. Thus, we may conclude that DII should have occurred during the interaction with the circularly polarized pump pulse. In view of the discussion in section 4.2.1, we may expect that DII is suppressed when ionization is caused by a circularly polarized pulse. A cigar-shaped nanoplasma will not be formed in this case for obvious reasons. However, on the basis of MD simulations, Mikarberidze [Mik11] has pointed out that DII occurs even during the excitation by single circularly polarized pulses. In this case, the nanoplasma formed within the doped droplet is not cigar-shaped, instead it is pan-cake or disc shaped. The eigenfrequency for oscillations parallel to the face of the pan-cake decreases as its diameter increases. This enables a resonant interaction with the laser pulse for a sufficiently large diameter of the nanoplasma pan-cake, very much as in the cigar-shaped case. We leave it for future investigations employing single circularly polarized pulses to examine the pan-caked shaped nanoplasma in greater detail.

Summary

In this chapter we have presented the results of pump-probe studies with intense 10 fs NIR laser pulses on rare-gas doped He nanodroplets. First, we examined the pump-probe delay dependence of integrated He^{2+} ion yields as a function of the nanodroplet size at a constant doping level. The optimal delay τ_{opt} increases with the size of the He nanodroplet. This clearly establishes the important role of the fast expanding He shells in the nanoplasma dynamics. These He shells are active participants in the dynamics. In spite of the significantly higher ionization potentials of He, the He shells are not passive or secondary contributors to the dynamics as some previous experimental investigations have concluded [DDP+07]. We examined the role of the laser intensities on integrated ion yields, by a simultaneous variation of the pump and probe intensities as well as by varying the ratio between them. In the limit of weak doping (up to ≈ 20 Xe atoms per droplet), for the case of simultaneous increase of pump and probe intensities, we found that optimal delays increased with intensity. The same is the case when the pump intensity is varied with the probe intensity held constant. We interpret these observations in conjunction with the fact that DII occurs during the interaction with the pump pulse. Since DII ensures that all He atoms in the droplets are completely ionized after the interaction with the pump, we conclude that the slow-down of droplet expansion leading to higher optimal delays results from increased charging of the Xe atoms at the center of the droplet. This is also in conjunction with the observations in numerical simulations of Mikaberidze [Mik11]. The trend is reversed when the doping is strong (≈ 29 Xe atoms per droplet) - optimal delays decrease with the simultaneous increase in the pump and probe intensity. For strong doping, this observation agrees with previous studies performed on large metal clusters (about 80 Ag atoms) in He nanodroplets [DTD+03]. From studies where the ratio of the pump and probe intensities is varied we interpret their roles as the following: The effect of the pump pulse can be understood by its role in causing inner-ionization. The probe is responsible for

modifying the recombination dynamics which occurs at long time delays after the interaction with the pump pulse. Thus, the probe is responsible for a secondary ionization that releases recombined electrons from excited states and for causing increased outer-ionization.

Once these facts are established, it is easy to understand the doping dependent pump-probe studies. We examined full KER spectra of He^{2+} ions as a function of the pump-probe delay. This allows us to examine differential ion yields at particular KER intervals as a function of delay. We find that the optimal delay is dependent on the KER of the ions for a given doping level. The variation of the optimal pump-probe delay with doping number also shows a step-like feature similar to that of ion yields under single-pulse excitation. We understand this in terms of the variation of nanoplasma electron densities resulting from the interaction with the pump pulse during which DII occurs. KER resolved measurements also indicated a possible double-resonance during the expansion of these composite clusters. The expansion of the outer He shells is significantly faster than the expansion of the dopant ion core.

Finally, we examined the anisotropy in ion emission by comparing the yields of He^{2+} ions in the 0^o- and 90^o- configurations. Whereas for doping up to 3.5 Xe atoms per droplet ion emission was isotropic, the ion yields for the 0^o-configuration were higher than for the 90^o- configuration when the doping level was 16 Xe atoms per droplet. Anisotropic ion emission is a result of asymmetric charging and expansion of the nanodroplet after its interaction with the pump. The role of the doping level in determining the anisotropy is again linked to DII. We compared the case of circularly polarized pump and probe pulses with the two linearly polarized configurations (0^o and 90^o) without changing the pulse intensity. The ion yields in the circularly polarized case were always higher than the 90^o-configuration while remaining lower than the 0^o case. This confirms that the anisotropy results from asymmetric charging in individual clusters. Since the occurrence of DII during the pump pulse is a pre-requisite for observable anisotropy in ion emission from weakly doped droplets, we may conclude that DII also ignites the droplet during its interaction with the circularly polarized pump pulse. This agrees with numerical investigations performed with single circularly polarized pulses where the formation of a pan-cake shaped nanoplasma was seen to be the reason for droplet ignition [Mik11]. Experimental investigations on the ignition of doped He nanodroplets with single circularly polarized pulses are worthwhile prospects for the future.

Chapter 6

Conclusions and Outlook

6.1 Summary

Doped He nanodroplets in intense few-cycle NIR pulses have presented a very interesting case for the study of dynamics on timescales of electronic ($\sim$ 10 fs) and atomic ($\sim$ 500 fs) motion. The two important conclusions we may draw from our work discussed in Chapters 1 to 5 are: (i) The hitherto unobserved phenomenon of DII in He nanodroplets occurring on a 10 fs timescale due to the formation of a cigar-shaped nanoplasma has been uncovered in our studies by combined efforts in experiment and theory, and (ii) the impact of a few dopant atoms, less than 10, on the ionic expansion induced resonant dynamics of large ($\sim 10^4$ atoms) droplets was investigated.

In the first part of this dissertation (Chapters 2 and 3), we introduced and motivated intense NIR field-ionization of rare-gas clusters. We emphasized the expansion-induced resonance absorption which is unique to mesoscopic nanoplasmas formed in these targets. The main results of the studies performed thus far on ion, electron and characteristic X-ray emission from these nanoplasmas, and the mechanisms behind them were discussed. The general methods adopted to generate rare-gas clusters for such studies and the specific details of our He nanodroplet source were presented in Chapter 3. We described the details of the doping process and the formulation used to estimate doping levels. Then, the TOF spectrometer and the laser system used in the complete experimental set up were elucidated.

In Chapter 4, we reported the results from our studies on the ionization of He nanodroplets doped with a well-controlled number of Xe, Kr or Ar atoms by intense 10 fs pulses with a central wavelength of 790 nm. The ignition of these droplets as a result of a resonant interaction with these pulses due to the formation of a cigar-shaped nanoplasma was observed. This resulted in the saturation of droplet charging and ionization of all the $\sim 10^4$ He atoms caused by just a few, less than 10, dopant atoms. This was appropriately called dopant induced ignition (DII). DII was found to be insensitive to the size of the He nanodroplet. However, a large number of dopants was required to trigger DII when lower pulse intensities or dopants with higher ionization potentials were used. In all these cases, the laser pulse intensity was chosen such that only the dopants were directly ionized by the laser field. This established the fact that a critical number of electrons

released from the dopants initiate the DII process. MD simulations performed under conditions identical to those of the experiment revealed that a transition from the field-ionization (FI) regime to the DII regime occurred for pulses with a width of $\approx$ 10 fs or more at this peak intensity (7×10^{14} W·cm^{-2}). Static FI of He atoms is caused by the electric field of the dopant ions at the droplet center which suppresses the Coulomb barrier in the surrounding He atoms. Prior to our studies, the only mechanism for resonant interaction between electrons in rare-gas cluster nanoplasmas and the driving intense NIR field relied on the expansion of the cluster due to ionic motion occurring on sub- or few-picosecond scales. Thus, the observation of DII has demonstrated very efficient absorption by the nanoplasma on the timescale of 10 fs. Numerical studies go on to predict the suppression of DII for pulse lengths $\lessapprox$ 7 fs and the domination of DII for pulse durations $\gtrapprox$15 fs.

The impact of few dopant atoms on the expansion-induced resonance of He nanodroplets was detailed in Chapter 5. These pump-probe studies employing two 10 fs pulses emphasized the important role of the He atoms in expansion-induced resonance of this composite system. This two-component plasma expands with two characteristic velocities. The outer shells consisting of He atoms expand fast. Consequently, the local electron density in this region becomes critical at 790 nm. This is followed by the slow expanding core containing dopant ions becoming resonant with the frequency of the driving laser field. The rate of expansion of the core is determined by the charging of the dopant ions. The optimal delay for the maximization of He^{2+} ion yields was crucially dependent on the number of dopant atoms in the nanodroplet. The variation of the optimal delay with the doping level was found to be very similar to that of the ion yields as a result of DII found in single-pulse studies. Thus, the influence of DII on the expansion-induced resonance was established. DII governs the electron densities in the nanoplasma after the pump pulse interacts with droplet. Consequently, the optimal delay is indirectly controlled by DII. The pump pulse is responsible for determining the level of inner-ionization in the nanoplasma, while the probe strongly modifies the recombination dynamics and causes outer-ionization. These studies have revealed the critical importance of doping on the short timescale ($\sim$ 10 fs) and the sub-picosecond dynamics of cluster nanoplasmas. Previous investigations on rare-gas and metal clusters grown in He nanodroplets [DDP$^+$07, DMP$^+$10] concluded that the role of the He shells in the atomi expansion of the nanoplasma was determined to be incidental and secondary. Not only did our studies prove that the dopant atoms are crucial to the ionization of the droplets, but also that they show conclusively that He plays an important role in the expansion-induced dynamics and the expansion velocity of the He shells plays a major role in determining the optimal time τ_{opt} when resonance occurs. These results present the urgent and compelling need for a revised view of intense NIR field-ionization dynamics of doped He nanodroplets and two-component clusters in general. We will suggest few ideas for future investigations and also point out open questions that remain to be answered by experiment and theory.

6.2 Outlook and perspectives

In figure 6.1 we compare the pump-probe delay dependence of He oligomer ion yields with that of $He^+$and He^{2+} ions from Xe_{16}@He_{15000} clusters. This indeed

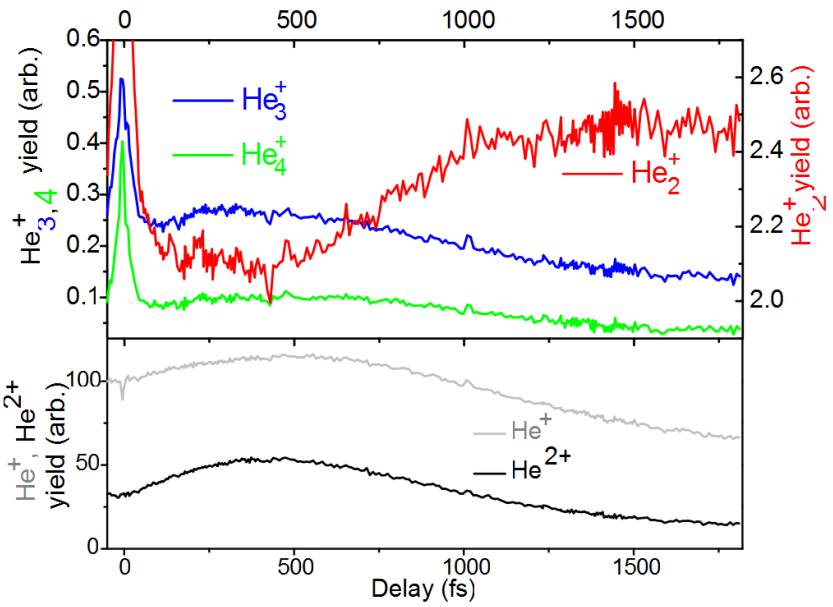

Figure 6.1: Yield of monomer and oligomer ions as indicated resulting from the interaction of $Xe_{16}@He_{15000}$ with identical pump and probe pulse of 10 fs with a peak intensity of $7 \times 10^{14}\,W \cdot cm^{-2}$.

presents a curious case. While, He_3^+ and He_4^+ ion yields have a delay dependence similar to that of $He^+$and He^{2+} ions, the delay dependence of the He dimer ion yields is entirely different. Different reaction channels can contribute to formation of the stable dimer ion. The trimer, the tetramer and higher order oligomers can fragment into the singly charged dimer and monomer states [HIFT95]. This is a possible channel for the dimer ion formation. It should be noted that the total binding energies of dimer and trimer ions for fragmentation into monomer species is less than 3 eV and is similar for larger cluster ions [HIFT95]. However, we saw in the preceding discussions that the energy per atom transferred from the laser field to the doped nanodroplets is much greater (e.g. section 4.3). The ponderomotive energy of the quasi-free electrons under probe excitation is at least 10 eV. It would be reasonable to expect that the weak bonds are destroyed under the action of the probe pulse either by electron impact or by barrier suppression. On the contrary the dimer ion signal grows with time at delays greater than 500 fs. But the generation of oligomer ions is not an isolated case of low-energy processes occurring in intense NIR field-ionization of various micrometer or nanometer sized targets. Formation of negative ions with similarly low binding energies has been reported in several cases [TARB$^+$11, TASBN04, NFY$^+$09]. However, mechanisms like Coulomb implosion proposed in some studies [NFY$^+$09] have been found insufficient to explain others [TASBN04]. Thus, several questions about basic processes going on during plasma relaxation and cooling remain open.

In our experimental campaign, we did not measure electron kinetic energy spectra due to technical reasons. Our interests lay in measurements on He ions and the design of the Daly detector was not suitable for measuring electrons. The efficiency of laser heating during DII will certainly have observable consequences on the electron spectra and provide valuable information about the process itself, in addition to ion KER measurements. Moreover, advances in femtosecond laser technology

have made it possible to generate few-cycle laser pulses with excellent control over the carrier-envelope phase (CEP) of the pulse [UHH02]. The importance of controlling the shape of the electric field within the envelope of intense few-cycle pulses and its consequences on the ionization dynamics of atoms and molecules has been demonstrated in several studies [GSM$^+$09, KFF$^+$09, FKP$^+$10]. Recently, a similar effect of CEP on electron emission from the ionization of dielectric nanospheres ($\sim$ 100 nm) was observed [ZFP$^+$11]. Asymmetric electron emission for energies about 60 times the ponderomotive energy of the laser pulse on account of CEP variation was measured. However, this study on pristine silica dielectric spheres was entirely non-resonant. In the case of two-component clusters we have demonstrated that a nanoplasma resonance builds up on the timescales of about 10 fs. The effect of CEP on this resonant charging mechanism is worth investigating. In this context, we should note that CEP effects are prominent only for pulses with a duration of $\approx$ 5 fs or less. Thus, two-pulse experiments employing 5 fs pulses with a very short delay between them will be required to study the CEP dependence of electron emission from DII.

The observation of DII with rare-gas doping has opened up the possibility of investigating resonant interactions on similar timescales with other easily ionizable constituents at the droplet center. Coinage metals would be an excellent choice for such studies since characteristics of doping large He nanodroplets with such atoms are well known [TS07, RDS$^+$05]. He nanodroplets containing rare-gas or coinage metal atoms at the center can be further decorated with alkali atoms on the surface by sequential two-stage doping [SL06]. The ionization of He atoms by laser driven electrons will occur both from the center going outwards as well as from the surface. Thus, the cigar-shaped nanoplasma may not be formed. This could possibly prevent the occurrence of DII. Such an observation would confirm the delicate dependence of DII on plasma morphology and possibly open a window to look at other effects occurring on similar timescales.

The formation of a cigar-shaped nanoplasma, which is the underlying reason for the occurrence of DII, results in the ultrafast absorption of the ionizing 10 fs pulse. This can be studied more explicitly and in greater detail by direct optical absorption measurements by employing a weak non-ionizing probe pulse. Apart from determining the attenuation of such a probe pulse, measuring the chirp induced on such a probe by the nanoplasma using standard FROG or SPIDER techniques [DR06] would give valuable information about the spectral properties of this nanoplasma. Recently, Köhn et al. [KF11] have also proposed schemes for investigating the resonant nanoplasma dynamics by a spectral interferometry technique similar to these techniques. Such approaches are relevant for investigating the frequency domain features of the cigar-shaped resonance. We may mention that the target used in our studies was too dilute and the particle density was not sufficient to perform such measurements. This effectively means that these measurements would have to be performed on the droplet beam close to the exit nozzle. The chamber that houses the nanodroplet source is necessarily at relatively high ambient pressures ($> 10^{-5}$ mbar). The controlled doping of droplets with foreign atoms by the pick-up method in such an environment requires careful and creative experimental design. Doping by laser ablation of a metal target or the use of a pulse nozzle may prove to be good strategies, if available.

An alternative way to perform optical studies on the cigar-shaped nanoplasma is by exploiting the inherently high densities in condensed media. Aggregates or impurities of a few dopant atoms in transparent host matrix can be formed *in situ* by careful synthesis procedures [WL97]. The cigar-shaped nanoplasma should also be formed around the embedded dopant aggregates in such media. However, care should be taken so that parasitic propagation effects such as pulse broadening or filamentation which may result from ionizing the host media themselves are avoided for realizing such scenarios. Much of this can be avoided by rendering these composite media into slices or as films significantly thinner than the Rayleigh range ($\sim 1\,\mathrm{mm}$), which is certainly possible. This also leads to a possible technological application. DII overcomes the need for atomic motion for resonant coupling with the laser field and leads to the ionization of atoms surrounding dopants. In optical media such plasma formation leads to a permanent refractive index change (or controlled damage). This is exploited in writing waveguides and other *in situ* structures in bulk transparent media using tightly focused femtosecond laser beams and is being investigated in several laboratories [GM08, THS$^+$03, EWH$^+$08]. Triggering DII using dopants in such media could not only enhance these effects but also localize them spatially, which is a desirable feature. Similar possibilities have also been proposed in the work of Mikaberidze [Mik11].

Helium nanodroplets provide enormous flexibility in designing composite dopant or embedded clusters which may not be possible by supersonic co-expansion of the constituents. In the case of He droplets a sequence of doping cells can be employed for nanoscale design [MKK$^+$09]. We propose a couple of studies with such targets: The use of very intense femtosecond pulses ($\sim 10^{17-18}\,\mathrm{W\cdot cm^{-2}},\ \sim 50\,\mathrm{fs}$) can lead to direct outer-ionization so that electrons overcome both the binding atomic and clusters potentials in one step before ionic motion sets in. As mentioned earlier (cf. section 2.2.4), this is the so-called cluster vertical ionization (CVI) scenario introduced in literature by Last and Jortner [LJ06]. Within the scope of CVI, lighter ions can overtake heavier ions during Coulomb explosion which correspondingly changes their kinetic energy distribution. Such effects can be studied unambiguously using clusters grown in He droplets. A straightforward design for such studies is to compare a composite three-component target H_2@Xe@He target to a D_2@Xe@He target (A@B@C means atoms of species A are at a core which is surrounded by shells of species B which are in turn surrounded by shells of C). One can even go so far as to heavily dope the droplets to evaporate almost all He atoms in the doping process, resulting in composite clusters made only of the dopant species.

Nextly, it may be possible to align entire molecular clusters in such environments. Embedded dopants transfer their rotational energies to the He atoms leading to evaporative cooling so that the droplet becomes their personal/private cryostat (terminology due to Toennies and Vilesov [TV04]). The embedded molecular cluster could possibly be aligned adiabatically [SS03]. CVI of such aligned molecular clusters again can lead to visible effects in ion kinetic energy spectra [Mik11].

Speaking of target design, recent studies have shown that chemically synthesized nanoparticles with a very uniform size distribution can be delivered into a monodisperse jet with a carrier-gas at useful densities ($\sim 10^6\,\mathrm{particles/cm^3}$) using an aerodynamic lens system [WM06]. There is an urgent need for studies employing such targets since effects of cluster size distribution can be avoided. Using such targets

along with measurements involving focal volume scanning [DMP$^+$10] will help in getting rid of averaging effects which often make a direct quantitative comparison of atomic scale simulations with experiments impossible [SSR06, FMBT$^+$10]. This will be a significant step towards gaining a better overall understanding of the physics of intense field-ionization in such mesoscopic plasmas. With very short pulses, a counter-intuitive anisotropy in ion emission in few-cycle intense NIR pulses was observed [SETZ$^+$10]. Such scenarios should be very interesting for composite cluster systems with constituents of very different atomic masses.

This dissertation began with A. H. Zewail's spirited remark about the femtosecond world. Having watched nanodroplets on a femtosecond timescale, it is appropriate to close by recalling R. P. Feynman's words (in 1959) about the nanoscopic world: "There's plenty of room at the bottom" [Fey60]. Indeed, there is plenty of room for creative exploration in these tiny nanodroplets[1]!

[1]It is a pleasant coincidence that Feynman began this famous lecture with a reference to Kammerlingh Onnes: "I imagine experimental physicists must often look with envy at men like Kamerlingh Onnes, who discovered a field like low-temperature physics..."

Appendix A

Atomic Units

Here a few definitions and conversion factors related to the use of *atomic units* (a.u.) are presented. The base units of this system are related to the dimensions of the hydrogen atom.

Base units and natural constants

Quantity	Physical description
$r_e = 1\text{a.u.} = 5.2918 \cdot 10^{-11}\text{m}$	Bohr radius of the K-shell of hydrogen
$m_e = 1\text{a.u.} = 9.1095 \cdot 10^{-31}\text{kg}$	Rest mass of the electron
$q_e = e = 1\text{a.u.} = 1.6022 \cdot 10^{-19}\text{A·s}$	Charge of the electron
$\hbar = m_e v_e r_e = 1\text{a.u.}$	Reduced Planck constant
$c = e^2/(\hbar\alpha) = 137\text{a.u.}$	Speed of light

The conversion factors to other common units are:

Conversion factors

Energy	$E[\text{eV}] = 27.2 \cdot E[\text{a.u.}]$
Momentum	$p[\text{N·s}] = 1.995 \cdot 10^{-24} \cdot p[\text{a.u.}]$
Time	$t[\text{s}] = 4.134 \cdot 10^{16} \cdot t[\text{a.u.}]$
Velocity	$v_e = 1\text{a.u.} = 2.1877 \cdot 10^{6}\text{m/s}$
Intensity of electromagnetic wave	$1\text{a.u.} = 35.1 \cdot 10^{15}\text{W/cm}^2$
Electric field	$1\text{a.u.} = 5.142208 \times 10^{11}\,\text{V/m}$

Bibliography

[ADK86] M.V. Ammosov, N.B Delone, and N.B. Krainov, *Tunnel ionization of complex atoms and of atomic ions in an alternating electromagnetic field*, Soviet Physics JETP **64** (1986), no. 6, 1191. 2.1.1

[AFM+79] P. Agostini, F. Fabre, G. Mainfray, G. Petite, and N.K. Rahman, *Free-free transitions following six-photon ionization of xenon atoms*, Phys. Rev. Lett. **42** (1979), no. 17, 1127–1130. 2.1

[ALC95] F. Ancilotto, P. B. Lerner, and M. W. Cole, J. Low Temp. Phys. **101** (1995), 1123. 3.3.1

[AM76] N.W. Ashcroft and N.D. Mermin, *Solid state physics*, Thomson Learning Inc., Florence, 1976. 2.2.2

[AMSC91] S. Augst, D. D. Meyerhofer, D. Strickland, and S. L. Chin, J. Opt. Soc. Am. B **8** (1991), 858. 2.1.1

[And02] John D. Anderson, *Modern compressible flow*, 2nd edition ed., McGraw-Hill Science Engineering, 2002. 3.2.1

[AT93] M.P. Allen and D.J. Tildesley, *Computer simulation in chemical physics*, vol. 397, Springer, 1993. 2.3

[BAF05] B.N. Breizman, A.V. Arefiev, and M.V. Fomytskyi, *Nonlinear physics of laser-irradiated microclusters*, Physics of plasmas **12** (2005), 056706. 5.3

[BDD+04] R. Butkus, R. Danielius, A. Dubietis, A. Piskarskas, and A. Stabinis, *Progress in chirped pulse optical parametric amplifiers*, Applied Physics B: Lasers and Optics **79** (2004), 693–700, 10.1007/s00340-004-1614-3. 3

[BHB10] M. Bonitz, C. Henning, and D. Block, *Complex plasmas: a laboratory for strong correlations*, Reports on Progress in Physics **73** (2010), 066501. 1

[BHM+93] J. J. Bollinger, D. J. Heinzen, F. L. Moore, Wayne M. Itano, D. J. Wineland, and Daniel H. E. Dubin, *Electrostatic modes of ion-trap plasmas*, Phys. Rev. A **48** (1993), no. 1, 525. 4.2.1

[BJ03] B.H. Bransden and C.J. Joachain, *Physics of atoms and molecules*, 2 ed., Pearson education, 2003. 2.2.6

[BK97] Thomas Brabec and Ferenc Krausz, *Nonlinear optical pulse propagation in the single-cycle regime*, Phys. Rev. Lett. **78** (1997), no. 17, 3282. 2.1.3, 2.1.3

[BK00] T. Brabec and F. Krausz, *Intense few-cycle laser fields: Frontiers of nonlinear optics*, Reviews of Modern Physics **72** (2000), no. 2, 545–591. 2.1.2

[BKN+90] H. Buchenau, E. L. Knuth, J. Northby, J. P. Toennies, and C. Winkler, *Mass spectra and time-of-flight distributions of helium cluster beams*, J. Chem. Phys **92** (1990), no. 11, 6875. 3.4, 3.2

[BL] C. K. Birdsall and A. B. Langdon, *Plasma physics via computer simulation. 1985*, Mac. Graw-Hill, New York. 2.3

[Boy08] R. Boyd, *Nonlinear optics*, 3 ed., Academic Press, April 11 2008. 2.1, 2.1.3, 2.1.3, 3.5.3

[BPB+88] L. R. Brewer, J. D. Prestage, J. J. Bollinger, Wayne M. Itano, D. J. Larson, and D. J. Wineland, Phys. Rev. A **38** (1988), no. 2, 859. 4.2.1

[BS57] H. A. Bethe and E. Salpeter, *Quantum mechanics of one- and two-electron atoms*, Springer, Berlin, 1957. 2.1.1, 4.2.1

[BS11] O. Bünermann and F. Stienkemeier, Eur. Phys. J. D **61** (2011), 645. 3.3.4, 4.1.1, 4.1.1

[BSCK92] T. Brabec, Ch. Spielmann, P. F. Curley, and F. Krausz, *Kerr lens mode locking*, Opt. Lett. **17** (1992), no. 18, 1292. 3.5.1

[BT56] K. L. Brown and G. W. Tautfest, *Faraday cup monitors for high energy electron beams*, no. 9, 696. 3.4.1

[BZW+94] U. Boesl, R. Zimmermann, C. Weickhardt, D. Lenoir, K.-W. Schramm, A. Kettrup, and E.W. Schlag, *Resonance-enhanced multiphoton ionization: a species-selective ion source for analytical time-of-flight mass spectroscopy*, Chemosphere **29** (1994), no. 7, 1429. 2.1

[Cam84] R. Campargue, J. Phys. Chem. **88** (1984), 4466. 3.1.1

[CK07] P.B. Corkum and F. Krausz, *Attosecond Science*, Nature Physics **3** (2007), 381–387. 1

[CKAK10] G. Chen, B. Kim, B. Ahn, and D.E. Kim, *Experimental investigation on argon cluster sizes for conical nozzles with different opening angles*, Journal of Applied Physics **108** (2010), no. 6, 064329. 3.1.2

[CL84] F.F. Chen and M. A. Lieberman, *Introduction to plasma physics and controlled fusion*, Plenum Press, New York, 1984. 1

[CMS03] P. Claas, S. O. Mende, and F. Stienkemeier, Rev. Sci. Instrum. **74** (2003), 4071. 3.3

[Cor94] P. B. Corkum, *Plasma perspective on strong field multiphoton ionization*, Physical Reviev Letters **71** (1994), no. 13, 1994. 2.1.2

[Dah00] David A. Dahl, International Journal of Mass Spectrometry **200** (2000), no. 1-3, 3. 3.4, 5.3

[Dal60] N. R. Daly, *Scintillation type mass spectrometer ion detector*, no. 3, 264. 3.4.1, 3.4.1, 3.20

[DDFP95] T. Ditmire, T. Donnelly, R. W. Falcone, and M. D. Perry, *Strong x-ray emission from high-temperature plasmas produced by intense irradiation of clusters*, Phys. Rev. Lett. **75** (1995), no. 17, 3122. 2.2.6

[DDP+07] T. Döppner, Th. Diederich, A. Przystawik, N. X. Truong, Th. Fennel, J. Tiggesbäumker, and K. H. Meiwes-Broer, *Charging of metal clusters in helium droplets exposed to intense femtosecond laser pulses*, Phys. Chem. Chem. Phys. **9** (2007), 4639. 1, 4.2.1, 4.3, 4.3, 5, 5.1, 5.1.2, 5.3, 6.1

[DDR+96] T. Ditmire, T. Donnelly, A. M. Rubenchik, R. W. Falcone, and M. D. Perry, *Interaction of intense laser pulses with atomic clusters*, Phys. Rev. A **53** (1996), no. 5, 3379–3402. 2.2.2, 2.2.2, 2.2.2, 2.2.2, 2.2.2, 2.2.2, 2.2.2, 2.2.5, 2.2.5, 2.2.7, 2.2.7, 3.4, 4, 5

[DFBG03] F. Dorchies, J. Stevefelt C. Stenz A. S. Boldarev F. Blasco, T. Caillaud, and V. A. Gasilov, Phys. Rev. A **68** (2003), 023201. 3.1.2

[DFD+05] T. Döppner, Th. Fennel, Th. Diederich, J. Tiggesbäumker, and K. H. Meiwes-Broer, *Controlling the coulomb explosion of silver clusters by femtosecond dual-pulse laser excitation*, Phys. Rev. Lett. **94** (2005), no. 1, 013401. 2.2.2, 3, 4

[DFR+05] T. Döppner, T. Fennel, P. Radcliffe, J. Tiggesbäumker, and K.H. Meiwes-Broer, *Strong field dual-pulse excitation of AgN*, The European Physical Journal D-Atomic, Molecular, Optical and Plasma Physics **36** (2005), no. 2, 165. 5.1.1

[DFR+06] T. Döppner, Th. Fennel, P. Radcliffe, J. Tiggesbäumker, and K.-H. Meiwes-Broer, *Ion and electron emission from silver nanoparticles in intense laser fields*, Phys. Rev. A **73** (2006), no. 3, 031202. 2.2.2, 5

[Dit97] T. Ditmire, *Atomic clusters in ultrahigh intensity light fields*, Contemporary Physics **38** (1997), no. 5, 315. 2.2.2, 4.3

[DMP+07] T. Döppner, JP Müller, A. Przystawik, J. Tiggesbäumker, and K.H. Meiwes-Broer, *The effect of volumetric weighting in the interaction of intense laser fields with clusters*, The European Physical Journal D-Atomic, Molecular, Optical and Plasma Physics **43** (2007), no. 1, 261. 5.1

[DMP+10] T. Döppner, J. P. Müller, A. Przystawik, S. Göde, J. Tiggesbäumker, K.-H. Meiwes-Broer, C. Varin, L. Ramunno, T. Brabec, and T. Fennel, *Steplike intensity threshold behavior of extreme ionization in laser-driven xenon clusters*, Phys. Rev. Lett. **105** (2010), 053401. 6.1, 6.2

[DR06] J. Diels and W. Rudolph, *Ultrashort laser pulse phenomena*, Academic Press, 2006. 2.1.3, 3.5.1, 6.2

[DRB+06] C. Deiss, N. Rohringer, J. Burgdörfer, E. Lamour, C. Prigent, J.P. Rozet, and D. Vernhet, *Laser-cluster interaction: x-ray production by short laser pulses*, Physical review letters **96** (2006), no. 1, 13203. 2.2.6, 2.3

[DTD+03] T. Döppner, S. Teuber, T. Diederich, T. Fennel, P. Radcliffe, J. Tiggesbäumker, and KH Meiwes-Broer, *Dynamics of free and embedded lead clusters in intense laser fields*, The European Physical Journal D-Atomic, Molecular, Optical and Plasma Physics **24** (2003), no. 1, 157. 5.3

[DZY+99] T. Ditmire, J. Zweiback, VP Yanovsky, TE Cowan, G. Hays, and KB Wharton, *Nuclear fusion from explosions of femtosecond laser-heated deuterium clusters*, Nature **398** (1999), no. 6727, 489. 2.2.2, 2.8, 2.2.7

[Ein05] A. Einstein, *Über einen die erzeugung und verwandlung des lichtes betreffenden heuristischen gesichtspunkt*, Annalen der Physik **322** (1905), no. 6, 132. 2.1

[Erg06] T. Ergler, *Fragmentation dynamics of d_2 in intense laser pulses*, Ph.D. thesis, Ruprecht-Karls-Universität, Heidelberg, Germany, 2006. 3.5.4

[EWH+08] L. Englert, M. Wollenhaupt, L. Haag, C. Sarpe-Tudoran, B. Rethfeld, and T. Baumert, *Material processing of dielectrics with temporally asymmetric shaped femtosecond laser pulses on the nanometer scale*, Applied Physics A: Materials Science & Processing **92** (2008), no. 4, 749. 6.2

[FDFRT81] J. Farges, MF De Feraudy, B. Raoult, and G. Torchet, *Structure and temperature of rare gas clusters in a supersonic expansion*, Surface Science **106** (1981), no. 1-3, 95–100. 2.2

[FDP+07] T. Fennel, T. Döppner, J. Passig, C. Schaal, J. Tiggesbäumker, and K.H. Meiwes-Broer, *Plasmon-enhanced electron acceleration in intense laser metal-cluster interactions*, Physical review letters **98** (2007), no. 14, 143401. 2.2.5, 2.11, 2.2.5, 5

[Fed97] M.V. Fedorov, *Atomic and free electrons in a strong light field*, World Scientific Pub Co Inc, 1997. 2.3

[Fey60] R.P. Feynman, *There's plenty of room at the bottom*, Engineering and Science **23** (1960), no. 5, 22. 6.2

[FFC82] P. Agostini F. Fabre, G. Petite and M. Clement, J. Phys. B **15** (1982), 1353. 2.1

[Fis10] B. Fischer, *Time-resolved investigation of h2 in cep-stabilized laser pulses*, Ph.D. thesis, Ruprecht-Karls-Universität, Heidelberg, Germany, 2010. 3.5.3, 3.5.4

[FKP+10] B. Fischer, M. Kremer, T. Pfeifer, B. Feuerstein, V. Sharma, U. Thumm, C.D. Schröter, R. Moshammer, and J. Ullrich, Physical review letters **105** (2010), no. 22, 223001. 1, 6.2

[FMBT+10] Th. Fennel, K.-H. Meiwes-Broer, J. Tiggesbäumker, P.-G. Reinhard, P.M. Dinh, and E. Suraud, Rev. Mod. Phys. **82** (2010), 1793. 1, 2.4, 2.2.1, 2.2.2, 2.2.4, 2.2.5, 2.2.5, 2.11, 2.2.6, 2.2.7, 2.2.7, 2.3, 2.3, 4, 4.3, 5, 5.2, 5.3, 6.2

[FMG84] R. L. Fork, O. E. Martinez, and J. P. Gordon, *Negative dispersion using pairs of prisms*, Optics letters **9** (1984), no. 5, 150–152. 3.5.2

[Fra02] G. W. Fraser, *The ion detection efficiency of microchannel plates (mcps)*, International Journal of Mass Spectrometry **215** (2002), no. 1-3, 13. 3.4.1

[FRB07] T. Fennel, L. Ramunno, and T. Brabec, *Highly charged ions from laser-cluster interactions: Local-field-enhanced impact ionization and frustrated electron-ion recombination*, Physical review letters **99** (2007), no. 23, 233401. 4.3, 5.1.2

[FZBB05] S. V. Fomichev, D. F. Zaretsky, D. Bauer, and W. Becker, *Classical molecular-dynamics simulations of laser-irradiated clusters: Nonlinear electron dynamics and resonance-enhanced low-order harmonic generation*, Physical Review A **71** (2005), no. 1, 013201. 2.2.2

[FZPCJ99] J. V. Ford, Q. Zhong, L. Poth, and A. W. Castleman Jr, *Femtosecond laser interactions with methyl iodide clusters*, The Journal of chemical physics **110** (1999), 6257. 2.2.4

[GCA+10] J.M. Glownia, J. Cryan, J. Andreasson, A. Belkacem, N. Berrah, CI Blaga, C. Bostedt, J. Bozek, LF DiMauro, L. Fang, et al., *Time-resolved pump-probe experiments at the lcls*, Optics Express **18** (2010), no. 17, 17620. 5.2

[GM31] Maria Göppert-Mayer, *Über elementarakte mit zwei quantensprüngen*, Annalen der Physik **401** (1931), no. 3, 273. 2.1

[GM08] R. R. Gattass and E. Mazur, *Femtosecond laser micromachining in transparent materials*, Nature Photonics **2** (2008), no. 4, 219. 6.2

[Gop09] R. Gopal, *Electron wave packet interferences in ionization with few-cycle laser pulses and the dissociative photoionization of d2 with ultrashort extreme ultraviolet pulses*, Ph.D. thesis, Ruprecht-Karls-Universität Heidelberg, 2009. 2.1.2

[Gre03] I. Grenthe, *Nobel lectures, chemistry, 1996-2000*, vol. 8, World Scientific Pub Co Inc, 2003. 1

[GSM+09] R. Gopal, K. Simeonidis, R. Moshammer, Th. Ergler, M. Dürr, M. Kurka, K.-U. Kühnel, S. Tschuch, C.D. Schröter, D. Bauer, J. Ullrich, A. Rudenko, O. Herrwerth, Th. Uphues, M. Schultze, E. Goulielmakis, M. Uiberacker, M. Lezius, and M. Kling, *Electron wavepacket interferences pointing towards holographic imaging in few-cycle pulses*, Phys. Rev. Lett. **103** (2009), 053001. 1, 6.2

[Gsp81] J. Gspann, *Helium microdroplet transparency in heavy atom collisions*, Physica B+ C **108** (1981), no. 1-3, 1309–1310. 3.2

[GSR09] C. Gnodtke, U. Saalmann, and J.-M. Rost, Phys. Rev. A **79** (2009), 041201. 4, 4.1.1, 4.2.1, 5.1.1

[GT03] R. E. Grisenti and J. P. Toennies, Phys. Rev. Lett. **90** (2003), 34501. 3.2

[Hab94] H. Haberland, *Clusters of atoms and molecules*, Springer-Verlag Berlin, 1994. 1, 2.2, 2.2.1, 5

[Hah97a] Y. Hahn, *Electron-ion recombination processes-an overview*, Reports on Progress in Physics **60** (1997), 691. 5.1.2

[Hah97b] ———, *Plasma density effects on the three-body recombination rate coefficients*, Physics Letters A **231** (1997), no. 1-2, 82. 5.1.2

[HBT+08] M. Hoener, C. Bostedt, H. Thomas, L. Landt, E. Eremina, H. Wabnitz, T. Laarmann, R. Treusch, A.R.B. Castro, and T. Möller, *Charge recombination in soft x-ray laser produced nanoplasmas*, Journal of Physics B: Atomic, Molecular and Optical Physics **41** (2008), 181001. 1, 4, 5.1.1

[Hec10] J. Hecht, *Short history of laser development*, Optical Engineering **49** (2010), 091002. 1

[HIFT95] H. Haberland, B. V. Issendorff, R. Fröchtenicht, and J. P. Toennies, *Absorption spectroscopy and photodissociation dynamics of small helium cluster ions*, Journal of Chemical Physics **102** (1995), no. 22, 8773. 6.2

[HJL06] A. Heidenreich, J. Jortner, and I. Last, *Cluster dynamics transcending chemical dynamics toward nuclear fusion*, Proceedings of the National Academy of Sciences **103** (2006), no. 28, 10589. 2.2.7

[HJPTP01] J. Harms, M. Barranco J. P. Toennies, and M. Pi, Phys. Rev. B **63** (2001), 184513. 3.2

[HKM91] H. Haberland, M. Karrais, and M. Mall, *A new type of cluster and cluster ion source*, Zeitschrift für Physik D Atoms, Molecules and Clusters **20** (1991), no. 1, 413. 5

[HKP10] G. Huber, C. Kränkel, and K. Petermann, *Solid-state lasers: status and future [invited]*, JOSA B **27** (2010), no. 11, B93. 1

[HO72] O. F. Hagena and W. Obert, J. Chem. Phys. **56** (1972), 1793. 1, 3.1.1, 3.1.2, 5

[HS09] Andreas Hermann and Peter Schwerdtfeger, J. Chem. Phys. **131** (2009), 244508. 3.3.2

[HSM+05] M. Hohenberger, D. R. Symes, K. W. Madison, A. Sumeruk, G. Dyer, A. Edens, W. Grigsby, G. Hays, M. Teichmann, and T. Ditmire, *Dynamic acceleration effects in explosions of laser-irradiated heteronuclear clusters*, Phys. Rev. Lett. **95** (2005), no. 19, 195003. 2.2.7, 5.3

[HTK96] J. Harms, J. P. Toennies, and E. L. Knuth, J. Chem. Phys. **106** (1996), 3348. 3.2

[HWY02] A. R. B. de Castro R. Döhrmann P. Gürtler T. Laarmann W. Laasch J. Schulz A. Swiderski K. von Haeften T. Möller B. Faatz A. Fateev J. Feldhaus C. Gerth U. Hahn E. Saldin E. Schneidmiller K. Sytchev K. Tiedtke R. Treusch H. Wabnitz, L. Bittner and M. Yurkov, *Multiple ionization of atom clusters by intense soft x-rays from a free-electron laser*, Nature **420** (2002), 482–485. 1

[IB00] K. Ishikawa and T. Blenski, *Explosion dynamics of rare-gas clusters in an intense laser field*, Physical Review A **62** (2000), no. 6, 063204. 2.2.2, 2.2.4, 2.2.5, 2.3, 2.3

[IKJ09] Daniel Irimia, Rob Kortekaas, and Maurice H. M. Janssen, *In situ characterization of a cold and short pulsed molecular beam by femtosecond ion imaging*, Phys. Chem. Chem. Phys. **11** (2009), 3958. 3.1.2

[ISR06] M.R. Islam, U. Saalmann, and J.M. Rost, *Kinetic energy of ions after coulomb explosion of clusters induced by an intense laser pulse*, Physical Review A **73** (2006), no. 4, 041201. 2.2.7, 4.3, 4.14, 4.3

[IVE+04] R. C. Issac, G. Vieux, B. Ersfeld, E. Brunetti, S. P. Jamison, J. Gallacher, D. Clark, and D. A. Jaroszynski, *Ultra hard x rays from krypton clusters heated by intense laser fields*, Physics of plasmas **11** (2004), 3491. 2.2.6

[Jac62] J. D. Jackson, *Classical electrodynamics*, John Wiley & Sons, New York, 1962. 2.2.2, 2.2.2, 2.2.5

[JCD06] Wolfgang Rudolph Jean-Claude Diels, *Ultrashort laser pulse phenomena*, second ed., Academic Press, 2006. 2.1.3, 2.1.3, 2.1.3

[JES88] J. Javanainen, J. H. Eberly, and Q. Su, *Numerical simulations of multiphoton ionization and above-threshold electron spectra*, Physical Review A **38** (1988), no. 7, 3430. 2.3

[JGZB04] Christian Jungreuthmayer, Michael Geissler, Jürgen Zanghellini, and Thomas Brabec, *Microscopic analysis of large-cluster explosion in intense laser fields*, Phys. Rev. Lett. **92** (2004), no. 13, 133401. 2.2.1, 2.2.4, 2.10, 2.3

[JK08a] J. Jha and M. Krishnamurthy, J. Phys. B **41** (2008), 041002. 4, 4.2.1, 5.1

[JK08b] J. Jha and M. Krishnamurthy, *Collisionless phenomena in heteronuclear clusters*, Applied Physics Letters **92** (2008), 191108. 1, 2.13, 2.2.6

[JL05] J. Jortner and I. Last, *Ultrafast nuclear dynamics and non-uniform coulomb explosion of heteroclusters*, Molecular Physics **103** (2005), no. 13, 1735–1743. 2.2.7

[JMK06] J. Jha, D. Mathur, and M. Krishnamurthy, *Engineering clusters for table-top acceleration of ions*, Applied physics letters **88** (2006), 041107. 2.2.7

[Jou08] Karl Jousten, *Handbook of vacuum technology*, Wiley-VCH, Berlin, 2008. 3.2.1

[KB06] M. Kundu and D. Bauer, *Nonlinear resonance absorption in the laser-cluster interaction*, Physical review letters **96** (2006), no. 12, 123401. 2.2.2, 2.3

[Kel64] L.V. Keldysh, *Ionization in the field of a strong electromagnetic wave*, Soviet Physics JETP **20** (1964), 1307. 2.1.1

[KF11] J. Köhn and T. Fennel, *Time-resolved analysis of strong-?eld induced plasmon oscillations in metal clusters by spectral interferometry with few-cycle laser fields*, Phys. Chem. Chem. Phys . **13** (2011), 8747. 6.2

[KFF+09] M. Kremer, B. Fischer, B. Feuerstein, V. L. B. de Jesus, V. Sharma, C. Hofrichter, A. Rudenko, U. Thumm, C. D Schröter, R. Moshammer, and J. Ullrich, *Electron localization in molecular fragmentation of H_2 by carrier-envelope phase stabilized laser pulses*, Phys. Rev. Lett. **103** (2009), no. 21, 213003. 1, 6.2

[KFK+11] S. R. Krishnan, L. Fechner, M. Kremer, V. Sharma, B. Fischer, N. Camus, J. Jha, M. Krishnamurthy, T. Pfeifer, R. Moshammer, J. Ullrich, F. Stienkemeier, M. Mudrich, A. Mikaberidze, U. Saalmann, and J. M. Rost, *Dopant induced ignition of helium nanodroplets in intense few-cycle laser pulses*, Phys. Rev. Lett. (accepted) (2011). 4, 4.2, 4.2.1, 5.2

[KGS+07] S. Kuma, H. Goto, M. N. Slipchenko, A. F. Vilesov, A. Khramov, and T. Momose, J. Chem. Phys. **127** (2007), 214301. 3.3.1, 3.3.2, 3.3.3, 3.3.3, 3.3.4, 4.1.1, 4.1.1, 4.3

[KH99] E. L. Knuth and U. Henne, *Average size and size distribution of large droplets produced in a free-jet expansion of a liquid*, J. Chem. Phys. **110** (1999), 2664. 3.2

[KHGM07] S. Kuma, A. F. Vilesov A. Khramov H. Goto, M. N. Slipchenko, and T. Momose, J. Chem. Phys. **127** (2007), 214301. 3.3.1, 3.3.2, 3.3.3

[KKB+99] T. C. Killian, S. Kulin, S. D. Bergeson, L. A. Orozco, C. Orzel, and S. L. Rolston, *Creation of an ultracold neutral plasma*, Phys. Rev. Lett. **83** (1999), 4776. 1

[KKM01] V. Kumarappan, M. Krishnamurthy, and D. Mathur, *Asymmetric high-energy ion emission from argon clusters in intense laser fields*, Physical Review Letters **87** (2001), no. 8, 85005. 2.2.4, 2.10, 4.3, 5.3

[KKM03a] ———, *Asymmetric emission of high-energy electrons in the two-dimensional hydrodynamic expansion of large xenon clusters irradiated by intense laser fields*, Physical Review A **67** (2003), no. 4, 043204. 2.2.5, 2.2.7, 5.1

[KKM03b] ———, *Explosions of water clusters in intense laser fields*, Physical Review A **67** (2003), no. 6, 063207. 2.2.4, 2.2.7

[KKMT01] V. Kumarappan, M. Krishnamurthy, D. Mathur, and LC Tribedi, *Effect of laser polarization on x-ray emission from ar clusters in intense laser fields*, Physical Review A **63** (2001), no. 2, 023203. 2.2.6

[KMK04] M. Krishnamurthy, D. Mathur, and V. Kumarappan, *Anisotropic "charge-flipping" acceleration of highly charged ions from clusters in strong optical fields*, Phys. Rev. A **69** (2004), no. 3, 033202. 2.2.7, 4.3

[KMM02] J. Kuepper, J. M. Merritt, and R. E. Miller, J. Chem. Phys. **117** (2002), 647. 3.3

[KMS02] K. Kondo, M. Mori, and T. Shiraishi, *X-ray generation from fs laser heated xe clusters*, Applied surface science **197** (2002), 138–144. 2.2.6

[KPG+98] T. Klar, M. Perner, S. Grosse, G. Von Plessen, W. Spirkl, and J. Feldmann, *Surface-plasmon resonances in single metallic nanoparticles*, Physical Review Letters **80** (1998), no. 19, 4249. 2.2.2

[Kär04] Franz X. Kärtner (ed.), *Few-cycle laser pulse generation and its applications*, 1 ed., Springer, 2004. 3.5.3

[Kra00] V. P. Krainov, *Inverse stimulated bremsstrahlung of slow electrons under coulomb scattering*, Journal of Physics B: Atomic, Molecular and Optical Physics **33** (2000), 1585. 2.2.5

[Kru03] W.L. Kruer, *The physics of laser plasma interactions*, vol. 73, Westview Pr, 2003. 2.2.2, 2.2.7

[KS02] V. P. Krainov and M. B. Smirnov, *Cluster beams in the super-intense femtosecond laser pulse*, Physics reports **370** (2002), no. 3, 237. 2.2.3, 2.2.3, 2.2.5

[KSK+99] L. Köller, M. Schumacher, J. Köhn, S. Teuber, J. Tiggesbäumker, and K. H. Meiwes-Broer, *Plasmon-enhanced multi-ionization of small metal clusters in strong femtosecond laser fields*, Phys. Rev. Lett. **82** (1999), no. 19, 3783–3786. 2.2.2, 2.8, 5, 5.1

[KSS07] V. P. Krainov, B. M. Smirnov, and M. B. Smirnov, *Femtosecond excitation of cluster beams*, Physics-Uspekhi **50** (2007), 907. 1, 2.2.1, 5.1.1

[Kun] M. Kundu, *Energy absorption, ionization, and harmonic emission in laser-irradiated atomic clusters*, Ph.D. thesis, Ruperto-Carola University of Heidelberg, Germany. 2.3

[Lam76] P. Lambropoulos, Adv. At. Mol. Phys. **12** (1976), 87. 2.1

[Lam85] P. Lambropoulos, *Mechanisms for multiple ionization of atoms by strong pulsed lasers*, Phys. Rev. Lett. **55** (1985), no. 20, 2141–2144. 2.1.3

[LB70] A.B. Langdon and C.K. Birdsall, *Theory of plasma simulation using finite-size particles*, Physics of Fluids **13** (1970), 2115. 2.3

[LDNS98] M. Lezius, S. Dobosz, D. Normand, and M Schmidt, *Explosion dynamics of rare gas clusters in strong laser fields*, Physical review letters **80** (1998), no. 2, 261. 2.2.7, 2.14, 5.3

[Leo94] W.R. Leo, *Techniques for nuclear and particle physics experiments: a how-to approach*, Springer Verlag, 1994. 2.13, 2.2.6

[Ley] *Leybold, gebrauchsanweisung für öldiffusionspumpe, dip 8000, 1996.* 3.6

[LJ99] I. Last and J. Jortner, *Quasiresonance ionization of large multicharged clusters in a strong laser field*, Physical Review A **60** (1999), no. 3, 2215. 2.2.1

[LJ01a] ———, *Nuclear fusion induced by coulomb explosion of heteronuclear clusters*, Physical Review Letters **87** (2001), no. 3, 33401. 2.2.7

[LJ01b] Isidore Last and Joshua Jortner, *Nuclear fusion driven by coulomb explosion of homonuclear and heteronuclear deuterium- and tritium-containing clusters*, Phys. Rev. A **64** (2001), no. 6, 063201. 2.2.7

[LJ06] I. Last and J. Jortner, *Effects of the nanoplasma on the energetics of coulomb explosion of molecular clusters in ultraintense laser fields*, Physical Review A **73** (2006), no. 1, 013202. 2.2.7, 6.2

[LL09] L.D. Landau and E.M. Lifschitz, *Course of theoretical physics: The classical theory of fields*, vol. 2, Pergamon Press., 2009. 2.2.2

[Lot68] W. Lotz, *Electron-impact ionization cross-sections and ionization rate coefficients for atoms and ions from hydrogen to calcium*, Zeitschrift für Physik A Hadrons and Nuclei **216** (1968), no. 3, 241–247. 2.2.5

[LPRV05a] E. Lamour, C. Prigent, J.P. Rozet, and D. Vernhet, *Physical parameter dependence of the x-ray generation in intense laser-cluster interaction*, Nuclear Instruments and Methods in Physics Research Section B: Beam Interactions with Materials and Atoms **235** (2005), no. 1-4, 408–413. 2.12, 2.2.6

[LPRV05b] E. Lamour, C. Prigent, J.P. Rozet, and D. Vernhet, *Physical parameter dependence of the x-ray generation in intense laser-cluster interaction*, Nuclear Instruments and Methods in Physics Research Section B: Beam Interactions with Materials and Atoms **235** (2005), no. 1-4, 408, The Physics of Highly Charged Ions. 2.2.6

[LSJ+97] I. Last, I. Schek, J. Jortner, et al., *Energetics and dynamics of coulomb explosion of highly charged clusters*, Journal of Chemical Physics **107** (1997), no. 17, 6685. 2.2.7, 2.2.7

[LST93] M. Lewerenz, B. Schilling, and J. P. Toennies, Chem. Phys. Lett. **206** (1993), 381. 3.2, 3.2.2, 3.10

[LST95] M. Lewerenz, B. Schilling, and J. P. Toennies, *Successive capture and coagulation of atoms and molecules to small clusters in large liquid helium clusters*, J. Chem. Phys. **102** (1995), no. 20, 8191. 3.3, 3.3.1, 3.3.1, 3.3.2, 3.3.2, 3.3.3, 3.3.3

[LVC+02] MA Lebeault, J. Viallon, J. Chevaleyre, C. Ellert, D. Normand, M. Schmidt, O. Sublemontier, C. Guet, and B. Huber, *Resonant coupling of small size-controlled lead clusters with an intense laser field*, The European Physical Journal D-Atomic, Molecular, Optical and Plasma Physics **20** (2002), no. 2, 233–242. 2.2.4, 5

[MFCLU+02] R. Moshammer, B. Feuerstein, J. Crespo Lopez-Urrutia, J. Deipenwisch, A. Dorn, D. Fischer, C. Höhr, P. Neumayer, C. D. Schröter, J. Ullrich, H. Rottke, C. Trump, M. Wittmann, G. Korn, and W. Sandner, *Correlated two-electron dynamics in strong-field double ionization*, Physical Review A **65** (2002), 035401. 2.1.2

[MFK02] R. Moshammer, D. Fischer, and H. Kollmus, *Many-particle quantum dynamics in atomic and molecular fragmentation*, ch. Recoil-Ion Momentum Spectroscopy and "Reaction Microscopes", pp. 37–62, Springer-Verlag, 2002. 3.1.1, 3.4, 3.4, 3.17, 3.4.1

[MFS+00] R. Moshammer, B. Feuerstein, W. Schmitt, A. Dorn, C. D. Schröter, J. Ullrich, H. Rottke, C. Trump, M. Wittmann, G. Korn, K. Hoffmann, and W. Sandner, *Momentum distributions of Ne^{n+} ions created by an intense ultrashort laser pulse*, Phys. Rev. Lett. **84** (2000), no. 3, 447–450. 2.1.2

[Mie08] G. Mie, *Beiträge zur optik trüber medien, speziell kolloidaler metallösungen*, Annalen der Physik **330** (1908), no. 3, 377. 2.2.2

[Mik11] Alexey Mikaberidze, *Atomic and molecular clusters in intense laser pulses*, Ph.D. thesis, Technischen Universität Dresden, 2011. 2.3, 2.3, 2.3, 4.1.1, 4.2, 5.1.1, 5.3, 5.3, 6.2

[Mil88] D. R. Miller, *Atomic and molecular beam methods*, ch. 2, Oxford University Press, Oxford, 1988. 3.1.1

[MJP08] S. Micheau, H. Jouin, and B. Pons, *Modified nanoplasma model for laser-cluster interaction*, Phys. Rev. A **77** (2008), no. 5, 053201. 2.2.5

[MKK+09] S. Müller, S. Krapf, T. Koslowski, M. Mudrich, and F. Stienkemeier, *Cold reactions of alkali-metal and water clusters inside helium nanodroplets*, Physical review letters **102** (2009), no. 18, 183401. 6.2

[MMNSV07] V. Mozhayskiy, V. K. Adamchuk M. N. Slipchenko, and A. F. Vilesov, J. Chem. Phys. **127** (2007), 094701. 3.3.2, 3.3.2, 3.3.3

[MMP01] HM Milchberg, SJ McNaught, and E. Parra, *Plasma hydrodynamics of the intense laser-cluster interaction*, Physical Review E **64** (2001), no. 5, 056402. 2.2.2, 2.2.2, 5.1.1, 5.2

[MPP+04] KW Madison, PK Patel, D. Price, A. Edens, M. Allen, TE Cowan, J. Zweiback, and T. Ditmire, *Fusion neutron and ion emission from deuterium and deuterated methane cluster plasmas*, Physics of Plasmas **11** (2004), 270. 2.2.7

[MSR08] Alexey Mikaberidze, Ulf Saalmann, and Jan M. Rost, *Energy absorption of xenon clusters in helium nanodroplets under strong laser pulses*, Phys. Rev. A **77** (2008), no. 4, 041201. 4.1.1, 4.2, 5.1.1, 5.2, 5.2, 5.14

[MSR09] A. Mikaberidze, U. Saalmann, and J.-M. Rost, Phys. Rev. Lett. **102** (2009), 128102. 1, 4, 4.1.1, 4.1.1, 4.2, 4.2.1, 4.9, 4.10, 5.2

[MTB+94] A. McPherson, BD Thompson, AB Borisov, K. Boyer, and CK Rhodes, *Multiphoton-induced x-ray emission at 4–5 kev from xe atoms with multiple core vacancies*, Nature **370** (1994), no. 6491, 631. 2.2.6

[MUF+03] R. Moshammer, J. Ullrich, B. Feuerstein, D. Fischer, A. Dorn, C. D. Schröter, J. R. Crespo Lopez-Urrutia, C. Hoehr, H. Rottke, C. Trump, et al., *Rescattering of ultralow-energy electrons for single ionization of ne in the tunneling regime*, Physical review letters **91** (2003), no. 11, 113002. 1

[NDSS96] M. Nisoli, S. De Silvestri, and O. Svelto, *Generation of high energy 10 fs pulses by a new pulse compression technique*, Appl. Phys. Lett. **68** (1996), 2793. 3.5.3

[NFY+09] T. Nakamura, Y. Fukuda, A. Yogo, M. Tampo, M. Kando, Y. Hayashi, T. Kameshima, AS Pirozhkov, T.Z. Esirkepov, T. A. Pikuz, et al., *Coulomb implosion mechanism of negative ion acceleration in laser plasmas*, Physics Letters A **373** (2009), no. 30, 2584. 6.2

[NM00] K. Nauta and R. E. Miller, J. Chem. Phys. **113** (2000), 10158. 3.3.1, 3.3.1

[Onn09] H. Kamerlingh Onnes, Proc. R. Netherlands Acad. Arts Sci. (KNAW) **11** (1909), 168. 3.2

[PAF+00] E. Parra, I. Alexeev, J. Fan, KY Kim, SJ McNaught, and HM Milchberg, *X-ray and extreme ultraviolet emission induced by variable pulse-width irradiation of ar and kr clusters and droplets*, Physical Review E **62** (2000), no. 5, 5931. 2.2.6

[PBNW94] GG Paulus, W. Becker, W. Nicklich, and H. Walther, *Rescattering effects in above-threshold ionization: a classical model*, Journal of Physics B: Atomic, Molecular and Optical Physics **27** (1994), L703. 2.2.5, 2.2.5

[PDG+06] S. Palaniyappan, A. DiChiara, I. Ghebregziabher, EL Huskins, A. Falkowski, D. Pajerowski, and BC Walker, Journal of Physics B: Atomic, Molecular and Optical Physics **39** (2006), S357. 2.2.4

[PDL+08] Christophe Prigent, Cornelia Deiss, Emily Lamour, Jean-Pierre Rozet, Dominique Vernhet, and Joachim Burgdörfer, *Effect of pulse duration on the x-ray emission from ar clusters in intense laser fields*, Phys. Rev. A **78** (2008), no. 5, 053201. 2.2.6

[Per95] Michael D. Perry, Science and Technology Review (1995), 24. 3.22

[Per96] A. L. Peratt, *Advances in numerical modeling of astrophysical and space plasmas*, Astrophysics and Space Science **242** (1996), 93. 1.1

[PF10] C. Peltz and T. Fennel, *Resonant charging of xe clusters in helium nanodroplets under intense laser fields*, The European Physical Journal D-Atomic, Molecular, Optical and Plasma Physics **63** (2010), 281. 3, 5.1.1, 5.1.2, 5.2, 5.2, 5.14

[PFA+84] G. Petite, F. Fabre, P. Agostini, M. Crance, and M. Aymar, *Nonresonant multiphoton ionization of cesium in strong fields: Angular distributions and above-threshold ionization*, Phys. Rev. A **29** (1984), no. 5, 2677. 2.1

[PKK97] M. Protopapas, C. H. Keitel, and P. L. Knight, *Atomic physics with super-high intensity lasers*, Reports on Progress in Physics **60** (1997), 389–486. 1, 2, 2.1.2

[Pla01] M. Planck, *On the law of distribution of energy in the normal spectrum*, Annalen der Physik **4** (1901), 553. 2.1

[PM94] Michael D. Perry and Gerard Mourou, *Terawatt to petawatt subpicosecond lasers*, Science **264** (1994), no. 5161, 917–924. 3

[POW] L. Prandtl, K. Oswatitsch, and K. Wieghardt, *Führer durch die strömungslehre*, Vieweg, Braunschweig 1990. 3.2.1

[PPM+06] F. Peano, F. Peinetti, R. Mulas, G. Coppa, and LO Silva, *Kinetics of the collisionless expansion of spherical nanoplasmas*, Physical review letters **96** (2006), no. 17, 175002. 4.3, 5.1.1

[PPR04] T. Pohl, T. Pattard, and J. M. Rost, *Coulomb crystallization in expanding laser-cooled neutral plasmas*, Physical review letters **92** (2004), no. 15, 155003. 1

[PPT66] A. M. Perelomov, V. S. Popov, and M. V. Terent'ev, Sov. Phys. JETP **23,** (1966), 924. 2.1.1

[PRRL09] D. Pentlehner, A. Slenczka U. Even N. Lavie R. Brown R. Riechers, B. Dick, and K. Luria, Rev. Sci. Inst. **80** (2009), 043302. 3.1.2

[PSW+94] J. Purnell, EM Snyder, S. Wei, AW Castleman, et al., *Ultrafast laser-induced coulomb explosion of clusters with high charge states*, Chemical physics letters **229** (1994), no. 4-5, 333–339. 2.2.4

[PZB08] S. V. Popruzhenko, D. F. Zaretsky, and D. Bauer, *Energy absorption and emission of harmonics by clusters subject to intense short laser pulses*, Laser Physics Letters **5** (2008), no. 9, 631. 2.2.2

[Ray78] Lord Rayleigh, *On the instability of jets*, Proc. Lond. math. Soc. **10** (1878), 4. 3.2

[RdJE+07] A. Rudenko, V.L.B. de Jesus, Th. Ergler, K. Zrost, C.D. Schröter, R. Moshammer, and J. Ullrich, *Correlated Two-Electron Momentum Spectra for Strong-Field Non-Sequential Double Ionization of He at 800nm*, Phys. Rev. Lett. **99** (2007), 263003–1. 1, 2.1.2

[RDS+05] P. Radcliffe, T. Döppner, M. Schumacher, S. Teuber, J. Tiggesbäumker, and K.-H. Meiwes-Broer, *Generation of highly charged and energetic ions from the interaction of strong laser pulses with coinage metal clusters*, Contributions to Plasma Physics **45** (2005), no. 5-6, 424. 6.2

[Ros09] J. M. Rost, *Complex non-equilibrium dynamics in plasmas*, European Review **17** (2009), no. 02, 249. 1

[RPS+11] S. Roy, D. Parks, KA Seu, R. Su, JJ Turner, W. Chao, EH Anderson, S. Cabrini, and SD Kevan, *Lensless x-ray imaging in reflection geometry*, Nature Photonics **5** (2011), no. 4, 243. 5.2

[RPSWB97] C. Rose-Petruck, KJ Schafer, KR Wilson, and CPJ Barty, *Ultrafast electron dynamics and inner-shell ionization in laser driven clusters*, Physical Review A **55** (1997), no. 2, 1182. 2.3

[RRT+11] R. Rajeev, KPM Rishad, T.M. Trivikram, V. Narayanan, and M. Krishnamurthy, *A thomson parabola ion imaging spectrometer designed to probe relativistic intensity ionization dynamics of nanoclusters*, Review of Scientific Instruments **82** (2011), 083303. 5.3

[RUMS00] J. H. Reho, K. K. Lehmann U. Merker, M. R. Radcliff, and G. Scoles, J. Phys. Chem. A **104** (2000), 3620. 3.3

[Saa06] U. Saalmann, *Resonant energy absorption of rare-gas clusters in strong laser pulses*, J. Mod. Opt. **53** (2006), 173. 1, 2.2.1, 2.4, 2.2.1, 2.2.2, 2.2.6, 2.2.6, 2.3, 2.3, 4, 4.2, 4.3, 5.2, 5.3

[SAZV03] E. Springate, SA Aseyev, S. Zamith, and MJJ Vrakking, *Electron kinetic energy measurements from laser irradiation of clusters*, Physical Review A **68** (2003), no. 5, 053201. 2.2.5

[SBBL88] G. Scoles, D. Bassi, U. Buck, and D. C. Lainé (eds.), *Atomic and molecular beam methods*, Oxford University Press, USA, 1988. 3.1.1, 3.1.1, 3.1

[SBC96] E. M. Snyder, S. A. Buzza, and A. W. Castleman, Jr, *Intense field-matter interactions: multiple ionization of clusters*, Physical review letters **77** (1996), no. 16, 3347–3350. 2.2.4

[Sc10] Lothar Strüder and CAMP-ASG collaboration, *Large-format, high-speed, x-ray pnccds combined with electron and ion imaging spectrometers in a multipurpose chamber for experiments at 4th generation light sources*, Nuclear Instruments and Methods in Physics Research Section A: Accelerators, Spectrometers, Detectors and Associated Equipment **614** (2010), no. 3, 483. 3

[SCFR94] A. Stingl, Christian Spielmann, Ferenc Krausz, and Robert Szipocs, *Generation of 11–fs pulses from a ti:sapphire laser without the use of prisms*, Opt. Lett. **19** (1994), no. 3, 204–206. 3.5.1

[SDT+96] YL Shao, T. Ditmire, JWG Tisch, E. Springate, JP Marangos, and MHR Hutchinson, *Multi-keV electron generation in the interaction of intense laser pulses with Xe clusters*, Physical review letters **77** (1996), no. 16, 3343–3346. 2.2.5

[SDT98] R. A. Smith, T. Ditmire, and J. W. G. Tisch, *Characterization of a cryogenically cooled high-pressure gas jet for laser-cluster interaction experiments*, no. 11, 3798. 3, 3.1.2, 3.1.2, 3.3, 3.1.2

[SETZ+10] E. Skopalová, Y. C. El-Taha, A. Zaïr, M. Hohenberger, E. Springate, J. W. G. Tisch, R. A. Smith, and J. P. Marangos, Phys. Rev. Lett. **104** (2010), 203401. 6.2

[SFM+02] I.Y. Skobelev, A.Y. Faenov, AI Magunov, TA Pikuz, AS Boldarev, VA Gasilov, J. Abdallach, GC Junkel-Vives, T. Auguste, S. Dobosz, et al., *X-ray spectroscopy diagnostic of a plasma produced by femtosecond laser pulses irradiating a cluster target*, Journal of Experimental and Theoretical Physics **94** (2002), no. 5, 966–976. 2.2.6

[SHT+00] E. Springate, N. Hay, JWG Tisch, MB Mason, T. Ditmire, MHR Hutchinson, and JP Marangos, *Explosion of atomic clusters irradiated by high-intensity laser pulses: Scaling of ion energies with cluster and laser parameters*, Physical Review A **61** (2000), no. 6, 063201. 4.3

[SKK+08] Mi-Young Song, Takako Kato, Daiji Kato, Izumi Murakami, and Y. Ralchenko, *Total and Partial Dielectronic and Radiative Recombination of Xe^{10+} Ions*, Journal of the Physical Society of Japan **77** (2008), no. 6, 064302. 3

[SKS91] D. E. Spence, P. N. Kean, and W. Sibbett, *60-fsec pulse generation from a self-mode-locked ti:sapphire laser*, Opt. Lett. **16** (1991), no. 1, 42. 1, 2, 3.5.1

[SL06] Frank Stienkemeier and Kevin K Lehmann, *Spectroscopy and dynamics in helium nanodroplets*, Journal of Physics B: Atomic, Molecular and Optical Physics **39** (2006), no. 8, R127. 1, 3.2, 3.5, 3.6, 3.3, 3.3, 3.3.1, 4.1.1, 6.2

[SLF+91] HR Siekmann, C. Lüder, J. Faehrmann, HO Lutz, and KH Meiwes-Broer, *The pulsed arc cluster ion source (PACIS)*, Zeitschrift für Physik D Atoms, Molecules and Clusters **20** (1991), no. 1, 417. 5

[SLS+95] A. Stingl, M. Lenzner, Ch. Spielmann, F. Krausz, and R. Szipocs, *Sub-10-fs mirror-dispersion-controlled ti:sapphire laser*, Optics letters **20** (1995), no. 6, 602. 3.5.1

[SM85] D. Strickland and G. Mourou, *Compression of amplified chirped optical pulses.*, Opt. Comm. **56** (1985), 219. 1, 2, 3.5.2

[SOBP04] F. Stienkemeier, F. Ancilotto M. Barranco O. Buenermann, R. Mayol, and M. Pi, Phys. Rev. B **70** (2004), 1. 3.2

[SPDC90] Robin Shakeshaft, R. M. Potvliege, Martin Dörr, and W. E. Cooke, *Multiphoton processes in an intense laser field. IV. The static-field limit*, Phys. Rev. A **42** (1990), no. 3, 1656–1668. 2.1.1

[SR02] C. Siedschlag and J.M. Rost, *Electron release of rare-gas atomic clusters under an intense laser pulse*, Physical review letters **89** (2002), no. 17, 173401. 2.2.2

[SR03] Ulf Saalmann and Jan-Michael Rost, *Ionization of clusters in intense laser pulses through collective electron dynamics*, Phys. Rev. Lett. **91** (2003), no. 22, 223401. 2.2.2, 2.2.2, 2.7, 4, 4.2, 5.2

[SR08] U. Saalmann and J.M. Rost, *Rescattering for extended atomic systems*, Physical review letters **100** (2008), no. 13, 133006. 2.2.5, 2.2.5

[SS03] H. Stapelfeldt and T. Seideman, *Colloquium: Aligning molecules with strong laser pulses*, Rev. Mod. Phys. **75** (2003), no. 2, 543–557. 6.2

[SSH+06] S. Sakabe, K. Shirai, M. Hashida, S. Shimizu, and S. Masuno, *Skinning of argon clusters by coulomb explosion induced with an intense femtosecond laser pulse*, Physical Review A **74** (2006), no. 4, 043205. 5.1

[SSM10] M. Strebel, F. Stienkemeier, and M. Mudrich, *Improved setup for producing slow beams of cold molecules using a rotating nozzle*, Phys. Rev. A **81** (2010), 033409. 3.2, 3.6

[SSR06] U. Saalmann, Ch. Siedschlag, and J. M. Rost, J. Phys. B **39** (2006), R39. 1, 2.2.2, 2.2.2, 2.6, 2.2.5, 2.2.5, 2.2.7, 2.3, 2.3, 4, 5.2, 6.2

[ST99] L. Gallmann N. Matuschek F. Morier-Genoud U. Keller V. Scheuer G. Angelow Sutter, G. Steinmeyer and T. Tschudi, Opt. Lett. **24** (1999), 631. 3.5.1

[STK+99] M. Schumacher, S. Teuber, L. Köller, J. Köhn, J. Tiggesbäumker, and K. H. Meiwes-Broer, *Clusters in strong laser fields: Comparison between carbon, platinum, and lead clusters*, The European Physical Journal D-Atomic, Molecular, Optical and Plasma Physics **9** (1999), no. 1, 411. 2.2.4

[SZS+11] Michael Schuricke, Ganjun Zhu, Jochen Steinmann, Konstantinos Simeonidis, Igor Ivanov, Anatoli Kheifets, Alexei N. Grum-Grzhimailo, Klaus Bartschat, Alexander Dorn, and Joachim Ullrich, *Strong-field ionization of lithium*, Phys. Rev. A **83** (2011), no. 2, 023413. 3.1.1

[TARB+11] S. Ter-Avetisyan, B. Ramakrishna, M. Borghesi, D. Doria, M. Zepf, G. Sarri, L. Ehrentraut, A. Andreev, PV Nickles, and S. Steinke, *MeV negative ion generation from ultra-intense laser interaction with a water spray*, Applied Physics Letters **99** (2011), 051501. 6.2

[TASBN04] S. Ter-Avetisyan, M. Schnürer, S. Busch, and P.V. Nickles, *Negative ions from liquid microdroplets irradiated with ultrashort and intense laser pulses*, Journal of Physics B: Atomic, Molecular and Optical Physics **37** (2004), 3633. 6.2

[TBH+09] H. Thomas, C. Bostedt, M. Hoener, E. Eremina, T. Fennel, K.H. Meiwes-Broer, M. Kuhlmann, E. Plönjes, R. Treusch, A.R.B. de Castro, and T. Möller, J. Phys. B **42** (2009), 134018. 3

[TDF+01] S. Teuber, T. Döppner, T. Fennel, J. Tiggesbäumker, and KH Meiwes-Broer, *Ionic recoil energies in the coulomb explosion of metal clusters*, The European Physical Journal D-Atomic, Molecular, Optical and Plasma Physics **16** (2001), no. 1, 59. 2.2.7

[TGB11] Daniela Rupp Sebastian Schorb Thomas Möller Robert Hartmann Daniel Rolles Artem Rudenko Ilme Schlichting Lothar Strüder Bill White Joachim Ullrich Ryan Coffee Tais Gorkhover, Marcus Adolph and Christoph Bostedt, *Pump-probe scattering experiments on exploding rare gas clusters at lcls x-fel*, 75th Annual Meeting of the DPG and DPG Spring Meeting, 2011. 1, 7, 5.2

[THG+10] NX Truong, P. Hilse, S. Göde, A. Przystawik, T. Döppner, T. Fennel, T. Bornath, J. Tiggesbäumker, M. Schlanges, G. Gerber, et al., *Optimal control of the strong-field ionization of silver clusters in helium droplets*, Physical Review A **81** (2010), no. 1, 013201. 2.2.2

[THS+03] R.S. Taylor, C. Hnatovsky, E. Simova, D.M. Rayner, VR Bhardwaj, and P.B. Corkum, *Femtosecond laser fabrication of nanostructures in silica glass*, Optics letters **28** (2003), no. 12, 1043. 6.2

[Tow02] C.H. Townes, *How the laser happened: Adventures of a scientist*, Oxford University Press, USA, 2002. 1

[TS07] J. Tiggesbäumker and F. Stienkemeier, *Formation and properties of metal clusters isolated in helium droplets*, Phys. Chem. Chem. Phys. **9** (2007), 4748. 3.3.1, 3.3.1, 3.11, 5, 6.2

[TV98] J. Peter Toennies and Andrei F. Vilesov, *Spectroscopy of atoms and molecules in liquid helium*, Annual Review of Physical Chemistry **49** (1998), no. 1, 1. 3.2

[TV04] J. Peter Toennies and Andrey F. Vilesov, *Superfluid helium droplets: A uniquely cold nanomatrix for molecules and molecular complexes*, Angewandte Chemie International Edition **43** (2004), no. 20, 2622. 1, 2.2, 3.2, 3.5, 3.2.2, 3.3.1, 4.1.1, 6.2

[UHH02] T. Udem, R. Holzwarth, and T. W. Hänsch, *Optical frequency metrology*, Nature **416** (2002), 233. 2.1.3, 6.2

[VdH81] H. C. Van de Hulst, *Light scattering by small particles*, Dover, 1981. 2.2.2, 2.2.2

[VK95] M. Vollmer and U. Kreibig, *Optical properties of metal clusters*, Springer Ser. Mat. Sci **25** (1995). 2.2, 2.2.2

[VK03] S. Vongehr and V. V Kresin, J. Chem. Phys. **119** (2003), 11124. 3.3.1

[VLG95] J.P. Verboncoeur, A.B. Langdon, and NT Gladd, *An object-oriented electromagnetic pic code*, Computer Physics Communications **87** (1995), no. 1-2, 199. 2.3

[WBK+01] K. B. Wharton, C. D. Boley, A. M. Komashko, A. M. Rubenchik, J. Zweiback, J. Crane, G. Hays, T. E. Cowan, and T. Ditmire, *Effects of nonionizing prepulses in high-intensity laser-solid interactions*, Physical Review E **64** (2001), no. 2, 025401. 2.2.6

[Wij10] H. Wijshoff, *The dynamics of the piezo inkjet printhead operation*, Physics Reports **491** (2010), no. 4-5, 77–177. 3.2

[Wiz79] J. D. Wiza, Nuclear Instruments and Methods **162** (1979), 587. 3.4.1

[WL97] Cai Weiping and Zhang Lide, *Synthesis and structural and optical properties of mesoporous silica containing silver nanoparticles*, J. Phys.: Condens. Matter **9** (1997), 7257. 6.2

[WM55] W. C. Wiley and I. H. McLaren, *Time-of-flight mass spectrometer with improved resolution*, no. 12, 1150. 3.4, 3.4, 3.4, 5.3

[WM06] X. Wang and P. H. McMurry, *An experimental study of nanoparticle focusing with aerodynamic lenses*, International Journal of Mass Spectrometry **258** (2006), no. 1, 30. 7, 6.2

[WSD+94] B. Walker, B. Sheehy, L.F. DiMauro, P. Agostini, K.J. Schafer, and K.C. Kulander, *Precision measurement of strong field double ionization of helium*, Phys. Rev. Lett. **73** (1994), no. 9, 1227–1230. 2.1.2

[WSKD96] B. Walker, B. Sheehy, K. C. Kulander, and L. F. DiMauro, *Elastic rescattering in the strong field tunneling limit*, Physical Review Letters **77** (1996), no. 25. 1

[WVGM01] J. Wörmer, J. Stapelfeldt V. Guzielski, and T. Möller, Chemical Physics Letters **159** (2001), 321. 3.1.2

[YI01] Gennady L. Yudin and Misha Yu. Ivanov, *Nonadiabatic tunnel ionization: Looking inside a laser cycle*, Phys. Rev. A **64** (2001), no. 1, 013409. 2.1.1

[ZB95] T. Zuo and A. D. Bandrauk, *Charge-resonance-enhanced ionization of diatomic molecular ions by intense lasers*, Phys. Rev. A **52** (1995), R2511—R2514. 2.2.2

[ZDP99] J. Zweiback, T. Ditmire, and M. D. Perry, Phys. Rev. A **59** (1999), R3166. 2.2.2, 2.8, 4, 5.1, 5.1.1

[Zew02] A. H. Zewail, *Voyage through time: walks of life to the nobel prize*, World Scientific Pub Co Inc, 2002. 1

[ZFP+11] S. Zherebtsov, T. Fennel, J. Plenge, E. Antonsson, I. Znakovskaya, A. Wirth, O. Herrwerth, F. Süßmann, C. Peltz, and I. Ahmad, *Controlled near-field enhanced electron acceleration from dielectric nanospheres with intense few-cycle laser fields*, Nature Physics **7** (2011), 656. 6.2

[ZMN+04] S. Zamith, T. Martchenko, Y. Ni, SA Aseyev, HG Muller, and MJJ Vrakking, *Control of the production of highly charged ions in femtosecond-laser cluster fragmentation*, Physical Review A **70** (2004), no. 1, 011201. 2.2.2

Acknowledgements

I am very grateful and deeply indebted to two remarkable scientists at the Max Planck Institut für Kernphysik (MPIK), Heidelberg, Germany, under whose supervision the work presented in this dissertation was carried out. Prof. Dr. Joachim Ullrich and Dr. Robert Moshammer guided me through the process of facing challenges and doing research. Interactions with Prof. Ullrich were intense and brief, very much like the pulses used in these experiments. They steered the dynamics of my research giving it direction while leaving enough room for ones own enterprise and ideas. It was admirable to see how he kept track of every detail of my work given his endless itinerary, and came up with some of the best insights. My work was guided in a continuous mode by Robert. Working and doing physics with Robert is a great pleasure. It was an education to discuss any aspect of physics with him. Robert urged me and other students to aim at a clear conceptual understanding with the simple questions: "What is the physics?" and "Can you explain it your grandmother?" As a result, along with guidance I found ample motivation, encouragement and freedom during the course of my work. I am also grateful to Prof. Dr. Selim Jochim for consenting to be one of my graduate advisors. The project itself was initiated as a part of the Max-Planck-India Partner Group with Prof. M. Krishnamurthy at the Tata Institute of Fundamental Research (TIFR), Mumbai, India. MK's experience with clusters was important for taking a quick plunge into this area. I wish to thank MK for expressing confidence in my abilities to handle this project and for initiating me into experimental physics. He is also a great motivator and friend.

The most fortunate turning point in this adventure was joining hands with Dr. Marcel Mudrich at University of Freiburg. All the experiments described in this work were done together with Marcel. It is an immense pleasure and a learning experience to work with Marcel. I greatly benefitted from his wide experience and skill. Due to Marcel's enterprise, learning about the He nanodroplet source in a short while became possible. I cherish this resonant interaction, both in scientific issues and in matters of taste, like Marcel's love for Indian cuisine. The physics was experimental and the fun was real! In this regard, I should thank Lutz Fechner for his resourceful inputs during the experiments and after that, and for proof-reading a good part of my thesis. We are grateful to Prof. Frank Stienkemeier at Uni. Freiburg for his cheerful and generous support. I am also grateful to Dr. Oliver Bünermann for helping us use his Monte-Carlo code for the estimation of doping levels and to Dr. Severin Müller for modifying the data acquisition program to suit our needs.

This fruitful and fortuitous collaboration involved working with a group of excellent theorists from the Max Planck Institut für Physik Komplexer Systeme, Dresden -

Dr. Alexey Mikarberidze. Prof. Dr. Ulf Saalmann and Prof. Dr. Jan-Michael Rost. I am very grateful Alexey for putting together a set of beautiful simulations in the wake of his Ph. D. examination within a short span of time. These were crucial to the success of our paper. Our collaboration also involved skiing lessons from Alexey for me at Riezlern. It is a pleasure to say "vielen Dank" to Ulf for his key role in the collaboration and for his encouragement during the course of my thesis work. Many nice and instructive discussions with him various aspects of laser-cluster interactions have gone a long way in my understanding and appreciation of the subject. I benefited greatly from his vast experience and thank him for his willingness to examine my thesis. I am grateful to Prof. Rost for his interest in the joint work and the personal attention he gave in preparing the manuscript, especially considering his endless list of responsibilities. Exchanging emails with him past mid-night, close to the submission of our paper, was both inspiring and humbling. And, thanks to Prof. Rost for showing me the way into "Mau Mau" (in Riezlern) - the German version of the card-game "Uno".

At Heidelberg, fellow colleagues in the Moshammer lab were ever-willing to support with the laser and other aspects of the experiments. These experiments were only possible due to the ready assistance of Manuel, Bettina, Vandana and Nicolas who are mentioned in chronological order. I thank Manuel for help inside and outside the lab, especially when I just landed in Germany. I also thank him for proof-reading a large part of my thesis. Bettina's wonderful amicability and patience made a significant difference to the lab. Her lessons on the laser and encouragement to learn dancing (outside the lab) serve the present and the future. Vandana is a great colleague to have, both as a scientist and a person. Her ever-ready assistance, even while carrying Viha, was crucial to the success of our work. I must thank Ram for being a good friend at and outside work, sharing the ups and downs for the journey. Ram and Vandana often created a home away from home for me in Heidelberg. I cherish our unforgettable association. It was very nice and timely to have Aditya's company at the Institute and outside. I am grateful to Aditya for his prompt assistance with troubleshooting in the lab. Invitations from him always set new standards of quality in dining. I am also grateful to Dr. Jagannath Jha at TIFR, Mumbai, for encouragement and support during the work.

The experimental hall in the Bothe lab runs on Dr. Claus-Dieter Schröter's remarkable energy with the able support of Bernd Knape. In spite of his many responsibilities, Claus-Dieter was ever-willing lend his expertise to the design and execution of our experiment. In the process, his eye for detail and technical knowledge were sources from which I learnt a lot. I am grateful to him and Bernd for all the efforts and inputs. I must thank Dr. Konstantinos Simeonedis for many good suggestions during the work. I am also grateful to the leaders of other groups in the Ullrich Division, Dr. Alexander Dorn, Dr. Daniel Fischer and Dr. Jose R. Crespo-Lopez Urrutia for their willingness to share equipment and ideas from time to time. I thank the members of the workshop at MPIK for many skillful pieces of machining that formed the building blocks of our experiments.

A special word of thanks goes to Dr. Thomas Pfeifer. Thomas always found time to help me with many technical aspects and to have plenty of discussions on physics. His appetite for science and insightful approach towards understanding were enthusiastic and infectious. It is pleasure to discuss any topic with Thomas. I am

grateful to him for making all this possible. It is also a pleasure to acknowledge many discussions on clusters with Thomas Fennel and Josef Tiggesbaümker at the University of Rostock.

I am grateful to Prof. G. Ravindra Kumar at TIFR, Mumbai, for letting me play with his picosecond laser as much as I wanted before I came to Heidelberg, and for recommending me to the MPIK. I am glad to thank Prem, Suman and Dr. Arnaud Couairon for our collaboration on filamentation which taught me many aspects of femtosecond pulses. I thank Prof. D. Mathur and Dr. A. Dharmadhikari at TIFR for the opportunities to work on ultrashort optics in their lab. It was nice to work with Sangeetha Hari at TIFR on the Thomson spectrometer.

It is very appropriate to express my gratitude and indebtedness to my physics and science teachers in the collegiate phase: Professors K. Venkataramaniah, K. Srinivasan, M. K. Sundaresan, Debendranath Sahoo, P. C. Sood, Shailesh Srivastava, Sivasankara Sai, Raj Kumar Jain, K. S. Umesh, O. S. K. S. Sastry, Subramanian, K. S. Narahari, C. N. Sundaresan, T. Ravi Kumar and R. Gowri Shankar. I am specially grateful to Prof. A. M. Rao, Clemson University, USA, for motivating and encouraging me to pursue doctoral research.

Colleagues in the Ullrich Division and the MPIK formed an inseparable part of the ups and downs of this journey. For all the good times, I'll remember Renate Hubele, Andreas Fischer (along with Julie), Helga Rietz, Alexander Sperl, Michael Schuricke, Bennaceur Najjari, Thomas Pflüger, Arne Senftleben, Kai-Uwe Kühnel, Katharina Kubicek, Andreas Kaldun, Kristina Meyer, Michael Schönwald, Phillip Raith, Katharina Schneider, Aaron LaForge, Anne Bochow and Ryan Chavez. I am grateful to Sven Augustin for a careful reading of the theory chapter of this thesis and to Kirstin Schnörr for many cheerful conversations. Marta Diaz and I were setting pace for each other in the thesis-writing-marathon, thanks to her lifting up my spirits on many occasions. And to Peter Caradonna for cheering us both all the way along. My cool and composed office-mate Moritz Kurka enabled a pleasant scientific atmosphere at work and assisted me in several domestic matters for which I am very grateful. My Indian colleagues and their families deserve a special mention for the many happy get-togethers we had - Gopi and Bhakti, Ashutosh and Sangeeta, Samanta and Farzana, Varun and Samta, Deepankar and Sonika, and Naveen.

Anil, Vidya, Vishnu, Ramya, Abdul, Shahina, Sampath, KK, Mathias, Tina, Goran, Biljana, Hernan and Florencia enriched life outside work in more ways than one. My sister Janani's sweet concern for me and my work is heartwarming. Back in India, Subbu, Vidya, Deepa, Suma and Sathya formed the family that took care of me during the entire course of work, and continue to do so.

Finally, I thank the tax-payers of this great country, Deutschland, who patronize the science done here through the Max Planck Society. I am grateful to the International Max Planck Research School - Quantum Dynamics (IMPRS-QD) for funding me through their stipendium. Danke sehr!

I dedicate this work to my life-givers: *Amma* and *Swami*. She brought me up and nourished me through tough times. He created the institutions where I received all my education without any monetary cost whatsoever, which given the Indian system is indeed a miracle!